

Path Integral Methods for Polarons in Materials

Bradley Andrew Alan Martin

SUBMITTED IN PARTIAL FULFILMENT OF THE
REQUIREMENTS FOR THE DEGREE OF DOCTOR OF
PHILOSOPHY OF IMPERIAL COLLEGE LONDON AND
THE DIPLOMA OF IMPERIAL COLLEGE LONDON BY



IMPERIAL COLLEGE LONDON
DEPARTMENT OF PHYSICS

SEPTEMBER 2024

To my mum, Debbie. You never got to see me grow into the person I am today, but as a young boy, you described me as a deep thinker. You encouraged me, with all your heart and through your actions, to never give up. So I dedicate my thesis to you. Although you are no longer with us, your resilience and support have never left me.

— STATEMENT OF ORIGINALITY —

I, Bradley Andrew Alan Martin, hereby declare that the thesis entitled “Path Integral Methods for Polarons in Materials” submitted to Imperial College London for the degree of Doctor of Philosophy is my original work and has not been submitted for any other degree or qualification at any other institution.

This thesis represents my independent research and analysis, and I affirm that all sources and references have been duly acknowledged. I have adhered to the academic integrity and ethical standards expected by Imperial College London, and all contributions from other sources have been properly cited.

I acknowledge that this work may be subject to plagiarism detection software and confirm that the content of this thesis is free from any form of academic dishonesty.

— COPYRIGHT STATEMENT —

The copyright of this thesis rests with the author. Unless otherwise indicated, its contents are licensed under a [Creative Commons Attribution-NonCommercial-NoDerivatives 4.0 International Licence](#) (CC BY-NC-ND 4.0).

Under this licence, you may copy and redistribute the material in any medium or format on the condition that; you credit the author, do not use it for commercial purposes and do not distribute modified versions of the work.

When reusing or sharing this work, ensure you make the licence terms clear to others by naming the licence and linking to the licence text.

Please seek permission from the copyright holder for uses of this work that are not included in this licence or permitted under UK Copyright Law.

— ABSTRACT —

This dissertation develops advanced theoretical techniques for modelling polarons in technologically significant materials, expanding upon Feynman's path integral approach[1]. Polarons, quasiparticles formed by the interaction of an electron or hole with lattice vibrations (phonons), play a fundamental role in determining charge transport properties, especially in semiconductors where electron-phonon interactions are crucial. Using Feynman's variational path integral approximation (FVA) [2] for the Fröhlich polaron [3], this work constructs a non-perturbative framework to model polaron dynamics, extending it to handle more complex electron-phonon interactions in real materials.

A significant contribution of this thesis is the generalisation of the material action to account for multiple phonon modes [4], thus reflecting the realistic phonon spectra of modern materials. Further extensions include treatments of the small Holstein polaron [5–7], anisotropic effective mass bands [8], and many-body polaron systems, enabling the path integral formalism to be applied to materials with complex lattice dynamics and multiple phonon branches. This approach enhances the predictive power of the formalism for material-specific phenomena.

Another critical advancement is improving the trial path integral action used in the variational approximation. Building on Feynman's spring-mass harmonic model, this thesis develops a more sophisticated trial action that couples the electron to multiple fictitious spring-mass particles. Additionally, an extended Feynman-Jensen inequality is introduced, incorporating higher-order cumulant corrections to improve the accuracy of calculated polaron properties such as self-energy and mobility across various electron-phonon coupling regimes.

The thesis also focuses on calculating dynamic response functions, including charge-carrier mobility and optical conductivity, using the Feynman-Hellwarth-Iddings-Platzman (FHIP) approximation [9]. The framework is expanded to more complex polaron models, such as multimode phonon systems and the Holstein small polaron. This results in a temperature- and frequency-dependent model for charge-carrier mobility. These results are rigorously

validated against Diagrammatic Monte Carlo (DMC) simulations [10], confirming the accuracy and applicability of the models to real-world materials.

This work introduces the open-source computational package, `PolaronMobility.jl` [11], implemented in Julia [12], which facilitates the numerical evaluation of polaron properties and response functions. This tool enables high-throughput computational screening of materials, bridging the gap between theoretical advancements and practical applications. The package has been demonstrated through case studies on methylammonium lead halide perovskites [4] and rubrene organic crystals [7], where polaron mobility, binding energy, and optical conductivity were calculated, showing how the methods developed here can provide valuable insights into material performance in optoelectronic applications.

Finally, the thesis conducts a high-throughput material classification study, evaluating over 1,200 materials from the Materials Project [13] and Liege [14] databases. This large-scale analysis identifies materials with potential for high-mobility applications based on parameters such as polaron effective mass, zero-point renormalisation energy, and room-temperature mobility. The findings offer a roadmap for discovering materials with optimal electron-phonon coupling characteristics for various technological applications.

In summary, this dissertation expands the theoretical and computational frameworks available for the study of polarons, providing a predictive tool for calculating temperature- and frequency-dependent charge transport properties. These developments lay the groundwork for future research into polaron dynamics and contribute significantly to the computational design of materials for use in semiconductors and optoelectronics.

— ACKNOWLEDGEMENTS —

I would like to express my deepest gratitude to all those who have supported me throughout the completion of this thesis.

First and foremost, I am profoundly grateful to my supervisors, Jarvist and Jenny, for their invaluable guidance, encouragement, and unwavering support throughout this research. Their insightful feedback and expert advice were instrumental in shaping the direction and quality of this work.

I also wish to thank the members of Frost group, Hanbo Yang, PK, Lucius ..., for their constructive criticism and thoughtful suggestions, which greatly enhanced the depth and clarity of my research throughout my PhD.

Special thanks to Xavier and Bogdan; Shawn and Artem; and Stefano ... for their collaboration and assistance with Your contributions were crucial to the successful completion of this project.

I am indebted to the Physics and Chemistry Departments at Imperial for providing the necessary resources and a conducive environment for my research. The administrative and technical support from the Experimental Solid State Group was greatly appreciated.

My heartfelt appreciation goes to my family and friends for their patience, understanding, and encouragement during the challenging times of this journey. Their constant support provided me with the motivation and strength to persevere.

Finally, I extend my gratitude to...

Thank you all for being part of this academic endeavour.

— CONTENTS —

List of Figures	12
List of Tables	20
List of Acronyms	22
List of Symbols	24
1 Introduction	27
1.1 The Polaron	27
1.2 Polaron Response Functions	28
1.3 Relevance: Semiconductor Materials	28
1.4 Thesis Overview	29
2 Background	31
2.1 Polaron Physics	31
2.1.1 A Brief History	33
2.1.2 Fröhlich's Large Polaron	37
2.1.3 Holstein's Small Polaron	44
2.2 The Feynman Path Integral & Variational Approach	50
2.2.1 Ground-State Polaron	50
2.2.2 Feynman-Jensen Variational Principle	54
2.2.3 Feynman's Quasi-Particle Trial Model	55
2.2.4 Weak- and strong- coupling limits	60
2.2.5 Feynman's polaron effective mass	61
2.2.6 Schultz's polaron effective size	62
2.2.7 Generalisation to n dimensions	63
2.2.8 Athermal FVA Numerical Results	65
2.2.9 Finite Temperature Polaron	66
2.2.10 Thermal FVA Numerical Results	71
2.3 Influence Functionals & Response Functions	75

2.3.1	Polaron DC Mobility	75
2.3.2	FHIP Polaron Mobility Numerical Results	83
2.3.3	The FHIP initial product state and low-temperature mobility . .	85
2.3.4	FHIP Memory Function Numerical Results	86
2.3.5	Optical Conductivity	92
2.3.6	DSG Optical Conductivity Numerical Results	94
2.3.7	Effective Multimode Mobility	100
2.4	Material Case Studies	109
2.4.1	Methylammonium Lead Halide Perovskite	109
2.4.2	Rubrene Organic Crystal	110
2.5	Outlook for this Thesis	113
3	Generalising the Material Path Integral Model	115
3.1	Multiple Phonon Modes	115
3.1.1	Multimodal Fröhlich Hamiltonian	116
3.1.2	Multiple Phonon Mode Path Integral	117
3.2	Lattice Polarons	119
3.2.1	Discrete-Time Path Integral	119
3.2.2	Continuous-Time Path Integral	122
3.2.3	Thermodynamic and Continuum Limits	123
3.2.4	The Effective Mass (Parabolic-Band) Approximation	124
3.3	The General Parabolic Polaron	127
3.3.1	General Phonon-Band Polarons	128
3.3.2	Effective-mass anisotropy	129
3.4	Many Polaron Theory	130
4	Improving the Trial Path Integral Model and Variational Approximation	132
4.1	Multiple Phonon Mode Variational Solution	132
4.1.1	Multiple Phonon Mode Free Energy	132
4.2	Lattice Polaron Variational Solution	134
4.2.1	Athermal Holstein Polaron	135
4.2.2	Thermal polarons	139
4.3	The General Parabolic Polaron Variational Solution	142
4.4	Multiple Fictitious Particles	145
4.4.1	Numerical Results	146
4.4.2	The additional parameters	147
4.4.3	Improving the Energy Bound	150
4.5	The Optimal Functional Solution	152
4.5.1	Generalised Trial Action	152

4.5.2	Self-consistent Equations	154
4.6	Cumulant Expansion Corrections	156
5	Computing Response Functions & Polaron Mobility	160
5.1	Numerical Evaluation of the Memory Function	160
5.2	Violation of the Mott-Ioffe-Regel criterion versus Planckian bound	162
5.3	Comparison to Diagrammatic Monte Carlo	163
5.4	Multiple Phonon Mode Dynamics	166
5.5	Multiple Fictitious Particle Dynamics	167
5.5.1	The Effect on Dynamics	167
5.6	The Holstein Model	169
5.6.1	Polaron Mobility	169
5.6.2	Holstein Memory Function at Zero Temperature	170
5.6.3	Holsten Optical Conductivity at Zero Temperature	172
5.6.4	Holsten Optical Conductivity at Finite Temperature	175
5.7	General Polaron Mobility	180
5.7.1	Specialising to the Fröhlich Model	181
5.7.2	Specialising to the Holstein Model	182
5.8	The Optimal Self-Consistent Response Function	183
5.8.1	Statics = Dynamics	183
6	Application for Materials	184
6.1	Methylammonium Lead Halide Perovskites	184
6.1.1	MAPI Polaron Free energy	186
6.1.2	MAPI DC Polaron Mobility	188
6.1.3	MAPI Polaron Optical Conductivity	189
6.1.4	MAPI Polaron Memory Function	191
6.1.5	Modelling Terahertz Spectroscopy Photoconductivity Dynamics in Metal-Halide Perovskites	193
6.2	Rubrene & Organic Crystals	196
6.2.1	Rubrene Athermal Properties	199
6.2.2	Rubrene Thermal Properties	199
6.2.3	Rubrene Complex Conductivity	200
6.3	Cubic & Anisotropic Materials	202
6.4	High-Throughput Material Classification	204
6.4.1	Polaron Zero-Point-Renormalisation Energy	204
6.4.2	Polaron Effective Mass	205
6.4.3	Room Temperature Polaron Mobility	207
7	Conclusion & Outlook	211

Appendices	223
A Path Integral Derivation	223
A.1 Particle interacting with a harmonic oscillator	224
B Feynman-Vernon Influence Functionals	225
C Memory Function Expansions	226
C.1 Contour integration of the memory function	226
C.2 $\text{Im}\chi$ expansion in Bessel-K functions	229
C.3 $\text{Re}\chi$ expansion in Bessel-I, Struve-L and ${}_1F_2$ hypergeometric functions .	232
D Coherent States	237

— LIST OF FIGURES —

<p>2.1 Electron-phonon coupling dependence of the Feynman athermal polaron theory in 2D (left) and 3D (right) in polaron units. Green is the negative of the variationally optimal ground-state energy E (units of $\hbar\omega_0$), purple is the polaron effective mass M (units of m_0), blue is the v (units of ω_0) variational parameter; red is the w (units of ω_0) variational parameter, orange is the polaron size R (units of r_0), and brown is the polaron spring-constant κ (units of $m_0\omega_0^2$).</p> <p>2.2 The temperature (T in units of $\hbar\omega_0/k_B$)- and electron-phonon α coupling-dependence of Ōsaka’s polaron in 2D (left) and 3D (right) for the free energy (top), Feynman effective mass (second row), the v variational parameter (third row) and the w variational parameter (bottom). In the top row, I plot the absolute value F of the free energy, such that for $\alpha = 0.1$, the value of F is positive for $T < 6\hbar\omega_0/k_B$ and negative above this temperature and the same sign at the other coupling strengths.</p> <p>2.3 The temperature (T in units of $\hbar\omega_0/k_B$)- and electron-phonon α coupling-dependence of Ōsaka’s polaron in 2D (left) and 3D (right) for the free energy (top), Feynman effective mass (second row), the v variational parameter (third row) and the w variational parameter (bottom). In the top row, I plot the absolute value F of the free energy, such that the dark curve indicates a change of sign where the free energy F in the small ‘island’ at weak coupling is positive.</p> <p>2.4 The temperature (T in units of the phonon frequency ($\hbar\omega_0/k_B$))- and electron-phonon α coupling-dependence of the polaron DC mobility (μ in units of $e\omega_0 m_0^{-1}$) for the Fröhlich model in 2D (left) and 3D (right).</p> <p>2.5 The electron-phonon α coupling- and frequency-dependence (Ω in units of ω_0) of the 2D (top) and 3D (bottom) Fröhlich polaron imaginary memory function $\text{Im } \Sigma(\Omega)$ (units of $\omega_0 m_0^{-1}$).</p>	<p>65</p> <p>73</p> <p>74</p> <p>84</p> <p>86</p>
-----------------------------------------------------------------------------------------------------------------------------------------------------------------------------------------------------------------------------------------------------------------------------------------------------------------------------------------------------------------------------------------------------------------------------------------------------------------------------------------------------------------------------------------------------------------------------------------------------------------------------------------------------------------------------------------------------------------------------------------------------------------------------------------------------------------------------------------------------------------------------------------------------------------------------------------------------------------------------------------------------------------------------------------------------------------------------------------------------------------------------------------------------------------------------------------------------------------------------------------------------------------------------------------------------------------------------------------------------------------------------------------------------------------------------------------------------------------------------------------------------------------------------------------------------------------------------------------------------------------------------------------------------------------------------------------------------------------------------------------------------------------------------------------------------------------------------------------------------------------------------------------------------------------------------------------------------------------------------------------------------------------------------------------------------------------------------------------------------------------------------------------------------------------------------------------------------------------------------------------------------------------------------------------------------------------------------------------------------------------------------------------------------------------------------------------------------------------------------------------------------------------------------------------------------------------------------------------------------------------------------------------------------------------------------------------------------------------------------------------------------------------------------------------------------------------------------------------------------	---------------------------------------------------

2.6	The temperature (T in units of $\hbar\omega_0/k_B$)- and frequency-dependence (Ω in units ω_0) of the imaginary component of the 2D Fröhlich polaron memory function $\text{Im } \Sigma(\Omega)$ (units of $\omega_0\omega_0^{-1}$) for electron-phonon couplings $\alpha = 1$ (top-left), 2 (top-right), 3 (middle-left), 4 (middle-right) and 5 (bottom).	89
2.7	The temperature (T in units of $\hbar\omega_0/k_B$)- and frequency-dependence (Ω in units ω_0) of the imaginary component of the 3D Fröhlich polaron memory function $\text{Im } \Sigma(\Omega)$ (units of $\omega_0\omega_0^{-1}$) for electron-phonon couplings $\alpha = 1$ (top-left), 2 (top-right), 3 (middle-left), 4 (middle-right), 5 (bottom-left) and 6 (bottom-right).	90
2.8	The electron-phonon α coupling- and frequency-dependence (Ω in units of ω_0) of the 2D (top) and 3D (bottom) Fröhlich polaron real conductivity $\text{Re } \sigma(\Omega)$ (units of $e^2\hbar^{-1}$).	94
2.9	The temperature (T in units of $\hbar\omega_0/k_B$)- and frequency-dependence (Ω in units of ω_0) of the real component of the 2D Fröhlich polaron conductivity $\text{Re } \sigma(\Omega)$ (units of $e^2\hbar^{-1}$) for electron-phonon couplings $\alpha = 1$ (top-left), 2 (top-right), 3 (middle-left), 4 (middle-right) and 5 (bottom)	97
2.10	The temperature (T in units of $\hbar\omega_0/k_B$)- and frequency-dependence (Ω in units of ω_0) of the real component of the 3D Fröhlich polaron conductivity $\text{Re } \sigma(\Omega)$ (units of $e^2\hbar^{-1}$) for electron-phonon couplings $\alpha = 1$ (top-left), 2 (top-right), 3 (middle-left), 4 (middle-right), 5 (bottom-left) and 6 (bottom-right). . .	98
2.11	Reprinted from ref. [20]. Crystal structure of methylammonium lead iodide ($\text{CH}_3\text{NH}_3\text{PbI}_3$) perovskite, referred to here as ‘MAPI’. The green octahedra represents the lead (Pb) atoms at the centre, coordinated by iodine (I) atoms at the vertices. The methylammonium (CH_3NH_3^+) organic cation occupies the spaces between the PbI_3 frameworks, interacting with the inorganic lattice. . .	109
2.12	Reprinted from ref. [73]. Crystal structure of rubrene showing its orthorhombic unit cell parameters. The unit cell dimensions are $a = 1.422$ nm, $b = 0.719$ nm, and $c = 2.686$ nm. The diagrams highlight the layered molecular arrangement within the unit cell, with the corresponding reciprocal lattice vectors displayed on the right, indicating spatial periodicity in the X, Y, and Z directions. . . .	111
4.1	Left: The electron-phonon coupling α dependence of the ground-state energy E (in units of $\hbar\omega_0$) of the 3D Fröhlich model (blue) and the parabolic Holstein model in 1D (red), 2D (green) and 3D (purple). Right: The electron-phonon coupling α dependence of the variational parameters v and w (in units of ω_0) for the 3D Fröhlich model (v blue , w red) and the parabolic Holstein model in 1D (v green , w purple), 2D (v orange , w brown) and 3D (v pink , w black).	136

4.2	The electron-phonon coupling α and adiabticity $\gamma = \hbar\omega/J$ (for $\gamma = 0.1, 0.5, 1.0, 1.5$ and 2.0) dependence of the parabolic Holstein ground-state energy in 1D (top-left), 2D (middle-left) and 3D (bottom-left), and polaron mass in 1D (top-left), 2D (middle-left) and 3D (bottom-left)	137
4.3	Polaron binding energy (in units of $\hbar\omega_0$) for the Holstein model with respect to the electron-phonon dimensionless coupling parameter α and adiabaticity $\gamma = \hbar\omega_0/J$. Top left: Comparison between the variational solution for the parabolic Holstein model (1D pink , 2D black and 3D light blue) to the DMC solution for the parabolic Holstein model (1D blue points , 2D red points and 3D green points) and tight-binding Holstein model (1D purple points , 2D orange points and 3D brown points). Top right: Comparison for the 1D parabolic Holstein model between the variational solution ($\gamma = 0.1$ purple , 0.3 orange and 0.5 brown) and the DMC solution ($\gamma = 0.1$ blue points , 0.3 red points and 0.5 green points). Bottom left: Comparison for the 2D parabolic Holstein model between the variational solution ($\gamma = 0.1$ purple , 0.3 orange and 0.5 brown) and the DMC solution ($\gamma = 0.1$ blue points , 0.3 red points and 0.5 green points). Bottom right: Comparison for the 3D parabolic Holstein model between the variational solution ($\gamma = 0.1$ purple , 0.3 orange and 0.5 brown) and the DMC solution ($\gamma = 0.1$ blue points , 0.3 red points and 0.5 green points). I also include the variational solution to the 3D Fröhlich model for comparison (pink)	138
4.4	Polaron binding energy (left) and effective mass (right) for the Holstein model in 1D (top), 2D (middle) and 3D (bottom) with respect to temperature (in units of the phonon frequency $\hbar\omega_0$), for values of the Holstein electron-phonon coupling $\alpha = 0.1, 2, 4, 6, 8, 10, 12$	140
4.5	Polaron variational parameters v (left) and w (right) for the Holstein model in 1D (top), 2D (middle) and 3D (bottom) with respect to temperature (in units of the phonon frequency $\hbar\omega_0$), for values of the Holstein electron-phonon coupling $\alpha = 0.1, 2, 4, 6, 8, 10, 12$	141

5.1 Comparison between the FHIP [17] (solid red line) and Mishchenko et al. [10] DMC (green dots with error bars) mobility (μ in units $e\omega_0/m_0$) temperature dependence (T in units of $\hbar\omega_0/k_B$) of the polaron mobility for $\alpha = 2.5$ (top-left), 4.0 (top-right) and 6.0 (bottom). The red dotted lines give the Mott-Ioffe-Regel (MIR) threshold.	163
5.2 Comparison between the FHIP [17] (solid lines) and Mishchenko et al. [10] DMC (dashed lines) mobility (μ in units $e\omega_0/m_0$) frequency dependence (Ω in units ω_0) for temperatures $T = 0.5\hbar\omega_0/k_B$ (black), $1.0\hbar\omega_0/k_B$ (green) and $2.0\hbar\omega_0/k_B$ (pink).	164
5.3 Real component of the complex conductivity $\text{Re } \sigma(\Omega)$ for the Fröhlich model for increasing number N of fictitious particles in the trial model. Left: The frequency-dependence of the real conductivity at $\alpha = 6$ and $\beta\omega_0 = 12.375$. Here I are in the regime for the maximum potential improvement on the trial model with the additional of fictitious particles. Despite minor improvements on the free energy approximation, the corresponding prediction for the real conductivity changes drastically due to the sensitivity of analytic continuation of the trial model. Right: Dependence of the ground-state ($T = 0$ K) real conductivity with the dimensionless electron-phonon coupling α . The real conductivity converges quickly to its optimal solution as soon as $N = 3$ with the maximal improvement occurring around $\alpha = 6$	168
5.4 Temperature dependence (T , in units of phonon frequency $\hbar\omega_0/k_B$) of the Holstein polaron DC mobility μ in 1D (top) and 2D (middle) and 3D (bottom).	169
5.5 Frequency dependence (Ω , in units of the phonon frequency ω_0) of the polaron imaginary memory function $\text{Im } \Sigma(\Omega)$ for the Holstein model in 1D (top), 2D (middle) and 3D (bottom).	171
5.6 Frequency dependence (Ω , in units of the phonon frequency ω_0) of the polaron optical conductivity $\sigma(\Omega)$ for the Holstein model in 1D (top), 2D (middle) and 3D (bottom).	173
5.7 Temperature dependence (T , in units of the phonon frequency $\hbar\omega_0/k_B$) of the polaron optical conductivity $\sigma(\Omega)$ for the 1D Holstein model for electron-phonon couplings $\alpha = 1$ (top-left), 2 (top-right), 3 (bottom-left) and 4 (bottom-right).	176
5.8 Temperature dependence (T , in units of the phonon frequency $\hbar\omega_0/k_B$) of the polaron optical conductivity $\sigma(\Omega)$ for the 2D Holstein model for electron-phonon couplings $\alpha = 1$ (top-left), 2 (top-right), 3 (middle-left), 4 (middle-right) and 5 (bottom).	177

5.9	Temperature dependence (T , in units of the phonon frequency $\hbar\omega_0/k_B$) of the polaron optical conductivity $\sigma(\Omega)$ for the 3D Holstein model for electron-phonon couplings $\alpha = 1$ (top-left), 2 (top-right), 3 (middle-left), 4 (middle-right), 5 (bottom-right) and 6 (bottom-right).	178
6.1	Left: Comparison of the polaron free energy as a function of temperature for MAPbI_3 , using the single effective phonon mode approach (blue) and the explicit multiple phonon mode approach (red). Top-right: Comparison of the two polaron variational parameters, v and w , for MAPbI_3 , with the single effective phonon mode approach (blue) and the explicit multiple phonon mode approach (red). Bottom: Comparison of the temperature-dependent mobility predicted for MAPbI_3 , using the single effective phonon mode approach (blue) and the explicit multiple phonon mode approach (red).	189
6.2	Temperature and frequency dependence of the real (left) and imaginary (right) components of the complex conductivity for MAPbI_3 , comparing two theoretical models for phonon interactions. The top row represents the single effective phonon mode approach, while the bottom row includes all explicit phonon branches.	190
6.3	Temperature and frequency dependence of the real (left) and imaginary (right) components of the polaron memory function for MAPbI_3 , comparing two theoretical models for phonon interactions. The top row uses a single effective phonon frequency, while the bottom row includes all explicit phonon branches.	192
6.4	Reprinted from ref. [89]. (a) Two-dimensional probe frequency vs. push–probe delay intensity map from a pump–push–THz probe experiment, with the pump–push delay set to 10 ps. (b) THz photoconductivity spectra showing the real and imaginary components of the complex conductivity ($\Delta\sigma = \Delta\sigma_{\text{Re}} + \Delta\sigma_{\text{Im}}$) before, during, and after the push. (c) Probe recovery time at different frequencies. (d) Simulated frequency-resolved conductivity using the FHIP polaron mobility theory, showing agreement with experimental peaks at 1.25 and 2.25 THz, corresponding to carrier-phonon coupling.	194
6.5	Polaron properties predicted from the variational parabolic Holstein and Fröhlich models for a bulk 3D Rubrene organic crystal. Top-left: The polaron binding energy (the polaron self-energy relative to the band extrema) F (meV) in Rubrene as a function of temperature (K). Top-right: Optimal variational parameters v and w (THz) as a function of temperature (K). Bottom The DC polaron mobility $\mu(T)$ ($\text{cm}^2\text{V}^{-1}\text{s}^{-1}$) as a function of temperature T (K).	197

6.6 Frequency dependence of the polaron complex conductivity (in units of S cm^{-1}) predicted by the variational parabolic Holstein and Fröhlich models for a bulk 3D Rubrene organic crystal, for temperatures $T = 0.48 \text{ K}, 100 \text{ K}, 200 \text{ K}, 300 \text{ K}$ and 400 K . The top row shows the real (left) and imaginary (right) components of the Fröhlich complex conductivity. The bottom row shows the components of the parabolic Holstein complex conductivity's real (left) and imaginary (right).	198
6.7 Both figures are taken from [8]. (left): The relative differences between the ground-state energy of the polaron determined using perturbation theory (which fully accounts for any anisotropy) and the Feynman variational approach (using my approximate treatment of anisotropy). (right): The relative difference between the effective masses was determined using perturbation theory and the Feynman variational approach (again, only approximately accounting for anisotropy). $m_{P,iso}^*$ is the isotropic effective mass, $m_{P,\perp}^*$ and $m_{P,z}^*$ are the in-plane and out-of-plane polaron effective masses.	202
6.8 The left panel shows the polaron energy E meV as a function of the electron-phonon coupling constant α , calculated using Feynman's variational path integral theory for various materials, with groups 15, 16, and 17 highlighted. The right panel compares the percentage energy difference between the weak-coupling perturbation theory and the Feynman result, showing increasing deviations at higher α , particularly beyond $\alpha = 6$, indicating the breakdown of perturbation theory in the strong-coupling regime.	204
6.9 Polaron effective mass as a function of the electron-phonon coupling constant α for 1258 materials, with group 15, 16, and 17 elements highlighted. The left panel shows the effective polaron mass at zero temperature, while the right panel displays the results at room temperature (300 K). The critical value of $\alpha = 6$ (red dashed line) marks the transition from weak to strong coupling.	205
6.10 Polaron mobility as a function of the electron-phonon coupling constant α at room temperature for 1258 materials, with group 15, 16, and 17 elements highlighted. The left plot shows mobility results using a single effective phonon mode based on Hellwarth and Biaggio's B scheme [21], while the right plot accounts for all phonon branches in the material. The red vertical line marks $\alpha = 6$, indicating a critical transition between weak and strong coupling regimes.	207

6.11 Polaron mobility at room temperature as a function of the electron-phonon coupling constant α (top row) and effective band mass m_e (bottom row) for 1258 materials, colour-coded by the band mass. The left column uses a single effective phonon mode from Hellwarth and Biaggio's B scheme [21], while the right column accounts for all phonon branches. A critical point at $\alpha = 6$ (red dashed line) marks the transition to the strong coupling regime, where mobility decreases sharply, especially for materials with larger band masses. 209

— LIST OF TABLES —

2.1 A (non-exhaustive) compendium of theoretical and computation results for studying polarons.	32
6.1 Parameters of the Feynman polaron model (single effective phonon mode) are used in this work. Relative high frequency (ϵ_∞) and static (ϵ_0) dielectric constants are given in units of the permittivity of free space (ϵ_{vac}). Frequency (f) is in THz. Effective mass (m_b) is in units of the bare electron mass. These data are as in Ref. [59].	185
6.2 Infrared activity of phonon modes in MAPbI_3 taken from [20], scaled to their ground-state polaron value by the multimodal $w = 2.6792$ factor for MAPbI_3 -e of this work (Table 6.3).	185
6.3 Athermal 0 K results. Dielectric electron-phonon coupling (α), Feynman athermal variational parameters (v and w) and polaron binding energy (E_b) for an effective phonon mode (top rows) and for multiple explicit phonon modes (bottom rows).	188
6.4 300 K Results. Dielectric electron-phonon coupling (α), Feynman thermal variational parameters (v and w), polaron free energy (F , meV), dc mobility (μ , $\text{cm}^2\text{V}^{-1}\text{s}^{-1}$), polaron effective mass (M , m^*) and Schultz polaron radius (r_f , Å) for an effective phonon mode (top rows) and for multiple explicit phonon modes from Table 6.2 (bottom rows).	188
6.5 3D Rubrene Bulk crystal data derived from [22]. Here g is the Holstein hole-phonon coupling element, ω_0 is the single-mode effective phonon frequency, J is the electron transfer/hopping integral, a is the geometric-meaned crystal lattice constant, γ is the Holstein adiabaticity unitless parameter, m_b is the effective hole band-mass, $\lambda^2 = (g/\hbar\omega_0)^2$ is the unitless squared hole-phonon coupling element and $\alpha = \lambda^2\gamma/6$ is the 3D unitless Holstein electron-phonon parameter.	196
6.6 Ground-state polaron properties for a Rubrene Bulk crystal calculated using the variational Holstein and Fröhlich models.	196

6.7 Room temperature (300 K) polaron properties for a Rubrene Bulk crystal calculated using the variational Holstein and Fröhlich models.	196
------------------------------------------------------------------------------------------------------------------------------------------------------	-----

— LIST OF ACRONYMS —

1D	One-dimensional
2D	Two-dimensional
3D	Three-dimensional
RHS	Right-hand Side
LHS	Left-hand Side
w.r.t	With Respect To
LO	<i>Longitudinal Optical</i>
DC	<i>Direct Current</i>
AC	<i>Alternating Current</i>
THz	<i>Terahertz</i>
FHIP	<i>Feynman-Hellwarth-Iddings-Platzman</i>
DSG	<i>Devreese-Sitter-Goovaerts</i>
CGS	<i>Centimetre-Gram-Second</i>
FVA	<i>Feynman Variational Approach</i>
PIMC	<i>Path Integral Monte Carlo</i>
DMC	<i>Diagrammatic Monte Carlo</i>
RES	<i>Relaxed Excited States</i>
FC	<i>Franck-Condon</i>
BTE	<i>Boltzmann Transport Equation</i>
CSPI	<i>Coherent State Path Integral</i>
IBM	<i>Independent Boson Model</i>

ZPR *Zero-Point Renormalisation*

TDSE *Time Dependent Schrödinger Equation*

— LIST OF SYMBOLS —

Greek symbols

\hbar	reduced Planck constant
τ	imaginary time coordinate
ω_*	phonon frequency
β	reciprocal thermodynamic temperature
δ	Dirac delta
δ_{ij}	Kronecker delta
κ	fictitious particle spring mass
Ω	external field frequency
σ	complex conductivity
Σ	polaron memory function
μ	polaron mobility
μ_0	electron and fictitious particle reduced mass
α	Fröhlich alpha
ρ_S	density function for action S
$\hat{\rho}$	electron density operator
γ	Holstein adiabaticity
Γ	Gamma function
ϵ	dielectric function
ϵ_0	static dielectric constant
ϵ_i	ionic dielectric constant
ϵ_∞	optical dielectric constant
ϵ_{vac}	vacuum permittivity
Φ	influence functional phase

Latin symbols

k	electron wavevector
q	phonon wavevector
r	electron position vector
x	phonon position vector
<i>t</i>	real time coordinate
<i>v</i>	polaron variational parameter
<i>w</i>	polaron variational parameter
V_0	3D unit cell volume
V_n	<i>n</i> -dimensional unit cell volume
k_B	Boltzmann constant
T	temperature parameter
m_f	fictitious particle mass
Z	partition function
z	complex impedance
G	trial polaron Green function
D_ω	phonon Green function of frequency ω
M	polaron effective mass
R	polaron effective radius
H	Hamiltonian
L	Lagrangian
S	polaron model action
S_0	polaron trial action
$M_{\mathbf{q}}$	electron-phonon coupling matrix
E	polaron ground-state energy
F	polaron Helmholtz free energy
J	transfer integral
J	external source field
E	electric field
D	electric displacement field
P	polarisation field
A	electric vector potential
<i>c</i>	speed of light
$c_{\mathbf{k}}^\dagger$	fermion creation operator

$c_{\mathbf{k}}$	fermion annihilation operator
$b_{\mathbf{q}}^{\dagger}$	boson creation operator
$b_{\mathbf{q}}$	boson annihilation operator

Polaron Units

ω_0	characteristic angular frequency
m_0	characteristic mass
r_0	characteristic length
e_0	electron charge

CHAPTER 1

INTRODUCTION

“The underlying physical laws necessary for the mathematical theory of a large part of physics and the whole of chemistry are thus completely known, and the difficulty is only that the exact application of these laws leads to equations much too complicated to be soluble. It, therefore, becomes desirable that approximate practical methods of applying quantum mechanics should be developed, which can lead to an explanation of the main features of complex atomic systems without too much computation.”

—Paul A. M. Dirac, *Quantum mechanics of many-electron systems*, 1929

In this dissertation, I develop methods that can offer fully predictive temperature- and frequency-dependent mobilities for various systems of technical interest, thereby offering design clues for and methods to screen new materials computationally. Specifically, this thesis aims to predict semiconductor materials ‘polaronic’ properties and how they impact the underlying electron transport. The key methodology used and expanded upon lies in Feynman’s path integral approach to quantum physics, which has proven to be a powerful approach to modelling the polaron.

1.1 The Polaron

The polaron is a quasiparticle formed from the interaction of charge carriers with the vibrational modes of a material’s atomic lattice. This can equivalently be thought of as a quantum field theory of a single charged fermion interacting with a bosonic field; this is the phonon field for the polaron. The formation of a polaron can significantly alter the properties of a material [15], and it is essential to understand polarons to predict the mobility of charge carriers accurately. The extent of a polaron can be large (encompassing multiple

lattice sites), where the polaron often moves around the material, or small (comparable or smaller than a lattice constant), where the polaron becomes localised to individual lattice sites. The large polaron is commonly modelled by the Fröhlich Hamiltonian [3], and the small polaron by the Holstein Hamiltonian [5, 6].

The key methodology this thesis builds upon is Feynman's variational path integral approximation (FVA) [2]. This method translates the Fröhlich polaron Hamiltonian into an action, which is used to derive the partition function for the system as a path integral. Since the phonon coordinates enter the action quadratically, the phonon path integral is Gaussian. Its closed-form expression results in an effective temporally non-local potential acting on the electron. This model action typically has no known exact solution. This partition function is then approximated by a trial partition function derived from a trial action, requiring that this partition function has a closed-form expression (typically limiting the trial action to be quadratic). Feynman chose this trial action to represent an electron harmonically coupled to a fictitious particle via a spring, his so-called ‘spring-mass model’. Using Jensen’s inequality for convex functions, Feynman derived an inequality for the polaron-free energy. An optimal upper bound is then found by varying the mass and spring constant of the trial model.

1.2 Polaron Response Functions

Further developments were also made using the Feynman-Vernon ‘influence functional’ method [16] to derive the reduced density matrix for a quantum system interacting with some external bath. The reduced density matrix can provide dynamic response functions such as optical conductivity and charge-carrier mobility. Building upon the success of the FVA, Feynman, Hellwarth, Iddings and Platzmann (FHIP) derived an approximate density matrix for the Fröhlich polaron model from a functional Taylor expansion of the polaron action about the optimal trial action [17]. This method was then used to predict the polaron mobility in FHIP and later the optical conductivity by Devreese, Sitter and Goovaerts (DSG) [18].

1.3 Relevance: Semiconductor Materials

Semiconductor materials have enormous technical applications ranging from photovoltaic cells and light-emitting diodes to field-effect transistors and solid-state lasers. A fundamental phenomenological quantity that influences the performance of a semiconductor is the charge-carrier mobility. The required mobility depends on the application; for example, a photovoltaic cell requires sufficient mobility to facilitate charge separation. As a phenomenological quantity, mobility is not a direct ground-state property. Instead,

mobility arises from competitive dynamic processes within a material and can be strongly temperature-dependent. Most mobility theories, like the Boltzmann Transport Equation (BTE) [19], use semi-classical approximations to model mobility, using an effective scattering time such as in Drude-like models or neglecting electron-phonon interactions as in the adiabatic Born-Oppenheimer approximation. Alternatively, the electron-phonon coupling is assumed to be weak or strong, so perturbative approaches can be taken. However, some semiconductors, such as lead halide perovskites, possess significant dielectric electron-phonon interactions, forming large polarons. These materials typically exhibit intermediate electron-phonon coupling strengths. Instead, one can use the path integral formulation of quantum mechanics to derive an inherently quantum mobility theory [2, 17]. Though based on a linear-response theory, this is non-perturbative and can provide a temperature and frequency-dependent mobility model valid to all orders in the electron-phonon coupling strength.

1.4 Thesis Overview

Although historically successful, the FVA and FHIP approaches to modelling polarons have not been extensively applied in the materials community. As such, much of the underlying theory has not been expanded upon and is only used for simple ‘toy models’. Likewise, these approaches have not been implemented in modern codes. Therefore, this thesis aims to generalise the applicability of these methods to more complicated models that might better represent technologically significant materials and implement them in a user-friendly computational Julia [12] package `PolaronMobility.jl` [11].

Overall, this thesis may be split into four main milestones that I have separated into four chapters:

Chapter 3 — Generalise the material action: In this chapter, I extend the effective model Lagrangian to provide greater material-specific detail, including multiple phonon branches, the small Holstein polaron, anisotropic bands and general many-body polaron theories formulated using coherent-state path integrals (CSPI) and quantum field theory techniques.

Chapter 4 — Improve the trial action: In this chapter, I extend the trial polaron Lagrangian beyond Feynman’s original spring-mass harmonic model (while retaining the analytic solution) to increase the accuracy of the variational approximation and the predicted response functions. These extensions include developing the variational method for the multimode Fröhlich polaron and small Holstein polaron, as well as generalising the trial action to couple the electron to multiple spring-masses, a general bath spectral-function with self-consistent equations, general many-body

polarons using the Independent Boson Model (IBM) as a trial action, and extending the Feynman-Jensen inequality with an infinite series of cumulant corrections.

Chapter 5 — Compute the response functions: In this chapter, I first confirm the accuracy of the FHIP method by comparing the predicted temperature- and frequency-mobility with Diagrammatic Monte Carlo (DMC) calculations by Mishchenko et al. [10]. Next, I generalise the FHIP method to compute the charge-carrier mobility and optical conductivity for more complicated models. This extends FHIP to the multimode Fröhlich polaron, the Holstein small polaron, the many spring-mass extended trial solution, general many-body polarons and for an optimal self-consistent solution that coincides with the optimal free energy solution.

Chapter 6 — Material classification: In this chapter, I apply these methods to calculate the polaronic properties of materials. Using the multimode extension to the Fröhlich polaron, I evaluate the polaron energy, mass, mobility and optical conductivity of bulk Methylammonium Lead Iodide Perovskites using material data from Brivio et al. [20] and compare the results to the single effective mode method of Hellwarth and Biaggio [21]. I use the small Holstein polaron extension to calculate the polaron energy, mass, mobility and optical conductivity of bulk Rubrene crystals using material data obtained from Ordejon et al. [22]. I use the anisotropic band extension to calculate the Zero-Point Renormalisation (ZPR) and polaron size with weak coupling perturbation results for dozens of II-VI, III-V and oxide semiconductor materials to characterise the validity of the continuum approximation in the Fröhlich model and the use of the perturbation approximation. The data for these materials was taken from Guster et al. [8]. Finally, do a high-throughput analysis of 1260 materials from the Materials Project [13] used in the Liege Dataset [14]. Here, I compare my ZPR results with those obtained from perturbation theory [23] and further calculate these materials' polaron mass and mobility.

Chapter 2 outlines the key existing research that precedes this dissertation and provides a heuristic re-derivation of the main theories of the Fröhlich [3] and Holstein [5, 6] polarons, Feynman's variational path integral approximation [2] and the FHIP approximation [17, 18, 21]. Likewise, I show the numerical results of these theories implemented in Julia in the `PolaronMobility.jl` package, some of which go further than in the literature.

Finally, in **Chapter 7**, I conclude this dissertation and discuss how this research could be expanded upon in future.

CHAPTER 2



BACKGROUND

“What I cannot create, I do not understand. Know how to solve every problem that has been solved.”

—Richard P. Feynman, *Feynman’s Last Chalkboard*, 1988

In this chapter, I will outline the key existing developments towards polaron physics in the last 90 years, which much of this thesis aims to build upon. I first provide a heuristic overview of the field’s historical developments. I then present a comprehensive re-derivation of the key theories of the Fröhlich and Holstein polarons, Feynman’s original variational path integral approach to approximating the polaron state and the Feynman-Hellwarth-Iddings-Platzman influence functional approach to approximating the polaron mobility and optical conductivity.

2.1 Polaron Physics

In this section, I begin with a brief conceptual overview of the critical advancements in polaron physics that this thesis builds upon, the central development of which started with seminal works of Herbert Fröhlich [3, 24] and Theodore Holstein [5, 6] who formalised rigorous quantum-field Hamiltonians for the large and small polarons respectively, and laid the standard theoretical groundwork for successive advancements which I outline in Table 2.1. I will then provide a comprehensive re-derivation of the Fröhlich large polaron and Holstein small polaron Hamiltonians.

Year	Authors	Research development	Refs
1933	Landau	Charge moving in a dielectric crystal	[25]
1946-1948	Landau & Pekar	Landau–Pekar model	[26–28]
1950-1954	Fröhlich	Large polaron Hamiltonian	[3, 24]
1955	Feynman	Variational path integral (athermal)	[2]
1959	Holstein	Small polaron Hamiltonian	[5, 6]
1959	Schultz	FVA polaron effective mass	[29]
1959	Feynman & Vernon	Influence functionals	[16]
1959-1961	Ōsaka	Variational path integral (thermal)	[30, 31]
1962	FHIP	Path integral mobility	[17]
1963	Kadanoff	BTE Fröhlich polaron mobility	[19]
1966-1971	Thornber	Nonlinear polaron mobility	[32–34]
1972	DSG	Path integral optical conductivity	[18]
1980-1984	Adamowski et al.	Optimal FVA functional solution	[35, 36]
1983-1985	De Raedt et al.	Lattice polaron path integral	[37, 38]
1986-1987	Peeters et al.	n -dimensional Fröhlich model	[39, 40]
1998-2000	Prokofev et al.	DMC Fröhlich polaron	[41, 42]
1999	Hellwarth et al.	Multimode polaron action	[21]
2001	Titantah et al.	PIMC Fröhlich polaron	[43]
1997-2004	Kornilovich et al.	CTPIMC lattice polarons	[44–50]
2001	Tempere et al.	Many polaron optical gas	[51]
2009	Tempere et al.	BEC-impurity polarons	[52]
2010	Devreese et al.	Many polaron FVA	[53]
2014-2015	Mishchenko et al.	DMC Holstein polaron	[54, 55]
2016	Klimin et al.	All coupling polaron response	[56–58]
2017	Frost	Calculating polaron mobility	[59]
2019	Mishchenko et al.	DMC Fröhlich mobility	[10]
2019-2022	Ichmoukhamedov et al.	General memory polaron	[60–62]
2020	Miglio et al.	Generalised Fröhlich model	[63]
2021	Franchini et al.	Polarons in materials	[15]
2021	Guster et al.	Anisotropic band polarons	[8]
2021	Houtput et al.	Anharmonic phonon FVA	[64]
2023	Martin et al.	Explicit multimode FVA polaron	[4]
2023	de Melo et al.	High-throughput polarons	[14, 23]
2024	Martin et al.	Holstein small polaron FVA	[7]
2024	Klimin et al.	Nonparabolic band polarons	[65]

Table 2.1: A (non-exhaustive) compendium of theoretical and computation results for studying polarons.

2.1.1 A Brief History

Landau and Pekar, 1933-1948

The self-localisation of an electron in a perfect crystal due to lattice deformations was investigated by Landau [25], who was concerned with the effect of lattice defects on materials such as sodium chloride. Later, the concept of a “polaron” was initially proposed and coined by Pekar [26–28] to describe the spontaneous trapping of an electron due to the induced polarisation of an atomic lattice in a strongly ionic material. Further developments on the exact definition of a polaron led to a joint paper by Pekar and Landau [66], where they calculated the effective mass of a large, strongly-coupled polaron. The polaron was established as a *quasiparticle* that consists of a charge carrier (such as an electron or hole) ‘dressed’ by a cloud of virtual phonon excitations that follow the charge carrier as it propagates through a polarisable medium. Suppose the polaron’s spatial delocalisation is large compared to the lattice parameter of a material. The material can be treated as a polarisable continuum, and we have a *large* polaron. However, when the extent of the polaron is of the order of the lattice parameter, we have a *small* polaron, and lattice effects cannot be ignored.

Fröhlich, 1950-1954

The theoretical groundwork for the large polaron theory was formally established by Fröhlich [3]. The Fröhlich Hamiltonian represents a simplistic physical system composed of a single conduction-band electron linearly coupled to a polarisation field. This polarisation field, carried by longitudinal optical phonons, is represented by a set of quantum harmonic oscillators with no dispersion and oscillating at the same frequency. The strength of the electron-phonon coupling is characterised by a dimensionless coupling constant called the ‘Fröhlich alpha parameter’ and can be determined from the properties of the material. Despite its simplistic representation, an exact solution to the Fröhlich Hamiltonian has evaded direct evaluation.

Feynman, 1955

In his 1955 paper, Feynman [2] reformulated the Fröhlich Hamiltonian as a Lagrangian by converting the electron and phonon creation and annihilation operators into their corresponding coordinates and momenta, followed by a Legendre transformation. After performing a Gaussian integration over the momenta, he obtained a Gaussian path integral over the phonon coordinates, which could be evaluated explicitly. The result was an exact *model* action, where the electron is coupled to a fictitious particle through a non-local Coulomb potential.

However, this path integral could not be solved exactly, as the remaining electron coordinates have a $1/r$ dependence, making the path integral non-Gaussian. To address this, Feynman proposed a *trial* action that approximates the main features of the model action but is quadratic in the electron coordinates, allowing for a solvable Gaussian path integral. The trial action describes an electron coupled to a fictitious massive particle via a harmonic potential that decays exponentially in time. By transforming the model and trial actions into imaginary time, Feynman obtained an expression for the quantum statistical partition function, which is a convex functional, allowing the application of Jensen's inequality. A variational inequality was then used to minimise the difference between the trial and model actions, providing an approximate upper bound on the polaron's ground-state self-energy.

Feynman's variational inequality involved two key variational parameters. The first, denoted by C , controlled the strength of the harmonic coupling, while the second, w , determined the decay rate of the coupling in time. Later in his paper, Feynman replaced C with v , representing the frequency of the harmonic coupling. Using this approach, Feynman calculated the polaron's ground-state energy and its effective mass for all electron-phonon coupling strengths.

Holstein, 1959

Holstein [5, 6] conducted a thorough theoretical analysis of small polaron formation and transport, focusing on charge carriers in molecular crystals where electron-phonon interactions play a critical role. His work is divided into two parts, with the first addressing the fundamental principles of polaron formation and mobility within tight-binding systems. Holstein uses a quantum mechanical framework to describe the interactions between an electron and the lattice's vibrational modes (phonons). The model considers explicitly that the electron interacts only with localised vibrational modes at the same site (Einstein oscillators) rather than with delocalised, collective modes such as Bloch or Debye phonons. Additionally, Holstein examines the linear interaction between the electron and phonons in terms of phonon displacement. He further assumes that phonons are confined to individual sites, neglecting inter-site phonon coupling and restricting the lattice distortion to the electron's local environment.

Ōsaka, 1959-1961

Ōsaka [30, 31], generalised Feynman's path integral variational approach to nonzero temperatures. Ōsaka achieved this by recognising that the equation of motion resulting from another more straightforward trial action produced the same equation of motion as Feynman proposed. Therefore, Ōsaka used the solution of the path integral of this more tractable action to obtain the temperature-dependent density matrix for the polaron state.

At zero temperature, Ōsaka's formulation is identical to Feynman's expression for the polaron self-energy.

Feynman & Vernon, 1959

Feynman and Vernon [16] introduced a powerful method for studying quantum systems interacting with external environments, focusing mainly on open systems and non-equilibrium dynamics. The central concept is the influence functional, which encapsulates the effects of an environment (modelled as a collection of harmonic oscillators) on a quantum system by integrating out the environmental degrees of freedom. This process results in an effective action for the system alone, enabling the study of how the environment induces dissipation and decoherence in the system. Crucially, the influence functional provides a formal framework for deriving the reduced density matrix of the system, which describes its state after tracing out the environment. This matrix captures the system's evolution in the presence of environmental interactions, allowing for the analysis of decoherence and the loss of quantum coherence over time. The formalism has far-reaching applications in quantum mechanics, particularly for quantum Brownian motion, quantum dissipative systems, and non-equilibrium quantum processes. Feynman and Vernon's work laid the foundation for understanding how environmental coupling influences quantum dynamics, with critical implications for quantum thermodynamics.

Feynman, Hellwarth, Iddings & Platzman, 1962

Feynman, Hellwarth, Iddings, and Platzman [17] (often referred to as "FHIP") developed an approximate expression for the polaron impedance function using a path-integral approach and the Feynman-Vernon influence functional formalism. This expression accounted for all frequencies of the applied electric field, all temperatures, and all electron-phonon coupling strengths. Unlike a variational approach, the impedance function was derived from a second-order functional expansion around the quadratic trial action previously introduced by Feynman in 1955 [2]. A crucial aspect of the derivation involved calculating the "memory function," which was obtained from the imaginary part of the dynamic structure factor. The structure factor, in turn, was derived from the electron density-density correlation function and evaluated via path integrals. The memory function encapsulated the polaron's dynamics and depended on variational parameters that minimised the polaron self-energy. These parameters were assumed to yield the most accurate predictions for polaron dynamics. The authors provided an explicit expression for the imaginary part of the memory function, from which they derived the DC mobility of the polaron and explored its behaviour in the limits of zero, low, and high temperatures.

Devreese, Sitter & Goovaerts, 1972

Starting from the approach used by [17], Devreese, Sitter & Goovaerts [18] (commonly referred to as ‘‘DSG’’) showed how to calculate the optical absorption of Fröhlich polarons, for all coupling, temperature and frequency. It was demonstrated that three different kinds of polaron excitations appear in the spectra produced from their expression: scattering states where, for example, one real phonon is excited; relaxed excited states (RES); and Franck-Condon (FC) states. It was found that these spectral features only appear from an expansion of the impedance function obtained in FHIP and not from the corresponding conductivity function that is the reciprocal of the impedance. This was argued as justification for the choice in FHIP to expand the impedance to second-order instead of the conductivity, which is more commonly used when studying the linear response of a system. Additionally, they explicitly provided the real and imaginary parts of the memory function as an infinite series of special functions (e.g. Bessel functions) and simplified forms of these series at zero temperature.

Hellwarth & Biaggio, 1999

Hellwarth & Biaggio [21], derived a Lagrangian that described a free electron interacting with a polar lattice with multiple infrared-active optical-phonon modes, in the presence of an applied field. From this Lagrangian, they derive an effective model action comparative to Feynman’s model action, except that it had a summation over terms differing in the phonon frequency and electron-phonon coupling strength corresponding to each phonon mode. Rather than use this effective action directly, they defined a single effective phonon frequency and electron-phonon coupling (for which they provided two different schemes to obtain) and used Ōsaka’s free energy minimisation procedure instead. They used the mobility equation derived in FHIP and their own derived Lorentz-Lorenz relation to produce accurate predictions for the room-temperature electron mobility and reflectivity in $\text{Bi}_{12}\text{SiO}_{20}$.

Mishchenko, Prokof’ev, Sakamoto & Svistunov, 1998-2000

Prokof’ev & Svistunov [41], in addition to Mishchenko & Sakamoto [42], performed a detailed study on the Fröhlich polaron model using a diagrammatic Monte Carlo method (DMC). They produced precise numerical data for the polaron self-energy, effective mass, the general structure of the polaron cloud and spectral density of the polaron from intermediate to strong electron-phonon couplings. Their method used a set of Green functions of the polaron, which they simulated using a standard diagrammatic expansion-Matsubara technique at zero temperature and related them to the polaron parameters. These

results are considered the ‘gold standard’ for the Fröhlich model and are often used as a theoretical benchmark to compare newer model predictions against.

2.1.2 Fröhlich’s Large Polaron

Fröhlich [3] studied a system whereby a charged particle in a dielectric medium polarises its surroundings. The resultant polarisation field interacts with the particle, and the particle then possesses self-energy in the field due to the changes it, in turn, causes in the field. A simple example is the motion of a free conduction band electron in an ionic crystal. This is a relevant model for physical materials and also theoretically interesting as it is a simple example of a non-relativistic quantum field theory of a fermion interacting with a bosonic quantum field. For a slow electron in the conduction band, the electronic dispersion relation ϵ_k is approximately quadratic in the momentum $\hbar\mathbf{k}$

$$\epsilon_k = \frac{\hbar^2 k^2}{2m_0}. \quad (2.1)$$

Here m_0 is the effective band mass of the electron and is usually different to the electronic mass m_e , and \mathbf{k} is the wave vector of the electron. Eq. (2.1) is typically only valid near the extrema of the valence and conduction bands, such as for slow conduction electrons. This results from a typical Bloch electron plane wave moving through a rigid lattice.

Fröhlich improved Bloch’s approximation by modelling an electron moving through a non-rigid isotropic polar lattice. The electron experiences an electrostatic potential generated by the displacement of ions from their lattice sites. For small ion displacements compared to the lattice spacing, this potential is one generated by an electric dipole. Since the lattice is polar, ion displacements that lead to electric polarisations interact more strongly with electrons than other types of displacements, which Fröhlich disregards. The electronic wave function varies slowly over many lattice spacings for sufficiently low-energy electrons. Therefore, the lattice can be approximated by a continuum such that the electric field, generated by the displacement of ions in the lattice, can be described by a macroscopic continuous polarisation field, $\mathbf{P}(\mathbf{r})$.

Classical field theory

From the usual definition of the electric displacement field $\mathbf{D}(\mathbf{r})$, the polarisation field is related to the total electric field intensity $\mathbf{E}(\mathbf{r})$ by (in CGS units),

$$\mathbf{E}(\mathbf{r}) = \mathbf{D}(\mathbf{r}) - 4\pi\mathbf{P}(\mathbf{r}). \quad (2.2)$$

Therefore, $-4\pi\mathbf{P}(\mathbf{r})$ is the contribution made by the lattice to the total electric field intensity. Since the main force acting on the electron is the polarisation field $\mathbf{P}(\mathbf{r})$ from the ionic

displacement, the classical equation of motion of the electron is

$$m_0 \mathbf{r} = 4\pi e \mathbf{P}(\mathbf{r}). \quad (2.3)$$

For a single free electron with charge e and position \mathbf{r} , the electric displacement is

$$\mathbf{D}(\mathbf{r}, \mathbf{r}) = -e \nabla \left(\frac{1}{|\mathbf{r} - \mathbf{r}|} \right), \quad (2.4)$$

such that $\nabla \times \mathbf{D}(\mathbf{r}, \mathbf{r}) = 0$ and $\nabla \cdot \mathbf{D}(\mathbf{r}, \mathbf{r}) = 4\pi e \delta(\mathbf{r} - \mathbf{r})$. This electric displacement represents the ‘external’ electric fields that act on the electron in the crystal. Since the displacement field is longitudinal ($\nabla \times \mathbf{D}(\mathbf{r}, \mathbf{r}) = 0$), the polarisation field generated by the electron will be longitudinal too (assuming that magnetic fields can be neglected). Therefore, if $\mathbf{P}(\mathbf{r})$ is the electric polarisation at the position \mathbf{r} , then the rotational part of the field must be zero,

$$\nabla \times \mathbf{P}(\mathbf{r}) = 0. \quad (2.5)$$

The electric field generated by the polarisation $-4\pi \mathbf{P}$ can be expressed by an electric potential $\Phi(\mathbf{r})$ given by Poisson’s equation,

$$-\nabla \Phi(\mathbf{r}) = -4\pi \mathbf{P}(\mathbf{r}). \quad (2.6)$$

The energy of the interaction between the electron and the lattice displacements is then

$$\begin{aligned} E_{e-l} &= - \int \mathbf{D}(\mathbf{r}, \mathbf{r}) \mathbf{P}(\mathbf{r}) d^3 \mathbf{r}, \\ &= \frac{e}{4\pi} \int \nabla \left(\frac{1}{|\mathbf{r} - \mathbf{r}|} \right) \nabla \Phi(\mathbf{r}) d^3 \mathbf{r}, \\ &= e\Phi(\mathbf{r}). \end{aligned} \quad (2.7)$$

The longitudinal modes of the lattice that generate the polarisation field are either optical lattice modes (where two adjacent ions move in opposite directions) or acoustic modes (where adjacent ions move in the same direction). Only the optical modes produce dipole moments that add constructively for small lattice displacements, generating a significant resultant polarisation. This is especially true of long-wavelength optical modes, which have the most significant interaction with the electron and are dispersion-less with constant vibrational frequency ω_0 . Fröhlich assumed that only these long-wavelength longitudinal optical (LO) modes had any considerable effect on the conduction electron and neglected all other lattice modes.

The total lattice polarisation has two contributions, one from high-frequency oscillations $\mathbf{P}_e(\mathbf{r})$ due to the deformation of the ions, and one from infrared oscillations due to ionic

displacement $\mathbf{P}_i(\mathbf{r})$

$$\mathbf{P}(\mathbf{r}) = \mathbf{P}_e(\mathbf{r}) + \mathbf{P}_i(\mathbf{r}). \quad (2.8)$$

Under an external field $\mathbf{D}(\mathbf{r})$ the equations of motion for these two polarisations are driven harmonic oscillator equations

$$\mathbf{P}_i(\mathbf{r}) + \omega_i^2 \mathbf{P}_i(\mathbf{r}) = \mathbf{D}(\mathbf{r}, \mathbf{r})/\gamma, \quad (2.9a)$$

$$\mathbf{P}_e(\mathbf{r}) + \omega_e^2 \mathbf{P}_e(\mathbf{r}) = \mathbf{D}(\mathbf{r}, \mathbf{r})/\delta, \quad (2.9b)$$

where $\omega_e/2\pi$ and $\omega_i/2\pi$ are the frequencies corresponding to the optical absorption in the high (electronic) and infrared regions, respectively. γ and δ are constants related to energy associated with the respective displacements. To determine these constants, we go to the zero-frequency “static” case where $\dot{\mathbf{P}} = 0$ and $\mathbf{D} = \epsilon_0 \mathbf{E}$, with ϵ_0 the total zero-frequency dielectric constant. In the zero-frequency limit, the polarisation is

$$4\pi \mathbf{P}(\mathbf{r}) = (\epsilon_0 - 1) \mathbf{E}(\mathbf{r}) = (1 - \epsilon_0^{-1}) \mathbf{D}(\mathbf{r}). \quad (2.10)$$

In the high-frequency limit, the frequency Ω of the external field \mathbf{D} satisfies $\omega_e \gg \Omega \gg \omega_i$ such that the lattice polarisation is not excited. In the high-frequency limit, the polarisation is

$$4\pi \mathbf{P}(\mathbf{r}) = 4\pi \mathbf{P}_e(\mathbf{r}) = (1 - \epsilon_\infty^{-1}) \mathbf{D}(\mathbf{r}), \quad (2.11)$$

where ϵ_∞ is the high-frequency dielectric constant. In the high-frequency limit, the ions can no longer keep up $\mathbf{P}_i \approx 0$, whereas the electronic oscillators can follow nearly adiabatically. Therefore, the \mathbf{P}_e term would be negligible compared to $\omega_e^2 \mathbf{P}_e$, and so for a field \mathbf{D} of equal strength, \mathbf{P}_e would have roughly the same value in the static limit as in the high-frequency limit. Hence, we can combine the two expressions above to obtain the ionic polarisation

$$\mathbf{P}_i(\mathbf{r}) = \mathbf{P}(\mathbf{r}) - \mathbf{P}_e(\mathbf{r}) = \frac{1}{4\pi} \left(\frac{1}{\epsilon_\infty} - \frac{1}{\epsilon} \right) \mathbf{D}(\mathbf{r}), \quad (2.12)$$

where \mathbf{P}_e in either limit will cancel. Now, using the equations of motion in the static limit ($\mathbf{P}_e = \mathbf{P}_i = 0$) and our expressions for \mathbf{P}_i and \mathbf{P}_e we find

$$\frac{1}{\gamma} = \frac{\omega_i^2}{4\pi} \left(\frac{1}{\epsilon_\infty} - \frac{1}{\epsilon_0} \right), \quad (2.13a)$$

$$\frac{1}{\delta} = \frac{\omega_e^2}{4\pi} \left(1 - \frac{1}{\epsilon_\infty} \right). \quad (2.13b)$$

Combined with the equation of motion for the electron, all three equations of motion can be obtained from the overall Lagrangian

$$L = \frac{1}{2}m_0\dot{\mathbf{r}}^2 + \frac{1}{2}\gamma \int [\dot{\mathbf{P}}_i^2(\mathbf{r}) - \omega_i^2\mathbf{P}_i^2(\mathbf{r})] d^3\mathbf{r} + \frac{1}{2}\delta \int [\dot{\mathbf{P}}_e^2(\mathbf{r}) - \omega_e^2\mathbf{P}_e^2(\mathbf{r})] d^3\mathbf{r} + \int \mathbf{D}(\mathbf{r}, \mathbf{r}) [\mathbf{P}_e(\mathbf{r}) + \mathbf{P}_i(\mathbf{r})] d^3\mathbf{r} + E_{zp} \quad (2.14)$$

by using the standard method of extremising the corresponding action $\delta S = \int dt \delta L = 0$ with \mathbf{r} , $\mathbf{P}_e(\mathbf{r})$ and $\mathbf{P}_i(\mathbf{r})$ as variables. E_{zp} is an arbitrary constant representing the polarisation field's zero-point energy without the electron's interaction.

The corresponding Hamiltonian can be derived via a Legendre transformation by noting that the conjugate momenta (defined as $\partial L / \partial \dot{X}$ with the generalised coordinate $X \in \{\mathbf{r}, \mathbf{P}_e(\mathbf{r}), \mathbf{P}_i(\mathbf{r})\}$) are $\mathbf{p} = m_0\dot{\mathbf{r}}$, $\Pi_e(\mathbf{r}) = \gamma\dot{\mathbf{P}}_e(\mathbf{r})$ and $\Pi_i(\mathbf{r}) = \delta\dot{\mathbf{P}}_i(\mathbf{r})$. Hence, the Hamiltonian is

$$H = \sum_X \frac{\partial L}{\partial \dot{X}} \dot{X} - L = \frac{\mathbf{p}^2}{2m_0} + \frac{1}{2} \int [\Pi_i^2(\mathbf{r})/\gamma + \gamma\omega_i^2\mathbf{P}_i^2(\mathbf{r})] d^3\mathbf{r} + \frac{1}{2} \int [\Pi_e^2(\mathbf{r})/\delta + \delta\omega_e^2\mathbf{P}_e^2(\mathbf{r})] d^3\mathbf{r} - \int \mathbf{D}(\mathbf{r}, \mathbf{r}) [\mathbf{P}_e(\mathbf{r}) + \mathbf{P}_i(\mathbf{r})] d^3\mathbf{r} - E_{zp}. \quad (2.15)$$

The canonically conjugate variables all obey the classical Poisson's Brackets

$$\left\{ \mathbf{p}_{el,j}, \mathbf{r}'_{el,j} \right\} = \delta'_{j,j}, \quad (2.16a)$$

$$\left\{ \mathbf{P}_j(\mathbf{r}), \Pi'_j(\mathbf{r}') \right\} = \delta'_{j,j} \delta(\mathbf{r} - \mathbf{r}'). \quad (2.16b)$$

Classically, when the electron is at rest, the force acting on the electron must vanish, and so $\Phi(\mathbf{r})$ must be minimum at $\mathbf{r} = \mathbf{r}$. However, the above Hamiltonian diverges as $\mathbf{r} \rightarrow \mathbf{r}$. This happens because the lattice has been approximated as a continuum. This can be accounted for by representing the polarisation vectors as a Fourier series and excluding terms with wavelengths shorter than the lattice constant. With this cut-off, $\Phi(\mathbf{r})$ will now have a minimum at $\mathbf{r} = \mathbf{r}$ and $\mathbf{P}(\mathbf{r}) = 0$. Nonetheless, when the electron is moving slowly, $\mathbf{P}(\mathbf{r}) \neq 0$ due to the time-dependent terms in the equation of motion, but $\mathbf{P}_e(\mathbf{r}) \ll \mathbf{P}_i(\mathbf{r})$ because $\omega_e^2 \gg \omega_i^2$. This means that for a slow electron, the displacement of ions in the lattice is primarily due to the infrared polarisation field $\mathbf{P}_i(\mathbf{r})$. Therefore, for a slow electron, the $\mathbf{P}_e(\mathbf{r})$ terms remain mostly constant and can be disregarded from the lattice dynamics. This gives Fröhlich's Hamiltonian for a slow electron in an ionic lattice to be

$$H = \frac{\mathbf{p}^2}{2m_0} + \frac{1}{2} \int [\Pi_i^2(\mathbf{r})/\gamma + \gamma\omega_i^2\mathbf{P}_i^2(\mathbf{r})] d^3\mathbf{r} - \int \mathbf{D}(\mathbf{r}, \mathbf{r}) \mathbf{P}_i(\mathbf{r}) d^3\mathbf{r} - E_{zp}. \quad (2.17)$$

Quantising Fröhlich's Hamiltonian

From now on, I will drop the ‘ i ’ index for the infrared polarisation field, and $\mathbf{P}(\mathbf{r})$ will represent the infrared ionic displacement polarisation field, with frequency ω_0 . To prepare this Hamiltonian for quantisation, Fröhlich introduced an auxiliary complex vector field $\mathbf{B}(\mathbf{r})$ that is defined by

$$\mathbf{B}(\mathbf{r}) = \sqrt{\frac{\gamma\omega_0}{2\hbar}} \left[\mathbf{P}(\mathbf{r}) + \frac{i}{\gamma\omega_0} \mathbf{\Pi}(\mathbf{r}) \right], \quad (2.18a)$$

$$\mathbf{B}^*(\mathbf{r}) = \sqrt{\frac{\gamma\omega_0}{2\hbar}} \left[\mathbf{P}(\mathbf{r}) - \frac{i}{\gamma\omega_0} \mathbf{\Pi}(\mathbf{r}) \right], \quad (2.18b)$$

where $\nabla \times \mathbf{B}(\mathbf{r}) = \nabla \times \mathbf{B}^*(\mathbf{r}) = 0$. Equivalently, this can be written in terms of the infrared polarisation field,

$$\mathbf{P}(\mathbf{r}) = \sqrt{\frac{\hbar}{2\gamma\omega_0}} [\mathbf{B}^*(\mathbf{r}) + \mathbf{B}(\mathbf{r})], \quad (2.19a)$$

$$\mathbf{\Pi}(\mathbf{r}) = i\sqrt{\frac{\gamma\hbar\omega_0}{2}} [\mathbf{B}^*(\mathbf{r}) - \mathbf{B}(\mathbf{r})]. \quad (2.19b)$$

Substituting these into (2.17) gives the Hamiltonian

$$H = \frac{\mathbf{p}^2}{2m_0} + \hbar\omega_0 \int \mathbf{B}^*(\mathbf{r}) \mathbf{B}(\mathbf{r}) d^3\mathbf{r} - \sqrt{\frac{\hbar}{2\gamma\omega_0}} \int \mathbf{D}(\mathbf{r}, \mathbf{r}) [\mathbf{B}^*(\mathbf{r}) + \mathbf{B}(\mathbf{r})] d^3\mathbf{r} - E_{zp}. \quad (2.20)$$

To quantise this Hamiltonian, $\mathbf{B}(\mathbf{r})$ is given a periodic boundary condition over a cube of volume $V_0 = L^3$ and is expressed as a Fourier series,

$$\mathbf{B}(\mathbf{r}) = \frac{1}{\sqrt{V_0}} \sum_{\mathbf{q}} \frac{\mathbf{q}}{q} b_{\mathbf{q}} e^{i\mathbf{q}\cdot\mathbf{r}}, \quad (2.21a)$$

$$\mathbf{B}^*(\mathbf{r}) = \frac{1}{\sqrt{V_0}} \sum_{\mathbf{q}} \frac{\mathbf{q}}{q} b_{\mathbf{q}}^* e^{-i\mathbf{q}\cdot\mathbf{r}}. \quad (2.21b)$$

The Fourier coefficients are given by

$$b_{\mathbf{q}} = \frac{1}{\sqrt{V_0}} \frac{\mathbf{q}}{q} \cdot \int d^3\mathbf{r} \mathbf{B}(\mathbf{r}) e^{-i\mathbf{q}\cdot\mathbf{r}}, \quad (2.22a)$$

$$b_{\mathbf{q}} = \frac{1}{\sqrt{V_0}} \frac{\mathbf{q}}{q} \cdot \int d^3\mathbf{r} \mathbf{B}^*(\mathbf{r}) e^{i\mathbf{q}\cdot\mathbf{r}}, \quad (2.22b)$$

where the components q_j of the wave-vector \mathbf{q} satisfy

$$q_j = \frac{2\pi}{V_0^{1/3}} n_j, \quad n_j = 0, \pm 1, \pm 2, \dots . \quad (2.23)$$

In the limit as the volume goes to infinity $V_0 \rightarrow \infty$ the sum over \mathbf{q} becomes

$$\sum_{\mathbf{q}} \rightarrow \frac{V_0}{(2\pi)^3} \int d^3\mathbf{q}. \quad (2.24)$$

The fact that $\mathbf{P}(\mathbf{r})$ and $\mathbf{\Pi}(\mathbf{r})$ are real functions imposes the following condition on the Fourier components $b_{\mathbf{q}}$ and $b_{\mathbf{q}}^*$,

$$b_{\mathbf{q}}^* = -b_{-\mathbf{q}}. \quad (2.25)$$

The infrared polarisation field and its momenta conjugate can be written in terms of $b_{\mathbf{q}}$ and $b_{\mathbf{q}}^*$

$$\mathbf{P}(\mathbf{r}) = \sqrt{\frac{\hbar}{2\gamma\omega_0 V_0}} \sum_{\mathbf{q}} \frac{\mathbf{q}}{q} \left[b_{\mathbf{q}}^* e^{-i\mathbf{q}\cdot\mathbf{r}} + b_{\mathbf{q}} e^{i\mathbf{q}\cdot\mathbf{r}} \right], \quad (2.26a)$$

$$\mathbf{\Pi}(\mathbf{r}) = i \sqrt{\frac{\gamma\hbar\omega_0}{2V_0}} \sum_{\mathbf{q}} \frac{\mathbf{q}}{q} \left[b_{\mathbf{q}}^* e^{-i\mathbf{q}\cdot\mathbf{r}} - b_{\mathbf{q}} e^{i\mathbf{q}\cdot\mathbf{r}} \right]. \quad (2.26b)$$

To derive the Poisson Bracket's for $b_{\mathbf{q}}$ and $b_{\mathbf{q}}^*$, note that $\mathbf{P}(\mathbf{r})$ and $\mathbf{\Pi}(\mathbf{r})$ are conjugate variables. This means that $\sqrt{\hbar/2\gamma\omega_0}(b_{\mathbf{q}}^* + b_{\mathbf{q}})$ and $i\sqrt{\hbar\omega_0/2\gamma}(b_{\mathbf{q}}^* - b_{\mathbf{q}})$ are conjugate too. Therefore, quantisation via Bose statistics gives

$$\left\{ b_{\mathbf{q}}^* + b_{\mathbf{q}}, b_{\mathbf{q}'}^* - b_{\mathbf{q}'} \right\} = \frac{2}{i\hbar} \delta_{\mathbf{q},\mathbf{q}'}, \quad (2.27)$$

and since commutators involving the same operator but different \mathbf{q} s vanish, the commutators are

$$\left\{ b_{\mathbf{q}}, b_{\mathbf{q}'}^* \right\} = \frac{1}{i\hbar} \delta_{\mathbf{q},\mathbf{q}'}, \quad (2.28a)$$

$$\left\{ b_{\mathbf{q}}, b_{\mathbf{q}'} \right\} = \left\{ b_{\mathbf{q}}^*, b_{\mathbf{q}'}^* \right\} = 0. \quad (2.28b)$$

The interaction energy between the electron and the infrared polarisation field can now be defined in terms of $b_{\mathbf{q}}$ and $b_{\mathbf{q}}^*$,

$$\begin{aligned} e\Phi(\mathbf{r}) &= - \int \mathbf{D}(\mathbf{r}, \mathbf{r}) \mathbf{P}(\mathbf{r}) d^3\mathbf{r} \\ &= - \sqrt{\frac{\hbar}{2\gamma\omega_0 V_0}} \int \mathbf{D}(\mathbf{r}, \mathbf{r}) \sum_{\mathbf{q}} \frac{\mathbf{q}}{q} \left[b_{\mathbf{q}}^* e^{-i\mathbf{q}\cdot\mathbf{r}} + b_{\mathbf{q}} e^{i\mathbf{q}\cdot\mathbf{r}} \right] d^3\mathbf{r}, \end{aligned} \quad (2.29)$$

Where to proceed, one integrates by parts to give

$$\begin{aligned} e\Phi(\mathbf{r}) &= 4\pi i \sqrt{\frac{e^2\hbar}{2\gamma\omega_0 V_0}} \int \delta(\mathbf{r} - \mathbf{r}) \sum_{\mathbf{q}} \frac{1}{q} [b_{\mathbf{q}}^* e^{-i\mathbf{q}\cdot\mathbf{r}} - b_{\mathbf{q}} e^{i\mathbf{q}\cdot\mathbf{r}}] d^3\mathbf{r} \\ &= 4\pi i \left(\frac{e^2\hbar}{2\gamma\omega_0 V_0} \right)^{1/2} \sum_{\mathbf{q}} \frac{1}{q} [b_{\mathbf{q}}^* e^{-i\mathbf{q}\cdot\mathbf{r}} - b_{\mathbf{q}} e^{i\mathbf{q}\cdot\mathbf{r}}]. \end{aligned} \quad (2.30)$$

Hence, for the Hamiltonian (written in symmetrised form), we get

$$\begin{aligned} H &= \frac{\mathbf{p}^2}{2m_0} + \frac{\hbar\omega_0}{2} \sum_{\mathbf{q}} [b_{\mathbf{q}}^* b_{\mathbf{q}} + b_{\mathbf{q}} b_{\mathbf{q}}^*] - E_{zp} \\ &\quad + 4\pi ie \left(\frac{\hbar}{2\gamma\omega_0 V_0} \right)^{1/2} \sum_{\mathbf{q}} \frac{1}{q} [b_{\mathbf{q}}^* e^{-i\mathbf{q}\cdot\mathbf{r}} - b_{\mathbf{q}} e^{i\mathbf{q}\cdot\mathbf{r}}]. \end{aligned} \quad (2.31)$$

The result for $\Phi(\mathbf{r})$ in Eq. (2.30) only holds if $\mathbf{q} \neq 0$, and the summations must exclude the case for when $\mathbf{q} = 0$. This situation represents an electron in a neutral, rigid lattice and must not be subjected to periodic boundary conditions. Otherwise, the periodic boundary conditions would repeat this charge since the volume V_0 contains a charge e . This cannot happen as it leads to a diverging overlap of the many long-range repulsive Coulomb interactions. To avoid this, an opposite ‘mirror’ charge $-e$ is distributed homogeneously over the volume V_0 , which compensates for the $\mathbf{q} = 0$ component of the electronic charge. So, the $\mathbf{q} = 0$ component does not contribute to the interaction energy. This is known as the homogeneous background charge.

To quantise, the electron momentum \mathbf{p} is replaced with the operator $i\hat{\nabla}_{\mathbf{r}}$, $b_{\mathbf{q}}$ and $b_{\mathbf{q}}^*$ by the operators $\hat{b}_{\mathbf{q}}$ and $\hat{b}_{\mathbf{q}}^\dagger$, and the Poisson Brackets by $i\hbar$ times the corresponding commutator

$$[b_{\mathbf{q}}, b_{\mathbf{q}'}^\dagger] = \delta_{\mathbf{q},\mathbf{q}'}, \quad (2.32a)$$

$$[b_{\mathbf{q}}, b_{\mathbf{q}'}] = [b_{\mathbf{q}'}, b_{\mathbf{q}'}^\dagger] = 0. \quad (2.32b)$$

The polarisation field can be viewed as a set of harmonic oscillators \mathbf{q} , all with the same frequency $\omega_0/2\pi$. The operators $b_{\mathbf{q}}$ and $b_{\mathbf{q}}^\dagger$ then represent the creation and annihilation operators, respectively, of quanta of polarisation with different wave-numbers \mathbf{q} but all with the same energy $\hbar\omega_0$. These quanta are usually referred to as *phonons*. Thus, $\hat{b}_{\mathbf{q}}$ and $\hat{b}_{\mathbf{q}}^\dagger$ possess ‘raising’ and ‘lowering’ properties when acting on a normalised eigenfunction $|n_{\mathbf{q}}\rangle$,

$$(\hat{b}_{\mathbf{q}}^\dagger)^n |0_{\mathbf{q}}\rangle = (n!)^{1/2} |n_{\mathbf{q}}\rangle \quad (2.33a)$$

$$(\hat{b}_{\mathbf{q}})^n |n_{\mathbf{q}}\rangle = (n!)^{1/2} |0_{\mathbf{q}}\rangle, \quad \hat{b}_{\mathbf{q}} |0_{\mathbf{q}}\rangle = 0. \quad (2.33b)$$

Fröhlich defined a single dimensionless parameter α that quantifies the strength of the electron-phonon interaction described by the last term in the Hamiltonian. This is defined by

The Fröhlich Dimensionless Coupling Constant

$$\alpha = \frac{2\pi e^2}{\hbar\gamma\omega_0^3} \sqrt{\frac{2m_0\omega_0}{\hbar}} = \frac{1}{\sqrt{2}} \left(\frac{1}{\epsilon_\infty} - \frac{1}{\epsilon_0} \right) \frac{e^2}{\hbar\omega_0 r_0}. \quad (2.34)$$

where I defined the characteristic length scale $r_0 \equiv \sqrt{\hbar/m_0\omega_0}$. The Fröhlich's Hamiltonian becomes

$$\hat{H} = -\frac{\hat{\nabla}_r^2}{2m_0} + \frac{\hbar\omega_0}{2} \sum_{\mathbf{q}} \left[\hat{b}_{\mathbf{q}}^\dagger \hat{b}_{\mathbf{q}} + \hat{b}_{\mathbf{q}} \hat{b}_{\mathbf{q}}^\dagger \right] - E_{zp} + \sum_{\mathbf{q}} (M_{\mathbf{q}} \hat{b}_{\mathbf{q}} e^{i\mathbf{q}\cdot\mathbf{r}} + M_{\mathbf{q}}^* \hat{b}_{\mathbf{q}}^\dagger e^{-i\mathbf{q}\cdot\mathbf{r}}), \quad (2.35)$$

with the interaction term

$$M_{\mathbf{q}} = i \frac{\hbar\omega_0}{q} \left(\frac{2\sqrt{2}\pi r_0 \alpha}{V_0} \right)^{1/2}. \quad (2.36)$$

The zero-point energy E_{zp} can be eliminated using the commutation relations where E_{zp} is given by

$$E_{zp} = \sum_{\mathbf{q}} \frac{\hbar\omega_0}{2}. \quad (2.37)$$

This results in

The Fröhlich Hamiltonian

$$\hat{H} = -\frac{\hat{\nabla}_r^2}{2m_0} + \frac{\hbar\omega_0}{2} \sum_{\mathbf{q}} \hat{b}_{\mathbf{q}} \hat{b}_{\mathbf{q}}^\dagger + \sum_{\mathbf{q}} (M_{\mathbf{q}} \hat{b}_{\mathbf{q}} e^{i\mathbf{q}\cdot\mathbf{r}} + M_{\mathbf{q}}^* \hat{b}_{\mathbf{q}}^\dagger e^{-i\mathbf{q}\cdot\mathbf{r}}). \quad (2.38)$$

The first term is the electron's band energy measured at the bottom of the conduction band. The second term gives the polarisation field's energy measured at the zero-point energy of the polarisation field. Finally, the third term is the electron's interaction energy when interacting with a long-wavelength longitudinal optical phonon.

2.1.3 Holstein's Small Polaron

Holstein studied the motion of an electron in a one-dimensional molecular crystal. We have a linear chain of N identical lattice particles without the charge carrier. Holstein considered these lattice particles diatomic molecules with fixed orientations and centres of gravity but variable internuclear separations. The lattice vibrations correspond to variations in the individual internuclear separations and are assumed to be uncoupled. If these vibrations are harmonic (i.e. the potential energy of a particular molecule is parabolic), the lattice

Hamiltonian is,

$$H_{\text{lattice}} = \frac{1}{2M} \sum_{n=1}^N p_n^2 + \frac{M}{2} \sum_{n=1}^N \omega_0^2 x_n^2, \quad (2.39)$$

where x_n is the deviation of an internuclear separation from its equilibrium position, $p_n \equiv -i\hbar\partial/\partial x_n$ is the corresponding canonical momentum, M is the nuclear mass and ω_0 is the harmonic vibrational frequency.

Holstein considered the motion of a single charge carrier formulated within the tight-binding approximation where one assumes that the one-electron potential may be written as the sum of molecular potentials,

$$V(\mathbf{r}, x_1, \dots, x_N) = \sum_{n=1}^N U(\mathbf{r} - n\mathbf{a}, x_n), \quad (2.40)$$

where \mathbf{r} is the electron position and \mathbf{a} is the unit lattice vector. The molecular potential U is assumed to be short-range, $U(\mathbf{a}, x_n) \ll U(0, x_n)$.

The electron eigenfunctions, $\phi(\mathbf{r} - n\mathbf{a}, x_n)$ are obtained from the Time-Independent Schrödinger Equation (TISE),

$$\left[-\frac{\hbar^2}{2m} \nabla^2 + U(\mathbf{r} - n\mathbf{a}, x_n) \right] \phi(\mathbf{r} - n\mathbf{a}, x_n) = E(x_n) \phi(\mathbf{r} - n\mathbf{a}, x_n). \quad (2.41)$$

with eigenvalues $E(x_n)$. The total wavefunction is then a linear superposition,

$$\psi(\mathbf{r}, x_1, \dots, x_N) = \sum_{n=1}^N c_n(x_1, \dots, x_n) \phi_n(\mathbf{r}, x_n), \quad (2.42)$$

of the molecular electron wave functions $\phi_n(\mathbf{r}, x_n)$ localised around the n th molecular site. The coefficients $c_n(x_1, \dots, x_n)$ depend on all the internuclear coordinates and should obey the time-dependent Schrödinger Equation (TDSE),

$$i\hbar \frac{\partial \psi}{\partial t} = \left[-\frac{\hbar^2}{2m} \nabla^2 + \sum_{n=1}^N U(\mathbf{r} - n\mathbf{a}, x_n) + \sum_{n=1}^N \left(-\frac{\hbar^2}{2M} \frac{\partial^2}{\partial x_n^2} + \frac{M}{2} \omega_0^2 x_n^2 \right) \right] \psi. \quad (2.43)$$

Multiplying on the left with $\phi_n^*(\mathbf{r}, x_n)$ and integrating over the electron coordinate \mathbf{r} we get,

$$\begin{aligned} & \sum_{m=1}^N T_{nm} \left[i\hbar \frac{\partial}{\partial t} - \sum_{j=1}^N \left(-\frac{\hbar^2}{2M} \frac{\partial^2}{\partial x_j^2} + \frac{M}{2} \omega_0^2 x_j^2 \right) - E(x_m) \right] c_m(x_1, \dots, x_m) \\ &= \sum_{\substack{n=1 \\ j \neq m}}^N \left[\int d\mathbf{r} \phi^*(\mathbf{r} - n\mathbf{a}, x_n) U(\mathbf{r} - j\mathbf{a}, x_j) \phi(\mathbf{r} - m\mathbf{a}, x_m) \right] c_m(x_1, \dots, x_m) \quad (2.44) \\ & - \frac{\hbar^2}{2M} \sum_{m=1}^N \int d\mathbf{r} \phi^*(\mathbf{r} - n\mathbf{a}, x_n) \left[2 \frac{\partial \phi(\mathbf{r} - m\mathbf{a}, x_m)}{\partial x_m} \frac{\partial c_m}{\partial x_m} + c_m \frac{\partial^2 \phi(\mathbf{r} - m\mathbf{a}, x_m)}{\partial x_m^2} \right], \end{aligned}$$

where,

$$T_{nm} \equiv \int d\mathbf{r} \phi^*(\mathbf{r} - n\mathbf{a}, x_n) \phi(\mathbf{r} - m\mathbf{a}, x_m) = \delta_{nm} + S_{nm}. \quad (2.45)$$

S_{nm} are overlap (non-orthogonality) integrals, assumed to be non-zero only for nearest neighbours and small compared to unity.

Multiply on the left by the inverse of the transfer matrix, $T_{nm}^{-1} \sim \delta_{nm} - S_{nm}$,

$$\begin{aligned} & \left[i\hbar \frac{\partial}{\partial t} - \sum_{j=1}^N \left(-\frac{\hbar^2}{2M} \frac{\partial^2}{\partial x_j^2} + \frac{M}{2} \omega_0^2 x_j^2 \right) - E(x_m) \right] c_n(x_1, \dots, x_m) \\ &= \sum_{\substack{l,m=1 \\ j \neq m}}^N T_{nl}^{-1} \left[\int d\mathbf{r} \phi^*(\mathbf{r} - n\mathbf{a}, x_n) U(\mathbf{r} - j\mathbf{a}, x_j) \phi(\mathbf{r} - m\mathbf{a}, x_m) \right] c_m(x_1, \dots, x_j) \\ & - \frac{\hbar^2}{2M} \sum_{l,m=1}^N T_{nl}^{-1} \int d\mathbf{r} \phi^*(\mathbf{r} - n\mathbf{a}, x_n) \left[2 \frac{\partial \phi(\mathbf{r} - m\mathbf{a}, x_m)}{\partial x_m} \frac{\partial c_m}{\partial x_m} + c_m \frac{\partial^2 \phi(\mathbf{r} - m\mathbf{a}, x_m)}{\partial x_m^2} \right]. \quad (2.46) \end{aligned}$$

Holstein simplifies this expression by imposing the *tight-binding* approximation. First, he assumes the smallness of overlap integrals (i.e. integrals involving electrons localised at different sites). These integrals are of two types: non-orthogonality integrals (i.e. S_{nm}) and any terms for which $l \neq m$. Therefore, any terms that contain products of more than one overlap integral are discarded,

$$\begin{aligned} & \sum_{\substack{l,m=1 \\ j \neq m}}^N T_{nl}^{-1} \left[\int d\mathbf{r} \phi^*(\mathbf{r} - n\mathbf{a}, x_n) U(\mathbf{r} - j\mathbf{a}, x_j) \phi(\mathbf{r} - m\mathbf{a}, x_m) \right] c_m(x_1, \dots, x_j) \\ &= \sum_{\substack{m=1 \\ j \neq m}}^N \left[\int d\mathbf{r} \phi^*(\mathbf{r} - n\mathbf{a}, x_n) U(\mathbf{r} - j\mathbf{a}, x_j) \phi(\mathbf{r} - m\mathbf{a}, x_m) \right] c_m(x_1, \dots, x_j) \quad (2.47) \\ & - \sum_{\substack{m=1 \\ j \neq m}}^N S_{nm} \left[\int d\mathbf{r} U(\mathbf{r} - j\mathbf{a}, x_j) |\phi(\mathbf{r} - m\mathbf{a}, x_m)|^2 \right] c_m(x_1, \dots, x_j). \end{aligned}$$

Second, Holstein assumes that due to the local character of the molecular potential U , terms containing products of electron wavefunctions and potentials localised to *different* sites are smaller than terms where two or more are localised to *the same* site,

$$\begin{aligned} & \sum_{\substack{m=1 \\ j \neq m}}^N \left[\int d\mathbf{r} \phi^*(\mathbf{r} - n\mathbf{a}, x_n) U(\mathbf{r} - j\mathbf{a}, x_j) \phi(\mathbf{r} - m\mathbf{a}, x_m) \right] c_m(x_1, \dots, x_j) \\ &= \sum_{\substack{m=1 \\ m \neq n}}^N \left[\int d\mathbf{r} U(\mathbf{r} - n\mathbf{a}, x_n) |\phi(\mathbf{r} - m\mathbf{a}, x_m)|^2 \right] c_m(x_1, \dots, x_j) \\ &+ \sum_{\substack{j=1 \\ j \neq n}}^N \left[\int d\mathbf{r} U(\mathbf{r} - j\mathbf{a}, x_j) |\phi(\mathbf{r} - n\mathbf{a}, x_n)|^2 \right] c_n(x_1, \dots, x_j), \end{aligned} \quad (2.48)$$

where the result is that one of the two summation indices is suppressed. Likewise, the term containing the overlap integral S_{nm} may be dropped.

Any terms in the TDSE involving derivatives of the electronic wavefunctions w.r.t the internuclear coordinates represent the effect of the nuclear kinetic energy on the localised electron wavefunctions. Holstein also assumes these terms to be negligible, so they may be discarded. Introducing the notations,

$$W_n(x_1, \dots, x_n) \equiv \sum_{m \neq n} \int d\mathbf{r} U(\mathbf{r} - m\mathbf{a}, x_m) |\phi(\mathbf{r} - n\mathbf{a}, x_n)|^2, \quad (2.49)$$

$$J(x_n, x_m) \equiv \int d\mathbf{r} \phi^*(\mathbf{r} - n\mathbf{a}) U(\mathbf{r} - n\mathbf{a}, x_n) \phi(\mathbf{r} - m\mathbf{a}, x_m), \quad (2.50)$$

and restricting $J(x_n, x_m)$ to nearest neighbours, the TDSE reduces to,

Holstein-Peierls Molecular Crystal TDSE

$$\begin{aligned} & \left[i\hbar \frac{\partial}{\partial t} - \sum_{m=1}^N \left(-\frac{\hbar^2}{2M} \frac{\partial^2}{\partial x_m^2} + \frac{M}{2} \omega_0^2 x_m^2 \right) - E(x_n) - W(x_1, \dots, x_n) \right] \\ & \times c_n(x_1, \dots, x_n) = \sum_{\pm} J(x_n, x_{n \pm 1}) c_{n \pm 1}(x_1, \dots, x_n). \end{aligned} \quad (2.51)$$

where the sum \sum_{\pm} is over the neighbours of site n .

$E(x_n)$ describes the intramolecular “on-site” interaction energy (often just referred to as *the* Holstein electron-phonon coupling) of the electron on site n and the molecule of site. This is related to the *inner*-sphere reorganisation energy.

$W_n(x_1, \dots, x_N)$ describes the intermolecular “off-site” interaction energy (often referred to as the ‘Peierls’ electron-phonon coupling) between the electron on site n and the other molecules on sites $m \neq n$. This is related to the *outer*-sphere reorganisation energy.

$J(x_n, x_{n\pm 1})$ are the transfer integrals and describe the energy associated with the overlap of the n -th site electron wavefunction and neighbouring sites’ molecular electronic wavefunctions ϕ . J therefore depends on the internuclear displacements x_n and $x_{n\pm 1}$.

Holstein introduced further simplifications to this molecular-crystal model:

1. He neglects the “off-site” intermolecular couplings $W_n(x_1, \dots, x_N) \rightarrow 0$.
2. He neglects the x -dependence of the transfer integral, which means a constant value between all neighbouring sites $J(x_n, x_{n\pm 1}) \rightarrow -J$.
3. He assumes a linear “on-site” intramolecular coupling, $E(x_n) = -gx_n$.

The TDSE is then,

Holstein Molecular Crystal TDSE

$$\left[i\hbar \frac{\partial}{\partial t} - \sum_{m=1}^N \left(-\frac{\hbar^2}{2M} \frac{\partial^2}{\partial x_m^2} + \frac{M}{2} \omega_0^2 x_m^2 \right) + gx_n \right] c_n(x_1, \dots, x_n) + J(c_{n+1} + c_{n-1}) = 0. \quad (2.52)$$

In second quantisations, the Holstein Hamiltonian becomes,

$$\hat{H} = -J \sum_{n=1}^N \hat{c}_n^\dagger (\hat{c}_{n+1} + \hat{c}_{n-1}) + \hbar\omega_0 \sum_{n=1}^N \hat{b}_n^\dagger \hat{b}_n + g \sum_{n=1}^N \hat{c}_n^\dagger \hat{c}_n (\hat{b}_n^\dagger + \hat{b}_n) \quad (2.53)$$

where \hat{c}_n^\dagger and \hat{c}_n are the fermion creation and annihilation operators for an electron/hole on site n , \hat{b}_n^\dagger and \hat{b}_n are the boson creation and annihilation operators for a phonon at site n , J is the constant transfer integral, ω_0 the Einstein-mode phonon frequency, N the number of lattice sites and g the electron-phonon coupling constant. In the momentum space, the Holstein Hamiltonian is,

The Holstein Hamiltonian

$$\hat{H} = -J \sum_{\mathbf{k}} \hat{c}_{\mathbf{k}}^\dagger \hat{c}_{\mathbf{k}} + \hbar\omega_0 \sum_{\mathbf{q}} \hat{b}_{\mathbf{q}}^\dagger \hat{b}_{\mathbf{q}} + \frac{g}{\sqrt{N}} \sum_{\mathbf{k}, \mathbf{q}} \hat{c}_{\mathbf{k}+\mathbf{q}}^\dagger \hat{c}_{\mathbf{k}} (\hat{b}_{-\mathbf{q}}^\dagger + \hat{b}_{\mathbf{q}}) \quad (2.54)$$

where the electronic and phononic wave numbers k and q assume N discrete values within the first Brillouin zone $-\frac{\pi}{a} < k, q < \frac{\pi}{a}$, where a the lattice constant. The electron dispersion

$\epsilon_{\mathbf{k}}$ is the typical tight-binding electron dispersion,

$$\epsilon_{\mathbf{k}} = -2J \sum_{i=1}^n \cos(k_i), \quad (2.55)$$

where n is the number of dimensions and k_i indicates the component of the electron wavevector along the i -th dimension. In analogy to the Fröhlich Hamiltonian in Eq. (2.17), we can express the electron-phonon coupling matrix as $M_{\mathbf{q}}$,

$$\begin{aligned} M_{\mathbf{q}} = M_0 &= \frac{g_n}{\sqrt{N}}, \\ &= \sqrt{\frac{2Jn\hbar\omega_0\alpha_H}{N}}, \end{aligned} \quad (2.56)$$

where g_n is the Holstein electron-phonon coupling strength in n dimensions and is parameterised by the *unitless* coupling constant α_H . As J is the main energy scale in this model, we also need to define another unitless parameter $\gamma \equiv \hbar\omega_0/J$, which is the ratio of the phonon energy and electron hopping amplitude and called the adiabaticity.

2.2 The Feynman Path Integral & Variational Approach

Feynman developed a variational principle to find the lowest energy of a system described by a path integral. This variational principle was applied to the Fröhlich model of the polaron [3] and was the first method to accurately predict the ground-state energy and effective mass of the polaron for all values of the electron-phonon coupling constant. We start with Fröhlich's Hamiltonian for a slow electron as given in Eq. (2.38) and cast the phonon creation and annihilation operators into their corresponding coordinates \hat{x}_q and momenta \hat{p}_q

$$\hat{x}_q = \frac{1}{\sqrt{2}} r_0 (\hat{b}_q^\dagger + \hat{b}_q), \quad \hat{p}_q = i\hbar \frac{1}{\sqrt{2}} \frac{1}{r_0} (\hat{b}_q^\dagger - \hat{b}_q), \quad (2.57)$$

or Fourier components

$$\hat{b}_q = \frac{1}{\sqrt{2}} \frac{1}{r_0} \left(\hat{x}_q + i \frac{\hat{p}_q}{m_0 \omega_0} \right), \quad \hat{b}_q^\dagger = \frac{1}{\sqrt{2}} \frac{1}{r_0} \left(\hat{x}_q - i \frac{\hat{p}_q}{m_0 \omega_0} \right), \quad (2.58)$$

which substituted into Eq. (2.38) gives

$$H = \frac{\hat{p}^2}{2m_0} + \frac{1}{2} \sum_q \left(\hat{p}_q^2 + \omega_0^2 \hat{x}_q^2 \right) + \sum_q M_q \hat{\rho}_q \hat{x}_q, \quad (2.59)$$

where $\hat{\rho}_q = e^{i\mathbf{q}\cdot\hat{\mathbf{r}}}$ is the electron density operator.

2.2.1 Ground-State Polaron

If the wavefunction $\psi(\mathbf{r}_i, x_i, t_i)$ corresponding to the polaron system is known at some initial time t_i , then the wavefunction at some later time t_f is given by,

$$\psi(\mathbf{r}_f, x_f, t_f) = \int d^3\mathbf{r}_i \int dx_i K(\mathbf{r}_f, x_f, t_f; \mathbf{r}_i, x_i, t_i) \psi(\mathbf{r}_i, x_i, t_i), \quad (2.60)$$

where $\mathbf{r} \equiv \mathbf{r}$ and $x \equiv \{x_q\}$ represents the set of all polarisation coordinate oscillators. $K(\mathbf{r}_f, x_f, t_f; \mathbf{r}_i, x_i, t_i)$ is commonly called the time-evolution “kernel” or “propagator” and gives the probability amplitude to go from the state of the system $\{\mathbf{r}_i, x_i\}$ at time t_i to the state of the system $\{\mathbf{r}_f, x_f\}$ at time t_f . It can be defined as,

$$\begin{aligned} K(\mathbf{r}_f, x_f, t_f; \mathbf{r}_i, x_i, t_i) &\equiv \langle \psi(\mathbf{r}_f, x_f) | e^{-i\hat{H}(t_f-t_i)} | \psi(\mathbf{r}_i, x_i) \rangle \\ &= \sum_n \psi_n(\mathbf{r}_f, x_f) \psi_n^*(\mathbf{r}_i, x_i) e^{-iE_n t_f}, \end{aligned} \quad (2.61)$$

where ψ_n are a complete orthonormal set of the Fröhlich Hamiltonian eigenfunctions and E_n are the corresponding energy eigenvalues. The ground-state energy can be obtained by

letting $\phi_0(x)$ be any function of the phonon coordinates x that is not orthogonal to the exact ground-state wavefunction $\psi_0(\mathbf{r}, x)$. The inner product of the kernel with $\phi_0(x)$ gives the probability amplitude $G_{0,0}$ for the system in the ground state to return to the ground state,

$$\begin{aligned} G_{0,0}(t_f) &= \langle \phi_0(x_f) | K(\mathbf{r}_f, x_f, t_f; \mathbf{r}_i, x_i, t_i) | \phi_0(x_i) \rangle \\ &= \int \int dx_f dx_i \phi_0^*(x_f) K(\mathbf{r}_f, x_f, t_f; \mathbf{r}_i, x_i, t_i) \phi_0(x_i) \\ &= \sum_n a_{n,0}(\mathbf{r}_f) a_{n,0}^*(\mathbf{r}_i) e^{-iE_n t_f}, \end{aligned} \quad (2.62)$$

where,

$$a_{n,0}(\mathbf{r}) = \int dx \phi_0^*(x) \psi_n(\mathbf{r}, x). \quad (2.63)$$

If we evaluate this for the electron to start and end at the same position (which we choose to be 0 for convenience), $\mathbf{r}_f = \mathbf{r}_i = 0$ from imaginary-time $i0$ to $-i\tau$ we obtain,

$$\begin{aligned} G_{0,0}(-i\tau) &= \langle \phi_0(x_f) | K(0, x_f, -i\tau; i0, x_i, 0) | \phi_0(x_i) \rangle \\ &= \int \int dx_f dx_i \phi_0^*(x_f) K(0, x_f, -i\tau; 0, x_i, i0) \phi_0(x_i) \\ &= \sum_n a_{n,0}(0) a_{n,0}^*(0) e^{-E_n \tau}, \end{aligned} \quad (2.64)$$

which in the limit as $\tau \rightarrow \infty$ picks out the ground-state of the system,

$$\lim_{\tau \rightarrow \infty} \sum_n a_{n,0}(0) a_{n,0}^*(0) e^{-E_n \tau} \rightarrow a_{0,0}(0) a_{0,0}^*(0) e^{-E_0 \tau}. \quad (2.65)$$

Therefore we find that ground-state energy E_{gs} ,

$$E_{gs} = \lim_{\tau \rightarrow \infty} \left[-\frac{1}{\tau} \ln G_{0,0}(-i\tau) \right]. \quad (2.66)$$

If we identify $\tau = \hbar/(k_B T) = \hbar\beta$ (where β is the thermodynamic beta) then the kernel $K(\mathbf{r}_f, x_f, -i\beta; \mathbf{r}_i, x_i, 0)$ is the same as the statistical density matrix $\rho(\mathbf{r}_f, x_f, \hbar\beta; \mathbf{r}_i, x_i, 0)$, and $G_{0,0}(-i\hbar\beta)$ is the same as the statistical partition function Z where,

$$Z(\beta) = \text{Tr} [\rho] = \int \int d\mathbf{r} dx \rho(\mathbf{r}, x, \mathbf{r}, x; \beta), \quad (2.67)$$

and is related to the Helmholtz free energy F by,

$$Z(\beta) = e^{-\beta F} = \text{Tr} [e^{-\beta \hat{H}}] = \sum_n e^{-\beta E_n}. \quad (2.68)$$

Therefore, we can rewrite the expression for the ground-state energy as,

$$E_{gs} = \lim_{\beta \rightarrow \infty} [F(\beta)] = \lim_{\beta \rightarrow \infty} \left[-\frac{1}{\beta} \ln Z(\beta) \right]. \quad (2.69)$$

Path Integral Expression

The kernel can be expressed explicitly as a path integral,

$$K(\mathbf{r}_f, x_f, t_f; \mathbf{r}_i, x_i, t_i) = \int_{\mathbf{r}_i, t_i}^{\mathbf{r}_f, t_f} \mathcal{D}\mathbf{r}(t) \int_{x_i, t_i}^{x_f, t_f} \mathcal{D}x(t) \exp \left\{ \frac{iS[\mathbf{r}(t), x(t)]}{\hbar} \right\}, \quad (2.70)$$

where the action $S[\mathbf{r}, x]$ is given by,

$$\begin{aligned} S[\mathbf{r}(t), x(t)] &= \frac{m_0}{2} \int_{t_i}^{t_f} dt \dot{\mathbf{r}}^2(t) + \frac{1}{2} \sum_{\mathbf{q}} \int_{t_i}^{t_f} dt \left(\dot{x}_{\mathbf{q}}^2(t) - \omega_0^2 x_{\mathbf{q}}^2(t) \right) \\ &\quad - \sum_{\mathbf{q}} M_{\mathbf{q}} \int_{t_i}^{t_f} dt \rho_{\mathbf{q}}(t) x_{\mathbf{q}}(t). \end{aligned} \quad (2.71)$$

Since the phonon coordinates $x(t)$ appear quadratically in the action, the path integral over them can be made to be Gaussian and done explicitly to simplify $G_{0,0}$,

$$G_{0,0}(t_f, t_i) = \prod_{\mathbf{q}} G_{\mathbf{q}}(t_f, t_i) \times \int_{0, t_i}^{0, t_f} \mathcal{D}\mathbf{r}(t) \exp \left\{ \frac{i}{\hbar} \frac{m_0}{2} \int_{t_i}^{t_f} dt \dot{\mathbf{r}}^2(t) \right\}, \quad (2.72)$$

where,

$$\begin{aligned} G_{\mathbf{q}}(t_f, t_i) &= \int_{-\infty}^{\infty} dx_{\mathbf{q}, f} dx_{\mathbf{q}, i} \phi_0^*(x_{\mathbf{q}, f}) \\ &\times \left[\int_{x_{\mathbf{q}, i}, t_i}^{x_{\mathbf{q}, f}, t_f} \mathcal{D}x_{\mathbf{q}}(t) \exp \left\{ \frac{i}{\hbar} \int_{t_i}^{t_f} dt \frac{1}{2} \left(\dot{x}_{\mathbf{q}}^2(t) - \omega_0^2 x_{\mathbf{q}}^2(t) \right) - M_{\mathbf{q}} \rho_{\mathbf{q}}(t) x_{\mathbf{q}}(t) \right\} \right] \phi_0(x_{\mathbf{q}, i}), \end{aligned} \quad (2.73)$$

To make the phonon path integral Gaussian, we can choose $\phi_0(x_{\mathbf{q}})$ to be the ground-state wave function of a simple harmonic oscillator,

$$\phi_0(x_{\mathbf{q}}) = \left(\frac{1}{\pi r_0^2} \right)^{1/4} \exp \left\{ -\frac{x_{\mathbf{q}}^2}{2r_0^2} \right\}, \quad (2.74)$$

Now the integrals in $G_{\mathbf{q}}$ can be solved analytically to give,

$$G_{\mathbf{q}}(t_f, t_i) = ()^{\frac{3}{2}} \exp \left\{ -\frac{|M_{\mathbf{q}}|^2}{2} \int_{t_i}^{t_f} \int_{t_i}^{t_f} dt ds \rho_{\mathbf{q}}(t) D_{\omega_{\mathbf{q}}}(t-s) \rho_{\mathbf{q}}^*(s) \right\}, \quad (2.75)$$

where generally,

Bare Phonon Green Function

$$\begin{aligned} D_{\omega_q}(t-s) &= \langle x_q(t)x_{-q}(s) \rangle_0 \\ &= n_{\omega_q} e^{i\omega_q|t-s|} + (n_{\omega_q} + 1)e^{-i\omega_q|t-s|}, \end{aligned} \quad (2.76)$$

is the equilibrium bare (non-interacting) phonon Green function and $n_{\omega_q} = (e^{\hbar\beta\omega_q} - 1)^{-1}$ is the Bose-Einstein distribution. For Einstein (dispersionless) modes ω_0 and low temperatures $D_{\omega_0}(t) \rightarrow e^{-i\omega_0|t|}$. The determinant of the bare phonon Green function can be evaluated to obtain the phonon partition function,

$$\begin{aligned} Z_{ph} &= \text{Tr } e^{-\beta\hat{H}} \\ &\equiv \prod_q \det(D_{\omega_q}^{-1})^{-1} = \det\left(\frac{\partial}{\partial\tau} + \omega_q\right) \\ &= \prod_{q,\omega_n} (-i\omega_n + \omega_q)^{-1} = \prod_q \prod_{n=1}^{\infty} \left[\left(\frac{2n\pi}{\hbar\beta}\right)^2 + \omega_q^2\right]^{-1} \\ &= \prod_q \frac{1}{2 \sinh(\hbar\omega_q\beta/2)} \end{aligned} \quad (2.77)$$

Feynman then obtained the total polaron kernel defined entirely in terms of the electron coordinate,

$$\begin{aligned} G_{0,0}(t_f, t_i) &= \int_{0,t_i}^{0,t_f} \mathcal{D}\mathbf{r}(t) \exp\left\{ \frac{i}{\hbar} \left[\frac{m_0}{2} \int_{t_i}^{t_f} dt \dot{\mathbf{r}}^2 \right. \right. \\ &\quad \left. \left. - \frac{1}{2} \sum_q |M_q|^2 \int_{t_i}^{t_f} \int_{t_i}^{t_f} dt ds \rho_q(t) D_{\omega_0}(t-s) \rho_q^*(s) \right] \right\}, \end{aligned} \quad (2.78)$$

where the summation of \mathbf{q} can be evaluated to give,

$$\begin{aligned} \sum_q |M_q|^2 \rho_q(t) \rho_q^*(s) &= |M_0|^2 V_0 \int \frac{d^3\mathbf{q}}{(2\pi)^3} \frac{e^{i\mathbf{q}\cdot(\mathbf{r}(t)-\mathbf{r}(s))}}{q^2} \\ &= |M_0|^2 \frac{V_0}{4\pi} \frac{1}{|\mathbf{r}(t) - \mathbf{r}(s)|}. \end{aligned} \quad (2.79)$$

Substituting the result of this summation and setting $t_i = 0$ gives the final form of $G_{0,0}$ to be

$$G_{0,0}(t_f) = \int_{0,0}^{0,t_f} \mathcal{D}\mathbf{r}(t) \exp\left\{ \frac{i}{\hbar} S_{\text{eff}}[\mathbf{r}(t)] \right\}, \quad (2.80)$$

where the new effective action S_{eff} is given by

$$S_{\text{eff}}[\mathbf{r}(t)] = \frac{m_0}{2} \int_0^{t_f} dt \dot{\mathbf{r}}(t)^2 - \frac{\alpha \hbar r_0 \omega_0^2}{2\sqrt{2}} \int_0^{t_f} \int_0^{t_f} dt ds \frac{e^{-i\omega_0|t-s|}}{|\mathbf{r}(t) - \mathbf{r}(s)|}. \quad (2.81)$$

where low temperature $\beta \gg 1$ is assumed. This new effective *model* action represents an electron coupled by a non-local time-retarded Coulomb potential to itself from an earlier time. If we do a Wick rotation back into imaginary time, we obtain the density matrix as a path integral.

$$\rho(\mathbf{r}_f, \hbar\beta; \mathbf{r}_i, 0) = \int_{\mathbf{r}_i, 0}^{\mathbf{r}_f, \hbar\beta} \mathcal{D}\mathbf{r}(\tau) \exp\left\{-\frac{S[\mathbf{r}(\tau)]}{\hbar}\right\}, \quad (2.82)$$

where the model action becomes

Feynman's Polaron *Model* Action

$$S = \frac{m_0}{2} \int_0^{\hbar\beta} d\tau \left(\frac{d\mathbf{r}(\tau)}{d\tau} \right)^2 - \frac{\alpha \hbar r_0 \omega_0^2}{2\sqrt{2}} \int_0^{\hbar\beta} d\tau \int_0^{\hbar\beta} d\sigma \frac{e^{-\omega_0|\tau-\sigma|}}{|\mathbf{r}(\tau) - \mathbf{r}(\sigma)|}. \quad (2.83)$$

Therefore, we can find the exact ground-state energy of the polaron using

$$E_{gs} = \lim_{\beta \rightarrow \infty} \left\{ \frac{1}{\beta} \ln \int_{0,0}^{0,\hbar\beta} \mathcal{D}\mathbf{r}(\tau) e^{-S[\mathbf{r}(\tau)]/\hbar} \right\}. \quad (2.84)$$

The power of this result is that the many-body problem involving an infinite number of phonons interacting with a single conduction electron has been reduced to a one-body problem with one integral with a temporal non-local effective potential. Due to the Coloumbic nature of this potential, the model action is not functionally-integrable. However, Feynman devised a variational approach to at least approximate it.

2.2.2 Feynman-Jensen Variational Principle

The model action cannot be solved exactly as a path integral since it is not quadratic in the electron coordinates. However, Feynman was able to obtain a variational upper-bound approximation of the ground-state energy of the polaron. Feynman noticed that he could use Jensen's inequality: for a set of real values f , the average of $\exp(f)$ exceeds the exponential of the average,

$$\langle \exp(f) \rangle \geq \exp(\langle f \rangle). \quad (2.85)$$

Therefore, if one can find another functionally-integrable trial action S_0 that closely approximates the model action S for the paths $\mathbf{r}(\tau)$ that most significantly contribute to the path integral, then Jensen's inequality can give a lower-bound on the partition function:

The Feynman-Jensen Variational Principle

$$\begin{aligned}
Z(\beta) &= \int_{0,0}^{0,\hbar\beta} \mathcal{D}\mathbf{r}(\tau) e^{-S[\mathbf{r}(\tau)]/\hbar} \\
&= \int_{0,0}^{0,\hbar\beta} \mathcal{D}\mathbf{r}(\tau) e^{-(S[\mathbf{r}(\tau)]-S_0[\mathbf{r}(\tau)])/\hbar} e^{-S_0[\mathbf{r}(\tau)]/\hbar} \\
&= \langle \exp([S - S_0]/\hbar) \rangle_{S_0} \cdot Z_{S_0}(\beta) \\
&\geq \exp\left(\langle S - S_0 \rangle_{S_0} / \hbar\right) \cdot Z_{S_0}(\beta).
\end{aligned} \tag{2.86}$$

The average taken with positive weight S_0 is given by

$$\langle S - S_0 \rangle_{S_0} = [Z_{S_0}(\beta)]^{-1} \int_{0,0}^{0,\hbar\beta} \mathcal{D}\mathbf{r}(\tau) (S - S_0) e^{-S_0[\mathbf{r}]/\hbar}, \tag{2.87}$$

where,

$$Z_{S_0}(\beta) = \int_{0,0}^{0,\hbar\beta} \mathcal{D}\mathbf{r}(\tau) e^{-S_0[\mathbf{r}(\tau)]/\hbar}, \tag{2.88}$$

is the partition function for the system described by the trial action S_0 . Therefore, using the relation between the partition function and the ground-state energy, we obtain

$$\begin{aligned}
E_{gs} &= \lim_{\beta \rightarrow \infty} \left[-\frac{1}{\beta} \ln Z(\beta) \right], \\
&\leq \lim_{\beta \rightarrow \infty} \left[-\frac{1}{\beta} \ln Z_{S_0}(\beta) - \frac{1}{\beta} \langle S - S_0 \rangle_{S_0} \right], \\
&\leq E_{gs}^0 - \lim_{\beta \rightarrow \infty} \left[\frac{1}{\beta} \langle S - S_0 \rangle_{S_0} \right],
\end{aligned} \tag{2.89}$$

where E_{gs}^0 is the ground-state energy of the trial system.

2.2.3 Feynman's Quasi-Particle Trial Model

The next step is determining which trial action, S_0 , to use. Feynman proposed multiple potential trial actions. His first choice corresponds to the free electron, $S_0 = \frac{m_0}{2} \int_0^{\hbar\beta} d\tau \dot{\mathbf{r}}^2(\tau)$ which gives the weak-coupling second-order perturbation method result $E_{gs} \leq -\hbar\omega_0\alpha$. His second choice was an electron in local potential $S_0 = \frac{m_0}{2} \int_0^\infty d\tau \dot{\mathbf{r}}^2(\tau) + \int_0^{\hbar\beta} d\tau V(\mathbf{r}(\tau))$. If this local-potential is Coulombic $V(\mathbf{r}(\tau)) = Q/\mathbf{r}(\tau)$, with a variational charge-like parameter Q , one obtains Landau's variational result for strong-coupling, $E_{gs} \leq -0.098\hbar\omega_0\alpha^2$. Instead, if the local-potential is harmonic $V(\mathbf{r}(\tau)) = \kappa\mathbf{r}^2(\tau)$, with a variational spring-constant parameter κ , then the upper-bound is improved to $E_{gs} \leq -0.106\hbar\omega_0\alpha^2$. However, Fröhlich and Feynman concluded that binding the electron to a position using a local potential would only give worse results at low couplings than for a free electron.

To obtain a method that works over the entire range of α , Feynman proposed coupling the electron to some fictitious particle with finite mass so that the electron is not bound to a position and is free to move. Motivated by the local harmonic potential outperforming the Coulombic potential and the comparative ease in corresponding derivation, Feynman chose to couple the electron and fictitious particle with a harmonic spring. The Hamiltonian for this harmonic spring-mass system is,

$$H_F = \frac{\mathbf{p}_{el}^2}{2m_0} + \frac{\mathbf{p}^2}{2m_f} + \kappa(\mathbf{r} - \mathbf{x})^2 \quad (2.90)$$

where \mathbf{p}_{el} and \mathbf{p} are the momentum of the electron and fictitious particle, m_0 and m_f are their masses, \mathbf{r} and \mathbf{x} their positions, and κ is the spring-constant. The Feynman polaron quasi-particle thus has a direct mechanistic interpretation.

The corresponding Lagrangian is obtained from the Legendre transformation and is given by,

Feynman's Spring-Mass Lagrangian

$$L = \frac{m_0}{2}\dot{\mathbf{r}}(t)^2 + \frac{m_f}{2}\dot{\mathbf{x}}(t)^2 - \frac{\kappa}{2}(\mathbf{r}(t) - \mathbf{x}(t))^2. \quad (2.91)$$

Following the same procedure as we did for deriving Feynman's effective Fröhlich action in Eq. (2.83), we see that the effective trial action just corresponds to the replacement,

$$-\frac{\alpha\hbar r_0\omega_0}{2\sqrt{2}}\frac{D_{\omega_0}(\tau - \sigma)}{|\mathbf{r}(\tau) - \mathbf{r}(\sigma)|} \longrightarrow \frac{\kappa w}{8}D_w(\tau - \sigma)[\mathbf{r}(\tau) - \mathbf{r}(\sigma)]^2, \quad (2.92)$$

where κ and w are now variational parameters and $D_w(\tau)$ is the same phonon Green function (Eq. (2.2.1)) in imaginary-time, but with the replacement $\omega_0 \rightarrow w$. The trial action is then,

Feynman's Polaron Trial Action

$$S_0 = \frac{m_0}{2} \int_0^{\hbar\beta} d\tau \left(\frac{d\mathbf{r}(\tau)}{d\tau} \right)^2 + \frac{\kappa w}{8} \int_0^{\hbar\beta} d\tau \int_0^{\hbar\beta} d\sigma D_w(\tau - \sigma) [\mathbf{r}(\tau) - \mathbf{r}(\sigma)]^2. \quad (2.93)$$

Substituting the model action S and trial action S_0 into the variational inequality gives,

$$E_{gs} \leq E_{gs}^0 - \lim_{\beta \rightarrow \infty} \frac{1}{\beta} \langle S - S_0 \rangle_{S_0}. \quad (2.94)$$

Using,

$$\begin{aligned} \frac{1}{\beta} \int_0^{\hbar\beta} \int_0^{\hbar\beta} d\tau d\sigma f(|\tau - \sigma|) &= \frac{2}{\beta} \int_0^{\hbar\beta} d\tau (\hbar\beta - \tau) f(|\tau|) \\ &\sim 2\hbar \int_0^{\hbar\beta} d\tau f(\tau) \quad (\text{as } \beta \rightarrow \infty), \end{aligned} \quad (2.95)$$

we get,

$$\lim_{\beta \rightarrow \infty} \frac{1}{\beta} \langle S \rangle_{S_0} = -\frac{\alpha \hbar r_0 \omega_0^2}{\sqrt{2}} \int_0^\infty d\tau D_{\omega_0}(\tau) \left\langle |\mathbf{r}(\tau) - \mathbf{r}(0)|^{-1} \right\rangle_{S_0}, \quad (2.96a)$$

$$\lim_{\beta \rightarrow \infty} \frac{1}{\beta} \langle S_0 \rangle_{S_0} = \frac{\kappa w}{4} \int_0^\infty d\tau D_w(\tau) \left\langle [\mathbf{r}(\tau) - \mathbf{r}(0)]^2 \right\rangle_{S_0}. \quad (2.96b)$$

To solve $\langle S \rangle_{S_0}$ and $\langle S_0 \rangle_{S_0}$ we concentrate on the $|\mathbf{r}(\tau) - \mathbf{r}(0)|^{-1}$ term in $\langle S \rangle_{S_0}$ and express it by a Fourier transform,

$$\begin{aligned} |\mathbf{r}(\tau) - \mathbf{r}(\sigma)|^{-1} &= \int \frac{d^3 \mathbf{q}}{(2\pi)^3} \frac{1}{q^2} e^{i\mathbf{q} \cdot [\mathbf{r}(\tau) - \mathbf{r}(0)]} \\ &\equiv \int \frac{d^3 \mathbf{q}}{(2\pi)^3} \frac{1}{q^2} \exp \left(\int_0^\infty dt \mathbf{J}_{\mathbf{q},\tau}(t) \cdot \mathbf{r}(t) \right), \end{aligned} \quad (2.97)$$

where we have defined an ‘external force’ function $\mathbf{J}_{\mathbf{q},\tau}(t) = i\mathbf{q} [\delta(t - \tau) - \delta(t)]$. Substituting this into $\langle S \rangle_{S_0}$ and $\langle S_0 \rangle_{S_0}$ simplifies them into,

$$\lim_{\beta \rightarrow \infty} \frac{1}{\beta} \langle S \rangle_{S_0} = -\frac{\alpha \hbar r_0 \omega_0^2}{\sqrt{2}} \int_0^\infty d\tau D_{\omega_0}(\tau) \int \frac{d^3 \mathbf{q}}{(2\pi)^3} \frac{1}{q^2} Z[\mathbf{J}_{\mathbf{q},\tau}(t)] \quad (2.98a)$$

$$\lim_{\beta \rightarrow \infty} \frac{1}{\beta} \langle S_0 \rangle_{S_0} = \frac{\kappa w}{4} \int_0^\infty d\tau D_w(\tau) \left(-\nabla_{\mathbf{q}}^2 Z[\mathbf{J}_{\mathbf{q},\tau}(t)] \Big|_{\mathbf{q}=0} \right), \quad (2.98b)$$

where,

$$Z[\mathbf{J}_{\mathbf{q},\tau}(t)] \equiv \left\langle \exp \left(\int_0^\infty dt \mathbf{J}_{\mathbf{q},\tau}(t) \cdot \mathbf{r}(t) \right) \right\rangle_{S_0}, \quad (2.99)$$

is the generating functional. The generating functional is also the intermediate scattering function, the temporal Fourier transform of the dynamical structure factor, and is proportional to the two-point electron density-density correlation function.

We need the ground-state energy E_{gs}^0 associated with the trial system. We can avoid directly evaluating the path integral Z_{S_0} by noting that,

$$\lim_{\beta \rightarrow \infty} Z_{S_0}(\beta) = \lim_{\beta \rightarrow \infty} \exp(-\beta E_{gs}^0) = \lim_{\beta \rightarrow \infty} \int_{-\infty}^\infty d\mathbf{r}' \int_{\mathbf{r}'} \mathcal{D}\mathbf{r}(\tau) \exp \left(-\frac{S_0[\mathbf{r}(\tau)]}{\hbar} \right). \quad (2.100)$$

So, differentiating both sides concerning κ ,

$$\frac{\partial E_{gs}^0}{\partial \kappa} = \frac{1}{\kappa} \lim_{\beta \rightarrow \infty} \frac{1}{\beta} \langle S_0 \rangle_{S_0} \quad (2.101)$$

and then integrating both sides,

$$E_{gs}^0 = \int_0^\kappa d\kappa' \frac{1}{\kappa'} \lim_{\beta \rightarrow \infty} \frac{1}{\beta} \langle S_0(\kappa') \rangle_{S_0}. \quad (2.102)$$

Since $E_{gs}^0 = 0$ when $\kappa = 0$ (i.e. the free particle). Hence, solving for the upper-bound to the ground-state energy has been reduced to solving $Z[J_{q,\tau}(t)]$, which, written explicitly, is,

$$Z[J_{q,\tau}(t)] = \frac{\oint \mathcal{D}\mathbf{r}(\tau) \exp\left(-\frac{S_0}{\hbar} + \int_0^\infty dt J_{q,\tau}(t) \cdot \mathbf{r}(t)\right)}{\oint \mathcal{D}\mathbf{r}(\tau) \exp\left(-\frac{S_0}{\hbar}\right)}. \quad (2.103)$$

We can solve the path integral in the numerator by the usual method of changing the path-integration variable to $\mathbf{r}'(\tau) \equiv \mathbf{r}(\tau) - \bar{\mathbf{r}}(\tau)$ where $\bar{\mathbf{r}}(\tau)$ is the path that extremises the trial action S_0 and with the boundary conditions $\bar{\mathbf{r}}(0) = \bar{\mathbf{r}}(\hbar\beta) = 0$. Thus, $\bar{\mathbf{r}}(\tau)$ contributes most to the path integral and is the classical path, whereas $\mathbf{r}'(\tau)$ are the ‘quantum fluctuations’ about the classical path. The path integral now only contains $\bar{\mathbf{r}}(\tau)$ quadratically, which then separates off as a normalisation factor that excludes the force term $J_{q,\tau}(t)$ and is equal to the denominator (i.e. the trial partition function $Z_{S_0}(\beta)$), so it cancels. $\bar{\mathbf{r}}(\tau)$ solves the classical equation of motion that is obtained by extremising the trial action S_0 and gives the following integral-differential equation of motion,

$$\frac{d^2\bar{\mathbf{r}}(t)}{dt^2} = \frac{\kappa w}{2} \int_0^\infty ds D_w(t-s) [\bar{\mathbf{r}}(t) - \bar{\mathbf{r}}(s)] - J_{q,\tau}(t), \quad (2.104)$$

which can be used to simplify $Z[J_{q,\tau}(t)]$ by eliminating the classical action term $S_0[\bar{\mathbf{r}}]$ to leave,

$$Z[J_{q,\tau}(t)] = \exp\left(\frac{1}{2} \int_0^\infty dt J_{q,\tau}(t) \cdot \bar{\mathbf{r}}(t)\right). \quad (2.105)$$

Now, all that is left is to solve the equation of motion to find the classical path $\bar{\mathbf{r}}(t)$. This can be done by first defining,

$$\mathbf{x}(t) \equiv \frac{w}{2} \int_0^\infty ds D_w(t-s) \bar{\mathbf{r}}(s). \quad (2.106)$$

Since $d|t-s|/dt = \text{sgn}(t-s)$ and $d\text{sgn}(t-s)/dt = 2\delta(t-s)$, we have,

$$\frac{d^2\mathbf{x}(t)}{dt^2} = w^2 [\mathbf{x}(t) - \bar{\mathbf{r}}(t)], \quad (2.107)$$

and

$$\frac{d^2\bar{\mathbf{r}}(t)}{dt^2} = \kappa [\bar{\mathbf{r}}(t) - \mathbf{x}(t)] - J_{\mathbf{q},\tau}(t), \quad (2.108)$$

where in the second equation and in the limit $\beta \rightarrow \infty$ we obtain the term,

$$\int_0^\infty ds D_w(t-s) = \int_0^\infty ds e^{-w|t-s|} = \frac{2}{w} - \frac{e^{-wt}}{w}, \quad t \in [0, \infty) \quad (2.109)$$

and we neglect the second transient term since it has a negligible contribution. These differential equations can be separated and solved to give the classical path as,

$$\bar{\mathbf{r}}(t) = \int_0^\infty ds g(t-s) J_{\mathbf{q},\tau}(s), \quad (2.110)$$

where,

$$\begin{aligned} g(t-s) &= \frac{1}{2\pi} \oint dz \frac{z^2 + w^2}{z^2(z^2 + v^2)} (e^{-z|t-s|} - 1) \\ &= i \left[\frac{1}{2} \text{Res}(z=0) + \text{Res}(z=iv) \right] \\ &= -\frac{1}{2v^2} \left[\frac{v^2 - w^2}{v} (1 - e^{-v|t-s|}) + w^2 |t-s| \right], \end{aligned} \quad (2.111)$$

with $v^2 \equiv w^2 + \kappa = (1 + M/m_0)w^2$. Substituting the solution for $\bar{\mathbf{r}}(t)$ into $Z[J_{\mathbf{q},\tau}(t)]$ then gives,

$$\begin{aligned} Z[J_{\mathbf{q},\tau}(t)] &= \exp \left(\frac{1}{2} \int_0^{\hbar\beta} dt \int_0^{\hbar\beta} ds J_{\mathbf{q},\tau}(t) \cdot g(t-s) \cdot J_{\mathbf{q},\tau}(s) \right) \\ &= \exp \left(r_0^2 \mathbf{q}^2 g(\tau - \sigma) \right). \end{aligned} \quad (2.112)$$

Finally, we can use the solution for $Z[J_{\mathbf{q},\tau}(t)]$ to determine $\langle S \rangle_{S_0}$,

$$\lim_{\beta \rightarrow \infty} \frac{1}{\beta} \langle S \rangle_{S_0} = -\frac{\alpha \hbar \omega_0^2}{\sqrt{\pi}} \int_0^\infty d\tau \frac{e^{-\tau \omega_0}}{\sqrt{G(\tau)}}, \quad (2.113)$$

where,

$$G(\tau) = -2g(\tau) = \frac{w^2}{v^2}\tau + \frac{v^2 - w^2}{v^3} (1 - e^{-v\tau}), \quad (2.114)$$

and also determine $\langle S_0 \rangle_{S_0}$ and E_{gs}^0 ,

$$\lim_{\beta \rightarrow \infty} \frac{1}{\beta} \langle S_0 \rangle_{S_0} = -\frac{3\hbar\kappa}{4v} = -\frac{3}{4}\hbar \frac{v^2 - w^2}{v}, \quad (2.115)$$

$$E_{gs}^0 = \frac{3}{2}\hbar(v - w). \quad (2.116)$$

Finally, we obtain the variational principle for the ground-state energy of the polaron,

Variational Polaron Ground-State Energy

$$E_{gs} \leq \frac{3\hbar}{4v} (v - w)^2 - \alpha\hbar\omega_0^2 \sqrt{\frac{1}{\pi}} \int_0^\infty d\tau \frac{e^{-\tau\omega_0}}{\sqrt{G(\tau)}}. \quad (2.117)$$

Here, v and w are to be varied to find the lowest approximate upper bound to the exact ground-state E_{gs} . Regarding these variational parameters the spring constant is $\kappa = v^2 - w^2$ and the fictitious mass is $m_f = (v^2 - w^2)/w^2$.

2.2.4 Weak- and strong- coupling limits

The original work of Feynman [2] provides several asymptotic estimates of this w parameter. The standard approximations often reproduced in textbooks are $w = 3$ for small α coupling and $w = 1$ for large α coupling.

Precise work requires a numeric solution, but these limits inform us that the internal polaron mode, as a function of electron-phonon coupling, starts as a harmonic of $3\omega_0$ and continuously red-shifts to the phonon fundamental frequency ω_0 .

For extremal values of the coupling α , w smoothly approaches limits of 1 and 3. The energy minimum in the weak-coupling (small alpha) limit occurs when v is near w . Therefore, Feynman set $v = (1 + \varepsilon)w$ where ε is small and expanded the energy expression (RHS of Eq. (2.117)) w.r.t ε . Feynman then minimised the energy first w.r.t ε and then w.r.t w and found that in the weak-coupling limit, the energy is least when,

$$\begin{aligned} \frac{w}{\omega_0} &= 3, \quad \frac{v}{\omega_0} = 3 \left[1 + \frac{2\alpha}{3w} \left(1 - \frac{2}{w} [\sqrt{w-1} - 1] \right) \right], \\ \frac{E_{gs}}{\hbar\omega_0} &\leq -\alpha - \left(\frac{\alpha}{9} \right)^2 - O(\alpha^4) \approx -\alpha - 0.0123\alpha^2 - O(\alpha^4). \end{aligned} \quad (2.118)$$

The result agrees well with the perturbative result E_{gs}^w ,

$$\frac{E_{gs}^w}{\hbar\omega_0} = -\alpha - 0.0159196220\alpha^2 - 0.000806070048\alpha^3 - O(\alpha^4). \quad (2.119)$$

In the strong-coupling (large alpha) limit, v is large, and w approaches one, so $w/v \ll 1$. Therefore, Feynman expanded the energy expression w.r.t w/v and then minimised the

energy w.r.t v and w and found that in the strong-coupling limit the energy is least when,

$$\frac{w}{\omega_0} = 1, \quad \frac{v}{\omega_0} = \frac{4\alpha^2}{9\pi} - 4 \left(\log 2 + \frac{1}{2}\gamma \right) + 1, \\ \frac{E_{gs}}{\hbar\omega_0} \leq -\frac{\alpha^2}{2\pi} - \frac{3}{2}(2\log 2 + \gamma) - \frac{3}{4} + O\left(\frac{1}{\alpha^2}\right) \approx -0.1061\alpha - 2.8294 + O\left(\frac{1}{\alpha^2}\right), \quad (2.120)$$

where $\gamma = 0.5772\dots$ is the Euler-Mascheroni constant. This is reasonable when compared to the result of the precise strong-coupling expansion E_{gs}^s ,

$$\frac{E_{gs}^s}{\hbar\omega_0} = -0.108513\alpha^2 - 2.836 - O\left(\frac{1}{\alpha^2}\right). \quad (2.121)$$

2.2.5 Feynman's polaron effective mass

Feynman found the effective polaron mass at zero temperature [2] by assuming that the electron moves with a small velocity \mathbf{v} from an initial coordinate $\mathbf{r}(0) = \mathbf{0}$ to a final coordinate $\mathbf{r}(\hbar\beta) = \mathbf{v}\hbar\beta$ in imaginary time $\hbar\beta$. Feynman then sought the total energy of the polaron and equated it to the form $E_0 + \frac{1}{2}Mv^2$ by expanding the expression of the total energy to quadratic order in the velocity \mathbf{v} . From the kinetic energy term, Feynman found the polaron effective mass,

The Polaron Effective Mass

$$M = m_0 \left[1 + \frac{\alpha\omega_0^3}{3\sqrt{\pi}} \int_0^\infty d\tau \frac{\tau^2 e^{-\tau\omega_0}}{[G(\tau)]^{3/2}} \right]. \quad (2.122)$$

Here, the variational parameter values minimise the polaron ground-state energy when $\mathbf{v} = 0$ in Eq. (2.117). From the values in Eq. (2.118) Feynman obtained the weak-coupling expression,

$$M = m_0 \left[1 + \frac{\alpha}{6} + 2.469136 \left(\frac{\alpha}{10} \right)^2 + 3.566719 \left(\frac{\alpha}{10} \right)^3 + \dots \right], \quad (2.123)$$

and from the values in Eq. (2.120) the strong-coupling expression,

$$M \approx m_0 \left[11.85579 - \frac{4}{3\pi}(1 + \ln 4)\alpha^2 + \frac{16}{81\pi^2}\alpha^4 \dots \right], \\ \approx m_0 \left[11.85579 - 1.012775\alpha^2 + 0.020141\alpha^4 + \dots \right]. \quad (2.124)$$

For comparison, the exact weak-coupling mass is,

$$M_w = m_0 \left[1 + \frac{\alpha}{6} + 2.362763 \left(\frac{\alpha}{10} \right)^2 + O(\alpha^4) \right], \quad (2.125)$$

and the exact strong-coupling result is,

$$M_s = m_0 \left[0.0227019 \alpha^4 + O(\alpha^2) \right]. \quad (2.126)$$

Alternatively, Schultz [29] used the ‘zeroth-order’ effective mass,

The ‘Zeroth-Order’ Polaron Effective Mass

$$M = m_0 + m_f = m_0 \left(\frac{v}{w} \right)^2, \quad (2.127)$$

which is obtained by approximating the model action S with the trial S_0 ; no higher-order expansion terms are included.

At finite temperatures, the effective polaron mass (as described by [67]) is proportional to the imaginary part of the complex impedance function $Z(\Omega, \beta)$ provided by [17] (Eqs. (35), (36) & (41)) in the zero frequency limit $\Omega \rightarrow 0$,

$$M(\beta) = e m_0 \lim_{\Omega \rightarrow 0} \left\{ \frac{\text{Im}Z(\Omega, \beta)}{\Omega} \right\}. \quad (2.128)$$

2.2.6 Schultz’s polaron effective size

Schultz [29] estimated the polaron size by calculating the root mean square distance between the electron and the fictitious particle. The reduced mass of their relative motion is:

$$\mu_0 = \frac{m_f m_0}{m_f - m_0}. \quad (2.129)$$

Schultz then used the ground-state harmonic oscillator wave function for the relative coordinate $\Delta r = \mathbf{r} - \mathbf{x}$ between the electron and the fictitious mass,

$$\phi_0(\Delta r) = \left(\frac{\mu_0 v}{\pi m_0 \omega_0 r_0^2} \right)^{3/4} \exp \left(-\frac{\mu_0 v \Delta r^2}{2 m_0 \omega_0 r_0^2} \right), \quad (2.130)$$

to define a polaron radius as the root mean square distance between the electron and the fictitious mass,

$$R \equiv \langle \Delta r^2 \rangle^{1/2} = \frac{r_0}{2} \left(\frac{3m_0\omega_0}{\mu_0 v} \right)^{1/2} = \frac{r_0}{2} \left(\frac{3\omega_0 v}{(v^2 - w^2)} \right)^{1/2}. \quad (2.131)$$

In the weak-coupling limit, with v and w given in Eq. 2.118, this expression for the polaron radius reduces to,

$$\frac{R}{r_0} \sim \frac{3}{4} \sqrt{\frac{6}{\alpha}}, \quad (2.132)$$

and in the strong-coupling limit (Eq. 2.120) the radius becomes,

$$\frac{R}{r_0} \sim \frac{3\sqrt{\pi}}{2\alpha}. \quad (2.133)$$

2.2.7 Generalisation to n dimensions

The form of the Fröhlich Hamiltonian in n dimensions was obtained by Peeters et al. [39] and is the same as in 3D, except that all the vectors will be n -dimensional and the Fröhlich electron-phonon coupling matrix $M_{\mathbf{q}}$ is different, as proportional to the Fourier transform of the n -dimensional generalisation of the Coulomb potential,

$$|M_{\mathbf{q}}|^2 = \frac{1}{V_n} \frac{|M_n|^2}{q^{n-1}}, \quad (2.134)$$

where V_n is the n -dimensional unit-cell volume of the crystal and the coefficient M_n is,

$$M_n = i\hbar\omega_0 \left(\alpha r_0 \Gamma \left(\frac{n-1}{2} \right) (2\sqrt{\pi})^{n-1} \right)^{1/2}, \quad (2.135)$$

where α is the usual Fröhlich dimensionless electron-phonon coupling and $\Gamma(x)$ is the Gamma function. This definition shows that the electron-phonon matrix diverges for 1D as $\lim_{x \rightarrow 0} \Gamma(x) \rightarrow \infty$. Due to the new scaling for the phonon wave-vector, \mathbf{q} , any summation or integrals over \mathbf{q} will be of the general form (assuming a dispersionless phonon frequency $\omega_{\mathbf{q}} = \omega_0$),

$$\sum_{\mathbf{q}} |M_{\mathbf{q}}|^2 \bullet_q \rightarrow |M_n|^2 \int \frac{d^n \mathbf{q}}{(2\pi)^n} \frac{1}{q^{n-1}} \bullet_q, \quad (2.136)$$

where \bullet_q are any other $|\mathbf{q}| = q$ -dependent terms in the integrand. Note that the volume terms have cancelled each other. To solve equations of this type, we transform the integral

to spherical coordinates,

$$|M_n|^2 \int \frac{d^n \mathbf{q}}{(2\pi)^n} \frac{1}{q^{n-1}} \bullet_q = \frac{|M_n|^2}{(2\pi)^n} \int_S dS \int_0^\infty dq q^{3-n} \bullet_q, \quad (2.137)$$

where $\int_S dS$ denotes the integral over the surface S of an n -dimensional ball; an $(n-1)$ -sphere. Assuming the integrand contains no angle-dependent terms (i.e. the integrand only depends on $|\mathbf{q}| = q$), this integral is,

$$\begin{aligned} \frac{|M_n|^2}{(2\pi)^n} \int_S dS \int_0^\infty dq q^{3-n} \bullet_q &= |M_n|^2 \frac{S_{n-1}}{(2\pi)^n} \int_0^\infty dq q^{3-n} \bullet_q \\ &= \frac{2|M_n|^2}{\Gamma\left(\frac{n}{2}\right) (2\sqrt{\pi})^n} \int_0^\infty dq q^{3-n} \bullet_q, \end{aligned} \quad (2.138)$$

where $S_{n-1} = 2\pi^{n/2}/\Gamma(\frac{n}{2})$ is the surface area of the unit $(n-1)$ -sphere of radius 1.

In the FVA, these q -space integrals typically have $\bullet_q = q^{2m} e^{-q^2 G}$ where m is zero or some positive integer and G is trial polaron Green function in Eq. (2.114). Therefore, all q -space integrals in the FVA to the n -dimensional Fröhlich model are typically of the form,

$$\begin{aligned} \sum_{\mathbf{q}} |M_{\mathbf{q}}|^2 q^{2m} e^{-q^2 G} &\rightarrow |M_n|^2 \frac{S_{n-1}}{(2\pi)^n} \int_0^\infty dq q^{3+2m-n} e^{-q^2 G} \\ &= \frac{1}{2} |M_n|^2 \frac{S_{n-1}}{(2\pi)^n} \Gamma\left(2+m-\frac{n}{2}\right) G^{\frac{n}{2}-m-2} \\ &= \frac{|M_n|^2}{(2\sqrt{\pi})^n} \frac{\Gamma(2+m-n/2)}{\Gamma(n/2)} G^{\frac{n}{2}-m-2}. \end{aligned} \quad (2.139)$$

In summary, these q -space integrals in the FVA to the n -dimensional Fröhlich model, including all the relevant units, are,

General q-space Integrals for the FVA to the Fröhlich Model

$$\sum_{\mathbf{q}} |M_{\mathbf{q}}|^2 (qr_0)^{2m} e^{-q^2 r_0^2 G} \rightarrow \frac{\hbar^2 \omega_0^2 \alpha r_0^{n-3}}{2\sqrt{\pi}} \frac{\Gamma(2+m-n/2) \Gamma(n/2-1/2)}{\Gamma(n/2)} G^{\frac{n}{2}-m-2}, \quad (2.140)$$

with G the polaron trial Green function, n the number of dimensions and m zero or some positive integer. For example, in the variational equation for the polaron energy (Eq. (2.117)) $m = 0$, for the effective mass calculation (Eq. (2.122)) and later during the polaron mobility calculation (see Eq. (2.203)) $m = 2$.

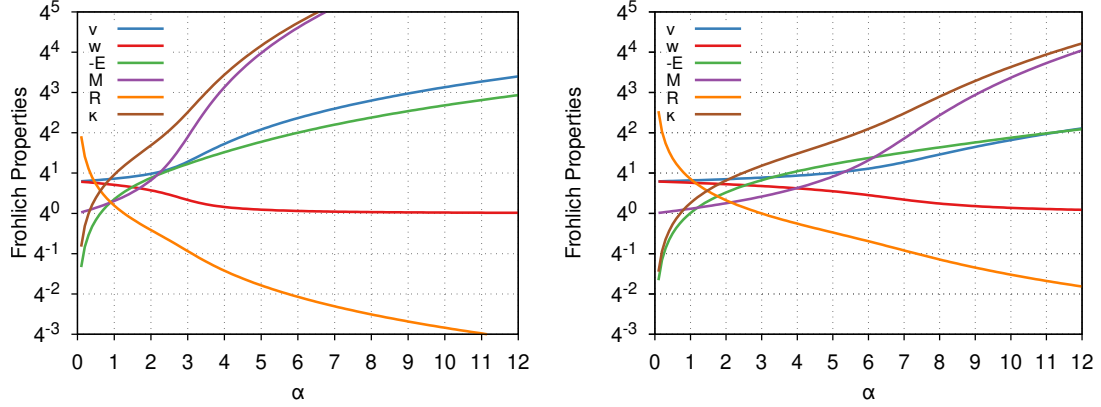


Figure 2.1: Electron-phonon coupling dependence of the Feynman athermal polaron theory in 2D (**left**) and 3D (**right**) in polaron units. **Green** is the negative of the variationally optimal ground-state energy E (units of $\hbar\omega_0$), **purple** is the polaron effective mass M (units of m_0), **blue** is the v (units of ω_0) variational parameter; **red** is the w (units of ω_0) variational parameter, **orange** is the polaron size R (units of r_0), and **brown** is the polaron spring-constant κ (units of $m_0\omega_0^2$).

From this n -dimensional formalism, one can derive scaling relations between n -dimensions and 3D for the FVA Fröhlich polaron energy E_n , effective mass M_n , memory function Σ_n (see Eq. (2.202)) and mobility μ_n (see Eq. (2.211)) [40],

Polaron Scaling Relations

$$E_n(\alpha) = \frac{n}{3} E_3(A_n \alpha), \quad (2.141a)$$

$$M_n(\alpha) = M_3(A_n \alpha), \quad (2.141b)$$

$$\Sigma_n(\alpha) = \Sigma_3(A_n \alpha), \quad (2.141c)$$

$$\mu_n(\alpha) = \mu_3(A_n \alpha), \quad (2.141d)$$

where A_n is,

$$A_n = \frac{3\sqrt{\pi}}{2n} \frac{\Gamma(n/2 - 1/2)}{\Gamma(n/2)}. \quad (2.142)$$

2.2.8 Athermal FVA Numerical Results

Fig. (2.1) shows the values of the polaron ground-state energy $-E$ (units $\hbar\omega_0$) (Eq. (2.117)), effective mass M (units m_0) (Eq. (2.129)), radius R (units r_0) (Eq. (2.131)), spring-constant $\kappa = v^2 - w^2$ (units $m_0\omega_0^2$) and the corresponding variational v (units ω_0) and w (units ω_0) parameters, for the 2D (left) and 3D (right) Fröhlich model for α ranging from 0 to 12. These polaron properties are all presented in their ‘polaron units’ form (\bullet_0) for easier comparison to Feynman’s original paper. The magnitude of the ground state energy starts at zero for zero coupling before a linear increase at weak coupling and then increases quadratically

at large coupling. The effective mass starts roughly equal to the conduction electron band-mass $M = 1m_0$ at small α and then grows exponentially larger at stronger couplings. The v and w variational parameters start as approximately equal with $v \approx w = 3\omega_0$ at weak couplings but diverge at strong couplings as w asymptotically approaches $w = 1\omega_0$, and v increases quadratically in α at a similar rate to the ground-state energy. Aside from the overall dimension-dependent scaling constant on the ground-state energy, the main difference between the 2D and 3D Fröhlich models value of α for which the polaron transitions from weak to strong coupling. In 3D, this occurs around $\alpha \approx 6$, whereas in 2D, it is $\alpha \approx 6/(3\pi/4) \approx 2.55$ as determined by the scaling relations in Eq. (2.141).

2.2.9 Finite Temperature Polaron

Ōsaka [30] extends Feynman's athermal path integral polaron model to the case at a finite temperature. This means that the variational principle for the ground-state energy of the polaron is replaced by the variation of the *free energy*. Ōsaka begins with the density matrix of the polaron system with the model action of the polaron at a finite temperature given by,

$$S = \frac{m_0}{2} \int_0^{\hbar\beta} d\tau \dot{\mathbf{r}}^2(\tau) - \frac{\alpha\hbar r_0\omega_0^2}{2\sqrt{2}} \int_0^{\hbar\beta} d\tau \int_0^{\hbar\beta} d\sigma \frac{D_{\omega_0}(\tau - \sigma)}{|\mathbf{r}(\tau) - \mathbf{r}(\sigma)|}. \quad (2.143)$$

Ōsaka then chose the trial action to be,

$$S_0 = \frac{m_0}{2} \int_0^{\hbar\beta} d\tau \dot{\mathbf{r}}^2(\tau) + \frac{\kappa w}{8} \int_0^{\hbar\beta} d\tau \int_0^{\hbar\beta} d\sigma D_w(\tau - \sigma) |\mathbf{r}(\tau) - \mathbf{r}(\sigma)|^2, \quad (2.144)$$

where $D_w(\tau)$ is the phonon Green function (Eq. (2.2.1)) with frequency w . The model and trial density matrices are then,

$$\rho_S(\mathbf{r}_f, \mathbf{r}_i; \hbar\beta) = \int_{\mathbf{r}(0)=\mathbf{r}_i}^{\mathbf{r}(\hbar\beta)=\mathbf{r}_f} \mathcal{D}\mathbf{r}(\tau) \exp\left(-\frac{S[\mathbf{r}(\tau)]}{\hbar}\right), \quad (2.145a)$$

$$\rho_{S_0}(\mathbf{r}_f, \mathbf{r}_i; \hbar\beta) = \int_{\mathbf{r}(0)=\mathbf{r}_i}^{\mathbf{r}(\hbar\beta)=\mathbf{r}_f} \mathcal{D}\mathbf{r}(\tau) \exp\left(-\frac{S_0[\mathbf{r}(\tau)]}{\hbar}\right). \quad (2.145b)$$

The variational principle for a finite temperature is then,

$$\rho_S(\mathbf{r}_f, \mathbf{r}_i; \hbar\beta) \geq \rho_{S_0}(\mathbf{r}_f, \mathbf{r}_i; \hbar\beta) \exp \langle S - S_0 \rangle_{S_0}, \quad (2.146)$$

where,

$$\langle S - S_0 \rangle_{S_0} = \frac{\int_{\mathbf{r}(0)=\mathbf{r}_i}^{\mathbf{r}(\hbar\beta)=\mathbf{r}_f} \mathcal{D}\mathbf{r}(\tau) (S[\mathbf{r}(\tau)] - S_0[\mathbf{r}(\tau)]) \exp\left(-\frac{S_0[\mathbf{r}(\tau)]}{\hbar}\right)}{\rho_{S_0}(\mathbf{r}_f, \mathbf{r}_i; \hbar\beta)}. \quad (2.147)$$

The RHS of the variational equation then has to be calculated and minimised w.r.t the variational parameters κ and w . The equation of motion obtained from the trial action S_0 is,

$$\begin{aligned} m_0 \ddot{\mathbf{r}}(\tau) &= \frac{\kappa w}{2} \int_0^{\hbar\beta} d\sigma D_w(\tau - \sigma) [\mathbf{r}(\tau) - \mathbf{r}(\sigma)] \\ &= \kappa \mathbf{r}(\tau) - \frac{\kappa w}{2} \int_0^{\hbar\beta} d\sigma D_w(\tau - \sigma) \mathbf{r}(\sigma), \end{aligned} \quad (2.148)$$

which we can use with the boundary conditions $\mathbf{r}(\hbar\beta) = \mathbf{r}_f$ and $\mathbf{r}(0) = \mathbf{r}_i$ to give the trial density matrix to be,

$$\rho_{S_0}(\mathbf{r}_i, \mathbf{r}_f; \hbar\beta) = Z_{\text{ph}} \exp\left\{-\frac{m_0}{2\hbar} (\mathbf{r}(\hbar\beta) \cdot \dot{\mathbf{r}}(\hbar\beta) - \mathbf{r}(0) \cdot \dot{\mathbf{r}}(0))\right\}, \quad (2.149)$$

where $Z_{\text{ph}} = \left(2 \sinh\left(\frac{\hbar\beta w}{2}\right)\right)^{-3}$ is the free phonon partition function. As the trial density matrix is quadratic in the harmonic oscillator coordinates, it is determined entirely by the classical path.

Now, directly solving for $\mathbf{r}(\tau)$ from the equation of motion is difficult, so instead Ōsaka considered a system with a different Lagrangian L' ,

$$L' = \frac{1}{2} \left(m_0 \dot{\mathbf{r}}^2 + M \dot{\mathbf{x}}^2 - \kappa (\mathbf{r} - \mathbf{x})^2 \right), \quad (2.150)$$

of a particle of mass m_0 coupled by a harmonic spring with a force constant κ to a particle of mass M . After integrating over the \mathbf{R} coordinate, the density matrix ρ' of the Lagrangian L' is given by,

$$\begin{aligned} \rho'(\mathbf{r}_i, \mathbf{r}_f; \hbar\beta) &= Z_{\text{ph}} \int_{\mathbf{r}(0)=\mathbf{r}_i}^{\mathbf{r}(\hbar\beta)=\mathbf{r}_f} \exp\left[-\frac{1}{2\hbar} \int_0^{\hbar\beta} d\tau (m_0 \dot{\mathbf{r}}^2 + M w^2 \mathbf{r}^2)\right] \\ &\quad + \frac{\kappa w}{8\hbar} \int_0^{\hbar\beta} d\tau \int_0^{\hbar\beta} d\sigma D_w(\tau - \sigma) \mathbf{r}(\tau) \mathbf{r}(\sigma) \mathcal{D}\mathbf{r}(\tau), \end{aligned} \quad (2.151)$$

where $w = \sqrt{\kappa/M}$. This new action has the same equation of motion with the same form as the previous action,

$$m_0 \ddot{\mathbf{r}}(\tau) = \kappa \mathbf{r}(\tau) - \frac{\kappa w}{2} \int_0^{\hbar\beta} d\sigma D_w(\tau - \sigma) \mathbf{r}(\sigma), \quad (2.152)$$

which, under the classical path approximation, gives the density matrix,

$$\rho'(\mathbf{r}_i, \mathbf{r}_f; \hbar\beta) = Z_{\text{ph}} \exp \left\{ -\frac{m_0}{2\hbar} (\mathbf{r}(\hbar\beta) \cdot \dot{\mathbf{r}}(\hbar\beta) - \mathbf{r}(0) \cdot \dot{\mathbf{r}}(0)) \right\}. \quad (2.153)$$

This means that the density matrix ρ' is the same as ρ , with the same equation of motion. Therefore, Ōsaka used the solution to the equation of motion in Eq. (2.152) to calculate the trial density matrix ρ_{S_0} where the trial action S_0 corresponds to the Lagrangian L' .

The key to calculating $\langle S - S_0 \rangle_{\mathbf{r}_i, \mathbf{r}_f}$ is to evaluate the generating functional $Z[J_{\mathbf{q},\tau}(t)]$ in Eq. (2.103) using the same method Feynman used, except that Ōsaka replaced the trial action S_0 with that of L' and instead evaluated the path integral in the generating functional $Z[J_{\mathbf{q},\tau}(t)]$ using the Lagrangian

$$L = \frac{m_0}{2} \dot{\mathbf{r}}^2 + \frac{m_f}{2} \dot{\mathbf{x}}^2 - \frac{\kappa}{2} (\mathbf{r} - \mathbf{x})^2 + \mathbf{J}_{\mathbf{q},\tau,\sigma}(t) \cdot \mathbf{r}, \quad (2.154)$$

where $\mathbf{J}_{\mathbf{q},\tau,\sigma}(t) = i\mathbf{q} [\delta(t - \tau) - \delta(t - \sigma)]$ as before. This Lagrangian is evaluated by first doing a change of variables

$$\mathbf{x}' = \mathbf{r} - \mathbf{x}, \quad \mathbf{r}' = \frac{m_f}{m_0} \mathbf{x} + \frac{m_0}{m_f + m_0} \mathbf{r}, \quad (2.155)$$

to give

$$L = \frac{m_f + m_0}{2} \dot{\mathbf{r}}'^2 + \mu_0 \dot{\mathbf{x}}'^2 - \frac{\kappa}{2} \mathbf{x}'^2 + \mu_0 \mathbf{J}_{\mathbf{q},\tau,\sigma}(t) \cdot \mathbf{x}' + m_0 \mathbf{J}_{\mathbf{q},\tau,\sigma}(t) \cdot \mathbf{r}'. \quad (2.156)$$

This gives equations of motion for \mathbf{x}' and \mathbf{r}' ,

$$\ddot{\mathbf{x}}' = v\mathbf{x}' - \frac{1}{m_0} \mathbf{J}_{\mathbf{q},\tau,\sigma}(t), \quad \ddot{\mathbf{r}}' = -\frac{1}{m_f + m_0} \mathbf{J}_{\mathbf{q},\tau,\sigma}(t), \quad (2.157)$$

where $v = \sqrt{\kappa/\mu_0}$ ($\mu_0 = m_f m_0 / (m_f + m_0)$ is the reduced mass of the electron and fictitious mass) as defined by Feynman. Ōsaka showed that the solution for \mathbf{x}' under the boundary conditions $\mathbf{x}'(0) = \mathbf{x}'_i$ and $\mathbf{x}'(\hbar\beta) = \mathbf{x}'_f$ is,

$$\begin{aligned} \mathbf{x}'(t) &= \frac{\mathbf{x}'_i \sinh(v[\hbar\beta - t]) + \mathbf{x}'_f \sinh(vt)}{v \sinh(v\hbar\beta)} + i\mathbf{q} \sinh(vt) \frac{\sinh(v[\hbar\beta - \tau]) - \sinh(v[\hbar\beta - \sigma])}{v \sinh(v\hbar\beta)} \\ &\quad - \frac{i\mathbf{q}}{v} \begin{cases} \sinh(v[t - \tau]) - \sinh(v[t - \sigma]) & t > \tau \\ -\sinh(v[t - \sigma]) & \sigma < t < \tau \\ 0 & t < \sigma, \end{cases} \end{aligned} \quad (2.158)$$

if $\tau > \sigma$, otherwise the conditional is,

$$\begin{cases} \sinh(v[t-\tau]) - \sinh(v[t-\sigma]) & t > \sigma \\ \sinh(v[t-\sigma]) & \sigma < t < \tau \\ 0 & t < \sigma. \end{cases} \quad (2.159)$$

Under the boundary conditions $\mathbf{r}'(0) = \mathbf{r}'_i$ and $\mathbf{r}'(\hbar\beta) = \mathbf{r}'_f$ the solution for \mathbf{r}' is,

$$\mathbf{r}'(t) = \mathbf{r}'_i + \frac{v^2(\mathbf{r}'_f - \mathbf{r}'_i) - i\mathbf{q}w^2(\tau - \sigma)}{\hbar\beta v^2} - i\mathbf{q}\frac{w^2}{v^2} \left[\left(\begin{array}{ll} t - \tau & t > \tau \\ 0 & t < \tau \end{array} \right) - \left(\begin{array}{ll} t - \sigma & t > \sigma \\ 0 & t < \sigma \end{array} \right) \right]. \quad (2.160)$$

Using the equations of motion, Ōsaka obtains the generating functional,

$$\begin{aligned} Z[J_{\mathbf{q},\tau}(t)] = & \exp \left(-\frac{\mu_0}{2\hbar} [\mathbf{x}'(\hbar\beta) \cdot \dot{\mathbf{x}}'(\hbar\beta) - \mathbf{x}'(0) \cdot \dot{\mathbf{x}}'(0)] \right. \\ & - \frac{m_f + m_0}{2\hbar} [\mathbf{r}(\hbar\beta) \cdot \dot{\mathbf{r}}'(\hbar\beta) - \mathbf{r}'(0) \cdot \dot{\mathbf{r}}'(0)] \\ & + \frac{\mu_0}{2\hbar} \int_0^{\hbar\beta} dt \mathbf{J}_{\mathbf{q},\tau,\sigma}(t) \cdot \mathbf{x}'(t) \\ & \left. + \frac{m_0}{2\hbar} \int_0^{\hbar\beta} dt \mathbf{J}_{\mathbf{q},\tau,\sigma}(t) \cdot \mathbf{r}'(t) \right). \end{aligned} \quad (2.161)$$

Ōsaka connects this to the original action S by identifying $\mathbf{r}'_{i,f}$ and $\mathbf{x}'_{i,f}$ to $\mathbf{r}_{i,f}$ and $\mathbf{x}_{i,f}$ respectively using the relations in Eq. (2.155) and then integrating over \mathbf{x}_i under the boundary condition $\mathbf{x}_i = \mathbf{x}_f$. Using this, the fact that $\lim_{\mathbf{q} \rightarrow 0} Z[J_{\mathbf{q},\tau}(t)] = Z_{S_0}$ and that the kinetic energy terms in $\langle S - S_0 \rangle$ cancel, Ōsaka obtained $\langle S \rangle_{S_0}$ as,

Finite Temperature Model Action Expectation

$$\begin{aligned} \langle S \rangle_{S_0} &= \frac{\alpha\hbar r_0 \omega_0^2}{2\sqrt{2}} \int_0^{\hbar\beta} d\tau \int_0^{\hbar\beta} d\sigma D_{\omega_0}(\tau - \sigma) \int \frac{d^3\mathbf{q}}{(2\pi)^3} \frac{1}{q^2} e^{-\frac{r_0^2 q^2}{2} G(\tau)} \\ &= \frac{\alpha\hbar r_0 \omega_0^2}{\sqrt{2}} \int_0^{\hbar\beta} d\tau (\hbar\beta - \tau) \frac{D_{\omega_0}(\tau)}{\sqrt{G(\tau)}}. \end{aligned} \quad (2.162)$$

Here $G(\tau)$ is now the finite temperature generalisation of (2.114) given by,

Finite Temperature Polaron Green Function

$$G(\tau) = \frac{w^2}{v^2} \tau \left(1 - \frac{\tau}{\hbar\beta}\right) - \frac{v^2 - w^2}{v^3} (D_v(\tau) - D_v(0)). \quad (2.163)$$

As $\langle S \rangle_{S_0}$ is independent of the boundary conditions, it can be obtained as before from the power series of \mathbf{q} of $Z[J_{\mathbf{q},\tau}(t)]$ to give,

Finite Temperature Trial Action Expectation

$$\begin{aligned} \langle S_0 \rangle &= \frac{3\kappa w \beta}{4} \int_0^{\hbar\beta} d\tau (\hbar\beta - \tau) D_w(\tau) G(\tau) \\ &= \frac{3\kappa\beta}{4v} \left(\frac{2}{v\hbar\beta} - \coth\left(\frac{v\hbar\beta}{2}\right) \right). \end{aligned} \quad (2.164)$$

Ōsaka then obtained the partition function from the diagonal part of the density matrix,

$$Z(\beta) = \rho_S(\mathbf{r}, \mathbf{r}; \hbar\beta) \geq \rho_{S_0}(\mathbf{r}, \mathbf{r}; \hbar\beta) \exp \langle S - S_0 \rangle_{S_0} = Z_{S_0}(\beta) \exp \langle S - S_0 \rangle_{S_0}, \quad (2.165)$$

to give the variational principle,

$$F(\beta) \leq F_{S_0}(\beta) + \frac{1}{\beta} \langle S - S_0 \rangle_{S_0}. \quad (2.166)$$

Now, in a similar way to Feynman, Ōsaka obtained the trial free energy $F_{S_0}(\beta)$ using,

$$\frac{\partial \log Z_{S_0}}{\partial \kappa} = \frac{\langle S_0 \rangle_{S_0}}{\kappa}, \quad (2.167)$$

and the fact that when $\kappa = 0$, $Z_{S_0} = V_0(m_0/2\pi\hbar^2\beta)^{3/2}$. By integrating $\partial \log Z_{S_0}/\partial \kappa$ with respect to κ , Ōsaka obtained,

$$\begin{aligned} F_{S_0}(\beta) &= -\frac{1}{\beta} \log Z_{S_0}(\beta) = -\frac{1}{\beta} \log \left(\frac{V_0}{r_0^3} \right) + \frac{3}{2\beta} \log(2\pi\hbar\omega_0\beta) - \frac{1}{\beta} \int_0^\kappa d\kappa' \frac{\langle S_0(\kappa') \rangle'}{\kappa'} \\ &= -\log \left(\frac{V_0}{r_0^3} \right) + \frac{3}{2\beta} \log(2\pi\hbar\omega_0\beta) + \frac{3\hbar}{2} \int_w^v du \left(\coth\left(\frac{\hbar\beta u}{2}\right) - \frac{2}{\hbar\beta u} \right), \end{aligned} \quad (2.168)$$

which gives,

Free Energy of the Trial Model

$$F_{S_0}(\beta) = -\frac{1}{\beta} \log \left(\frac{V_0}{r_0^3} \right) + \frac{3}{2\beta} \log(2\pi\hbar\omega_0\beta) + \frac{3}{\beta} \log \left(\frac{w \sinh(\hbar\beta v/2)}{v \sinh(\hbar\beta w/2)} \right). \quad (2.169)$$

If one finds the variational parameters v and w that give the lowest upper-bound to the free

energy, then the average energy of the polaron state is given by,

$$E = -\frac{\partial}{\partial \beta} \left(F_{S_0} + \langle S - S_0 \rangle_{S_0} \right). \quad (2.170)$$

These results generalise Feynman's variational parameter for the polaron at zero temperature to finite temperatures parameterised by the thermodynamic beta parameter $\beta = 1/(k_B T)$. In this zero temperature limit, $\beta \rightarrow \infty$, Ōsaka's result reduces to Feynman's.

2.2.10 Thermal FVA Numerical Results

In Figs. (2.2) and (2.3) are line and contour plots that show the temperature and coupling dependence of the 2D (left column) and 3D (right column) Fröhlich model. These figures show (top row) the polaron free energy $|F|(\hbar\omega_0)$, (second row) the polaron effective mass $M(m_0)$, (third row) values of the $v(\omega_0)$ variational parameter and (bottom row) values of the $w(\omega_0)$ variational parameter. All parameters approach their athermal values at low temperatures.

I show the absolute value of the free energy so that I can use a log scale. Interestingly, this reveals a region with a slightly positive total polaron free energy. This suggests that polarons do not form at these finite temperatures at weak coupling. This region vanishes at zero temperature $T = 0$ and above temperatures $T > 6\hbar\omega_0/k_B$, and above $\alpha > 1$ in 2D and $\alpha > 2$ in 3D. As phonons typically have frequencies of order $\omega_{ph} \sim 1 \text{ THz}2\pi$, this upper-temperature limit is roughly on the order of $T \sim 288 \text{ K}$. In the intermediate regime, the free energy forms a maximum around $T \sim \hbar\omega/k_B \sim 48 \text{ K}$, which shifts to lower temperatures towards zero at zero coupling.

At weak and intermediate couplings, the polaron effective mass shows a clear maximum around $T \sim 2^{-2}\hbar\omega_0/k_B$. The effective mass is $M \sim 1m_0$ at very low couplings. Towards strong coupling, the effective mass is roughly constant for temperatures $T < \hbar\omega_0/k_B$ and then exponentially decreases towards the band mass as the temperature increases above the Debye temperature.

At weak and intermediate couplings, the variational parameters v and w show a minimum around $T \sim 2^{-2}\hbar\omega_0/k_B$ coinciding with the effective mass maximum. Both parameters show an exponential increase for temperatures above the Debye temperature $T > \hbar\omega_0/k_B$ towards larger couplings. Their relative difference is zero, as indicated by the effective mass approaching the band mass.

For each quantity, the difference between the 2D and 3D Fröhlich model is determined entirely by the scaling relations in Eq. (2.141). Note that I did not directly use these relations in calculating the 2D results; nonetheless, the scaling relation is evident in Fig. (2.3) by the

multiplicative scaling of the α -axis with $\alpha_{2D} \sim \frac{3\pi}{4} \alpha_{3D}$. Notably, the 2D and 3D differences are lessened asymptotically at temperatures far above the Debye temperature. In this limit, both dimensions give similar results in the polaron energy, effective mass and variational parameters for a given coupling α .

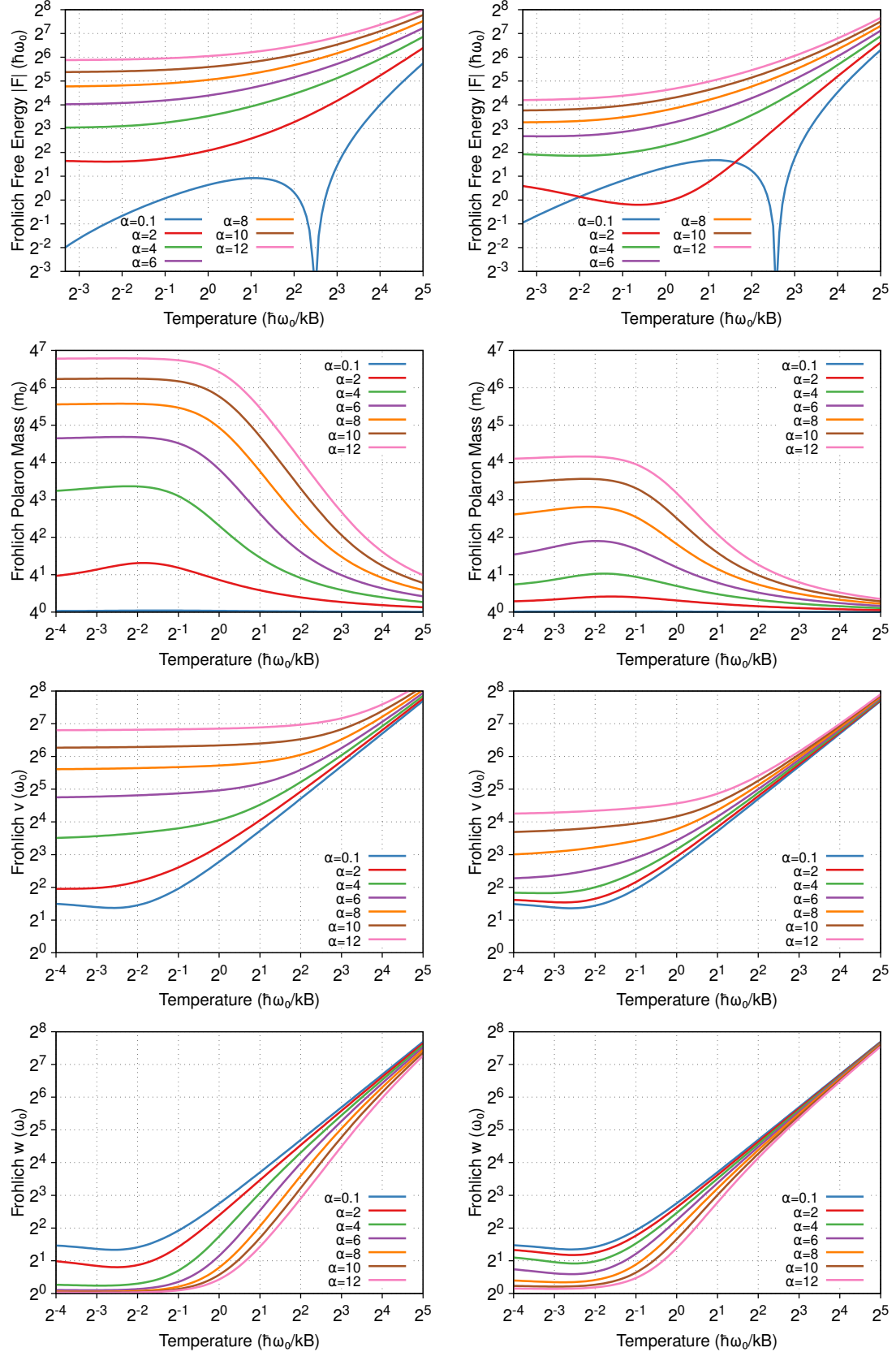


Figure 2.2: The temperature (T in units of $\hbar\omega_0/k_B$)- and electron-phonon α coupling-dependence of Ōsaka's polaron in 2D (left) and 3D (right) for the free energy (top), Feynman effective mass (second row), the v variational parameter (third row) and the w variational parameter (bottom). In the top row, I plot the absolute value $|F|$ of the free energy, such that for $\alpha = 0.1$, the value of F is positive for $T < 6\hbar\omega_0/k_B$ and negative above this temperature and the same sign at the other coupling strengths.

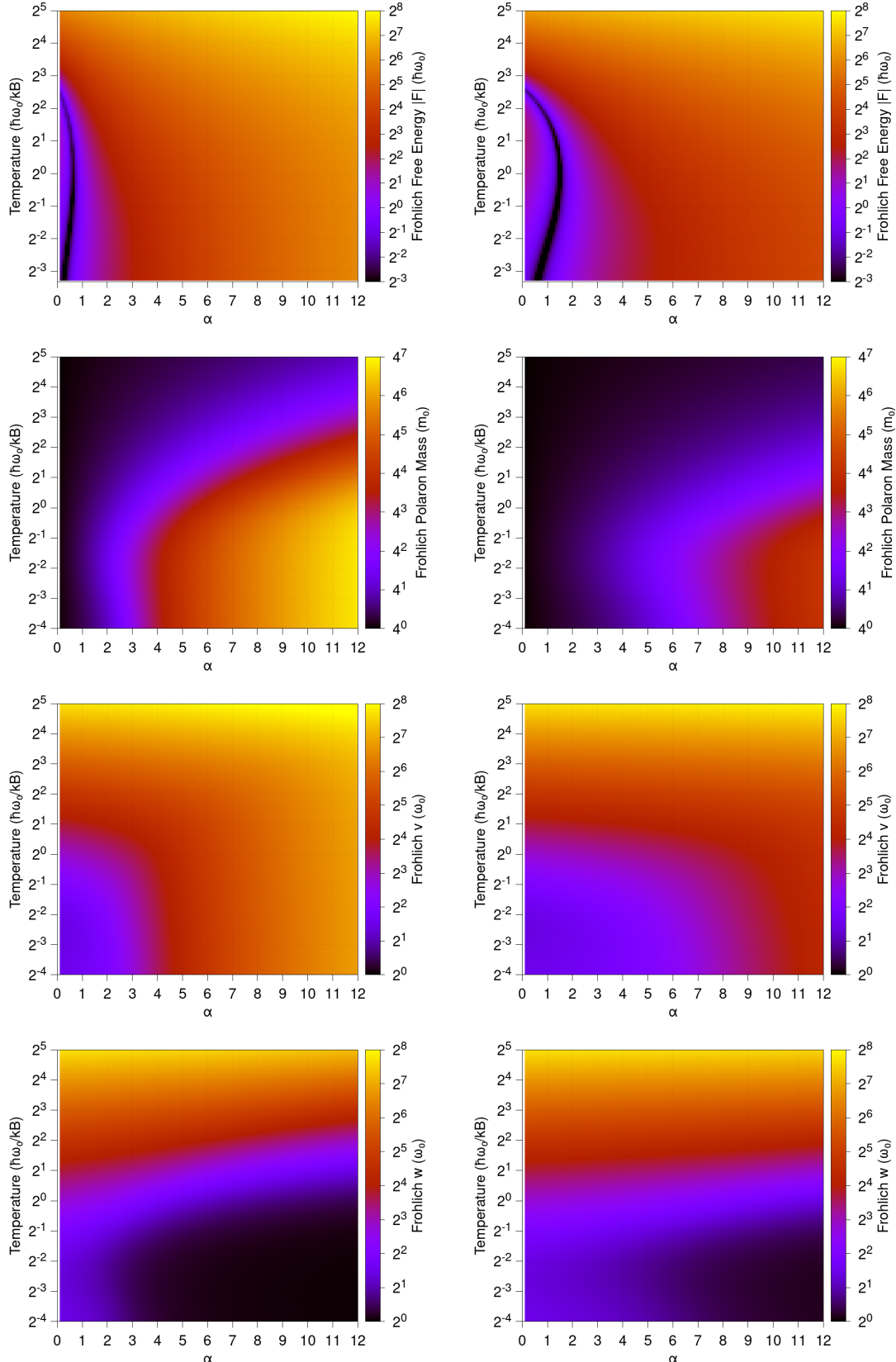


Figure 2.3: The temperature (T in units of $\hbar\omega_0/k_B$)- and electron-phonon α coupling-dependence of Ōsaka's polaron in 2D (left) and 3D (right) for the free energy (top), Feynman effective mass (second row), the v variational parameter (third row) and the w variational parameter (bottom). In the top row, I plot the absolute value $|F|$ of the free energy, such that the dark curve indicates a change of sign where the free energy F in the small ‘island’ at weak coupling is positive.

2.3 Influence Functionals & Response Functions

2.3.1 Polaron DC Mobility

FHIP [17] derived an expression for the response of the Feynman polaron to weak, spatially uniform, time-varying electric fields. The current induced by the motion of the electron under the influence of a weak alternating electric field $\mathbf{E} = E_0 \exp(i\Omega t)$ is generally,

$$j(\Omega) = \frac{E(\Omega)}{z(\Omega)}, \quad (2.171)$$

where $z(\Omega)$ is the complex impedance function. It is assumed that the material is isotropic so that $j = \langle \dot{r} \rangle$, where $\langle r \rangle = E/(i\Omega z(\Omega))$ is the expectation of the electron displacement in the r direction. In the time domain, this is,

$$\langle r(t) \rangle = -i \int_{-\infty}^{\infty} dt' G(t-t') E(t'), \quad (2.172)$$

$G(t)$ is the Green function corresponding to the *linear* electron displacement at a time t due to a delta function pulsed electric field at a time zero $t = 0$. The Fourier transform of $G(t)$ is,

$$\int_{-\infty}^{\infty} dt G(t) e^{-i\Omega t} = G(\Omega) = \frac{1}{\Omega z(\Omega)}, \quad (2.173)$$

where $G(t) = 0$ for $t < 0$. Under the influence of the external electric field $E(t)$, the Föhlich Hamiltonian gains an additional term $-\mathbf{E} \cdot \mathbf{r}$. If ρ is the density matrix of the system, then the expected electron position at a time t is,

$$\langle \mathbf{r}(t) \rangle = \text{Tr} \{ \mathbf{r} \rho(t) \}. \quad (2.174)$$

Furthermore, we assume that the system is initially in thermal equilibrium $\rho(t=0) = \exp(-\beta H)$, then the density matrix at any later time t is obtained from the time evolution equation,

$$i\hbar \frac{\partial \rho}{\partial t} = [H, \rho]. \quad (2.175)$$

Therefore,

$$\rho(t) = \exp \left\{ -\frac{i}{\hbar} \int_0^t [H(s) - \mathbf{r}(s) \cdot \mathbf{E}(s)] ds \right\} \rho(0) \exp \left\{ +\frac{i}{\hbar} \int_0^t [H'(s) - \mathbf{r}'(s) \cdot \mathbf{E}'(s)] ds \right\}, \quad (2.176)$$

where $\rho(0) \propto \exp(-\hbar\beta \sum_{\mathbf{q}} \omega_{\mathbf{q}} b_{\mathbf{q}}^\dagger b_{\mathbf{q}})$ such that only the phonon oscillators are initially in thermal equilibrium at temperature $(k_B\beta)^{-1}$. Due to the electron-phonon coupling, the entire polaron system will quickly return to thermal equilibrium as the electron is

perturbed since the energy of the electron ($\sim 1/\text{volume}$) is tiny relative to the heat bath of the system of phonon oscillators. As an aside, since \mathbf{E} is not an operator and the system is in thermodynamic equilibrium, then $\mathbf{E}'(s) = \mathbf{E}(s)$. Still, FHIP treats them separately as the more general case, such as in a non-linear response system. We can write $\text{Tr } \rho(t)$ as the path integral generating functional,

$$\begin{aligned} \text{Tr } \rho(t) &= Z[\mathbf{E}, \mathbf{E}'] \\ &= \int \mathcal{D}\mathbf{r}(t)\mathcal{D}\mathbf{r}'(t) \exp\left(\frac{i}{\hbar}\Phi[\mathbf{r}(t), \mathbf{r}'(t)] - \frac{i}{\hbar} \int_{-\infty}^{\infty} dt [\mathbf{E}(t) \cdot \mathbf{r}(t) - \mathbf{E}'(t) \cdot \mathbf{r}'(t)]\right), \end{aligned} \quad (2.177)$$

where $\Phi[\mathbf{r}(t), \mathbf{r}'(t)]$ is given by

FHIP Model Influence Functional Phase

$$\Phi = - \int_0^{\infty} dt \int_0^{\infty} dt' \int \frac{d^3\mathbf{q}}{(2\pi)^3} |M_{\mathbf{q}}|^2 \left\{ D_{\omega_{\mathbf{q}}}(t-t') \left(e^{i\mathbf{q} \cdot [\mathbf{r}(t)-\mathbf{r}(t')]} - e^{i\mathbf{q} \cdot [\mathbf{r}'(t)-\mathbf{r}'(t')]} \right) - D_{\omega_{\mathbf{q}}}^*(t-t') \left(e^{i\mathbf{q} \cdot [\mathbf{r}(t)-\mathbf{r}'(t')]} - e^{i\mathbf{q} \cdot [\mathbf{r}'(t)-\mathbf{r}(t')]} \right) \right\}. \quad (2.178)$$

For Fröhlich's Hamiltonian we set $\omega_{\mathbf{q}} = \omega_0$ and the interaction term $M_{\mathbf{q}}$ is given by Eq. (2.36).

The double path integral $\mathcal{D}\mathbf{r}(t)\mathcal{D}\mathbf{r}'(t)$ is only over closed paths satisfying the boundary condition $\mathbf{r}(t) - \mathbf{r}'(t) = 0$ at times $t \rightarrow \pm\infty$. Since the electric field is weak, we can expand $\langle \mathbf{r}(t) \rangle$ to first-order and find the linear response Green function for $\mathbf{r}(t)$, which can be obtained from the first functional derivative of the partition function concerning $\mathbf{E}(t) - \mathbf{E}'(t)$ as $t \rightarrow \infty$ when the steady state is reached. This gives,

$$G(t-t') = -\frac{\hbar^2}{2} \frac{1}{Z} \frac{\delta^2 Z[\mathbf{E}, \mathbf{E}']}{\delta \mathbf{E}(t, t') \delta \mathbf{E}'(t, t')} \Big|_{\mathbf{E}=\mathbf{E}'=0}, \quad (2.179)$$

where $Z = Z[0, 0]$ is the partition function that acts as the normalisation constant. In FHIP, they set the electric field to a sum of two delta functions,

$$\mathbf{E}(s) = [\epsilon \delta(s-t') + \eta \delta(s-t)] \mathbf{e}, \quad (2.180a)$$

$$\mathbf{E}'(s) = [\epsilon \delta(s-t') - \eta \delta(s-t)] \mathbf{e}, \quad (2.180b)$$

to give,

$$G(t-t') = \frac{\hbar^2}{2Z} \frac{\partial^2 Z(\epsilon, \eta)}{\partial \eta \partial \epsilon} \Big|_{\eta=\epsilon=0}. \quad (2.181)$$

Thus, the problem of finding the Green function $G(t-t')$ is reduced to that of finding the dependence of the generating function path integral $Z[\mathbf{E}, \mathbf{E}']$ on the forcing functions $\mathbf{E}(t)$ and $\mathbf{E}'(t)$. The path integral in $Z[\mathbf{E}, \mathbf{E}']$ depends on the functional $\Phi[\mathbf{r}(t), \mathbf{r}'(t)]$ which

contains terms similar to the model action S (athermal expression in Eq. (2.83) or thermal expression in Eq. (2.162)). However, note that this is now the real-time version of the model action (obtained from a Wick rotation).

Approximating the polaron complex impedance

The path integral $Z[\mathbf{E}, \mathbf{E}']$ cannot be evaluated exactly. However, it can be approximated by the trial influence functional $\Phi_{S_0}[\mathbf{r}(t), \mathbf{r}'(t)]$,

Trial Influence Functional Phase

$$\Phi_{S_0} = Mw^3 \int_0^\infty dt \int_0^\infty dt' \left\{ D_w(t-t') \left([\mathbf{r}(t) - \mathbf{r}(t')]^2 - [\mathbf{r}'(t) - \mathbf{r}'(t')]^2 \right) - D_w^*(t-t') \left([\mathbf{r}(t) - \mathbf{r}'(t')]^2 - [\mathbf{r}'(t) - \mathbf{r}'(t')]^2 \right) \right\}. \quad (2.182)$$

This contains terms similar to the trial action S_0 (such as the athermal trial action in Eq. (2.93) and thermal trial action in Eq. (2.164), but Wick-rotated from the imaginary-time variable to the real-time variable) in which the attractive Coulomb-like potential is roughly replaced by the simpler attractive parabolic potential centred at the mean position of the electron in the past (weighted by an exponential decay with time where w is the decay factor). In FHIP, it is assumed that the Wick-rotation of the trial partition function Z_{S_0} (the athermal partition function given by Eq. (2.100) and the thermal partition function by Eq. (2.169)), which offers the best approximation to the partition function of the actual model system via either Feynman's (athermal) or Ōsaka's (thermal) variational principle, can describe the dynamical behaviour of the polaron.

Therefore, in FHIP, they approximate the model generating functional $Z[\mathbf{E}, \mathbf{E}']$ with the zeroth and first terms from the expansion of the path integral around the trial action,

$$\begin{aligned} Z[\mathbf{E}, \mathbf{E}'] &\approx \int \mathcal{D}\mathbf{r}(t) \mathcal{D}\mathbf{r}'(t) e^{\frac{i}{\hbar}(\Phi_{S_0} + \int dt [\mathbf{E} \cdot \mathbf{r} - \mathbf{E}' \cdot \mathbf{r}'])} \\ &+ i \int \mathcal{D}\mathbf{r}(t) \mathcal{D}\mathbf{r}'(t) e^{\frac{i}{\hbar}(\Phi_{S_0} + \int dt [\mathbf{E} \cdot \mathbf{r} - \mathbf{E}' \cdot \mathbf{r}'])} (\Phi - \Phi_{S_0}) \\ &\equiv Z_{S_0}[\mathbf{E}, \mathbf{E}'] + Z_1[\mathbf{E}, \mathbf{E}']. \end{aligned} \quad (2.183)$$

Calculating the zeroth term of the complex impedance

The zeroth term $Z_{S_0}[\mathbf{E}, \mathbf{E}']$ is the classical response and is the same as the alternative model presented by Ōsaka of two masses coupled by a harmonic spring under the influence of a linear force \mathbf{J} (Eq. (2.154)), where $\mathbf{J} = \mathbf{E}$. This term is then reanalysed as the sum of two normal mode harmonic oscillators so that $Z_{S_0}[\mathbf{E}, \mathbf{E}']$ is written as the product of two factors,

one for each harmonic oscillator. The first oscillator has a mass $m_1 = M + m_0 = m_0 v^2 / w^2$ and frequency $\omega_1 = 0$ coupled by $\mathbf{J}_1(t) = \mathbf{E}(t)$, and the second oscillator has mass $m_2 = Mm_0/(M+m_0)$, frequency $\omega_2 = v\omega_0$ and coupling $\mathbf{J}_2(t) = -Mm_0/(M+m_0)\mathbf{E}(t) = \mathbf{E}(t)(v^2 - w^2)/v^2$.

$Z_{S_0}[\mathbf{E}, \mathbf{E}']$ is then given by,

$$Z_{S_0}[\mathbf{E}, \mathbf{E}'] = \exp \left\{ \frac{i}{4\pi} \int_{-\infty}^{+\infty} d\Omega (\mathbf{E}(-\Omega) - \mathbf{E}'(\Omega)) \times [(\mathbf{E}(\Omega) + \mathbf{E}'(\Omega)) Y_0(\Omega) + i(\mathbf{E}(\Omega) - \mathbf{E}'(\Omega)) A_0(\Omega)] \right\}, \quad (2.184)$$

where,

$$G_0(\Omega) = \lim_{\varepsilon \rightarrow 0^+} \left\{ i \frac{\Omega^2 - w^2}{(\Omega - i\varepsilon)^2} \left[(\Omega - i\varepsilon)^2 - v^2 \right] \right\}, \quad (2.185)$$

and,

$$A_0(\Omega) = \frac{\pi}{2} \lim_{\varepsilon \rightarrow 0^+} \left\{ \frac{2w^2}{v^2 \beta \varepsilon^2} [\delta(\Omega + \varepsilon) - \delta(\Omega - \varepsilon)] + \frac{v^2 - w^2}{v^3} \left[1 + \frac{2}{e^{\beta v} - 1} \right] [\delta(\Omega + v) + \delta(\Omega - v)] \right\}, \quad (2.186)$$

where $\mathbf{E}(\Omega)$ is the Fourier transform of $\mathbf{E}(t)$. To obtain the classical Green function $G_0(t - t')$, in FHIP they substitute,

$$\mathbf{E}(\Omega) = (\epsilon e^{-i\Omega t'} + \eta e^{i\Omega t}) \hat{\mathbf{q}}, \quad (2.187a)$$

$$\mathbf{E}'(\Omega) = (\epsilon e^{-i\Omega t'} - \eta e^{i\Omega t}) \hat{\mathbf{q}}, \quad (2.187b)$$

into $Z_{S_0}[\mathbf{E}, \mathbf{E}']$ and find the *linear term* of order $\epsilon\eta$. The zeroth order approximation to $G(t - t')$ is then,

$$G_0(t - t') = \frac{1}{2\pi} \int_{-\infty}^{\infty} d\Omega G_0(\Omega) e^{i\Omega(t-t')}, \quad (2.188)$$

which is the classical response of the system.

Calculating the first correction term of the complex impedance

To include the first order of quantum corrections to the classical response of the electron, FHIP uses the $Z_1[\mathbf{E}, \mathbf{E}']$ path integral to obtain the first order approximation $G_1(t - t')$ to $G(t - t')$. To evaluate $Z_1[\mathbf{E}, \mathbf{E}']$ they first look at the $\Phi \exp(i\Phi_{S_0}/\hbar)$. Substituting the equation for Φ into $\Phi \exp(i\Phi_{S_0}/\hbar)$, the resulting expression contains terms \mathcal{T} that have

the form,

$$\mathcal{T} = \int \mathcal{D}\mathbf{r}(t) \mathcal{D}\mathbf{r}'(t) e^{\frac{i}{\hbar}\Phi_{S_0}} \left\{ \int \frac{d^3\mathbf{q}}{(2\pi)^3} |M_{\mathbf{q}}|^2 \int_{-\infty}^{\infty} dt \int_{-\infty}^{\infty} dt' D_{\omega_{\mathbf{q}}}(t-t') e^{i\mathbf{q} \cdot (\mathbf{r}(t)-\mathbf{r}(t'))} \right\}. \quad (2.189)$$

The two other terms in $\Phi \exp(i\Phi_{S_0}/\hbar)$ come from the correlations between electron paths in the density matrix $\rho(\mathbf{r}, \mathbf{r}', t)$ (i.e. off-diagonal terms) and are similar to \mathcal{T} , but with different replacements of \mathbf{r} with \mathbf{r}' . To evaluate \mathcal{T} one has to evaluate the path integral,

$$\begin{aligned} \mathcal{R}(\mathbf{q}, s, s') &= \int_{\mathbf{r}=\mathbf{r}'} \mathcal{D}\mathbf{r}(t) \mathcal{D}\mathbf{r}'(t) \exp \left\{ i\mathbf{q} \cdot [\mathbf{r}(s) - \mathbf{r}(s')] + \frac{i}{\hbar} \Phi_{S_0} \right\} \\ &= Z_{S_0} \left\langle e^{i\mathbf{q} \cdot [\mathbf{r}(s) - \mathbf{r}(s')]} \right\rangle_{\Phi_{S_0}}, \end{aligned} \quad (2.190)$$

where $Z_{S_0} \equiv Z_{S_0}[0, 0]$. This gives \mathcal{T} to be,

$$\mathcal{T} = \int_{-\infty}^{\infty} ds \int_{-\infty}^{\infty} ds' D_{\omega_0}(s-s') \int \frac{d^3\mathbf{q}}{(2\pi)^3} |M_{\mathbf{q}}|^2 \left\langle e^{i\mathbf{q} \cdot [\mathbf{r}(s) - \mathbf{r}(s')]} \right\rangle_{\Phi_{S_0}}. \quad (2.191)$$

The solution to $\mathcal{R}(\mathbf{q}, s, s')$ is the same form as $Z_{S_0}[\mathbf{E}, \mathbf{E}']$ in Eq. (2.184) except for the non-primed components,

$$\mathbf{E}(\Omega) = \left(\epsilon e^{-i\Omega t'} + \eta e^{-i\Omega t} \right) \hat{\mathbf{q}} + \mathbf{q} \left(e^{-i\Omega s} - e^{-i\Omega s'} \right), \quad (2.192a)$$

$$\mathbf{E}'(\Omega) = \left(\epsilon e^{-i\Omega t'} - \eta e^{-i\Omega t} \right) \hat{\mathbf{q}}, \quad (2.192b)$$

to give,

$$\begin{aligned} \mathcal{R}(\mathbf{q}, t, t') &= Z_{S_0} \exp \left\{ \frac{iq^2}{4\pi} \int_{-\infty}^{\infty} d\Omega \left| e^{i\Omega\tau} - e^{i\Omega\sigma} \right|^2 (Y_0 + iA_0) \right. \\ &\quad + \frac{i\mathbf{q}_r}{2\pi} \int_{-\infty}^{\infty} d\Omega \left(e^{i\Omega\tau} - e^{i\Omega\sigma} \right) \left(\epsilon Y_0 e^{-i\Omega t'} + i\eta A_0 e^{-i\Omega t} \right) \\ &\quad \left. + \frac{i\mathbf{q}_r}{2\pi} \int_{-\infty}^{\infty} d\Omega \left(e^{-i\Omega\tau} - e^{-i\Omega\sigma} \right) \eta e^{i\Omega t} (Y_0 + iA_0) \right\}, \end{aligned} \quad (2.193)$$

where,

$$Z_{S_0} = \exp \left[\frac{i}{\pi} \int_{-\infty}^{\infty} d\Omega \eta e^{i\Omega t} \left(\epsilon Y_0 e^{-i\Omega t'} + i\eta A_0 e^{-i\Omega t} \right) \right], \quad (2.194)$$

for $\mathbf{q} = 0$. Similarly, for the primed components,

$$\mathbf{E}(\Omega) = \left(\epsilon e^{-i\Omega t'} + \eta e^{-i\Omega t} \right) \hat{\mathbf{q}} - \mathbf{q} e^{-i\Omega\sigma}, \quad (2.195a)$$

$$\mathbf{E}'(\Omega) = \left(\epsilon e^{-i\Omega t'} - \eta e^{-i\Omega t} \right) \hat{\mathbf{q}} - \mathbf{q} e^{-i\Omega\tau}. \quad (2.195b)$$

To obtain $G_1(t - t')$ we need the first-order derivative of $\mathcal{R}(\mathbf{q}, \tau, \sigma)$ with respect to ϵ and η and then setting $\epsilon = \eta = 0$. The result is (including a 1/3 for averaging over the isotropic dimensions of \mathbf{q}),

$$\begin{aligned} r(\mathbf{q}, \tau, \sigma) = & \left\{ \frac{i}{2\pi} \int_{-\infty}^{\infty} d\Omega Y_0 e^{i\Omega(t-t')} - \frac{q^2}{24\pi^2} \int_{-\infty}^{\infty} d\Omega \left(e^{i\Omega\tau} - e^{i\Omega\sigma} \right) Y_0 e^{-i\Omega t'} \right. \\ & \times \int_{-\infty}^{\infty} d\Lambda \left[\left(e^{i\Lambda\tau} - e^{i\Lambda\sigma} \right) iA_0(\Lambda) e^{-i\Lambda t} + \left(e^{i\Lambda\tau} - e^{i\Lambda\sigma} \right) e^{i\Lambda t} (Y_0(\Lambda) + iA_0(\Lambda)) \right] \Bigg\} \\ & \times \exp \left\{ \frac{ik^2}{4\pi} \int_{-\infty}^{\infty} d\Omega \left| e^{i\Omega\tau} - e^{i\Omega\sigma} \right|^2 (Y_0 + iA_0) \right\}. \end{aligned} \quad (2.196)$$

The first term is the classical response $G_0(t - t')$, and the later terms correspond to the trial path integral with no applied electric field $\epsilon = \eta = 0$. Hence, in total $r(\mathbf{q}, \tau, \sigma)$ is the \mathbf{q} -dependent term in $\langle S_0 - S'_0 \rangle_{S'_0, S_0}$, where the classical response G_0 has cancelled with the normalisation and does not contribute to the quantum corrections to the response, G_1 . We can do a change of variables $u = \tau - \sigma$ and perform the integral on σ in Eq. (2.191) to give,

$$\begin{aligned} r(\mathbf{q}, u) = & -\frac{q^2}{6\pi^2} \int_{-\infty}^{\infty} d\Omega (1 - \cos(\Omega u)) Y_0(\Omega) (Y_0(\Omega) + 2iA_0(\Omega)) e^{i\Omega(t-t')} \\ & \times \exp \left\{ \frac{ik^2}{2\pi} \int_{-\infty}^{\infty} d\Omega' (1 - \cos(\Omega' u)) (Y_0(\Omega') + iA_0(\Omega')) \right\}, \end{aligned} \quad (2.197)$$

where $Y_0(-\Omega) = Y_0^*(\Omega)$ and $A_0(-\Omega) = A_0(\Omega)$. $r(\mathbf{q}, u)$ contributes to $G_1(u)$ and since it is already of the form of a Fourier transform, we can find the contribution $r(\mathbf{q}, \Omega)$ to $G_1(\Omega)$ by omitting the Fourier integral on Ω and the factor $e^{-\Omega(t-t')}$ to give,

$$\begin{aligned} r(\mathbf{q}, \Omega) = & -\frac{q^2}{6\pi^2} (1 - \cos(\Omega u)) Y_0(\Omega) (Y_0(\Omega) + 2iA_0(\Omega)) \\ & \times \exp \left\{ \frac{ik^2}{2\pi} \int_{-\infty}^{\infty} d\Omega' (1 - \cos(\Omega' u)) (Y_0(\Omega') + iA_0(\Omega')) \right\}. \end{aligned} \quad (2.198)$$

To obtain $\langle S - S_0 \rangle_{S'_0, S_0}$ we multiply $r(\mathbf{q}, u)$ by $y(u) + ia(u)$ and integrate on u . Feynman evaluated this integral by splitting the range of u from 0 to ∞ and from $-\infty$ to 0, where in the latter, he put $u \rightarrow -u$ to make all integrals on u positive. The integral in the exponent

is $-q^2/2$ times $G(u)$,

$$\begin{aligned} G(u) &= -\frac{i}{\pi} \int_{-\infty}^{\infty} d\Omega (1 - \cos(\Omega u)) [Y_0(\Omega) + iA_0(\Omega)] \\ &= \frac{i}{\pi} (\mathbf{Y}_0(u) + \mathbf{Y}_0(-u)) + 2(\mathbf{A}_0(0) - \mathbf{A}_0(u)) \\ &= 2 \frac{v^2 - w^2}{v^3} \frac{\sin(vu/2) \sin(v[u - i\hbar\omega_0\beta]/2)}{\sinh(v\hbar\omega_0\beta/2)} - i \frac{w^2}{v^2} u \left(1 - \frac{u}{i\hbar\omega_0\beta}\right), \end{aligned} \quad (2.199)$$

where $u > 0$. $\mathbf{Y}_0(t)$ and $\mathbf{A}_0(t)$ are the inverse Fourier transforms of $Y_0(\Omega)$ and $A_0(\Omega)$ where we note that $\mathbf{Y}_0(u) = 0$ for $u < 0$. Therefore, overall for $r(q, u)$ is,

$$\begin{aligned} r(q, u) &= \frac{-q^2}{3\pi} Y_0(\Omega) [Y_0(\Omega) + 2iA_0(\Omega)] \\ &\times \int_0^{\infty} du (1 - \cos(\Omega u)) [y(u) + y(-u) + 2ia(u)] e^{-\frac{1}{2}q^2G(u)}, \end{aligned} \quad (2.200)$$

which contributes to G_1 . A similar calculation is also done to obtain the \mathcal{T} terms that come from the primed \mathbf{r}' components in $\Phi \exp(i\Phi_{S_0}/\hbar)$. Once all are obtained, they are summed together, and the q integral gives the first contribution to $G_1(\Omega)$ as,

$$G_1^{(1)}(\Omega) = -iY_0^2(\Omega)\Omega\Sigma(\Omega), \quad (2.201)$$

where,

FHIP Memory Function

$$\Sigma(\Omega) = \frac{1}{\Omega} \int_0^{\infty} dt (1 - e^{i\Omega t}) \text{Im}S(t), \quad (2.202)$$

with,

$$S(t) = \frac{2}{3} \int \frac{d^3\mathbf{q}}{(2\pi)^3} |M_{\mathbf{q}}|^2 q^2 D_{\omega_{\mathbf{q}}}(t) e^{-r_0^2 q^2 G(t)/2}, \quad (2.203)$$

which for the Fröhlich Hamiltonian gives,

FHIP Fröhlich Dynamical Structure Factor

$$S(t) = \frac{2\alpha}{3\sqrt{\pi}} D_{\omega_0}(t) [G(t)]^{-3/2}. \quad (2.204)$$

Next, the second term is obtained analogously from Φ_{S_0} . It can be evaluated by differentiating \mathcal{R} (and thus on $r(q, u)$) twice concerning \mathbf{q} and then setting $\mathbf{q} = 0$ in the expression. This results in an integral on u ,

$$G_1^{(2)}(\Omega) = -i4Y_0^2(\Omega) \int_0^{\infty} du (1 - e^{i\Omega u}) S_0(u) = -i4Y_0^2(\Omega) \frac{C\Omega^2}{w(\Omega^2 - w^2)}, \quad (2.205)$$

where,

$$S_0(u) = C \operatorname{Im} \left(e^{i w u} + 2n(\beta w) \cos(wu) \right) = C \sin(wu). \quad (2.206)$$

This gives the final result for the first-order change in G as,

$$G_1(\Omega) = G_1^{(1)}(\Omega) + G_1^{(2)}(\Omega) = -iY_0^2(\Omega) \left[\Omega\Sigma(\Omega) + \frac{4C}{w} \frac{\Omega^2}{\Omega^2 - w^2} \right]. \quad (2.207)$$

Hence, FHIP find an approximate form for $G(\Omega)$ composed out of the zeroth and first-order terms of the Green function,

$$G(\Omega) = G_0(\Omega) + G_1(\Omega), \quad (2.208)$$

from which they find the impedance to first-order in $G_1(\Omega)$,

$$\begin{aligned} \Omega z(\Omega) &= \frac{1}{G(\Omega)} \approx \frac{1}{G_0(\Omega) + G_1(\Omega)} \\ &\approx \frac{1}{G_0(\Omega)} - \frac{1}{G_0^2(\Omega)} G_1(\Omega). \end{aligned} \quad (2.209)$$

FHIP argue that this expanded form is more accurate than $z \sim (G_0 + G_1)^{-1}$ by considering a simple example of a free particle perturbed by a harmonic oscillator. The structure of the actual $G(\Omega)$ in this example includes a resonance at the oscillator frequency which is not present in $z \sim (G_0 + G_1)^{-1}$. This resonance is present if one expands $z(\Omega)$. Therefore, FHIP use this expanded form, which is written explicitly as

FHIP Complex Impedance Function

$$z(\Omega) \approx i(\Omega - \Sigma(\Omega)). \quad (2.210)$$

The first term (Ω) on the right-hand side is a free-particle term, while $\Sigma(\Omega)$ contains the corrections from the electron-phonon interactions. All of the dependence on the trial influence functional Φ_{S_0} is contained within $G(t)$, which appears in the exponential term in $S(t)$ (Eq. (2.204)). This exponential term describes the non-linear scattering of the electron due to its interaction with the phonon field oscillators. If the phonon oscillators are linearly coupled to the electron's coordinate, then Eq. (2.210) is exact regardless of the choice of Φ_{S_0} . Otherwise, beyond a linear electron-phonon coupling approximation, Eq. (2.210) includes these higher-order interactions approximately by finding their effect for a trial influence functional Φ_{S_0} that seeks to imitate the actual influence functional Φ . In FHIP, they expect Eq. (2.210) to be an excellent approximation to the actual impedance of the polaron.

Thornber investigated an extension beyond linear response [33], where they evaluate the steady-state response of the electron in a finite electric field of arbitrary strength.

Calculating the polaron mobility

To obtain a general expression for the dissipation, or equivalently the mobility, of the polaron in FHIP, they recognise that the dc mobility μ_{dc} for the polaron is,

FHIP DC Mobility

$$\mu_{dc}^{-1} = \lim_{\Omega \rightarrow 0} \text{Im}\Sigma(\Omega). \quad (2.211)$$

In FHIP, they rewrite $\text{Im}\Sigma(\Omega)$ into a more convenient form for calculation (which may have been true at the time due to their computational capabilities but is no longer necessarily true) by using contour integration. They recognise that since $S(u)$ is analytic between $u = \text{real}$ and $u = \text{real} + i\beta$, the contour of integration can be changed from along the real axis to one which goes first from 0 to $i\beta/2$ up the imaginary axis and then from $i\beta/2$ to $i\beta/2 + \infty$ parallel to the real axis. In the case of Fröhlich's Hamiltonian they obtain for $\text{Im}\Sigma(\Omega)$,

$$\text{Im}\Sigma(\Omega) = -\frac{2\alpha}{3\sqrt{\pi}} \frac{\beta^{3/2} \sinh(\Omega\beta/2)}{\Sigma \sinh(\beta/2)} \left(\frac{v}{w}\right)^3 \int_0^\infty \frac{\cos(\Omega x)\cos(x) dx}{[x^2 + a^2 - b \cos(vx)]^{3/2}}, \quad (2.212)$$

where $a^2 \equiv \beta^2/4 + R\beta \coth(\beta v/2)$, $b \equiv R\beta/\sinh(\beta v/2)$ and $R \equiv (v^2 - w^2)/(w^2 v)$.

$\text{Im}\Sigma(\Omega)$ has maxima when Ω is equal to a frequency where absorption can happen to go to an excited polaron state, and the width of these maxima correspond to the state lifetimes for phonon emission. In FHIP, they compute $\text{Im}\Sigma(\Omega)$ by expanding Eq. (2.212) in an infinite power series of K modified Bessel functions of the second kind where only the first few terms are required for convergence in most cases.

In Appendix C, I have reproduced the contour integration for $\text{Im}\Sigma(\Omega)$ and also provided the contour integration for $\text{Re}\Sigma(\Omega)$ as well.

2.3.2 FHIP Polaron Mobility Numerical Results

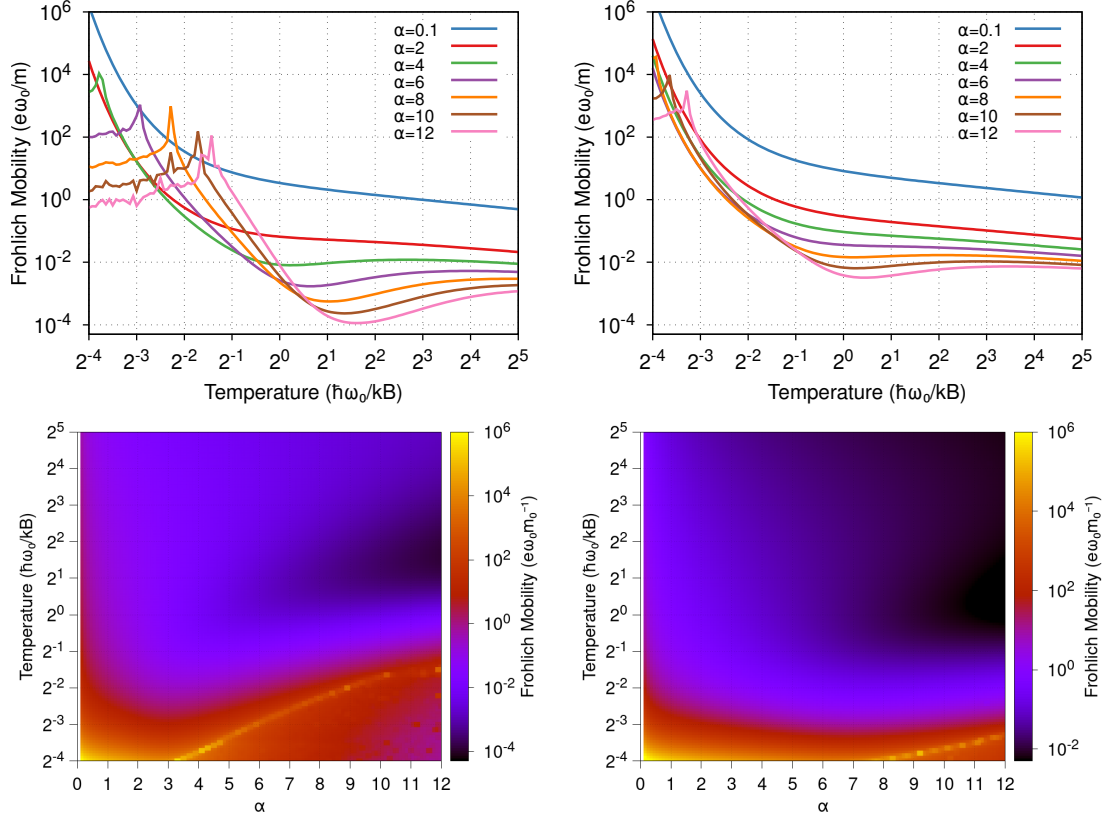


Figure 2.4: The temperature (T in units of the phonon frequency ($\hbar\omega_0/k_B$))- and electron-phonon α coupling-dependence of the polaron DC mobility (μ in units of $e\omega_0 m_0^{-1}$) for the Fröhlich model in 2D (left) and 3D (right).

Fig. (2.4) shows line (top) and contour (bottom) plots of the DC mobility derived in FHIP for the 2D (left) and 3D (right) Fröhlich model. First, I note the numerical errors caused by strong coupling and low temperatures. These arise due to limited numerical machine precision in capturing low values of the memory function $\Sigma(\Omega)$, which results in noise in mobility calculation since the memory function and mobility have a reciprocal relationship. Rather than plateauing to a finite value, the FHIP mobility in this region should exponentially increase to infinity as the temperature approaches zero.

Nonetheless, we see an interesting non-monotonic behaviour in the mobility for sufficiently large couplings with a minimum around the Debye temperature $T = T_D = \hbar\omega_0/k_B$, which is of the order $T_D \sim 48$ K for LO phonon modes. The transition typically indicates a change in regime from band-like transport below the Debye temperature to thermally-activated ‘lattice-hopping’ transport above this temperature. However, as Mishchenko et al. [10] noted, the Fröhlich polaron is defined in a continuum, where the notion of lattice-hopping is inconsistent. Instead, this minimum arises from a competition between decreasing phonon excitations below $T < T_D$ and significant effective mass renormalisation above $T > T_D$. For sufficiently large temperatures, the thermally excited phonons eventually succeed in

stripping the polaron of its phonon cloud. Then, the mobility follows the $\mu \sim T^{-1/2}$ power law predicted by the Boltzmann Transport Equation (BTE).

2.3.3 The FHIP initial product state and low-temperature mobility

One source of controversy around the FHIP polaron mobility lies in its low-temperature expression compared to that derived from other approaches, such as the BTE [19]. In FHIP [17], they assume a factorised initial product state, which results in an incorrect low-temperature weak-coupling approximation for the DC-mobility with a spurious ‘ 2β ’ appearing in the denominator of the mobility,

FHIP Low Temperature DC Mobility

$$\mu_{\text{FHIP}} = \left(\frac{w}{v}\right)^3 \frac{3e}{2m_0\omega_0} \frac{\exp(\hbar\omega_0\beta)}{2\alpha\hbar\omega_0\beta} \exp\left(\frac{v^2 - w^2}{w^2 v \omega_0^{-1}}\right). \quad (2.213)$$

This observation is important for understanding the ‘ $3/2\beta$ ’ discrepancy between the low-temperature FHIP DC-mobility and Kadanoff’s DC-mobility [19] derived from the BTE,

$$\mu_K = \left(\frac{w}{v}\right)^3 \frac{e}{2m_0\omega_0} \frac{\exp(\hbar\omega_0\beta)}{\alpha} \exp\left(\frac{v^2 - w^2}{w^2 v \omega_0^{-1}}\right). \quad (2.214)$$

Some have argued that this discrepancy is due to taking the incorrect order of the limits $\Omega \rightarrow 0$ and $\alpha \rightarrow 0$ in calculating the impedance [68]. An alternative form of the low-temperature dc-mobility was derived by Los [69–71] and Sels [72]. Their mobility results differ by a factor of 3 from Kadanoff and by a factor of 2β from FHIP,

$$\mu_L = \left(\frac{w}{v}\right)^3 \frac{3e}{2m_0\omega_0} \frac{\exp(\hbar\omega_0\beta)}{\alpha} \exp\left(\frac{v^2 - w^2}{w^2 v \omega_0^{-1}}\right). \quad (2.215)$$

Sels and Brosens [72] show that the difference with Kadanoff is because the relaxation time approximation (neglecting the non-vanishing in-scattering term) used by Kadanoff violates particle number conservation, whereas FHIP does not. However, as mentioned above, the FHIP approximation relies on a nonphysical initial state for Feynman’s polaron model. Further, Los [70, 71] shows that not using a factorised initial state of the electron-phonon system results in corrections (although small) due to proper inclusion of initial correlations between the electron and the phonons.

Correcting the FHIP method may involve using a non-factorised initial state for the polaron density matrix. This would alter the influence functional to include an additional dependence on the imaginary-time paths of the electron. The reduced density matrix

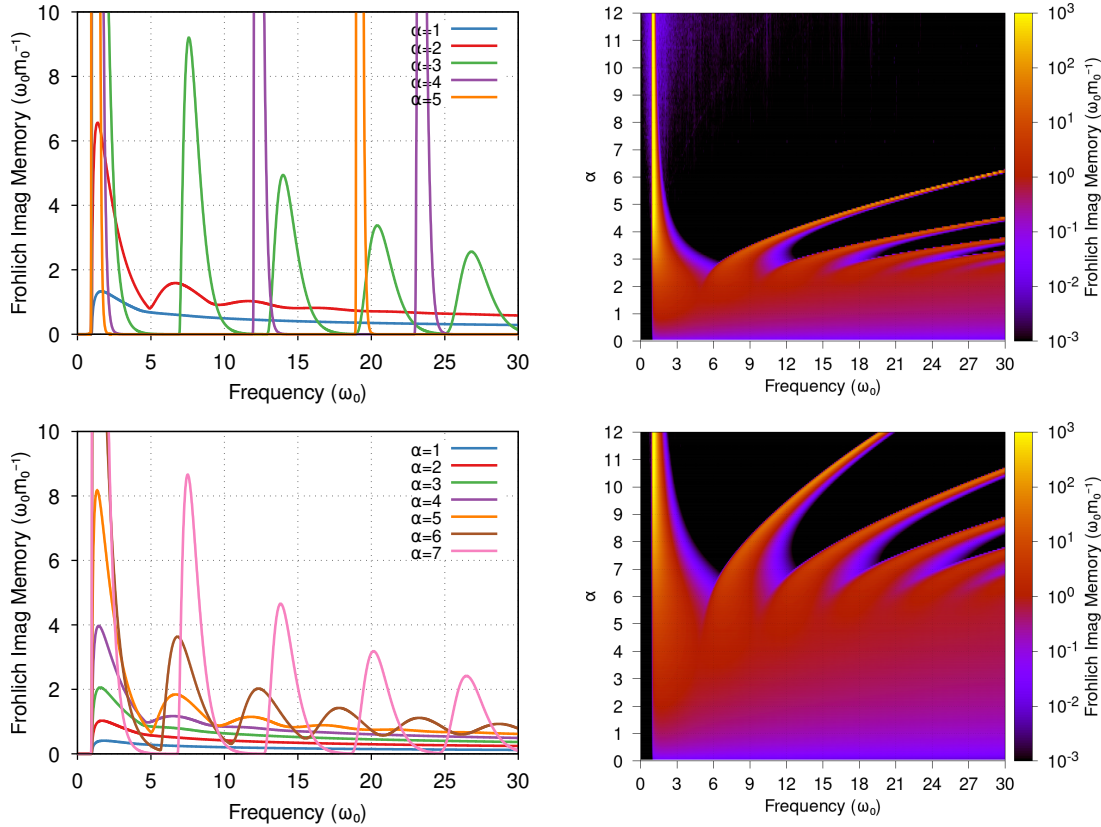


Figure 2.5: The electron-phonon α coupling- and frequency-dependence (Ω in units of ω_0) of the 2D (**top**) and 3D (**bottom**) Fröhlich polaron imaginary memory function $\text{Im } \Sigma(\Omega)$ (units of $\omega_0 m_0^{-1}$).

would then have an additional integration over these *imaginary*-time paths to produce a triple path integral. The initial state would then be the reduced equilibrium density matrix for the *entire* model system, as defined by Ōsaka, rather than just the equilibrium density matrix for the phonon system used in FHIP. The trial influence functional would then also include additional dependence on the imaginary-time paths. This involves generalising the real-time variable to a complex time variable over the so-called Keldish contour used in modern formulations of the influence functional method.

Ultimately, I do not use the low-temperature form of the FHIP mobility (Eq. (2.3.3)) in this work. Instead, I perform a direct numerical integration of the integral in the memory function Σ in Eq. (2.202). Whilst the FHIP mobility has incorrect low-temperature behaviour, as my application of the FHIP polaron theory will primarily be to determine the room-temperature mobility, this is safely in the temperature range in most materials for which the FHIP mobility is correct.

2.3.4 FHIP Memory Function Numerical Results

Athermal Memory Function

Fig. 2.5 presents the imaginary part of the memory function $\text{Im}\Sigma(\Omega)$ for the Fröhlich polaron model, showing its dependence on both frequency Ω (in units of the phonon frequency ω_0) and the electron-phonon coupling strength α for 2D (top) and 3D (bottom) systems. The memory function $\Sigma(\Omega)$, being the inverse Fourier transform of the polaron's response to external perturbations, provides insight into how the polaron interacts with the phonon field, particularly with regard to energy dissipation through multi-phonon processes. This function, central to understanding polaron dynamics, captures how phonon excitations lead to energy losses and is directly related to the polaron's optical properties.

In the 2D system (top panel), for weak coupling ($\alpha = 1$), the imaginary part of the memory function shows a sharp, distinct peak at a low frequency. This peak corresponds to the primary interaction between the electron and the longitudinal optical (LO) phonons, where energy is dissipated as the polaron moves through the lattice. As the coupling strength increases, additional peaks emerge at higher frequencies. These correspond to multi-phonon processes, where the polaron absorbs or emits multiple phonons as it interacts with the lattice vibrations. The positions of these peaks are approximately at $\Omega = \omega_0 + n \cdot v$, where v is a variational parameter related to the strength of the electron-phonon interaction, similar to what is observed in the Holstein model. The heat map on the right for 2D reveals a clear pattern where the memory function becomes more pronounced at higher frequencies as α increases, indicating stronger coupling leading to more complex polaron-phonon interactions.

In the 3D system (bottom panel), the memory function shows a similar pattern but with more pronounced broadening at higher frequencies than in 2D. For small α , the memory function exhibits a sharp peak at a low frequency, representing single-phonon dissipation processes. As α increases, multi-phonon processes dominate, leading to several higher-frequency peaks. As in the 2D case, these peaks can be interpreted as transitions between different energy levels of the polaron, where the electron absorbs or emits multiple phonons simultaneously. The peaks are spaced according to $\Omega = \omega_0 + n \cdot v$, consistent with previous analyses of polaron dynamics. The heat map for 3D highlights the broadening of the memory function at higher coupling strengths, with a more continuous distribution of dissipation processes across a wide range of frequencies as α increases. This behaviour is consistent with the results in DSG [18], where it was shown that the polaron interacts with multiple phonons at strong coupling, leading to enhanced dissipation and complex optical absorption features.

Physically, the behaviour of the imaginary part of the memory function can be understood in terms of the increasing complexity of the polaron-phonon interaction as the coupling strength increases. At weak coupling ($\alpha = 1$), the polaron is only weakly dressed by the phonon cloud, and energy dissipation primarily occurs through single-phonon processes,

as reflected in the sharp peak at low frequencies. As the coupling strength increases, the polaron becomes more strongly dressed by phonons, leading to multi-phonon processes where the polaron can absorb or emit several phonons simultaneously. These processes are reflected in the emergence of additional peaks at higher frequencies, as seen in 2D and 3D cases. The broadening of the peaks at higher coupling strengths, particularly in 3D, reflects that the polaron interacts with a larger number of phonon modes, leading to more diffuse energy dissipation.

This broadening and the emergence of higher-order peaks as α increases also indicate a transition to more complex polaron dynamics, where the polaron's effective mass is significantly renormalised due to its interaction with the phonon cloud. As described in the DSG paper, this renormalisation leads to a shift in the peak positions and the broadening of the absorption features, which is directly related to the enhanced dissipation seen in the memory function at higher coupling strengths.

Thermal Memory Function

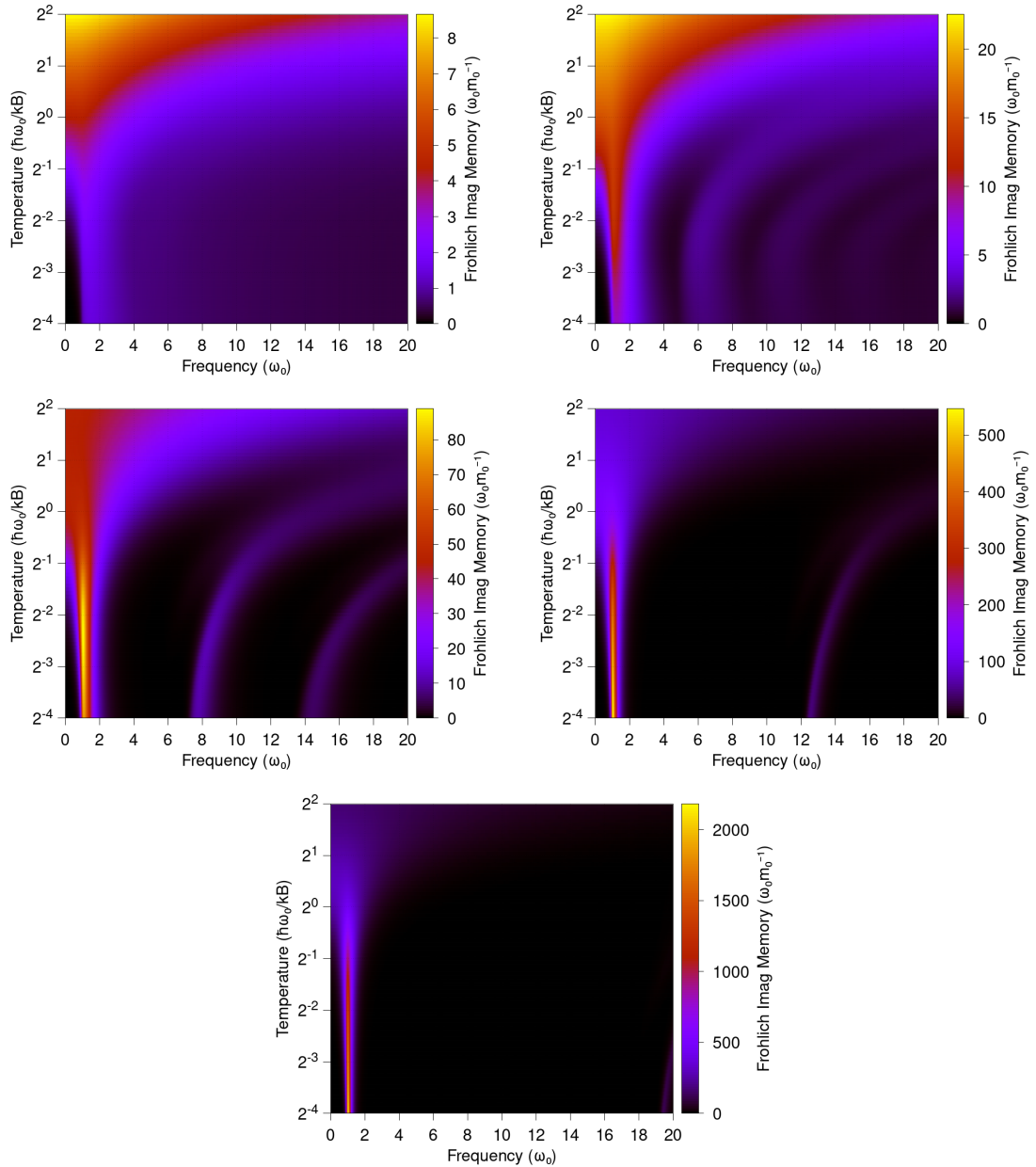


Figure 2.6: The temperature (T in units of $\hbar\omega_0/k_B$)- and frequency-dependence (Ω in units ω_0) of the imaginary component of the 2D Fröhlich polaron memory function $\text{Im } \Sigma(\Omega)$ (units of $\omega_0\omega_0^{-1}$) for electron-phonon couplings $\alpha = 1$ (**top-left**), 2 (**top-right**), 3 (**middle-left**), 4 (**middle-right**) and 5 (**bottom**).

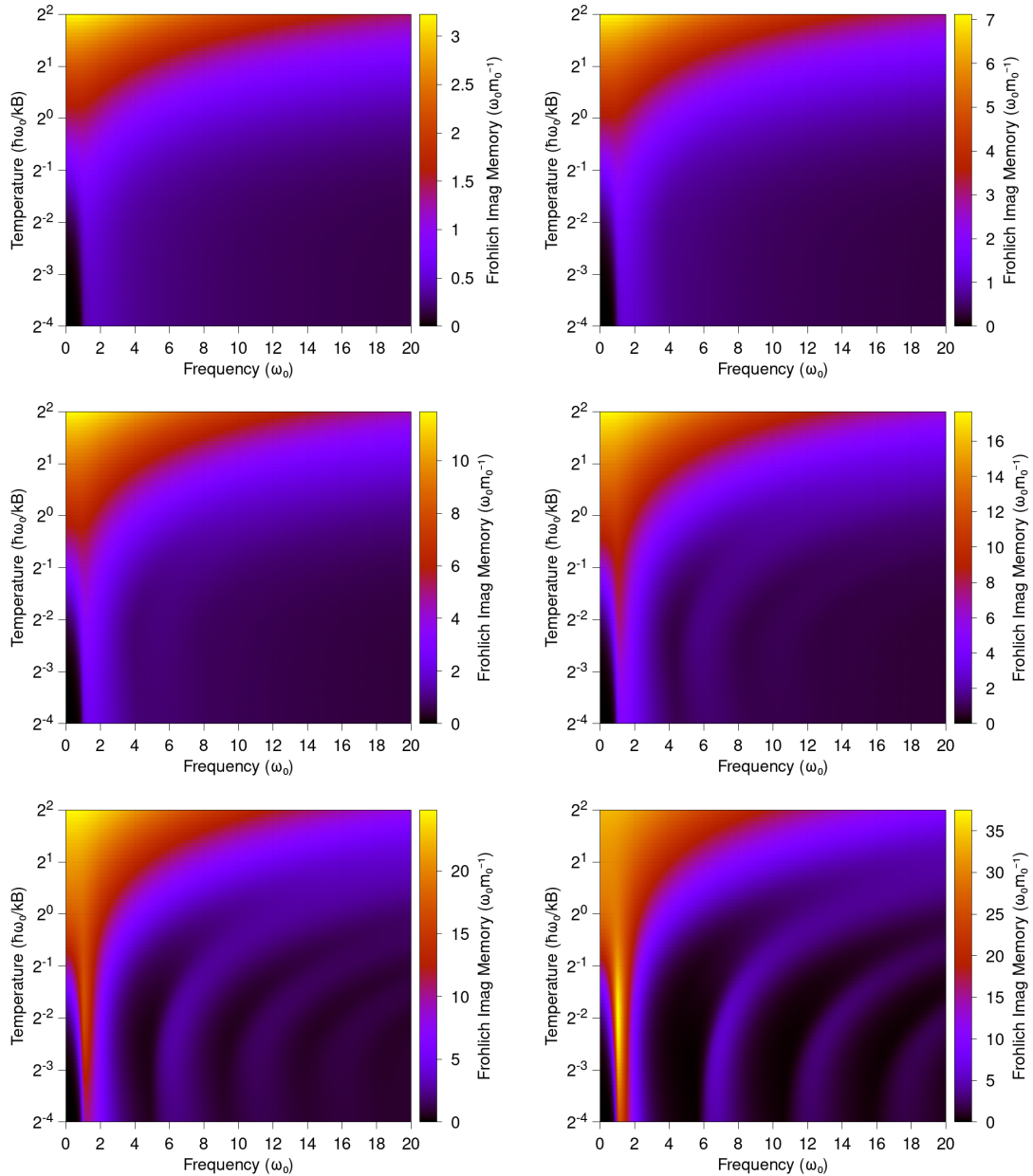


Figure 2.7: The temperature (T in units of $\hbar\omega_0/k_B$)- and frequency-dependence (Ω in units ω_0) of the imaginary component of the 3D Fröhlich polaron memory function $\text{Im } \Sigma(\Omega)$ (units of $\omega_0 \omega_0^{-1}$) for electron-phonon couplings $\alpha = 1$ (**top-left**), 2 (**top-right**), 3 (**middle-left**), 4 (**middle-right**), 5 (**bottom-left**) and 6 (**bottom-right**).

Figs. 2.6 and 2.7 display the temperature and frequency dependence of the imaginary part of the polaron memory function, $\text{Im}\Sigma(\Omega)$, for the 2D (Fig. 2.6) and 3D (Fig. 2.7) Fröhlich polaron models across different electron-phonon coupling strengths α . The memory function measures the energy dissipation processes within the polaron system due to the interactions between the electron and the phonon field. The dependence of $\text{Im}\Sigma(\Omega)$ on temperature and frequency offers key insights into how the complexity of these dissipation processes evolves as both temperature and coupling strength increase, with distinct differences between 2D and 3D systems.

In the 2D case (Fig. 2.6), the memory function shows a sharp increase in magnitude as both coupling strength and temperature rise. For $\alpha = 1$ (top-left), the dissipation is concentrated at lower frequencies and higher temperatures, with a smooth and relatively weak overall response. As temperature increases, the memory function becomes slightly more pronounced. Still, it remains largely limited to lower frequencies, suggesting that single-phonon processes dominate the energy dissipation in the weak coupling regime. As α increases to 2 and beyond (top-right and middle-left panels), the memory function shows more prominent features, particularly at higher frequencies and temperatures. For $\alpha = 3$, the energy dissipation peaks at intermediate frequencies and becomes more sensitive to temperature, indicating the onset of multi-phonon processes. At stronger coupling ($\alpha = 4$ and $\alpha = 5$, middle-right and bottom panels), the magnitude of $\text{Im}\Sigma(\Omega)$ grows significantly, with dissipation extending across a wide frequency range and occurring at lower temperatures. The sharp increase in energy dissipation, especially at high frequencies and low temperatures, points to complex multi-phonon interactions dominating as the polaron becomes heavily dressed by the phonon cloud.

In the 3D case (Fig. 2.7), the memory function exhibits a more gradual increase in magnitude as coupling strength and temperature rise. For $\alpha = 1$ (top-left), the energy dissipation is relatively weak and confined to low frequencies and high temperatures, similar to the 2D case. However, as the coupling strength increases to $\alpha = 2$ and $\alpha = 3$ (top-right and middle-left panels), the memory function broadens and shifts to higher frequencies, with a more gradual rise in dissipation compared to the 2D system. The dissipation remains concentrated at intermediate and high temperatures, but as α increases to $\alpha = 4$ and beyond (middle-right and bottom panels), the memory function becomes significantly more pronounced, with dissipation extending across both low and high frequencies. The peaks in $\text{Im}\Sigma(\Omega)$ shift smoothly with temperature, reflecting a more distributed interaction between the polaron and the phonon modes in three-dimensional systems.

Comparing the two figures, it is evident that dimensionality plays a critical role in shaping the memory function's behaviour. In 2D, the memory function exhibits sharper transitions, particularly for $\alpha \geq 3$, with more abrupt increases in energy dissipation at higher

frequencies and temperatures. The sharper transitions in 2D suggest that the polaron-phonon interactions are more sensitive to temperature and coupling strength changes in lower-dimensional systems. This results in stronger energy dissipation at moderate to strong coupling, as the polaron experiences more significant interactions with the phonon field. In contrast, the 3D case shows a more gradual and continuous evolution of the memory function, with energy dissipation increasing steadily across the frequency range as α increases. The broader, more distributed peaks in 3D suggest that the polaron interacts with a larger number of phonon modes, resulting in a smoother dissipation pattern across temperatures and frequencies.

Overall, the memory function becomes more pronounced with increasing coupling strength, as multi-phonon processes play a larger role in energy dissipation. However, the sharper transitions and larger memory effects in 2D indicate that lower-dimensional systems exhibit more pronounced energy dissipation at comparable coupling strengths and temperatures. These results highlight the importance of dimensionality in determining the strength and nature of electron-phonon interactions and the energy dissipation processes in polaron systems.

2.3.5 Optical Conductivity

Devreese, Sitter and Gooverts [18] (otherwise referred to as “DSG”) expand upon the work done in FHIP by evaluating the optical absorption coefficient (i.e. the optical conductivity) of the polaron. To obtain this coefficient, they compare the expansion of the conductivity $\sigma(\Omega) = 1/z(\Omega)$ to the expansion of the impedance (used by FHIP) $z(\Omega)$ and find further justification for the accuracy of the impedance function expansion. This, in turn, provides a more accurate expression for the frequency-dependent complex mobility $\mu(\Omega)$. To achieve this, they find an expression for the real component of the impedance function $\text{Re}\Sigma(\Omega)$. They then evaluate both $\text{Re}\Sigma(\Omega)$ and $\text{Im}\Sigma(\Omega)$ at zero temperature ($\beta = \infty$) by deriving involved analytical expressions.

DSG state the relation between the optical absorption coefficient $\Gamma(\Omega)$ and the impedance $z(\Omega)$ of polarons as,

Optical Absorption

$$\Gamma(\Omega) = \frac{1}{c\epsilon_0 n} \text{Re} \left\{ \frac{1}{z(\Omega)} \right\}, \quad (2.216)$$

where ϵ_0 is the dielectric constant of the vacuum, n is the index of refraction of the medium, and c is the speed of light. DSG find that for the expansion of $z(\Omega)$ at zero temperature, the optical absorption coefficient requires both the real $\text{Re}z(\Omega)$ and imaginary $\text{Im}z(\Omega)$

components of the impedance (or of $\Sigma(\Omega)$). They obtain the expression,

$$\Gamma_z(\Omega) = \frac{1}{c\epsilon_0 n} \lim_{\beta \rightarrow \infty} \frac{\text{Im}\Sigma(\Omega)}{\Omega^2 - 2\Omega\text{Re}\Sigma(\Omega) + |\Sigma(\Omega)|^2}. \quad (2.217)$$

If the expansion of the conductivity $1/z(\Omega)$ is used instead then they obtain,

$$\Gamma_\sigma(\Omega) = \frac{\text{Im}\Sigma(\Omega)}{\Omega^2} \left(\frac{\Omega^2 - w^2}{\Omega^2 - v^2} \right)^2. \quad (2.218)$$

DSG rigorously takes the zero temperature limit $\beta \rightarrow \infty$. By taking the limit directly in the expression for $\Sigma(\Omega)$ in Eq. (2.202). The real and imaginary components at zero temperature ($\beta = \infty$) are,

$$\text{Re}\Sigma(\Omega) = \text{Im} \int_0^\infty du \frac{[1 - \cos(\Omega u)] e^{iu}}{\Omega [R(1 - e^{ivu}) - iu]^{3/2}}, \quad (2.219a)$$

$$\text{Im}\Sigma(\Omega) = \text{Im} \int_0^\infty du \frac{\sin(\Omega u) e^{iu}}{\Omega [R(1 - e^{ivu}) - iu]^{3/2}}, \quad (2.219b)$$

where $R = (v^2 - w^2)/(w^2 v)$. By using a binomial expansion of the denominator of the integrand, we get,

$$\text{Re}\Sigma(\Omega) = \frac{2\alpha}{3\Omega} \frac{v^3}{w^3} \sum_{n=0}^{\infty} C_{-3/2}^n (-1)^n R^n \times \text{Im} \int_0^\infty du \frac{[1 - \cos(\Omega u)] e^{i(1+nv)u}}{[R - iu]^{3/2+n}}, \quad (2.220a)$$

$$\text{Im}\Sigma(\Omega) = \frac{2\alpha}{3\Omega} \frac{v^3}{w^3} \sum_{n=0}^{\infty} C_{-3/2}^n (-1)^n R^n \times \text{Im} \int_0^\infty du \frac{\sin(\Omega u) e^{i(1+nv)u}}{[R - iu]^{3/2+n}}, \quad (2.220b)$$

where C_r^n are the binomial coefficients. For $\text{Im}\Sigma(\Omega)$ at $\beta = \infty$ DSG find the expansion,

$$\begin{aligned} \text{Im}\Sigma(\Omega) &= \frac{2\alpha}{3\Omega} \frac{v^3}{w^3} \sum_{n=0}^{\infty} C_{-3/2}^n (-1)^n \frac{(2R)^n}{(2n+1)!!} \\ &\times |\Omega - 1 - nv|^{n+1/2} e^{-|\Omega - 1 - nv|R} \frac{1 + \text{sgn}(\Omega - 1 - nv)}{2}, \end{aligned} \quad (2.221)$$

where $(2n+1)!! = (2n+1) \dots 5 \cdot 3 \cdot 1$ indicates the double factorial. In FHIP, they stated the first two terms of this expansion. FHIP find that following the same procedure for $\text{Re}\Sigma(\Omega)$ is far more complicated and has poor convergence properties. Therefore, DSG transform the integrals in Eq. (2.220b) to integrals with rapidly convergent integrands to

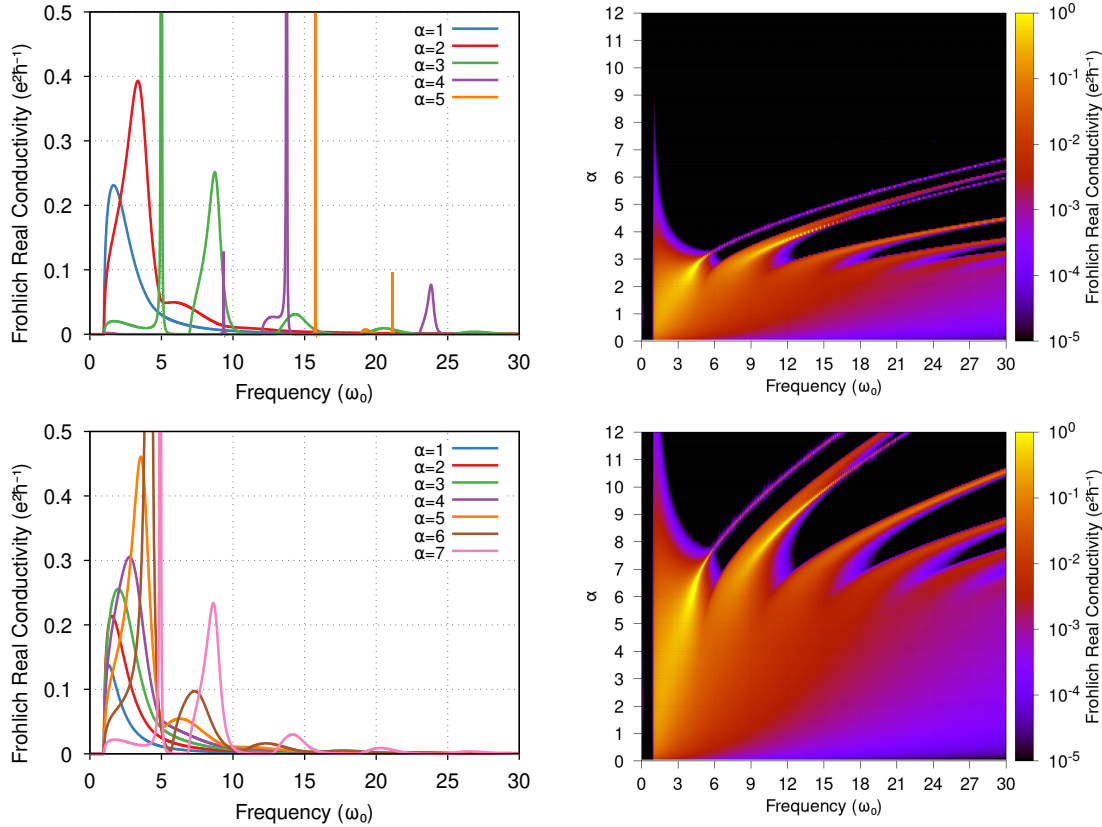


Figure 2.8: The electron-phonon α coupling- and frequency-dependence (Ω in units of ω_0) of the 2D (top) and 3D (bottom) Fröhlich polaron real conductivity $\text{Re } \sigma(\Omega)$ (units of $e^2 \hbar^{-1}$).

give the result,

$$\begin{aligned} \text{Re}\Sigma(\Omega) = & -\frac{2\alpha}{3\Omega} \frac{v^3}{w^3} \sum_{n=0}^{\infty} \frac{1}{\Gamma(n+3/2)} \int_0^{\infty} dx \left[\left(n + \frac{1}{2} \right) x^{n-1/2} e^{-Rx} - Rx^{n+1/2} e^{-Rx} \right] \\ & \times \ln \left| \frac{(1+nv+x)^2}{\Omega^2 - (1+nv+x)^2} \right|^{1/2}. \end{aligned} \quad (2.222)$$

From these expansions of $\text{Re}\Sigma(\Omega)$ and $\text{Im}\Sigma(\Omega)$ DSG evaluate the optical absorption coefficient.

In Appendix C, I have derived the expansions of $\text{Re}\Sigma(\Omega)$ and $\text{Im}\Sigma(\Omega)$ for finite temperatures in terms of hypergeometric functions.

2.3.6 DSG Optical Conductivity Numerical Results

Athermal Optical Conductivity

Fig 2.8 shows the real part of the polaron optical conductivity $\sigma(\Omega)$ for the Fröhlich model, plotted as a function of frequency Ω (in units of the phonon frequency ω_0) and the electron-phonon coupling constant α , for both 2D (top) and 3D (bottom) systems. The left panels display the optical conductivity for various values of α , while the right panels present heat maps that illustrate how the conductivity changes as a function of frequency and coupling strength. This optical conductivity describes how polarons absorb energy from the electromagnetic field as they interact with phonons, providing insights into the polaron's dynamic properties across different coupling regimes. The results align with the polaron theory discussed in DSG [18] and provide detailed insight into the polaron's optical response in 2D and 3D settings.

In the 2D system (top panel), the real part of the optical conductivity shows sharp peaks at specific frequencies, particularly for small α (weak coupling). For $\alpha = 1$, a single sharp peak appears around $\Omega/\omega_0 \approx 5$, corresponding to the polaron's interaction with the lattice through one-phonon processes. As α increases, the peaks shift slightly toward higher frequencies, and new peaks emerge, indicating multi-phonon processes. These additional peaks at higher frequencies correspond to situations where the polaron absorbs multiple phonons as it interacts with the optical field. The positions of these peaks follow the relation $\Omega = \omega_0 + n \cdot v$, where v is Feynman's variational parameter, consistent with what was found in DSG. The heat map to the right clearly shows how the conductivity broadens as α increases, with the peaks becoming less sharp and more spread out at higher coupling strengths. This broadening reflects stronger polaron-phonon coupling, where multi-phonon processes become increasingly dominant, leading to a wider range of frequencies over which the polaron absorbs optical energy.

In the 3D system (bottom panel), the optical conductivity follows a similar pattern but shows an even more pronounced broadening of the peaks as α increases. For small α , the conductivity exhibits a sharp peak around $\Omega/\omega_0 \approx 6$, similar to the 2D case, corresponding to one-phonon processes. However, as α increases, the additional peaks at higher frequencies become more evident, and the peaks broaden significantly, indicating that multi-phonon processes are more dominant in the 3D system. As in the 2D case, the heat map reveals the broadening of the conductivity spectrum at larger α values, with the peaks becoming smoother and spreading over a broader frequency range. This trend highlights that in 3D systems, the polaron interacts with a greater number of phonon modes, leading to more complex optical absorption behaviour. As α grows, the polaron's mass is more strongly renormalised by its interaction with the phonon cloud, which contributes to the overall broadening of the optical conductivity spectrum.

Physically, the results illustrate how increasing the electron-phonon coupling strength α enhances the polaron's interaction with the phonons, leading to more complex optical

conductivity spectra. At weak coupling ($\alpha = 1$), the polaron primarily interacts with a single phonon mode, resulting in a sharp, distinct peak in the optical conductivity. As α increases, the polaron becomes more strongly dressed by the phonon cloud, leading to additional peaks corresponding to multi-phonon interactions. These higher-order peaks are more pronounced in 3D systems due to the larger number of phonon modes available, which allow for more distributed energy absorption by the polaron. The shift and broadening of the peaks with increasing α reflect the renormalisation of the polaron's effective mass, as the interaction with phonons slows down its response to the electromagnetic field and causes the polaron to absorb energy over a wider frequency range.

The heat maps further emphasise these trends. For small α , the optical conductivity is concentrated around a single peak. Still, as the coupling strength increases, the conductivity becomes more continuous and spread out, indicating a transition from simple single-phonon absorption to more complex multi-phonon processes. In 3D, this broadening is more pronounced than in 2D, reflecting that in higher dimensions, the polaron interacts with a larger number of phonon modes, leading to more diffuse energy absorption. This result aligns with the findings in the DSG paper, where it was shown that at stronger coupling, the polaron's interaction with the phonon cloud becomes more complex, leading to broader optical conductivity spectra.

Overall, the real part of the Fröhlich polaron optical conductivity evolves with both the electron-phonon coupling strength α and the system's dimensionality. In 2D, the conductivity shows sharp peaks that broaden and shift as α increases, reflecting the growing role of multi-phonon processes. In 3D, this broadening is even more pronounced, indicating that the polaron interacts with many phonon modes in higher-dimensional systems. The emergence of multi-phonon peaks at higher frequencies and the broadening of the spectrum as α increases are consistent with the renormalisation of the polaron's mass and its more complex interaction with the phonon field. These results provide detailed insights into the dynamic behaviour of the polaron in 2D and 3D systems, with the optical conductivity serving as a key indicator of how the polaron absorbs energy from the optical field.

Thermal Optical Conductivity

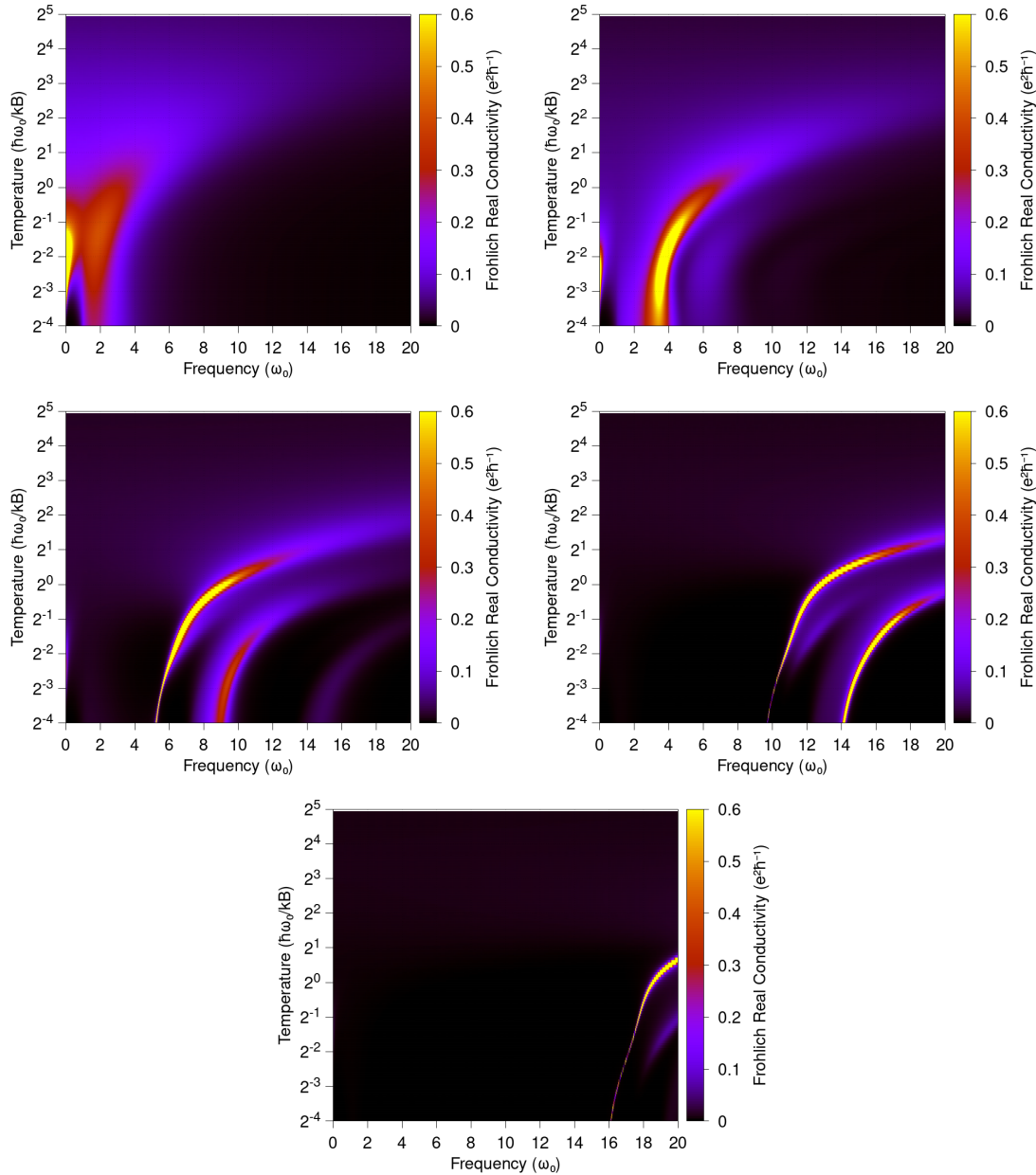


Figure 2.9: The temperature (T in units of $\hbar\omega_0/k_B$)- and frequency-dependence (Ω in units of ω_0) of the real component of the 2D Fröhlich polaron conductivity $\text{Re } \sigma(\Omega)$ (units of $e^2\hbar^{-1}$) for electron-phonon couplings $\alpha = 1$ (top-left), 2 (top-right), 3 (middle-left), 4 (middle-right) and 5 (bottom)

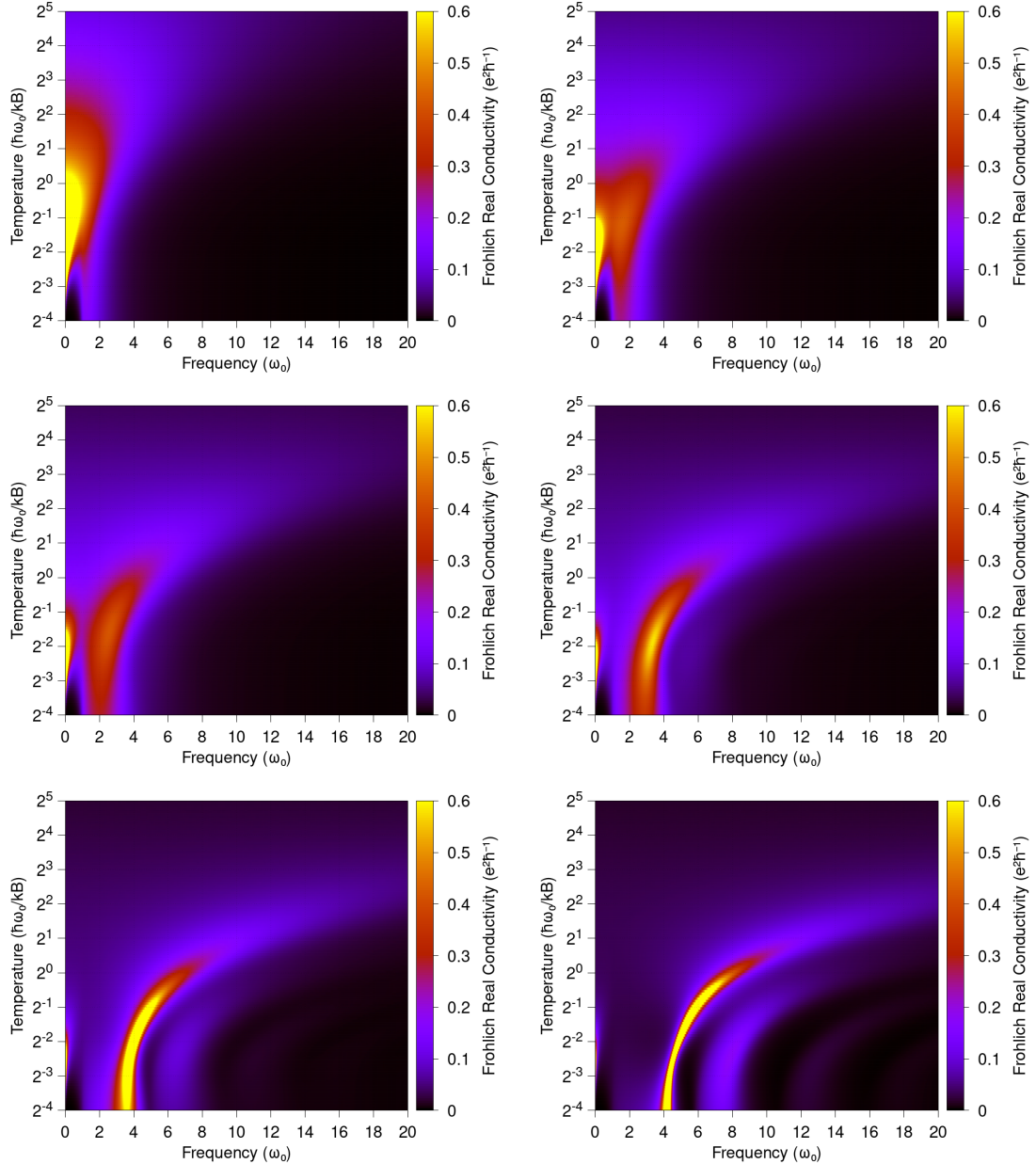


Figure 2.10: The temperature (T in units of $\hbar\omega_0/k_B$)- and frequency-dependence (Ω in units of ω_0) of the real component of the 3D Fröhlich polaron conductivity $\text{Re } \sigma(\Omega)$ (units of $e^2\hbar^{-1}$) for electron-phonon couplings $\alpha = 1$ (**top-left**), 2 (**top-right**), 3 (**middle-left**), 4 (**middle-right**), 5 (**bottom-left**) and 6 (**bottom-right**).

Figs. 2.9 and 2.10 The two figures present the temperature and frequency dependence of the real part of the optical conductivity $\sigma(\Omega)$ for the 2D (Fig. 2.9) and 3D (Fig. 2.10 Fröhlich polaron models for various electron-phonon coupling strengths α . The optical conductivity reflects how the polaron interacts with an external electromagnetic field, providing key insights into the transport properties of the polaron as it absorbs and dissipates energy. The temperature dependence in both figures demonstrates how phonon interactions become more complex as both temperature and coupling strength increase, influencing the ability of the polaron to conduct optical energy.

In the 2D case (Fig. 2.9), for weak coupling ($\alpha = 1$, top-left), the optical conductivity is concentrated at low temperatures and low frequencies, with a single distinct peak. As temperature increases, this peak gradually broadens, but the overall magnitude of the conductivity remains low, indicating limited energy absorption in this weak coupling regime. The smooth transition suggests that single-phonon processes dominate at low temperatures. As α increases to 2 and 3 (top-right and middle-left panels), the peaks shift to higher frequencies and temperatures, and the conductivity becomes more pronounced, indicating stronger interactions between the polaron and the phonon cloud. At $\alpha = 3$, distinct features emerge as the optical conductivity shifts to intermediate frequencies, reflecting the onset of multi-phonon processes. For stronger coupling strengths ($\alpha = 4$ and $\alpha = 5$, middle-right and bottom panels), the peaks in the conductivity move further to higher frequencies and broaden considerably as the polaron interacts with a larger number of phonon modes. The enhanced optical response at higher frequencies and temperatures in these stronger coupling regimes suggests that the polaron is heavily dressed by the phonons, leading to more complex energy absorption patterns.

In the 3D case (Fig. 2.10), the overall behaviour is similar, but the transitions are more gradual, and the peaks in the optical conductivity are less sharp than in the 2D case. For $\alpha = 1$ (top-left), the conductivity is concentrated at low temperatures and frequencies, similar to 2D, but with broader features. As α increases to 2 and 3 (top-right and middle-left panels), the peaks shift toward higher frequencies, and the conductivity increases with temperature. Still, the transitions remain smooth, indicating a more distributed interaction between the polaron and the phonon field in 3D systems. At stronger coupling strengths ($\alpha = 4, 5, 6$, middle-right, bottom-left, and bottom-right panels), the conductivity becomes more pronounced, with peaks appearing at higher temperatures and frequencies. However, the transitions are still smoother compared to the 2D case. The broader distribution of optical conductivity in 3D reflects the increased number of phonon modes available for interaction, leading to a more continuous energy absorption spectrum.

Comparing the two figures, the system's dimensionality plays a crucial role in determining the behaviour of the optical conductivity. In 2D, the conductivity exhibits sharper peaks

and abrupt transitions as frequency and temperature increase, indicating more localised and sensitive interactions between the polaron and the phonons. The sharper transitions in 2D suggest that the polaron's optical response is more strongly influenced by temperature and coupling strength changes, particularly at higher frequencies where multi-phonon processes become dominant. In contrast, the 3D case shows smoother, broader peaks that shift gradually with increasing temperature and frequency, reflecting a more distributed interaction in three-dimensional systems, where the polaron interacts with a larger number of phonon modes over a broader frequency range.

Overall, the optical conductivity becomes more pronounced as the coupling strength increases, with multi-phonon processes playing a larger role at higher temperatures and frequencies. However, the sharper transitions and higher conductivity values observed in 2D indicate that lower-dimensional systems exhibit more sensitive and pronounced optical absorption at comparable coupling strengths and temperatures. These results highlight the impact of dimensionality on polaron dynamics and suggest that lower-dimensional systems may experience more significant optical responses due to stronger electron-phonon interactions.

2.3.7 Effective Multimode Mobility

Hellwarth and Biaggio [21] extended the Fröhlich model to where multiple phonon modes are present in a polar cubic material. They did this by deriving the full classical field Lagrangian that describes one conduction-band electron with charge $-e$, isotropic band mass m_0 and position $\mathbf{r}(t)$, which is coupled to a polar cubic lattice that possesses many infrared-active modes with varying strengths and frequencies. They derive an effective electron-phonon coupling constant that generalises Fröhlich's α parameter. Then, rather than explicitly incorporating the frequencies of multiple phonon modes into the Feynman path integral polaron model, they propose two different schemes for deriving an effective longitudinal optical phonon frequency. This enables them to directly use Ōsaka's finite-temperature variational principle for determining the temperature-dependent variational parameters v and w needed to evaluate the FHIP mobility.

As usual with Fröhlich polarons, they assume that the lattice unit cell is small compared to the electron wavelength such that the lattice polarisation density $\mathbf{P}(\mathbf{r}, t)$ can be treated as continuous. All other electrons are bound in fully occupied valence bands. The system is then perturbed by a homogeneous electric field $\mathbf{E}^{\text{ext}}(t)$. The polarisation density is composed of many independent terms $\mathbf{P}_j(\mathbf{r}, t)$ where $j = 1, \dots, m; m + 1, \dots, m + M$ correspond to the m infrared (lattice) and M ultraviolet (bound electron) modes of the

material such that,

$$\mathbf{P}(\mathbf{r}, t) = \sum_{j=1}^{m+M} \mathbf{P}_j(\mathbf{r}, t), \quad (2.223)$$

where it will be useful to separate the transverse (divergence-less) $\mathbf{P}_j^{\text{Tr}}(\mathbf{r}, t)$ and longitudinal (curl-free) $\mathbf{P}_j^{\text{L}}(\mathbf{r}, t)$ parts of the polarisation fields.

Classical Lagrangian and action

Hellwarth's and Biaggio's Lagrangian are presented as

$$\begin{aligned} L = & \int d^3\mathbf{r} \left\{ \sum_{j=1}^{m+M} \frac{2\pi}{\mathcal{K}_j^2} \left[\left(\frac{\partial \mathbf{P}_j(\mathbf{r}, t)}{\partial t} \right)^2 - \mathcal{W}_j^2 \mathbf{P}_j^2(\mathbf{r}, t) \right] + \mathbf{P}^L(\mathbf{r}, t) \cdot \mathbf{D}^{\text{el}}(\mathbf{r}, t) \right. \\ & \left. - \frac{1}{8\pi} \left[\left(\frac{\partial \mathbf{A}(\mathbf{r}, t)}{\partial t} \right)^2 - (\nabla \times \mathbf{A}(\mathbf{r}, t))^2 \right] + \frac{1}{c} \mathbf{A}(\mathbf{r}, t) \cdot \frac{\partial \mathbf{P}^{\text{Tr}}(\mathbf{r}, t)}{\partial t} \right\} \\ & \frac{1}{2} \int d^3\mathbf{r} \int d^3\mathbf{r}' \mathbf{P}(\mathbf{r}, t) \cdot \overset{\leftrightarrow}{\mathbf{G}}(\mathbf{r} - \mathbf{r}') \cdot \mathbf{P}(\mathbf{r}', t) \\ & + \frac{m_0}{2} \left(\frac{d\mathbf{r}(t)}{dt} \right)^2 + e\mathbf{r}(t) \cdot \mathbf{E}^{\text{ext}}(t) \end{aligned} \quad (2.224)$$

where $\mathbf{A}(\mathbf{r}, t)$ is the total electric vector potential (assumed purely transverse, i.e. Coulomb gauge), $\mathbf{D}^{\text{el}}(\mathbf{r}, t)$ is the longitudinal, un-shielded Coulomb field of the electron given by,

$$\mathbf{D}^{\text{el}}(\mathbf{r}, t) = \nabla \frac{e}{|\mathbf{r} - \mathbf{r}(t)|}, \quad (2.225)$$

and finally $\overset{\leftrightarrow}{\mathbf{G}}(\mathbf{r} - \mathbf{r}')$ is the dipole-dipole kernel given by $-\nabla^2 |\mathbf{r} - \mathbf{r}'|'^{-1}$. The first term in the Lagrangian describes the kinetic and potential energy of the lattice modes where \mathcal{W}_j and \mathcal{K}_j denote the frequencies and oscillator strengths of the isolated lattice modes. The dipole-dipole kernel $\overset{\leftrightarrow}{\mathbf{G}}(\mathbf{r})$ demonstrates a divergent self-interaction as $\mathbf{r} \rightarrow \mathbf{r}'$, so to remove this self-interaction and better imitate the finite size of a unit cell, Hellwarth and Biaggio introduce a cut-off distance $r_0 \sim$ inter-atomic distance. They choose $\overset{\leftrightarrow}{\mathbf{G}}(\mathbf{r})$ to be given by,

$$G_{ab}(\mathbf{r}) = \begin{cases} \frac{3r_ar_b}{|\mathbf{r}|^5} - \frac{\delta_{ab}}{|\mathbf{r}|^3}, & |\mathbf{r}| > r_0, \\ 0, & |\mathbf{r}| \leq r_0. \end{cases} \quad (2.226)$$

so drops to zero at and below this cut-off.

Transforming the action to frequency and reciprocal space

The polarisation $\mathbf{P}_j(\mathbf{r}, t)$ and electric field $\mathbf{A}(\mathbf{r}, t)$ coordinates appear up to quadratically in the Lagrangian (Eq. (2.224)) but are coupled. Hellwarth and Biaggio seek to uncouple these coordinates by transforming them to normal coordinates by rewriting the action corresponding to Eq. (2.224) in terms of the Fourier transforms of the fields (denoted with a tilde),

$$\tilde{\mathbf{P}}_j^{\text{Tr/L}}(\mathbf{q}, \Omega) = \int dt \int d^3 r \mathbf{P}_j^{\text{Tr/L}}(\mathbf{r}, t) e^{i\Omega t - i\mathbf{q}\cdot\mathbf{r}}, \quad (2.227)$$

$$\tilde{\mathbf{A}}(\mathbf{q}, \Omega) = \int dt \int d^3 r \mathbf{A}(\mathbf{r}, t) e^{i\Omega t - i\mathbf{q}\cdot\mathbf{r}}, \quad (2.228)$$

$$\tilde{\mathbf{D}}^{\text{el}}(\mathbf{q}, \Omega) = \int dt \int d^3 r \mathbf{D}^{\text{el}}(\mathbf{r}, t) e^{i\Omega t - i\mathbf{q}\cdot\mathbf{r}}, \quad (2.229)$$

$$\tilde{\mathbf{G}}_{ab}(\mathbf{q}) = \int dt \int d^3 r \mathbf{G}_{ab}(\mathbf{r}) e^{-i\mathbf{q}\cdot\mathbf{r}}, \quad (2.230)$$

where $\tilde{\mathbf{P}}(\mathbf{q}, \Omega) = \tilde{\mathbf{P}}^{\text{L}}(\mathbf{q}, \Omega) + \tilde{\mathbf{P}}^{\text{Tr}}(\mathbf{q}, \Omega)$. Since the electron wave function is assumed larger than the cut-off distance r_0 , Hellwarth and Biaggio keep only the lowest-order terms of the dipole-dipole kernel and write,

$$G_{ab}(\mathbf{q}) = \begin{cases} \frac{4\pi}{3} \left(\delta_{ab} - \frac{3k_a k_b}{q} \right), & q \ll \frac{1}{r_0} \\ 0, & \text{larger } q. \end{cases} \quad (2.231)$$

Fourier transforming and assuming the absence of any terms where q is not $\ll r_0^{-1}$, Hellwarth and Biaggio obtain the frequency and wave-vector version of the action,

$$\begin{aligned} S = & \frac{1}{(2\pi)^4} \int d\Omega \int d^3 \mathbf{q} \left\{ \sum_{j=1}^{m+M} 2\pi \frac{\Omega^2 - \mathcal{W}_j^2}{\mathcal{K}_j^2} \left[\left| \tilde{\mathbf{P}}^{\text{Tr}}(\mathbf{q}, \Omega) \right|^2 + \left| \tilde{\mathbf{P}}^{\text{L}}(\mathbf{q}, \Omega) \right|^2 \right] \right. \\ & + \tilde{\mathbf{P}}^{\text{L}}(\mathbf{q}, \Omega)^* \cdot \tilde{\mathbf{D}}^{\text{el}}(\mathbf{q}, \Omega) \\ & + \frac{1}{8\pi} \left(\frac{\Omega^2}{c^2} - q^2 \right) \left| \tilde{\mathbf{A}}(\mathbf{q}, \Omega) \right|^2 \\ & + i \frac{\Omega}{c} \tilde{\mathbf{A}}(\mathbf{q}, \Omega)^* \cdot \tilde{\mathbf{P}}^{\text{Tr}}(\mathbf{q}, \Omega) \\ & \left. + \frac{2\pi}{3} \left[\left| \tilde{\mathbf{P}}^{\text{Tr}}(\mathbf{q}, \Omega) \right|^2 - 2 \left| \tilde{\mathbf{P}}^{\text{L}}(\mathbf{q}, \Omega) \right|^2 \right] \right\} + S^{\text{el}}[\mathbf{r}(t)], \end{aligned} \quad (2.232)$$

where $S^{\text{el}}[\mathbf{r}(t)]$ is the action that depends on the electron coordinates $\mathbf{r}(t)$ (the last line of the Lagrangian in Eq. (2.224)).

Effective action for the electron-phonon interaction

Hellwarth and Biaggio follow the same procedure as [2] to evaluate the quantum-mechanical unitary transformation matrices $U(\mathbf{r}_{el,f}, \mathbf{P}_f, t_f; \mathbf{r}_{el,i}, \mathbf{P}_i, t_i)$ with path integrals over the polarisation fields $\mathbf{P}(\mathbf{r}, t)$ and electron position $\mathbf{r}(t)$,

$$U(\mathbf{r}_{el,f}, \mathbf{P}_f, t_f; \mathbf{r}_{el,i}, \mathbf{P}_i, t_i) = \int_{\mathbf{r}_{el,i}, t_i}^{\mathbf{r}_{el,f}, t_f} \mathcal{D}\mathbf{r}(t) \times \int_{\mathbf{P}_i, t_i}^{\mathbf{P}_f, t_f} \mathcal{D}\mathbf{P}(\mathbf{r}, t) \exp \left\{ \frac{iS[\mathbf{r}(t), \mathbf{P}(\mathbf{r}, t)]}{\hbar} \right\}, \quad (2.233)$$

where $S[\mathbf{r}(t), \mathbf{P}(\mathbf{r}, t)]$ is the action functional corresponding to the Lagrangian in Eq. (2.224). The path integral over all trajectories of the polarisation coordinates $\mathbf{P}(\mathbf{r}, t)$ can be done precisely as before since they only appear up to quadratic order in the Lagrangian. Hellwarth and Biaggio evaluate the matrix element $\langle 0 | U(\mathbf{r}_{el,f}, \mathbf{P}_f, t_f; \mathbf{r}_{el,i}, \mathbf{P}_i, t_i) | 0 \rangle$ where the polarisation coordinate paths begin and end in the ground state for all unperturbed polarisation oscillators. The result is an effective model action akin to Feynman's (Eq. (2.83)) where the polarisation coordinates have been replaced by their classical solutions with no external field $\tilde{\mathbf{A}}(\mathbf{q}, \Omega) = 0$. For the transverse part of the polarisation density, the classical solution $\tilde{\mathbf{P}}_{C,j}^{\text{Tr}}(\mathbf{q}, \Omega)$ obeys the equation of motion,

$$4\pi \frac{\Omega^2 - \mathcal{W}_j^2}{\mathcal{K}_j^2} \tilde{\mathbf{P}}_{C,j}^{\text{Tr}}(\mathbf{q}, \Omega) + \frac{4\pi}{3} \tilde{\mathbf{P}}_C^{\text{Tr}}(\mathbf{q}, \Omega) + i\frac{\Omega}{c} \tilde{\mathbf{A}}(\mathbf{q}, \Omega) = 0, \quad (2.234)$$

and the longitudinal part of the polarisation density, the classical solution $\tilde{\mathbf{P}}_{C,j}^L(\mathbf{q}, \Omega)$ obeys the equation of motion,

$$4\pi \frac{\Omega^2 - \mathcal{W}_j^2}{\mathcal{K}_j^2} \tilde{\mathbf{P}}_{C,j}^L(\mathbf{q}, \Omega) - \frac{8\pi}{3} \tilde{\mathbf{P}}_C^L(\mathbf{q}, \Omega) + \tilde{\mathbf{D}}^{\text{el}}(\mathbf{q}, \Omega) = 0. \quad (2.235)$$

Hellwarth and Biaggio found the solution to these equations of motion to be,

$$\tilde{\mathbf{P}}_C^{\text{Tr}}(\mathbf{q}, \Omega) = \sum_{j=1}^{m+M} \tilde{\mathbf{P}}_{C,j}^{\text{Tr}}(\mathbf{q}, \Omega) = -i\frac{\Omega}{c} \tilde{\mathbf{A}}(\mathbf{q}, \Omega) \frac{\alpha(\Omega)}{1 - (4\pi/3)\alpha(\Omega)}, \quad (2.236)$$

and,

$$\tilde{\mathbf{P}}_C^L(\mathbf{q}, \Omega) = \sum_{j=1}^{m+M} \tilde{\mathbf{P}}_{C,j}^L(\mathbf{q}, \Omega) = \frac{\alpha(\Omega)}{1 + (8\pi/3)\alpha(\Omega)} \tilde{\mathbf{D}}^{\text{el}}(\mathbf{q}, \Omega), \quad (2.237)$$

where,

$$\alpha(\Omega) = \frac{1}{4\pi} \sum_{j=1}^{m+M} \frac{\mathcal{K}_j^2}{\mathcal{W}_j^2 - \Omega^2}, \quad (2.238)$$

is the polarisability of a single-unit cell. Substituting $\tilde{\mathbf{P}}_C^{\text{Tr}}(\mathbf{q}, \Omega)$ and $\tilde{\mathbf{P}}_C^L(\mathbf{q}, \Omega)$ into the model action S gives the effective model action,

$$S^{\text{eff}} = S^{\text{el}}[\mathbf{r}(t)] + S^{\text{int}} + S^{\text{norm}}, \quad (2.239)$$

where S^{norm} is a normalisation term that cancels in the matrix element $\langle 0 | U | 0 \rangle$. S^{int} is an effective interaction term given by,

$$S^{\text{int}} = \frac{1}{2(2\pi)^4} \int d\Omega \int d^3\mathbf{q} B(\Omega) \tilde{\mathbf{D}}^{\text{el}}(\mathbf{q}, \Omega)^* \cdot \tilde{\mathbf{D}}^{\text{el}}(\mathbf{q}, \Omega), \quad (2.240)$$

where $B(\Omega)$ was obtained from the relation $\tilde{\mathbf{P}}_C^L(\mathbf{q}, \Omega) = B(\Omega) \tilde{\mathbf{D}}^{\text{el}}(\mathbf{q}, \Omega)$ and is,

$$B(\Omega) = \frac{1}{4\pi} \left(1 - \frac{1}{\epsilon(\Omega)} \right) = \frac{\alpha(\Omega)}{1 + (8\pi/3)\alpha(\Omega)} = \frac{1}{4\pi} \sum_{j=1}^{m+M} \frac{\kappa_j^2}{\omega_j^2 - \Omega^2}. \quad (2.241)$$

$B(\Omega)$ is the macroscopic polarisability, where each term in the sum of $B(\Omega)$ acts as a harmonic longitudinal lattice mode with a frequency ω_j and coupling constant κ_j that linearly coupled to the conduction electron field $\tilde{\mathbf{D}}^{\text{el}}$.

Hellwarth and Biaggio use the Born-Oppenheimer approximation as in the original Fröhlich model by assuming that the bound-electrons (ultraviolet oscillators) response speed is near instantaneous. Therefore, the short-wavelength limit ϵ_∞ of the dielectric constant accounts for the electronic contribution when the ions are immobile. Otherwise, the contribution corresponding to ionic displacements is assumed to be described by the static dielectric constant ϵ_0 . Therefore, the ions slowly follow the harmonic movement of the electron with a time delay. Hellwarth and Biaggio separate $B(\Omega)$ into infrared and optical contributions where the latter is represented by ϵ_∞ so that

$$B(\Omega) = \tilde{B}(\Omega) + \frac{1}{4\pi} \left(1 - \frac{1}{\epsilon_\infty} \right) \quad (2.242)$$

where

$$\tilde{B}(\Omega) = \frac{1}{4\pi} \sum_{j=1}^m \frac{\kappa_j^2}{\omega_j^2 - \Omega^2}. \quad (2.243)$$

This $\tilde{B}(\Omega)$ is the infrared contributions of m polar infrared lattice modes and replaces $B(\Omega)$ when neglecting the ultraviolet contributions. Hence, since the zero frequency limit is represented by ϵ_0 , we can obtain the familiar Pekar factor

$$\sum_{j=1}^m \frac{\kappa_j^2}{\omega_j^2} = \frac{1}{\epsilon_\infty} - \frac{1}{\epsilon_0}. \quad (2.244)$$

Now it is assumed that the ultraviolet contributions are summarised by ϵ_∞ and an effective band mass m_0 that replaces the electron mass m_e in the effective action S^{eff} . The space-time integral action is needed, so Hellwarth and Biaggio transform the effective action by evaluating the integrals over Ω and \mathbf{q} . The frequency integral in S^{int} corresponds to a Fourier-like transform

$$\int \frac{d\Omega}{2\pi} \frac{e^{-i\Omega t}}{\omega_j^2 - \Omega^2} = \frac{ie^{-i\omega_j|t|}}{2\omega_j}. \quad (2.245)$$

and the transform $\tilde{\mathbf{D}}^{\text{el}}(\mathbf{q}, \Omega)$ is calculated from Eq. (2.229) to give

$$\tilde{\mathbf{D}}^{\text{el}}(\mathbf{q}, \Omega) = 4\pi ie \int dt e^{i\Omega t} \frac{e^{-i\mathbf{q}\cdot\mathbf{r}(t)}}{q}. \quad (2.246)$$

Substituting these into S^{int} gives

$$\begin{aligned} S^{\text{int}} &= \frac{ie^2}{(2\pi)^2} \int d^3\mathbf{q} \frac{1}{q^2} \int dt \int dt' e^{i\mathbf{q}\cdot[\mathbf{r}(t)-\mathbf{r}(t')]} \sum_{j=1}^m \left(\frac{\kappa_j^2}{\omega_j} e^{-i\omega_j|t-t'|} \right) \\ &= i \frac{e^2}{4} \int dt \int dt' \frac{1}{|\mathbf{r}(t) - \mathbf{r}(t')|} \sum_{j=1}^m \left(\frac{\kappa_j^2}{\omega_j} e^{-i\omega_j|t-t'|} \right). \end{aligned} \quad (2.247)$$

Hellwarth and Biaggio find the final form of the effective action, akin to Feynman's, to be

$$S^{\text{p}} = \frac{m_0}{2} \int dt \left(\frac{d\mathbf{r}(t)}{dt} \right)^2 + \int dt \mathbf{E}^{\text{ext}} \cdot \mathbf{r}(t) + \frac{i\hbar\omega_p}{2\sqrt{2}} \sum_{j=1}^m \alpha_j \int dt \int dt' \frac{e^{-i\omega_j|t-t'|}}{|\mathbf{r}(t) - \mathbf{r}(t')|} \quad (2.248)$$

where we have excluded the infinite normalisation term due to the phonon oscillators (this does not affect the electron coordinate $\mathbf{r}(t)$ and so can be ignored). The effective action is written in terms of “polaron units”: frequencies are measured relative to a standard lattice frequency ω_p , time in units of ω_p^{-1} , energy $\hbar\omega_p$, lengths $\sqrt{\hbar/(m_0\omega_p)}$, temperature $\hbar\omega_p/k_B$ and mobility $e/(m_0\omega_p)$.

The dimensionless coupling constants α_j generalise the Fröhlich version to multiple phonon modes j and is given by

$$\alpha_j = \frac{\kappa_j^2}{\omega_p \omega_j} \frac{e^2}{\hbar} \left(\frac{m_0}{2\hbar\omega_p} \right)^{1/2}. \quad (2.249)$$

For a single phonon branch with frequency $\omega = \omega_p$ and strength κ then this coupling constant reduces to the familiar α ,

$$\alpha = \frac{\kappa^2}{\omega_p^2} \frac{e^2}{\hbar} \left(\frac{m_0}{2\hbar\omega_p} \right)^{1/2} = \left(\frac{1}{\epsilon_\infty} - \frac{1}{\epsilon_0} \right) \frac{e^2}{\hbar} \left(\frac{m_0}{2\hbar\omega_p} \right)^{1/2}. \quad (2.250)$$

The dielectric function

To compare to the experiment, Hellwarth and Biaggio seek an expression for the dielectric function $\epsilon(\Omega)$. They first obtain the classical solution for the magnetic vector potential $\tilde{\mathbf{A}}_C(\mathbf{q}, \Omega)$ and find that it obeys the equation of motion

$$\frac{1}{4\pi} \left(\frac{\Omega^2}{c^2} - q^2 \right) \tilde{\mathbf{A}}_C(\mathbf{q}, \Omega) - i \frac{\Omega}{c} \tilde{\mathbf{P}}^{\text{Tr}}(\mathbf{q}, \Omega) = 0. \quad (2.251)$$

By substituting the classical solution for $\tilde{\mathbf{P}}_C^{\text{Tr}}(\mathbf{q}, \Omega)$ in Eq. (2.236) into the equation of motion for $\tilde{\mathbf{A}}_C(\mathbf{q}, \Omega)$ in Eq. (2.251) they find that the classical transverse solutions must also obey (for all \mathbf{q})

$$\left[\frac{1}{4\pi} \left(\frac{\Omega^2}{c^2} - q^2 \right) + \frac{\Omega^2}{c^2} \frac{\alpha(\Omega)}{1 - (4\pi/3)\alpha(\Omega)} \right] \tilde{\mathbf{A}}_C(\mathbf{q}, \Omega) = 0, \quad (2.252)$$

from which they obtain the Lorentz-Lorenz relation for the dielectric function $\epsilon(\Omega)$,

$$\epsilon(\Omega) = n^2(\Omega) = \frac{1 + (8\pi/3)\alpha(\Omega)}{1 - (4\pi/3)\alpha(\Omega)}, \quad (2.253)$$

where $n(\Omega) = qc/\Omega$ is the refractive index.

Obtaining a single effective phonon frequency

Hellwarth and Biaggio use the mobility result from FHIP combined with Ōsaka's temperature-dependent variational parameters. To do this, they reduce the many infrared longitudinal phonon mode frequencies to a single effective frequency. To do this, they first compare their athermal effective action in Eq. (2.248) to the thermal effective action derived by Ōsaka in Eq. (2.144). From this comparison, they see that the inclusion of multiple phonon modes converts the influence functional phase Φ (Eq. (2.178)) to a sum over terms differing only in the phonon frequencies ω_j and coupling constants α_j

$$\Phi = -\frac{\hbar^2}{2\sqrt{2}\pi^2} \sum_j \alpha_j r_j \omega_j^2 \int_0^\infty dt \int_0^\infty dt' \int d^3\mathbf{q} \left\{ D_{\omega_j}(t-t') \left(\frac{e^{i\mathbf{q} \cdot [\mathbf{r}(t)-\mathbf{r}(t')]} }{q^2} - \frac{e^{i\mathbf{q} \cdot [\mathbf{r}'(t)-\mathbf{r}'(t')]} }{q^2} \right) - D_{\omega_j}^*(t-t') \left(\frac{e^{i\mathbf{q} \cdot [\mathbf{r}(t)-\mathbf{r}'(t')]} }{q^2} - \frac{e^{i\mathbf{q} \cdot [\mathbf{r}'(t)-\mathbf{r}'(t')]} }{q^2} \right) \right\}. \quad (2.254)$$

In [21], they propose two schemes, labelled ‘A’ and ‘B’, to reduce this expression to a single term with an effective frequency ω_{eff} and an effective coupling constant κ_{eff} . They then take the “polaron frequency” to be equal to this effective frequency $\omega_p = \omega_{\text{eff}}$.

In the first scheme, ‘A’, they seek an effective time kernel $H_{\text{eff}}(t)$ defined by,

$$H_{\text{eff}}(t) \sim \alpha_{\text{eff}} D_{\omega_{\text{eff}}}(t) \quad (2.255)$$

which has the properties

$$H_{\text{eff}}(0) = \sum_{j=1}^m H_j(0). \quad (2.256)$$

This is fulfilled by taking,

Hellwarth ‘A’ Scheme Effective Phonon Mode

$$\frac{\kappa_{\text{eff}}^2}{\omega_{\text{eff}}} \coth\left(\frac{\hbar\omega_{\text{eff}}\beta}{2}\right) = \sum_{j=1}^m \frac{\kappa_j^2}{\omega_j} \coth\left(\frac{\hbar\omega_j\beta}{2}\right), \quad (2.257)$$

and,

$$\frac{dH_{\text{eff}}(t)}{dt} \Big|_{t=0} = \sum_{j=1}^m \frac{dH_j(t)}{dt} \Big|_{t=0}. \quad (2.258)$$

This requires,

$$\kappa_{\text{eff}}^2 = \sum_{j=1}^m \kappa_j^2. \quad (2.259)$$

The second scheme, ‘B’, seeks to find the single effective frequency ω_{eff} and coupling constant κ_{eff} to match,

$$\int_0^{\hbar\beta} dt H_{\text{eff}}(it) = \sum_{j=1}^m \int_0^{\hbar\beta} dt H_j(it), \quad (2.260)$$

where they now used the imaginary-time kernel $H(it)$. They found that this expression is fulfilled by,

Hellwarth ‘B’ Scheme Effective Phonon Mode

$$\frac{\kappa_{\text{eff}}^2}{\omega_{\text{eff}}^2} = \sum_{j=1}^m \frac{\kappa_j^2}{\omega_j^2}. \quad (2.261)$$

The second scheme also requires that,

$$\frac{dH_{\text{eff}}(it)}{dt} \Big|_{t=0} = \sum_{j=1}^m \frac{dH_j(it)}{dt} \Big|_{t=0} \quad (2.262)$$

which also requires,

$$\kappa_{\text{eff}}^2 = \sum_{j=1}^m \kappa_j^2. \quad (2.263)$$

CHAPTER 2 - BACKGROUND

Despite considering temperature dependence, the final result of the second ‘B’ scheme is independent of temperature as the temperature terms cancel.

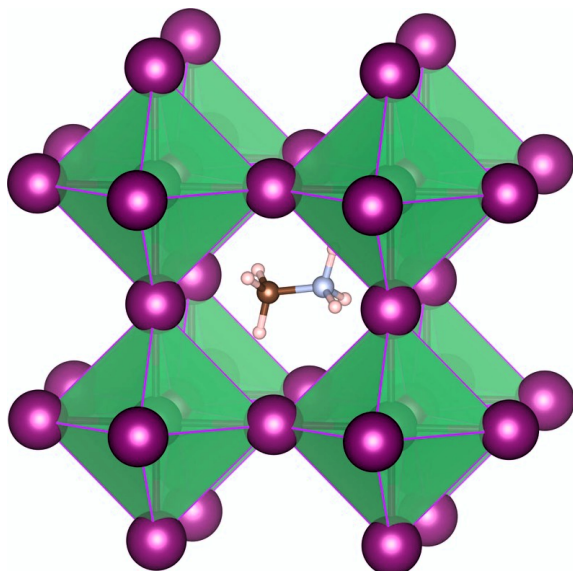


Figure 2.11: Reprinted from ref. [20]. Crystal structure of methylammonium lead iodide ($\text{CH}_3\text{NH}_3\text{PbI}_3$) perovskite, referred to here as ‘MAPI’. The green octahedra represents the lead (Pb) atoms at the centre, coordinated by iodine (I) atoms at the vertices. The methylammonium (CH_3NH_3^+) organic cation occupies the spaces between the PbI_3 frameworks, interacting with the inorganic lattice.

2.4 Material Case Studies

2.4.1 Methylammonium Lead Halide Perovskite

Methylammonium lead iodide (MAPI, $\text{CH}_3\text{NH}_3\text{PbI}_3$) is a hybrid organic-inorganic perovskite that has gained significant attention for its remarkable optoelectronic properties, making it a leading material in perovskite solar cells. MAPI crystallises in a perovskite structure (see Fig. 2.11) with the general formula ABX_3 , where A is the organic methylammonium (MA) cation, B is the lead (Pb) cation, and X is the iodide (I) anion. This material exhibits excellent light absorption, long charge carrier diffusion lengths, and high power conversion efficiency in photovoltaic devices. This has driven substantial research into its structural, thermal, and electronic properties.

The structural behaviour of MAPI is temperature-dependent, exhibiting three distinct crystallographic phases: orthorhombic, tetragonal, and cubic. At low temperatures, MAPI adopts an orthorhombic structure, transitions to a tetragonal phase at moderate temperatures, and further transitions into a cubic structure at high temperatures, typically above 327 K. These phase transitions are critical to the material’s properties, as they affect the symmetry, lattice dynamics, and the alignment of the MA cations within the perovskite cage, which, in turn, influence its optoelectronic characteristics.

In the study by Brivio et al. [20], the lattice dynamics and vibrational spectra of MAPI in its orthorhombic, tetragonal, and cubic phases were analysed using first-principles density functional theory (DFT) calculations. The study focused on understanding how the vibrational modes and phonon interactions evolve across the different phases and how these dynamics contribute to the stability and performance of MAPI in optoelectronic applications.

In the orthorhombic phase (below ~ 160 K), the MA cations are highly ordered, and the structure is relatively rigid, resulting in distinct vibrational modes characteristic of low symmetry. As the temperature increases and MAPI transitions into the tetragonal phase (around 160–327 K), the MA cations become more dynamically disordered, allowing for greater rotational freedom. This leads to softening specific phonon modes and lowering the vibrational energy. The study found that in the tetragonal phase, the vibrational spectra show a mix of soft lattice modes and strong coupling between the MA cations and the Pb-I cage.

In the cubic phase, the MA cations exhibit near-complete rotational disorder at high temperatures. The cubic symmetry increases the MA cations' rotational freedom within the Pb-I framework, resulting in further phonon softening and highly anharmonic lattice vibrations. The cubic phase is highly dynamic, with significant coupling between the organic cation motions and the inorganic lattice. Brivio et al. [20] highlighted that this dynamic disorder plays a crucial role in stabilising the cubic phase and impacts the material's electronic properties, such as its bandgap, which slightly changes with temperature.

The vibrational spectra for each phase were analysed in detail to understand the phonon modes contributing to the structural stability and thermal properties of MAPI. The study revealed that the softening of low-frequency phonon modes, particularly in the tetragonal and cubic phases, is associated with the material's propensity for dynamic disorder, affecting the performance of perovskite-based devices. Specifically, the MA cations' dynamic behaviour and the resulting lattice fluctuations can influence charge carrier recombination, affecting the efficiency and stability of solar cells.

2.4.2 Rubrene Organic Crystal

Rubrene, a polycyclic aromatic hydrocarbon, is a well-known organic semiconductor recognized for its high charge-carrier mobility and superior performance in organic field-effect transistors (OFETs) and organic light-emitting diodes (OLEDs). With a chemical formula of $C_{42}H_{28}$, rubrene's molecular structure consists of four fused phenyl rings. Its exceptional intrinsic mobility, exceeding $10\text{ cm}^2V^{-1}s^{-1}$ in single-crystal form, makes it one of the most efficient organic materials for electronic devices.

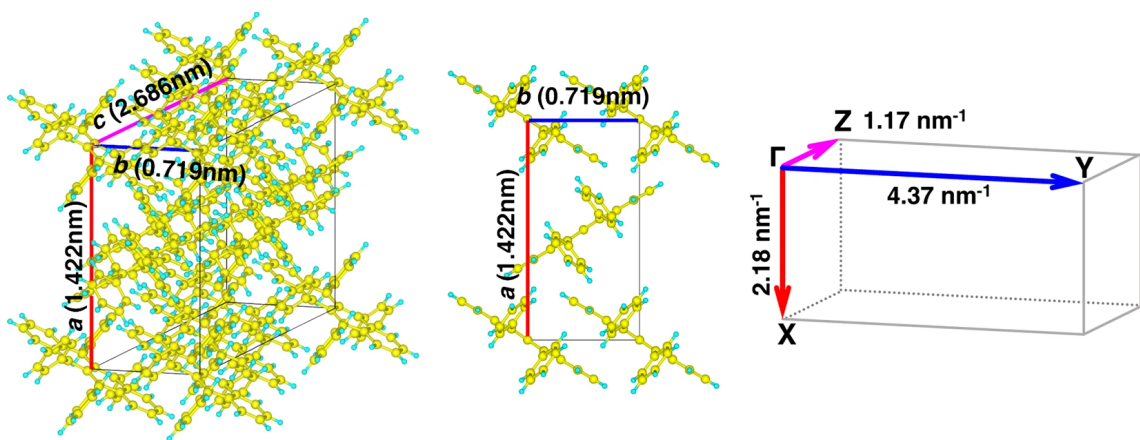


Figure 2.12: Reprinted from ref. [73]. Crystal structure of rubrene showing its orthorhombic unit cell parameters. The unit cell dimensions are $a = 1.422 \text{ nm}$, $b = 0.719 \text{ nm}$, and $c = 2.686 \text{ nm}$. The diagrams highlight the layered molecular arrangement within the unit cell, with the corresponding reciprocal lattice vectors displayed on the right, indicating spatial periodicity in the X, Y, and Z directions.

Rubrene's charge transport properties are highly anisotropic, meaning its mobility depends on the crystallographic direction. This anisotropy is deeply rooted in its crystal packing, where rubrene molecules form π - π stacked columns, facilitating efficient one-dimensional charge transport along specific directions. Figure 2.12 illustrates the orthorhombic crystal structure of rubrene, highlighting the molecular arrangement and unit cell dimensions, which are critical to understanding its anisotropic behaviour. The figure shows how the π - π stacking occurs along the crystallographic axes, promoting high mobility in certain directions. Meanwhile, weaker van der Waals interactions along the perpendicular directions reduce mobility.

A key factor affecting rubrene's performance in electronic devices is electron-phonon coupling—the interaction between charge carriers (electrons or holes) and lattice vibrational modes (phonons). Strong electron-phonon coupling increases charge carrier scattering, thus reducing mobility. Understanding electron-phonon coupling is crucial for enhancing device efficiency in rubrene, where weak van der Waals forces dominate the intermolecular interactions. The study by Ordejón et al. [22] used ab initio calculations, including density functional theory (DFT), to explore how electron-phonon interactions influence rubrene's charge transport. It focused mainly on low-frequency phonon modes—intermolecular vibrations—that impact mobility.

The study revealed that electron-phonon coupling in rubrene is also anisotropic, with phonon modes coupling to charge carriers differently depending on the transport direction. Phonon modes associated with the π - π stacking direction, which facilitate efficient charge transport, exhibit weaker electron-phonon coupling compared to those in directions per-

pendicular to the stacking. This weaker coupling along the π -stacking direction preserves high carrier mobility, contributing to rubrene's outstanding performance in OFETs.

Low-frequency phonon modes, especially those related to intermolecular vibrations and molecular rotations, were identified as major contributors to electron-phonon coupling. These modes can distort the lattice, increasing charge carrier scattering. The study also showed that electron-phonon coupling in rubrene is weaker than in inorganic semiconductors. However, it still limits the maximum achievable mobility, particularly at higher temperatures where phonon activity increases. Furthermore, lattice dynamics in rubrene contributed to charge localisation effects, where stronger electron-phonon interactions at certain phonon frequencies trap charge carriers, further reducing mobility. This effect becomes more pronounced in disordered or polycrystalline rubrene due to the material's flexibility and weaker intermolecular forces.

2.5 Outlook for this Thesis

Chapter 2 introduced foundational methods for modelling polaron dynamics, focusing on Feynman's variational path integral approximation (FVA) [2] and the Fröhlich model [3]. The FVA offers a non-perturbative technique for approximating polaron properties by applying variational principles to a trial action, where a simple harmonic spring coupling models the interaction between an electron and a phonon bath. This was traditionally used in the Fröhlich polaron model, simplifying the electron-phonon interaction by considering a parabolic electron band and a single optical phonon mode. Alongside the FVA, the Feynman-Hellwarth-Iddings-Platzman (FHIP) [17] approximation has been used to extend FVA to calculate dynamic response functions, such as charge-carrier mobility. At the same time, the Devreese-Sitter-Goovaerts (DSG) [18] theory provides a framework for calculating optical conductivity.

Despite the utility of these models, several limitations restrict their applicability to real material systems. The Fröhlich model itself is a highly idealised representation of electron-phonon interactions, neglecting the complexities of multiple phonon modes, anisotropic and non-parabolic electronic band structures, and phonon dispersion that are present in technologically relevant materials, such as organic semiconductors and perovskites. Notably, the FVA and FHIP methods have not been extended to handle small polarons, which provide a more natural description of polarons in organic crystals where strong localised electron-phonon interactions and significant lattice distortions dominate. Small polaron models, such as the Holstein model [5, 6], account for these lattice effects and localised electron behaviour, making them more suitable for describing organic materials where lattice dynamics significantly affect charge transport.

Moreover, the FHIP mobility model and DSG theory of optical conductivity are further limited by their oversimplified treatment of the electron-phonon interaction. Both approaches assume the electron is initially in a nonphysical, factorised product state with the phonon bath, simplifying the analysis but introducing inaccuracies. Additionally, they do not incorporate phonon dispersion in the Feynman trial model, a critical aspect in many materials. For instance, while DSG predicts sharp phonon peaks in the optical conductivity due to Franck-Condon (FC) transitions and Relaxed Excited States (RES), these features do not align with the more precise results from Diagrammatic Monte Carlo (DMC) simulations. Mishchenko et al. [10] show significant discrepancies from the sharp peaks predicted by DSG, suggesting that these features may result from un converged solutions. Sels [72] also highlighted this issue, where he pointed out that the Jensen-Feynman inequality, central to FVA, cannot be used to precisely determine the optical absorption spectrum, further limiting the method's accuracy in predicting optical conductivity.

Furthermore, Hellwarth and Biaggio [21] illustrate a key limitation in applying FVA. While they extended the FHIP approach to account for multiple phonon modes in polar lattices, their model simplifies complex interactions by reducing them to a single effective phonon mode within the FVA framework. Though computationally expedient, this reduction fails to capture the full complexity of electron-phonon interactions in real materials, where multiple phonon branches with distinct characteristics contribute to the transport properties.

These limitations motivate the developments presented in the later chapters of this thesis. Chapter 3 introduces significant extensions to the FVA and FHIP methods to address these issues, particularly by incorporating more realistic descriptions of electron-phonon interactions in large and small polarons. The FVA framework is generalised to account for multimode phonon systems and anisotropic electron bands, moving beyond the simplified single-mode approaches used in earlier models. Additionally, applying the FVA to the Holstein model for small polarons in organic materials provides a more accurate description of polaronic dynamics in systems with critical lattice effects. These extended models are further validated by comparisons with DMC simulations, ensuring their accuracy for predicting mobility and optical conductivity in complex materials. Ultimately, these developments aim to overcome the limitations of the simpler methods discussed in Chapter 2, providing more robust theoretical tools for understanding polaron transport and optical properties in real-world systems.

CHAPTER 3

GENERALISING THE MATERIAL PATH INTEGRAL MODEL

Greensite “... in a sense God did hand us the exact wave function . . . - it’s a Feynman path integral, and the only question is . . . ”

Feynman “... how to do the integral, yeah!”

—Jeff Greensite and Richard Feynman, *Variational Calculations in Quantum Field Theory*, 1988

In this chapter, I focus on generalising the *model* path integral to more complicated systems beyond the original Fröhlich Hamiltonian. To extend the applicability of the variational method to more materials, I generalise the model path integral to multiple phonon modes in the Fröhlich Hamiltonian; lattice polaron as described by the Holstein Hamiltonian; general electron-phonon interactions for a (possibly anisotropic) parabolic-band electron; and many polarons using coherent-state path integrals.

3.1 Multiple Phonon Modes

IN simple polar materials with two atoms in the basis, the single triply-degenerate optical phonon branch is split by dielectric coupling into the singly-degenerate longitudinal-optical mode and double-degenerate transverse-optical modes. Only the longitudinal-optical mode is infrared active and contributes to the Fröhlich dielectric electron-phonon interaction.

The infrared activity of this mode drives the formation of the polaron. Similarly, in a more complex material, the range of infrared active modes contributes to the polaron stabilisation. This relationship is, however, slightly obscured by the algebra in Eq. (2.34), and instead, this electron-phonon coupling seems to emerge from bulk phenomenological quantities. The Pekar factor, $\frac{1}{\epsilon_\infty} - \frac{1}{\epsilon_0}$ being particularly opaque. Rearranging the Pekar factor as

$$\left(\frac{1}{\epsilon_\infty} - \frac{1}{\epsilon_0} \right) = \frac{\epsilon_j^{\text{ionic}}}{\epsilon_\infty \epsilon_0}, \quad (3.1)$$

we can now see that the Fröhlich α is proportional to the ionic dielectric contribution $\epsilon_j^{\text{ionic}}$, as would be expected from appreciating that this is the driving force for polaron formation.

3.1.1 Multimodal Fröhlich Hamiltonian

The relative static dielectric constant is composed out of the high-frequency optical component (from the response of the electronic structure), and then the THz scale vibrational motion of the ions, $\epsilon_0 = \epsilon_\infty + \sum_j \epsilon_j$. This vibrational contribution is typically calculated by summing the infrared activity of the individual harmonic modes as Lorentz oscillators [74]. This infrared activity can be obtained by projecting the Born effective charges along the dynamic matrix (harmonic phonon) eigenvectors. The overall dielectric function across the phonon frequency range can be written as

$$\epsilon_{\alpha\beta}^0(\omega) = \epsilon_{\alpha\beta}^\infty + \sum_j^{\text{modes}} \epsilon_{\alpha\beta j}^{\text{ionic}}(\omega) = \epsilon_{\alpha\beta}^\infty + \frac{4\pi e^2}{V_0} \sum_{j\nu\mu} \frac{\sum_{\alpha'} Z_{\alpha\alpha'}^{*\mu} u_{\mu j}^{\alpha'} \sum_{\beta'} Z_{\beta\beta'}^{*\nu} u_{\nu j}^{\beta'}}{(\omega_j^2 - \omega^2)} \quad (3.2)$$

where e is the electron charge, V_0 the unit cell volume, $Z_{\alpha\beta}^{*\nu}$ is the Born effective charge tensor at atom ν , $u_{\mu j}^\alpha$ is the dynamic matrix eigenvector at atom μ for the j th phonon branch, ω_j is the dispersionless LO phonon frequency for the j th phonon branch and ω is the reduced frequency.

Considering the isotropic case (and therefore picking up a factor of $\frac{1}{3}$ for the averaged interaction with a dipole) and expressing the static (zero-frequency) dielectric contribution in terms of the infrared activity of a mode, $\epsilon_j^{\text{ionic}}$ is,

$$\epsilon^{\text{ionic}}(\hat{q}) = \sum_j^{\text{modes}} \epsilon_j^{\text{ionic}}(\hat{q}) = \frac{4\pi e^2}{V_0} \sum_j^{\text{modes}} \frac{\left(\sum_{\nu\alpha\beta} q^\alpha Z_{\alpha\beta}^{*\nu} u_{\nu j}^\beta \right)^2}{q^2 \omega_j^2}. \quad (3.3)$$

This provides a clear route to defining α_j for individual phonon branches, with the simple constitutive relationship that $\alpha = \sum_j \alpha_j$,

$$|M_{\mathbf{q}}|^2 = \sum_j^{\text{modes}} \frac{4\pi\hbar(\hbar\omega_j)^{3/2}}{\sqrt{2m_0}V_0q^2} \alpha_j(\hat{q}) = \frac{2\pi\hbar}{V_0q^2} \sum_j^{\text{modes}} \frac{\omega_j \epsilon_j^{\text{ionic}}(\hat{q})}{\epsilon_{\infty}(\hat{q})\epsilon_0(\hat{q})} \quad (3.4)$$

where,

Multimode Fröhlich Dimensionless Coupling

$$\alpha_j = \frac{1}{4\pi\epsilon_0} \frac{\epsilon_j}{\epsilon_{\infty}\epsilon_0} \frac{e^2}{\hbar} \left(\frac{m_0}{2\hbar\omega_j} \right)^{\frac{1}{2}}. \quad (3.5)$$

This concept of decomposing α into constituent pieces associated with individual phonon modes is implicit in the effective mode scheme of Hellwarth and Biaggio (Eqs. (??) to (2.263)), and has also been used by Verdi, [75] and Devreese [53].

Verbist [75] proposed an extended Fröhlich model Hamiltonian in Eq. (2.38) with a sum over multiple (m) phonon branches,

Multimode Fröhlich Polaron Hamiltonian

$$\hat{H} = \frac{p^2}{2m_0} + \sum_{\mathbf{q},j} \hbar\omega_j b_{\mathbf{q},j}^\dagger b_{\mathbf{q},j} + \sum_{\mathbf{q},j} (M_{\mathbf{q},j} b_{\mathbf{k},j} e^{i\mathbf{q}\cdot\mathbf{r}} + M_{\mathbf{q},j}^* b_{\mathbf{q},j}^\dagger e^{-i\mathbf{q}\cdot\mathbf{r}}). \quad (3.6)$$

Here, the index j indicates the j th phonon branch. The interaction coefficient is given by,

$$M_{\mathbf{q},j} = i \frac{2\hbar\omega_j}{|\mathbf{q}|} \left(\sqrt{\frac{\hbar}{2m_0\omega_j}} \frac{\alpha_j \pi}{V_0} \right)^{1/2}, \quad (3.7)$$

with α_j as in Eq. (3.5).

3.1.2 Multiple Phonon Mode Path Integral

From the Multimodal Fröhlich Hamiltonian, we get the following extended model action to use within the Feynman variational theory,

$$S_j[\mathbf{r}(\tau)] = \frac{m_0}{2} \int_0^{\hbar\beta} d\tau \left(\frac{d\mathbf{r}(\tau)}{d\tau} \right)^2 - \frac{\hbar^{3/2}}{2\sqrt{2m_0}} \alpha_j \omega_j^{3/2} \int_0^{\hbar\beta} d\tau \int_0^{\hbar\beta} d\sigma \frac{D_{\omega_j}(\tau - \sigma)}{|\mathbf{r}(\tau) - \mathbf{r}(\sigma)|}. \quad (3.8)$$

where I introduce the reduced thermodynamic temperature for the j th phonon branch $\beta = 1/(k_B T)$. $D_{\omega_j}(\tau)$ is the phonon Green's function for a phonon with frequency ω_j ,

$$D_{\omega_j}(\tau) = n_{\omega_j} e^{\omega_j |\tau|} + (n_{\omega_j} + 1) e^{-\omega_j |\tau|}. \quad (3.9)$$

This form of action is consistent with Hellwarth and Biaggio's deduction that multiple phonon branches result in the interaction term simply becoming a sum over terms with phonon frequency ω_j and coupling constant α_j dependencies as shown in Eq. (2.248).

3.2 Lattice Polarons

Hans De Raedt and Ad Lagendijk [37, 38] derived the discrete path integral for a lattice polaron, which was then further developed by Pavel Kornilovitch [44–50]. Kornilovitch derived the continuous path integral limit of the lattice polaron and developed a Continuous-time Path Integral Monte Carlo method for calculating properties of small polarons, focusing on the Holstein model and a lattice version of the Fröhlich model (which allows for long-range electron-phonon coupling).

The path integral for the partition function of a system is a sum of all possible position and momentum paths in phase space. In the continuum large-polaron model, the sum over all momentum paths can be made as the momentum paths are continuous and unbounded, and the parabolic electronic dispersion is quadratic in momentum. Therefore, the corresponding momentum path integral is an evaluable Gaussian functional integral.

For the small lattice polaron, the electronic dispersion is that of a tight-binding model and is not quadratic. Likewise, the momentum and position paths are discrete, and the ‘path-integral’ is an infinite summation rather than a functional integral.

In the following section, I present the derivation of the discrete-time path integral for the Holstein model. I then take the continuous-time limit and show that the continuous-time path integral has the same form as the standard phase-space path integral but with the Holstein Hamiltonian.

3.2.1 Discrete-Time Path Integral

We begin with the Holstein Hamiltonian in a mixed representation:

$$\begin{aligned}
 H &= H_0 + H_1 + H_2, \\
 H_0 &= \frac{1}{2M} \sum_{i=1}^N p_i^2, \\
 H_1 &= \frac{M\omega_0^2}{2} \sum_{i=1}^N x_i^2 + g \sum_{n=1}^N x_n c_n^\dagger c_n, \\
 H_2 &= -J \sum_{i=1}^N c_i^\dagger c_{i+1} + c_{i+1}^\dagger c_i,
 \end{aligned} \tag{3.10}$$

the phonons are expressed in their momenta p_i and positions x_i where i labels the corresponding lattice site. M is the mass of one lattice site (here, we assume all of them to have the same mass), and ω_0 is the dispersionless phonon frequency where we assume to

have only one mode (i.e. Einstein mode). The electron description remains in terms of the creation and annihilation operators c_i^\dagger, c_i on a lattice-site i .

In deriving the path integral, a system's quantum statistical partition function may be obtained by inserting successive resolutions of identity within the definition of a quantum trace. In the limit of an infinite number of insertions, the Trotter-Suzuki expression [76, 77] gives a direct equality between this discretised partition function Z_M and the total partition function Z :

$$\begin{aligned} Z &\equiv \text{Tr}\left\{e^{-\beta H}\right\} = \lim_{M \rightarrow \infty} Z_M, \\ Z_M &= \text{Tr}\left\{\left[e^{-\Delta\tau H_0} e^{-\Delta\tau H_1} e^{\Delta\tau H_2}\right]^M\right\}, \end{aligned} \quad (3.11)$$

where $\Delta\tau = \beta/M$ is the amount of imaginary-time between time-slices.

For the case of a lattice polaron, we have the time-discretised partition function,

$$Z_M = c_1 \Delta\tau^{-\frac{MN}{2}} \sum_{\{r_j\}} \int \left\{ \prod_{j=1}^M \prod_{n=1}^N dx_{n,j} \right\} e^{S_{\text{ph}}} \prod_{l=1}^M I_{\Delta r_l}(2\tau J), \quad (3.12)$$

where $\Delta r_l = r_{l+1} - r_l$ is the change in the electron position across one time-slice and is an integer multiple of the lattice spacing a .

The discretised boson action is,

$$S_{\text{ph}} = \sum_{j=1}^M \sum_{n=1}^N \left(\frac{(\Delta x_{n,j})^2}{2\Delta\tau} + \frac{\Delta\tau\omega^2 x_{n,j}^2}{2} + g_H \Delta\tau x_{n,j} \delta_{n,r_j} \right). \quad (3.13)$$

The kinetic portion of the discretised action for the fermion on a lattice is,

$$I_{\Delta r_l}(z) = \frac{1}{N} \sum_{n=1}^N \cos\left(\frac{2\pi n \Delta r_l}{Na}\right) \exp\left(-z \cos\left(\frac{2\pi n}{N}\right)\right), \quad (3.14)$$

which is a discrete form of the modified Bessel function of the first-kind $I_m(z)$ [78, (10.32.3)] where here we have $m = \Delta r_l = r_{l+1} - r_l$ and $z = 2J\Delta\tau$. This becomes the normal modified Bessel function in the thermodynamic limit $N \rightarrow \infty$.

The bosonic integrals are Gaussian and so have closed-form expressions. By expanding the bosonic coordinates in Fourier modes,

$$x_{n,j} = \frac{1}{\sqrt{M}} \sum_{q=0}^{M-1} v_{n,j} \exp\left(\frac{2\pi jq}{M}\right), \quad (3.15)$$

we can diagonalise the bosonic action,

$$S_{\text{ph}} = \sum_{n=1}^N \sum_{q=0}^{M-1} \left(\frac{|\nu_{n,j}|^2}{\Delta\tau D_q^{-1}} + \frac{\Delta\tau g_H \nu_{n,q}}{\sqrt{M}} \sum_{j=1}^M \delta_{n,r_j} \exp\left(\frac{2\pi j q}{M}\right) \right), \quad (3.16)$$

where

$$D_q^{-1} = 1 - \cos\left(\frac{2\pi q}{M}\right) + \frac{\Delta\tau^2 \omega_0^2}{2}, \quad (3.17)$$

is the inverse of the free-phonon Green function. Integrating over $\nu_{n,q}$ gives,

$$\begin{aligned} Z_M &= c_2 Z_M^{ph} Z_M^{\text{el}}, \\ Z_M^{ph} &= \left(\prod_{q=0}^{M-1} D_q^{1/2} \right)^N, \\ Z_M^{\text{el}} &= \sum_{\{r_j\}} \left(\prod_{j=1}^M I_{\Delta r_j}(2\Delta\tau J) \right) \exp\left(\Delta\tau^2 \sum_{i=1}^M \sum_{j=1}^M F(i-j) \delta_{r_i, r_j}\right), \end{aligned} \quad (3.18)$$

where c_2 is just a collation of normalisation factors which will drop out of any expectation values and,

$$F(l) = \frac{\Delta\tau g_H^2}{4M} \sum_{q=0}^{M-1} D_q \cos\left(\frac{2\pi q l}{M}\right), \quad (3.19)$$

is the memory function that fully encodes the electron-lattice interaction over all imaginary times.

Now the kinetic portion of the action is

$$K_M[r_j] = \sum_{j=1}^M \ln \left\{ I_{\Delta r_j}(2J\Delta\tau) \right\}. \quad (3.20)$$

This path integral has no closed-form solution, even for a free electron. Regardless, we could choose the kinetic part of the trial action to be quadratic still, with an effective mass m_e ,

$$K_{M,\text{trial}}[r_j] = \frac{m_e}{2a^2} \sum_{j=1}^M \left(\frac{\Delta r_j}{\Delta\tau} \right)^2 \Delta\tau. \quad (3.21)$$

The quasi-particle mass term m_e is a variational parameter that minimises the difference between the trial and model actions. However, as the electron positions are discrete (restricted to the lattice positions), the trial path integral would be a discrete Gaussian sum,

not a Gaussian integral:

$$Z_{M,\text{trial}} \sim \sum_{\{r_j\}} \exp(K_{M,\text{trial}}[r_j]). \quad (3.22)$$

This sum has no closed-form solution and would have to be evaluated numerically, defeating my goal of using the Feynman variational method to leverage computationally efficient analytic solutions, and directly apply the FHIP theory.

Therefore, I will take the continuum limit since we aim to use the Feynman variational method. First, I go to the continuous-time limit of the Holstein path integral.

3.2.2 Continuous-Time Path Integral

To obtain the continuous-time limit of the partition function, we first explicitly remove the summation over N lattice sites from the kinetic action. Doing so, we find that we have a product of these lattice-site summations for each time slice,

$$Z_M^{\text{el}} = \frac{1}{(2N)^M} \sum_{\{r_j\}} \sum_{\{n_j\}} \exp \left\{ i \sum_{j=1}^M \frac{2\pi n_j}{Na} \Delta r_j - 2\Delta\tau J \sum_{j=1}^M \cos \left(\frac{2\pi n_j}{N} \right) \right\}, \quad (3.23)$$

where n_j now depends on j . I have used the fact that the kinetic action is even with respect to n and that $\cos(x) = (\exp(ix) + \exp(-ix))/2$ to change the limits of the n_j summations from $\{n_j \mid n_j \in [1, N]\}$ to $\{n_j \mid n_j \in [-N, N], n_j \neq 0\}$. Note that the summations over n_j exclude $n_j = 0$.

We now have a summation of all possible paths a particle can take on the lattice within M time-steps. From the kinetic action, we can see that $2\pi n_j/Na \equiv \Delta k_j$ plays the role of a discrete lattice-momenta multiplying the changes in the electron position Δr_j .

Our electronic partition function is in the form of a discrete phase-space path integral. Therefore, in the continuous-time limit $M \rightarrow \infty$ and $\Delta\tau \rightarrow 0$, the partition function may be written as

$$Z = C Z_{\text{ph}} \sum_{r(\tau)} \sum_{k(\tau)} \exp\{S_{\text{eff}}\}, \quad (3.24)$$

where C is the accumulation of normalisation factors. The positions $r(\tau)$ and lattice-momenta $k(\tau)$ are still restricted to N discrete values. The effective action is

$$\begin{aligned} S_{\text{eff}} &= K[k(\tau), r(\tau)] - V_{\text{eff}}[r(\tau)], \\ K &= -\frac{2J}{\hbar} \int_0^{\hbar\beta} d\tau \cos(ak(\tau)) + i \int_0^{\hbar\beta} d\tau k(\tau) \dot{r}(\tau), \\ V_{\text{eff}} &= \frac{g_H^2}{4\hbar} \int_0^{\hbar\beta} \int_0^{\hbar\beta} d\tau d\tau' D_{\omega_0}(\tau - \tau') \delta_{r(\tau), r(\tau')}, \end{aligned} \quad (3.25)$$

where the summations over j have become imaginary-time integrals and

$$\begin{aligned} \lim_{\Delta\tau \rightarrow 0} \{\Delta r_j\} &\rightarrow r(\tau), \\ \lim_{\Delta\tau \rightarrow 0} \{\Delta r_j / \Delta\tau\} &\rightarrow dr(\tau)/d\tau \equiv \dot{r}(\tau), \\ \lim_{\Delta\tau \rightarrow 0} \{\Delta k_j\} &\rightarrow k(\tau) \equiv 2\pi n(\tau)/Na. \end{aligned} \quad (3.26)$$

Here $D_{\omega_0}(\tau)$ is the thermal (imaginary-time) phonon Green's function. So far, we have derived the discrete-time Holstein path integral by starting with the Holstein Hamiltonian in a mixed representation, including phonon, electron-phonon coupling, and electronic components. We used the Trotter-Suzuki expression to discretise the quantum statistical partition function into a form suitable for path integral methods. We then expressed the partition function in terms of Bosonic and Fermionic actions, applied Gaussian integration to the Bosonic coordinates, and incorporated a variational trial action for the kinetic part of the path integral. Finally, we transitioned towards the continuum limit by reformulating the partition function in terms of continuous imaginary-time integrals, leading to an effective action that encapsulates the interactions and dynamics of the electron-phonon system.

3.2.3 Thermodynamic and Continuum Limits

In the thermodynamic limit $N \rightarrow \infty$, the summation over all discrete k paths becomes continuous and can be identified with the electron quasi-momentum $k(\tau)$. The discrete sums over k become continuous functional (path) integrals over quasi-momentum paths confined to the first Brillouin Zone.

$$Z = CZ_B \int_{r \in a\mathbf{Z}} \mathcal{D}r(\tau) \int_{k \in [-\frac{\pi}{a}, \frac{\pi}{a}]} \mathcal{D}k(\tau) e^{S_{\text{eff}}}. \quad (3.27)$$

The electron position is still restricted to the lattice, represented above by the set of integers, \mathbf{Z} , multiplied by the lattice constant, a .

In the continuum limit $a \rightarrow 0$, the electron position can take any real value $r \in \mathbf{R}$, and the momentum is unbounded, $k \in (-\infty, \infty)$. Here, I assume that $a \ll 1$ so that these conditions on the electron position and momentum are approximately satisfied.

This partition function is the standard representation of the phase-space path integral,

$$Z = C \int \mathcal{D}r(\tau) \int \mathcal{D}k(\tau) \exp \left\{ i \int_0^{\hbar\beta} d\tau k(\tau) \dot{r}(\tau) - \frac{1}{\hbar} \int_0^{\hbar\beta} d\tau H_{\text{eff}}[r(\tau), k(\tau)] \right\}, \quad (3.28)$$

where the Hamiltonian is the tight-binding Hamiltonian with an additional non-local effective interaction term,

Holstein Hamiltonian with an Effective Interaction

$$H_{\text{eff}} \approx 2J \cos(ak(\tau)) + g_H^2 \int_0^{\hbar\beta} d\tau' D_{\omega_0}(\tau - \tau') \delta_{r(\tau), r(\tau')} \quad (3.29)$$

We could have started with this phase-space path integral, substituted in the Holstein Hamiltonian and performed the path integration over the lattice coordinates to arrive at the same result. Therefore, we may substitute a higher-dimensional tight-binding Hamiltonian to generalise to higher dimensions. The effective interaction term will be similar but with a generalised Kronecker-Delta dependent on vector positions $\mathbf{r}(\tau)$.

3.2.4 The Effective Mass (Parabolic-Band) Approximation

We still face difficulty in applying the variational method. The presence of the cosine in the kinetic action (from the tight-binding band structure) renders the overall action non-convex, even in imaginary time, so Jensen's inequality does not hold.

To make progress, we assume that $ak \ll 1$ and thereby make a parabolic (effective-mass) approximation. Since we have made the continuum approximation, this is a reasonable assumption. From the cosine form of the tight-binding band structure, and using the small-angle approximation $\cos(\theta) = 1 - \theta^2$,

$$\cos(ak(\tau)) \approx 1 - \frac{a^2[k(\tau)]^2}{2}, \quad (3.30)$$

In one dimension, the kinetic action is approximated by,

$$K = 2J\hbar\beta - \frac{1}{2m_0} \int_0^{\hbar\beta} d\tau [k(\tau)]^2 + i \int_0^{\hbar\beta} d\tau k(\tau) \dot{r}(\tau), \quad (3.31)$$

where the band-mass is $m_0 = \hbar^2/2Ja^2$. By making this approximation, the functional integral over $k(\tau)$ is the same Gaussian form as for a free particle and can be solved exactly.

Overall, I get a parabolic-band Holstein effective action in n -dimensions,

Parabolic Holstein Model Action

$$S_{\text{eff}}^{(H)} = \frac{m_0}{2} \int_0^{\hbar\beta} d\tau \dot{\mathbf{r}}^2 - \frac{g_H^2}{\hbar} \int_0^{\hbar\beta} \int_0^{\hbar\beta} d\tau d\tau' D_{\omega_0}(\tau - \tau') \delta_{\mathbf{r}(\tau), \mathbf{r}(\tau')} \quad (3.32)$$

I have excluded the $2nJ\hbar\beta$ term since this is just the band-minimum energy absorbed into the normalisation factor C for the partition function.

I reiterate my approximations to derive this action, which I will use in my numeric results. First, I went to the thermodynamic limit, which means I do not expect this model to capture any finite-size effects. Second, I make the continuum approximation so that the electron paths can be assumed to be continuous and the electron quasi-momenta unbounded. Third, I approximate the tight-binding (cosine) band with a parabolic band.

This final effective-mass approximation means there is a missing contribution when I integrate across reciprocal space; I expect it to break down entirely near the Brillouin-Zone boundaries. Nonetheless, the model has a genuinely short-range electron-phonon coupling. Upon integrating the phonons, the short-range electron-phonon coupling presents a non-local point-like interaction of the electron with itself through imaginary time, which is only non-zero when the electron crosses its prior path.

Since the effective model has a Kronecker-delta-like interaction, the *phonon* momentum is (correctly) bounded to remain within the first Brillouin zone. We can see this from the integral representation of the Kronecker delta,

$$\delta_{r,r'} = \frac{a}{2\pi} \int_{-\pi/a}^{\pi/a} dq e^{iq(r-r')} \quad (3.33)$$

Therefore, the effective model includes a correct lattice description regarding the phonons.

We can generalise the Kronecker-delta to arbitrary dimensions n in Cartesian coordinates

$$\delta_{\mathbf{r}, \mathbf{r}'} = \frac{V_n}{(2\pi)^n} \int_{-\pi/a}^{\pi/a} d\mathbf{q} e^{i\mathbf{q} \cdot (\mathbf{r} - \mathbf{r}')} \quad (3.34)$$

where, for example, for a cubic unit cell, $V_3 = a^3$. Alternatively, the methodology used by Feynman for the Fröhlich Hamiltonian uses a Spherical coordinate representation of the Kronecker-delta in n -dimensions:

$$\delta_{\mathbf{r}, \mathbf{r}'} = \frac{V_n S_{n-1}}{(2\pi)^n} \int_0^{\Lambda_n} dq q^{n-1} e^{iq(r-r')} \quad (3.35)$$

where Λ_n is some momentum cutoff, I assume that the system has rotational invariance so that the angular components of $\mathbf{q} \cdot \mathbf{r}$ can be integrated over to give $S_{n-1} = 2\pi^{n/2}/\Gamma(n/2)$ the surface-“area” of an n -dimensional sphere where $\Gamma(x)$ is the Gamma function.

From this work on the Holstein model, we now have everything we need to establish the machinery for a general variational method for polarons—one that we can apply to an arbitrary electron-phonon Hamiltonian.

3.3 The General Parabolic Polaron

The Hamiltonian for a general polaron model [79] can be written in second-quantisation form and momentum-basis as,

General Polaron Hamiltonian

$$H = \sum_{\mathbf{k}} \epsilon_{\mathbf{k}} c_{\mathbf{k}}^\dagger c_{\mathbf{k}} + \sum_{\mathbf{q}} \hbar \omega_{\mathbf{q}} b_{\mathbf{q}}^\dagger b_{\mathbf{q}} + \sum_{\mathbf{k}, \mathbf{q}} M_{\mathbf{k}, \mathbf{q}} c_{\mathbf{k}+\mathbf{q}}^\dagger c_{\mathbf{k}} (b_{-\mathbf{q}}^\dagger + b_{\mathbf{q}}) \quad (3.36)$$

where $\epsilon_{\mathbf{k}}$ is the electron band energy for momentum \mathbf{k} , $c_{\mathbf{k}}^\dagger$ and $c_{\mathbf{k}}$ are the electron creation and annihilation operators for an electron with momentum \mathbf{k} , $\omega_{\mathbf{q}}$ is the phonon frequency for momentum \mathbf{q} , $b_{\mathbf{q}}^\dagger$ and $b_{\mathbf{q}}$ are the phonon creation and annihilation operators for a phonon with momentum \mathbf{q} , $M_{\mathbf{k}, \mathbf{q}}$ is the electron-phonon coupling matrix which describes the strength of the interaction.

For a model describing a parabolic band electron linearly coupled to harmonic phonons, the path integral over the phonon operators is Gaussian and can be evaluated analytically. The resultant electron action describes a temporally non-local self-interaction acting on the electron,

$$S[\mathbf{r}(\tau)] = \frac{m_0}{2} \int_0^{\hbar\beta} d\tau \dot{\mathbf{r}}^2(\tau) - \frac{1}{\hbar} \int_0^{\hbar\beta} d\tau \int_0^{\hbar\beta} d\tau' D_{\omega_0}(\tau - \tau') \Phi[\mathbf{r}(\tau), \mathbf{r}(\tau')], \quad (3.37)$$

where $D_{\omega_0}(\tau)$ is the imaginary-time thermal phonon propagator and self-interaction functional is,

$$\Phi[\mathbf{r}(\tau), \mathbf{r}(\tau')] = \sum_{\mathbf{q}} |M_{\mathbf{q}}|^2 \rho_{\mathbf{q}}[\mathbf{r}(\tau)] \rho_{-\mathbf{q}}[\mathbf{r}(\tau')]. \quad (3.38)$$

Here $\rho_{\mathbf{q}}[\mathbf{r}(\tau)] = e^{i\mathbf{q}\cdot\mathbf{r}(\tau)}$ is the density for the electron derived from corresponding first-quantisation density operator and $M_{\mathbf{q}}$ is a general electron-phonon coupling matrix element. The polaron self-interaction functional is where the specific electron-phonon coupling presents itself in this machinery.

For the Fröhlich model, the self-interaction functional is,

$$\begin{aligned} \Phi_F[\mathbf{r}(\tau), \mathbf{r}(\tau')] &= \sum_{\mathbf{q}} \frac{g_F^2}{V_n q^{n-1}} e^{i\mathbf{q}\cdot(\mathbf{r}(\tau)-\mathbf{r}(\tau'))}, \\ &= g_F^2 \int \frac{d^n q}{(2\pi)^n} \frac{e^{i\mathbf{q}\cdot(\mathbf{r}(\tau)-\mathbf{r}(\tau'))}}{q^{n-1}}, \\ &= \frac{g_F^2 S_{n-1}}{(2\pi)^n} \frac{1}{|\mathbf{r}(\tau) - \mathbf{r}(\tau')|}, \end{aligned} \quad (3.39)$$

where $S_{n-1} = 2\pi^{n/2}/\Gamma(n/2)$ is the hypervolume of the unit $(n-1)$ -sphere and the phonon momentum is unbounded, $0 \leq q < \infty$. The Fröhlich model makes the continuum approximation of the lattice, $\lim_{V_n \rightarrow \infty} V_n^{-1} \sum_{\mathbf{q}} \sim \int d^n q / (2\pi)^n$, where V_n is the n -dimensional crystal volume.

For the Holstein model in n isotropic dimensions (n -dimensional hypercube) self-interaction functional is

$$\begin{aligned}\Phi_H [\mathbf{r}(\tau), \mathbf{r}(\tau')] &= g_H^2 \sum_{\mathbf{q}} e^{i\mathbf{q} \cdot (\mathbf{r}(\tau) - \mathbf{r}(\tau'))}, \\ &= g_H^2 a^n \int \frac{d^n q}{(2\pi)^n} e^{i\mathbf{q} \cdot (\mathbf{r}(\tau) - \mathbf{r}(\tau'))}, \\ &= g_H^2 \delta_{\mathbf{r}(\tau)\mathbf{r}(\tau')},\end{aligned}\tag{3.40}$$

where δ_{ij}^n is the n -dimensional Kronecker Delta functional and $-\pi/a \leq q \leq \pi/a$. This could be adapted to any Brillouin-Zone geometry. We could also use Spherical-Coordinates as in the Fröhlich model where instead $0 \leq q \leq \Lambda_n$ with Λ_n is a momentum cutoff given by the radius of an n -ball with volume $\frac{(2\pi)^n}{V_n}$:

$$\Lambda_n = 2\sqrt{\pi} \left(V_n \Gamma \left(\frac{n}{2} + 1 \right) \right)^{1/n}.\tag{3.41}$$

3.3.1 General Phonon-Band Polarons

We can now develop the variational path integral method for this generalised polaron action and specialise to a specific case by using an explicit expression for the electron-phonon coupling in the self-interaction functional as we have above for the Fröhlich and Holstein models. I will assume that we are only working with one parabolic-band electron so that the self-interaction functional contains depends on the electron position only through the term $e^{i\mathbf{q} \cdot (\mathbf{r}(\tau) - \mathbf{r}(\tau'))}$. If this is true, we can use Feynman's derivation of the variational path integral method.

I would also like to discuss the potential for direct numeric evaluation of the momentum integrals. The momentum integral can be evaluated numerically, either by substituting an explicit form for the electron-phonon matrix $|M_{\mathbf{q}}|^2$ and phonon dispersion $\omega_{\mathbf{q}}$ and then using a numerical integration algorithm like Gauss-Kronod. Many closed-forms for the electron-phonon matrix $|M_{\mathbf{q}}|^2$ and phonon dispersion $\omega_{\mathbf{q}}$ are known, such as for acoustic phonons, Bogoliubov-Fröhlich polaron, impurities etc. We could use such an analytic expression in our integrals, which may then admit closed-form solutions or be evaluated numerically.

For real materials, we could instead use electronic structure methods to evaluate $|M_{\mathbf{q}}|^2$ and $\omega_{\mathbf{q}}$ on a standard reciprocal space grid. These would then enter the variational method as

arrays evaluated at the electron/hole band-extremum (e.g. the gamma-point $\mathbf{k} = \mathbf{0}$). Our q -integrands above would become tensor products concatenated over all q -points.

3.3.2 Effective-mass anisotropy

In the degenerate anisotropic uni-axial case, I propose to naïvely incorporate the anisotropy into the Feynman approach (which is one-dimensional due to the underlying isotropy of the Fröhlich Hamiltonian) by treating the two directions independently with effective masses m_{\perp} and m_{\parallel} .

I then use the variational principle separately in each direction to find the variational parameters $v_{\perp/\parallel}$ and $w_{\perp/\parallel}$ that give the lowest upper-bound to the ground-state energy $E_{\perp/\parallel}$ for each direction.

The variational parameters can then be used to obtain the effective polaron masses M_{\perp} and M_{\parallel} using Eq. (2.129) and polaron radii R_{\perp} and R_{\parallel} using Eq. (2.131).

To make comparisons with the isotropic case, I define an effective ground-state energy by taking the arithmetic mean of the uniaxial components of the ground-state energy,

$$E = \frac{2E_{\perp} + E_{\parallel}}{3}. \quad (3.42)$$

Similarly, I define an effective radius of the anisotropic polaron by finding the radius of a sphere with the same volume as the ellipsoidal anisotropic polaron. This means taking the geometric mean of the uni-axial components of the polaron radius,

$$R = \left(R_{\perp}^2 R_{\parallel} \right)^{1/3}. \quad (3.43)$$

The two averaging methods are justified as they only give a ground-state energy and polaron radius consistent with those evaluated by the original model [2] when applied to an isotropic material.

3.4 Many Polaron Theory

So far, I have derived path integrals using the eigenvalues of the position and momenta operators of the Polaron Hamiltonian. However, there is another construction based on the eigenvalues of the Fock-Space annihilation operators resulting in the so-called *Coherent-State Path Integrals* (CSPI) [80].

Intuitively, CSPI allows us to construct a path integral directly from the second-quantised form of the Hamiltonian rather than the first-quantised form. Statistically, this corresponds to constructing the *grand-canonical* ensemble partition function in the path integral formalism compared to the canonical ensemble partition function we have been using previously. Thus, using CSPIs allows us to construct path integrals for systems with varying particle numbers and may allow us to generalise the variational principle to non-quadratic kinetic action.

Excluding electronic spin degrees-of-freedom and the potential for multiple phonon branches, we may write the general polaron Hamiltonian:

$$H_{\text{polaron}} = \sum_{\mathbf{k}n} \epsilon_{\mathbf{k}n} c_{\mathbf{k}n}^\dagger c_{\mathbf{k}n} + \sum_{\mathbf{q}j} \hbar\omega_{\mathbf{q}j} b_{\mathbf{q}j}^\dagger b_{\mathbf{q}j} + \sum_{\mathbf{k}mn, \mathbf{q}j} M_{\mathbf{k}mn, \mathbf{q}j} c_{\mathbf{k}+ \mathbf{q}m}^\dagger c_{\mathbf{k}n} \left(b_{-\mathbf{q}j}^\dagger + b_{\mathbf{q}j} \right) \quad (3.44)$$

The coherent state path integral for the polaron Hamiltonian H_{polaron} :

$$Z_{\text{polaron}} = \int D[\bar{c}, c] \int D[\bar{b}, b] e^{-S_{\text{el}}[\bar{c}, c] - S_{\text{ph}}[\bar{b}, b] - S_{\text{el-ph}}[\bar{c}, c, \bar{b}, b]} \quad (3.45)$$

with the free-electron action:

$$S_{\text{el}} [\bar{c}, c] = \sum_{\mathbf{k}n} \int_0^{\hbar\beta} d\tau \bar{c}_{\mathbf{k}n}(\tau) [\partial_\tau - \epsilon_{\mathbf{k}n} - \mu] c_{\mathbf{k}n}(\tau) \quad (3.46)$$

the free-phonon action:

$$S_{\text{ph}} [\bar{b}, b] = \sum_{\mathbf{q}j} \int_0^{\hbar\beta} d\tau \bar{b}_{\mathbf{q}j}(\tau) [\partial_\tau - \omega_{\mathbf{q}j}] b_{\mathbf{q}j}(\tau) \quad (3.47)$$

and the electron-phonon interaction action:

$$\begin{aligned} S_{\text{el-ph}} [\bar{c}, c, \bar{b}, b] &= \sum_{\mathbf{k}mn, \mathbf{q}j} M_{\mathbf{k}mn, \mathbf{q}j} \int_0^{\hbar\beta} d\tau \bar{c}_{\mathbf{k}+ \mathbf{q}m}(\tau) c_{\mathbf{k}n}(\tau) b_{\mathbf{q}j}(\tau) \\ &\quad + \sum_{\mathbf{k}mn, \mathbf{q}j} M_{\mathbf{k}mn, \mathbf{q}j} \int_0^{\hbar\beta} d\tau \bar{b}_{-\mathbf{q}j}(\tau) \bar{c}_{\mathbf{k}+ \mathbf{q}m}(\tau) c_{\mathbf{k}n}(\tau) \end{aligned} \quad (3.48)$$

The phonon contribution to the action is quadratic and may be integrated to give:

$$Z_{\text{ph}}^0 \exp \left\{ \frac{1}{2} \sum_{\mathbf{q}, \mathbf{k}, \mathbf{k}'} M_{\mathbf{k}, \mathbf{q}} M_{\mathbf{k}', \mathbf{q}}^* \int_0^{\hbar\beta} \int_0^{\hbar\beta} d\tau d\tau' \bar{c}_{\mathbf{k}}(\tau) c_{\mathbf{k}-\mathbf{q}}(\tau) D_{\omega_{\mathbf{q}}}^0(\tau - \tau') \bar{c}_{\mathbf{k}'-\mathbf{q}}(\tau') c_{\mathbf{k}'}(\tau') \right\} \quad (3.49)$$

where $D_{\omega_{\mathbf{q}}}^0(\tau)$ is the bare phonon kernel for a harmonic oscillator and $Z_{\text{ph}}^0 = \det [D^0]^{-1/2}$ is the non-interacting phonon partition function.

The coherent state path integral for the polaron Hamiltonian H_{polaron} :

$$Z_{\text{polaron}} = \int D\bar{c} Dc \exp \left\{ -S_{\text{polaron}} [\bar{c}(\tau), c(\tau)] \right\} \quad (3.50)$$

with action:

$$\begin{aligned} S_{\text{polaron}} [\bar{c}(\tau), c(\tau)] &= \sum_{\mathbf{k}} \int_0^{\hbar\beta} d\tau \bar{c}_{\mathbf{k}}(\tau) [\partial_{\tau} - \epsilon_{\mathbf{k}} - \mu] c_{\mathbf{k}}(\tau) \\ &\quad - \frac{1}{2} \sum_{\mathbf{k}, \mathbf{q}} |M_{\mathbf{k}, \mathbf{q}}|^2 \int_0^{\hbar\beta} \int_0^{\hbar\beta} d\tau d\tau' \bar{c}_{\mathbf{k}}(\tau) c_{\mathbf{k}+\mathbf{q}}(\tau) D_{\omega_{\mathbf{q}}}^0(\tau - \tau') \bar{c}_{\mathbf{k}+\mathbf{q}}(\tau') c_{\mathbf{k}}(\tau') \end{aligned} \quad (3.51)$$

CHAPTER 4



IMPROVING THE TRIAL PATH INTEGRAL MODEL AND VARIATIONAL APPROXIMATION

[The] [m]ost important part of doing physics is the knowledge of approximation.

—Lev Landau, *Unknown, Unknown*

In this chapter, I extend the trial polaron Lagrangian beyond Feynman's original spring-mass harmonic model (while retaining the analytic solution) to increase the accuracy of the variational approximation and the predicted response functions. These extensions include developing the variational method for the multimode Fröhlich polaron and small Holstein polaron, as well as generalising the trial action to couple the electron to multiple spring-masses, a general bath spectral-function with self-consistent equations, general many-body polarons using the Independent Boson Model (IBM) as a trial action, and extending the Feynman-Jensen inequality with an infinite series of cumulant corrections.

4.1 Multiple Phonon Mode Variational Solution

4.1.1 Multiple Phonon Mode Free Energy

The energy of the trial system S_0 and the internal energy $\langle S_0 \rangle_{S_0}$ remains unchanged and is as presented by Osaka [30]. However, as the model action S has been generalised to

include multiple phonon modes, I derive a multiple phonon mode extension to the internal energy of the model action,

Multiple Phonon Mode Model Action Expectation

$$\langle S \rangle_{S_0} = \sum_{j=1}^m \frac{\hbar\alpha_j\omega_j^2}{\sqrt{\pi}} \int_0^{\hbar\beta} d\tau \frac{D_{\omega_j}(\tau)}{\sqrt{G(\tau)}}, \quad (4.1)$$

These are similar to Hellwarth and Biaggio's single mode versions, but with the single effective phonon frequency ω_0 substituted with the branch dependent phonon frequencies ω_j . There are m with index j phonon branches.

Summing F_0 in Eq. (4.19a), $\langle S_0 \rangle_{S_0}$ in Eq. (4.1), and $\langle S \rangle_{S_0}$ in Eq. (4.19b), I obtain a generalised variational inequality for the contribution to the free energy of the polaron from the j th phonon branch with phonon frequency ω_j and coupling constant α_j , and 2 variational parameters v and w ,

$$F(\beta) \leq F_0 - \langle S_0 \rangle_{S_0} - \sum_{j=1}^m \langle S_j \rangle_{S_0}. \quad (4.2)$$

I obtain variational parameters v and w that minimise the free energy expression and will be used in evaluating the polaron mobility. Considering only one phonon branch ($m = 1$) simplifies to Ōsaka's free energy. Feynman's original athermal version can be obtained by taking the zero-temperature limit ($\beta \rightarrow \infty$).

4.2 Lattice Polaron Variational Solution

There are two main difficulties for the small lattice polaron. First, the electronic dispersion is that of a tight-binding model and is not quadratic. Second, the momentum and position paths are discrete, and the ‘path-integral’ is an infinite summation rather than a functional integral. Therefore, the corresponding ‘path-integral’ is a non-Gaussian summation rather than a typical Gaussian functional integral. To apply the Feynman variational approximation, the trial path integral must have the same measure as the original system, but since the paths are discrete, even if the trial path integral were Gaussian, a Gaussian sum does not have a closed-form expression, unlike a Gaussian integral. Even if we approximate the paths to be continuous to bypass this issue, unlike for the Fröhlich model, we cannot choose the kinetic action of the trial path-integral to be identical to the Holstein kinetic action as it is non-Gaussian. We would then have an additional term, the difference between the trial and actual kinetic actions. To apply the Feynman-Jensen inequality, we need this term to be convex; this is no longer guaranteed.

To circumnavigate these issues in pursuit of tangible results, I instead chose to approximate the Holstein kinetic action with an approximate parabolic form with an effective band mass, much like the Fröhlich model. I then allow the electron paths to be unconstrained such that the momentum integrals for the electron are unbounded and can be evaluated to give the standard Gaussian kinetic action. I could keep the momentum integrals bounded to the first Brillouin zone and still have a closed-form expression for the kinetic action; however, in addition to the standard Gaussian form, there are error functions that make it unclear how the resulting path integral could be evaluated - if it is even possible. By making these approximations, it is possible to follow the usual variational procedure with the same trial action as the Fröhlich model. I should note that the Holstein electron-phonon interaction is still treated correctly, and the phonon quasi-momenta is still confined to the first Brillouin zone.

By following the standard procedure for the Fröhlich model, I derive an approximate variational inequality for the lattice polaron free energy that fully accounts for the lattice electron-phonon integral despite allowing the electron not to be confined to individual lattice sites. Despite the latter approximation, this model still captures many typical features of small lattice polaron.

A critical difference between the Holstein and Fröhlich models is the domain of the reciprocal-space integral. For the Fröhlich model, this is over all of reciprocal space and has spherical symmetry, whereas the Holstein model integral is bounded (by the error function) to the first Brillouin Zone (and formally reflects the crystal symmetry). Physically,

this is an ultraviolet momentum cutoff due to the discrete lattice in the Holstein model, without which the integrals (in all spatial dimensions) catastrophically diverge.

The Fröhlich model also diverges in 1D, whereas the Holstein converges for all dimensionalities.

I provide results for the abstract Holstein model and compare these results to Ragni's Diagrammatic Monte Carlo results and the Fröhlich Hamiltonian. I look at one- to three-dimensional models.

The Fröhlich model is of academic interest as most continuum materials are relatively isotropic. For the Holstein model, organic semiconductors are often highly anisotropic, and the varying behaviour is of direct technical interest.

To characterise the models, I consider:

1. The energy and character of the athermal quasi-particle (polaron) state versus coupling.
2. The temperature dependence of the polaron mobility and polaron energy.
3. The frequency dependence of the polaron mobility and optical conductivity.

4.2.1 Athermal Holstein Polaron

I start with the zero temperature polaron in 1D, 2D and 3D for the parabolic Holstein model and the three-dimensional Fröhlich model. I present the models in a unitless presentation where the adiabaticity $\gamma = 1$ ($\omega_0 = J = 1$). I also assume that two dimensionless coupling alpha parameters, α_H and α_F , used in the parabolic Holstein and Fröhlich models produce similar physical regimes within either model for a point of comparison. Therefore, I will compare these two models to a single alpha parameter $\alpha \equiv \alpha_H = \alpha_F$.

Polaron Variational Parameters

In Fig. (4.1) are the polaron variational parameters v and w of the Holstein and Fröhlich polarons as a function of the electron-phonon dimensionless coupling parameter α . The Holstein model has a noticeably different variational solution than the Fröhlich model, with a distinct discontinuity in three dimensions. This transition is smoother for one- and two-dimensions and occurs at $\alpha \approx 2n$, where n is the dimensionality of the model. I interpret this transition as physically corresponding to forming a small-polaron state.

In both models, w asymptotes to $\omega_0 = 1$ at large electron-phonon coupling α , with a more abrupt transition in the Holstein model. The v parameters have a different strong coupling dependency on α . In the Fröhlich model at large α , $v_F \sim \alpha^2$ whereas in the Holstein

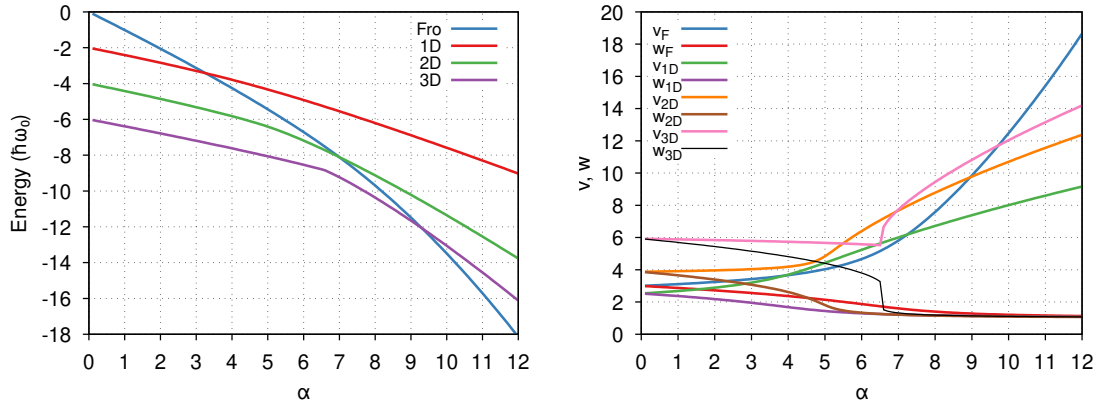


Figure 4.1: **Left:** The electron-phonon coupling α dependence of the ground-state energy E (in units of $\hbar\omega_0$) of the 3D Fröhlich model (blue) and the parabolic Holstein model in 1D (red), 2D (green) and 3D (purple). **Right:** The electron-phonon coupling α dependence of the variational parameters v and w (in units of ω_0) for the 3D Fröhlich model (v blue, w red) and the parabolic Holstein model in 1D (v green, w purple), 2D (v orange, w brown) and 3D (v pink, w black).

model $v_H \sim \sqrt{\alpha}$. Another noticeable difference is the weak coupling limit ($\alpha \rightarrow 0$) where the Fröhlich model parameters asymptotes are $v_F = w_F = 3$, whereas Holstein are $v_H = w_H \approx 2n$.

Polaron Ground-state Energy

Fig. (4.1) is the variational solution for the free energy of the one-, two- and three-dimensional parabolic Holstein model (with $J = \omega_0 = 1$ in this unitless presentation) with respect to the electron-phonon coupling parameter α . I also compare the variational solution to the three-dimensional Fröhlich model ($\omega_0 = 1$).

The athermal polaron energy at $\alpha = 0$ corresponds to the band extrema for either model. In the Fröhlich model, this is zero $E_F(\alpha = 0) = 0$, and for the Holstein model, this is $E_H(\alpha = 0) = 2nJ$ with n the dimensionality. The athermal energy in the Fröhlich model is approximately linear for small alpha $E_F \sim -\hbar\omega_0\alpha$ and quadratic for large alpha $E_F \sim -\hbar\omega_0\alpha^2$. The athermal energy in the parabolic Holstein model is also linear for small alpha $E_H + 2nJ \sim -J\alpha/2$ (which is the same for all dimensions), but the large alpha behaviour is not quadratic and is instead linear and dependent on the number of dimensions $E_H + 2nJ \sim -Jn\alpha$.

In Fig. (4.3), I now vary the adiabaticity $\gamma = \hbar\omega_0/J = 0.1, 0.3$ and 0.5 in the parabolic Holstein model for dimensions $n = 1, 2$ and 3 and compare these variational results with diagrammatic Monte-Carlo (DMC) results provided by Ragni (for values of $\alpha = 0$ to 5 which are shown more closely in the inset figures). Our variational solutions agree with Ragni's DMC results for all dimensions and adiabaticities. The adiabaticity affects the lower alpha energy of the polaron below the small polaron transition around $\alpha = 2n$

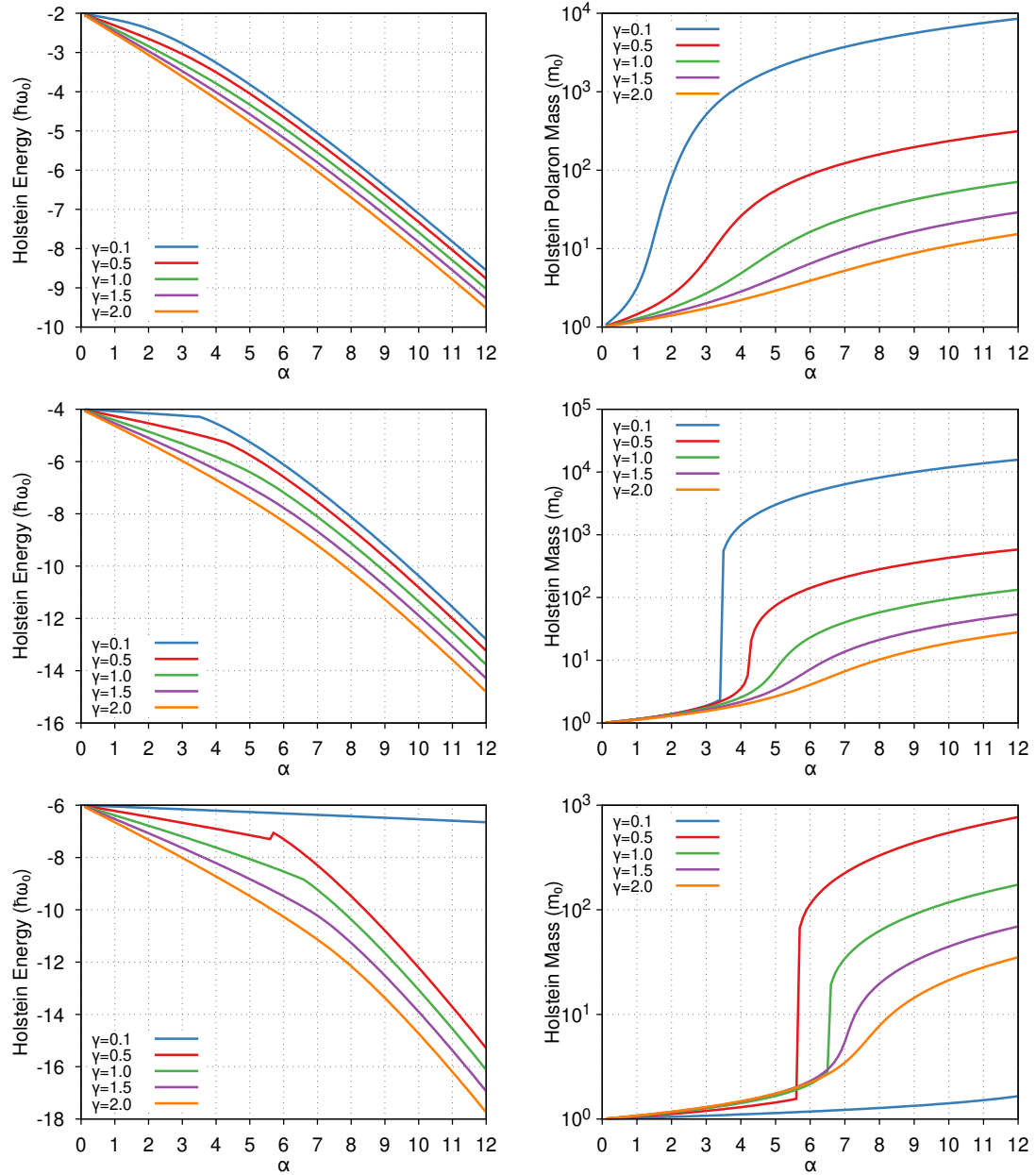


Figure 4.2: The electron-phonon coupling α and adiabticity $\gamma = \hbar\omega/J$ (for $\gamma = 0.1, 0.5, 1.0, 1.5$ and 2.0) dependence of the parabolic Holstein ground-state energy in 1D (top-left), 2D (middle-left) and 3D (bottom-left), and polaron mass in 1D (top-right), 2D (middle-right) and 3D (bottom-right).

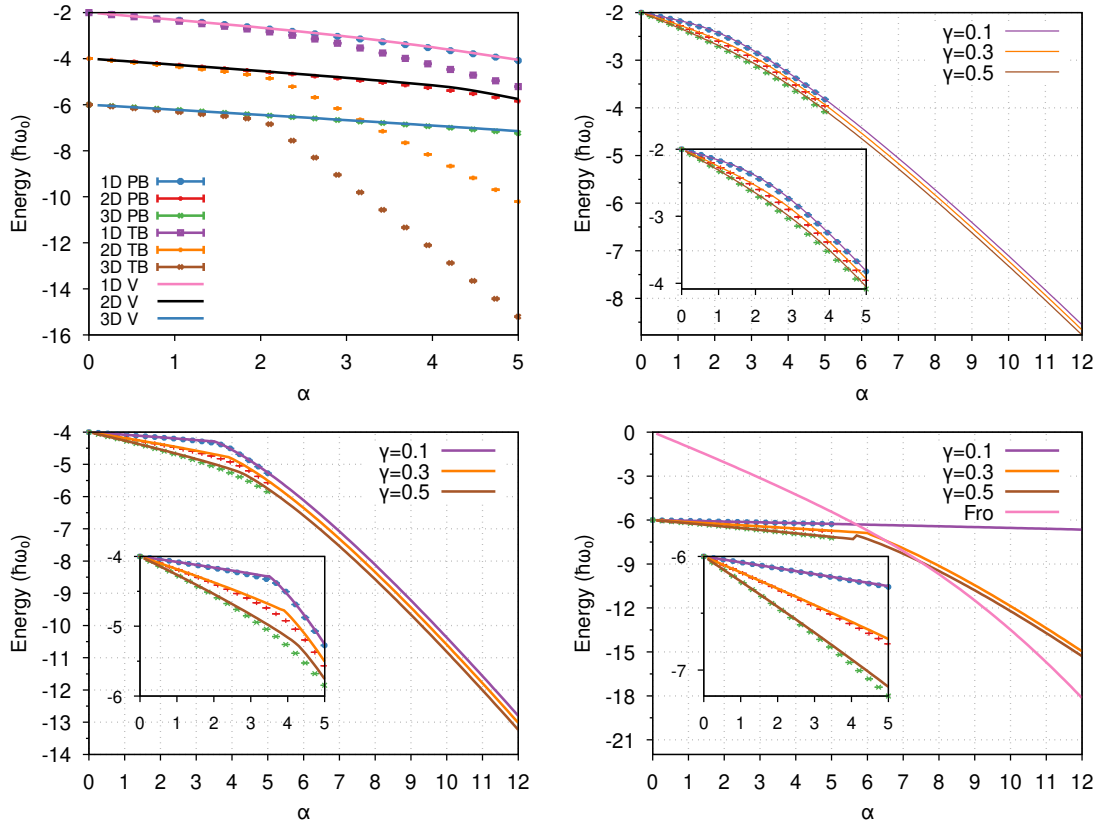


Figure 4.3: Polaron binding energy (in units of $\hbar\omega_0$) for the Holstein model with respect to the electron-phonon dimensionless coupling parameter α and adiabaticity $\gamma = \hbar\omega_0/J$.

Top left: Comparison between the variational solution for the parabolic Holstein model (1D pink, 2D black and 3D light blue) to the DMC solution for the parabolic Holstein model (1D blue points, 2D red points and 3D green points) and tight-binding Holstein model (1D purple points, 2D orange points and 3D brown points).

Top right: Comparison for the 1D parabolic Holstein model between the variational solution ($\gamma = 0.1$ purple, 0.3 orange and 0.5 brown) and the DMC solution ($\gamma = 0.1$ blue points, 0.3 red points and 0.5 green points).

Bottom left: Comparison for the 2D parabolic Holstein model between the variational solution ($\gamma = 0.1$ purple, 0.3 orange and 0.5 brown) and the DMC solution ($\gamma = 0.1$ blue points, 0.3 red points and 0.5 green points).

Bottom right: Comparison for the 3D parabolic Holstein model between the variational solution ($\gamma = 0.1$ purple, 0.3 orange and 0.5 brown) and the DMC solution ($\gamma = 0.1$ blue points, 0.3 red points and 0.5 green points). I also include the variational solution to the 3D Fröhlich model for comparison (pink).

and increases the sharpness of this transition for smaller adiabaticity. We note that in three dimensions with $\gamma < 1$, this transition momentarily *reduces* the polaron binding energy in the variational solution, which is not replicated in the DMC results – more DMC data for $\alpha > 5$ may be required to determine if this is an artefact of the parabolic Holstein model or just the variational solution. In Fig. (4.3) we also show (bottom-right sub-figure) a comparison of the DMC results for the *parabolic-band* Holstein model with the original *tight-binding-band* Holstein model where we see that the two models predict similar energies below the small-polaron transition, but the tight-binding model shows a sharper, dimension-independent transition at $\alpha = 2$ and larger polaron-binding energy above this transition.

4.2.2 Thermal polarons

I now look at the finite temperature dependence of the polaron in two- and three-dimensions for the parabolic Holstein model (top sub-figures) and the three-dimensional Fröhlich model (bottom sub-figure), for values of the electron-phonon coupling $\alpha = 0.1, 2, 4, 6, 8, 10, 12$. Here we also take a unitless presentation with $\omega_0 = J = 1$.

Polaron Free Energy

Fig. (4.4) shows the temperature dependence of the polaron free energy. In the parabolic Holstein model, the polaron-free energy transitions from the ground-state energy at very low temperatures to $E_H = -2nJ - \alpha nJ$ at large temperatures with the transition point occurring around the Debye temperature $T_D = \hbar\omega_0/k_B$. Comparatively, whilst the Fröhlich model also shows a transition around the Debye temperature, above this temperature, the polaron free energy increases as $E_F \sim -T^{1/2}$ without bound.

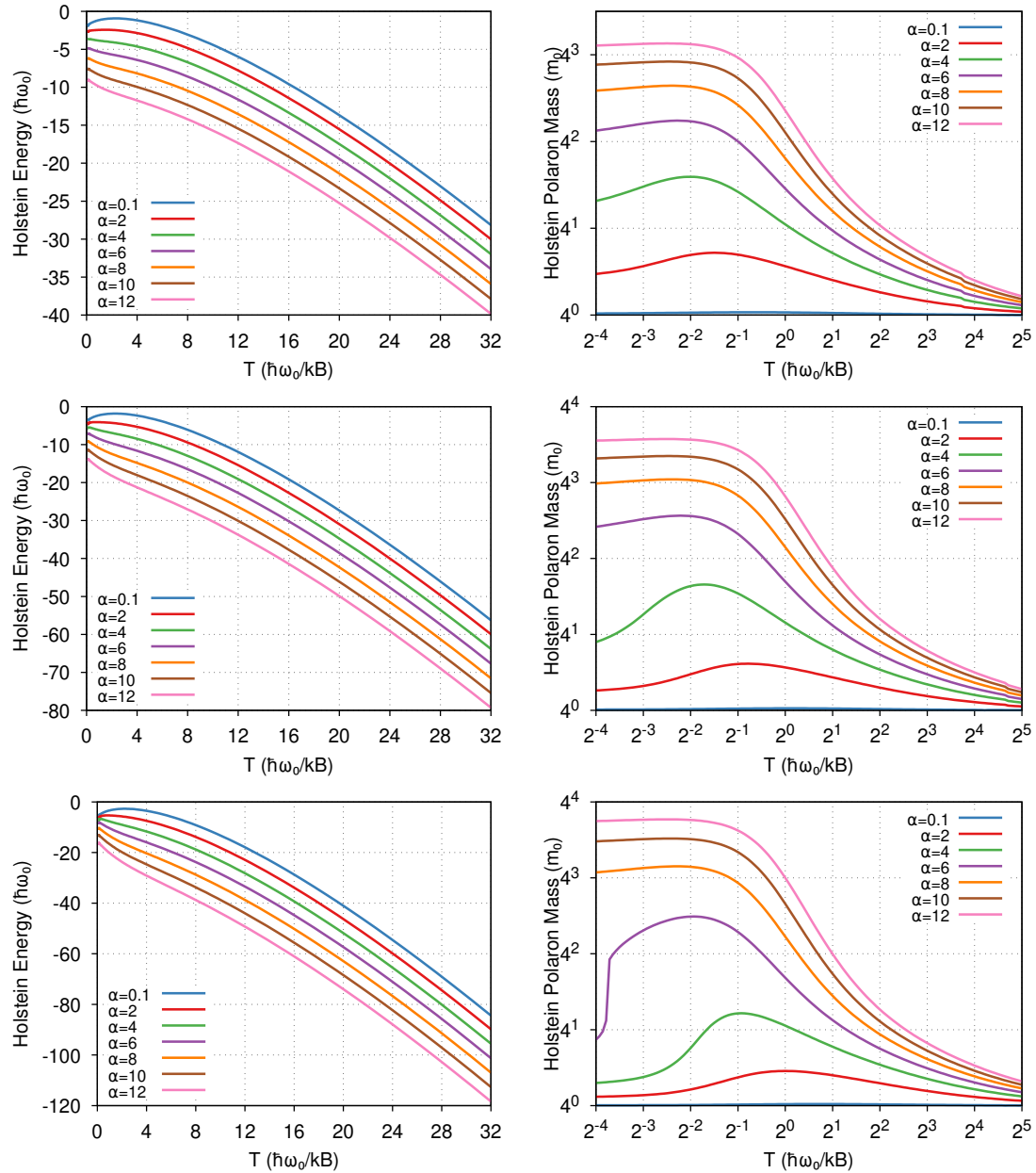


Figure 4.4: Polaron binding energy (left) and effective mass (right) for the Holstein model in 1D (top), 2D (middle) and 3D (bottom) with respect to temperature (in units of the phonon frequency $\hbar\omega_0$), for values of the Holstein electron-phonon coupling $\alpha = 0.1, 2, 4, 6, 8, 10, 12$

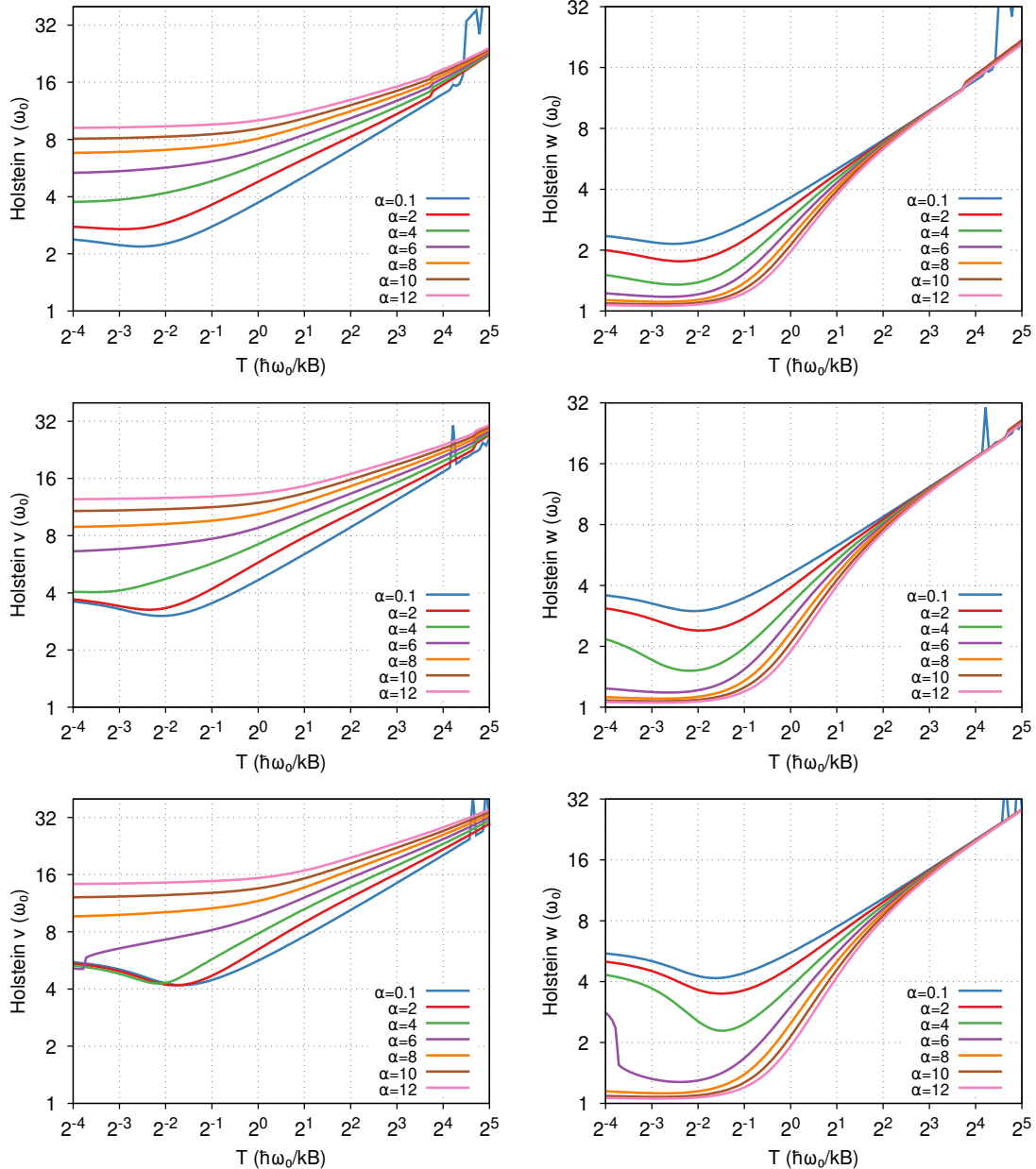


Figure 4.5: Polaron variational parameters v (left) and w (right) for the Holstein model in 1D (top), 2D (middle) and 3D (bottom) with respect to temperature (in units of the phonon frequency $\hbar\omega_0$), for values of the Holstein electron-phonon coupling $\alpha = 0.1, 2, 4, 6, 8, 10, 12$

4.3 The General Parabolic Polaron Variational Solution

Following the procedure for the Fröhlich model [2, 4], we derive a variational inequality for a general *parabolic-band* polaron, moving the model-specific evaluation into the self-interaction function.

The variational method for the polaron developed by Feynman gives a lower upper-bound to the polaron free energy,

$$\begin{aligned} F &\leq F_0(\beta) - \frac{1}{\hbar\beta} \langle S_{\text{pol}} - S_0 \rangle_{S_0}, \\ &\leq F_0(\beta) - \frac{1}{\hbar^2\beta} \int_0^{\hbar\beta} d\tau \int_0^{\hbar\beta} d\tau' D_{\omega_0}(\tau - \tau') \langle \Phi_{\text{pol}} - \Phi_0 \rangle_{S_0}, \end{aligned} \quad (4.3)$$

where the expectation $\langle O \rangle_{S_0}$ is defined as

$$\langle O \rangle_{S_0} \equiv \frac{\int \mathcal{D}^3 r(\tau) O e^{-S_0[\mathbf{r}(\tau)]}}{\int \mathcal{D}^3 r(\tau) e^{-S_0[\mathbf{r}(\tau)]}}. \quad (4.4)$$

Here $S_0[\mathbf{r}(\tau)]$ is a trial action that is chosen to best approximate the polaron model-action $S_{\text{pol}}[\mathbf{r}(\tau)]$, with the requirement that the path integral for S_0 can be analytically evaluated. The trial-action is typically chosen to be at most quadratic in the electron coordinate $\mathbf{r}(\tau)$ for this reason. We use the original 1955 quasi-particle trial action of Feynman,

$$S_0[\mathbf{r}(\tau)] = \frac{m_0}{2} \int_0^{\hbar\beta} d\tau \dot{\mathbf{r}}^2(\tau) + \frac{1}{\hbar} \int_0^{\hbar\beta} d\tau \int_0^{\hbar\beta} d\tau' D_w(\tau - \tau') \Phi_0 [\mathbf{r}(\tau), \mathbf{r}(\tau')], \quad (4.5)$$

where the trial self-interaction functional is a simple quadratic,

$$\Phi_0[\mathbf{r}(\tau), \mathbf{r}(\tau')] = \hbar w \kappa [\mathbf{r}(\tau) - \mathbf{r}(\tau')]^2. \quad (4.6)$$

The κ and w variational parameters have a direct interpretation as the spring-constant and oscillation frequency of a quasi-particle. We have integrated the interaction with the phonon-field and replaced it with a fictitious mass coupled to our electron by a spring, representing the phonon drag. This trial model (the quasi-particle) is often reparameterised in terms of v and w variational parameters where $\kappa = m_0(v^2 - w^2)$.

The expectation value of the trial action $\langle S_0 \rangle_{S_0}$ and the free energy of the trial system $F_0(\beta)$ are as given by Ōsaka [30],

$$\langle S_0 \rangle_{S_0} = \frac{n\hbar\beta}{4} \frac{v^2 - w^2}{v} \left(\frac{2}{v\hbar\beta} - \coth \left(\frac{v\hbar\beta}{2} \right) \right), \quad (4.7)$$

$$F_0(\beta) = \frac{n}{\beta} \log \left(\frac{w \sinh(\hbar\beta v/2)}{v \sinh(\hbar\beta w/2)} \right). \quad (4.8)$$

All the expectation values in the variational expression can be evaluated from $\langle e^{i\mathbf{q} \cdot (\mathbf{r}(\tau) - \mathbf{r}(\tau'))} \rangle_{S_0}$, which for the trial model has a closed-form expression ,

$$\langle e^{i\mathbf{q} \cdot (\mathbf{r}(\tau) - \mathbf{r}(\tau'))} \rangle_{S_0} = \exp \left[-\hbar q^2 G(\tau - \tau') / 2m_0 \right], \quad (4.9)$$

where the imaginary-time thermal polaron Green's function $G(\tau)$ is given by,

$$G(\tau) = \tau \left(1 - \frac{\tau}{\hbar\beta} \right) + \frac{v^2 - w^2}{v^3} \left[D_v(0) - D_v(\tau) - v\tau \left(1 - \frac{\tau}{\hbar\beta} \right) \right], \quad (4.10)$$

where D is the phonon propagator from Eq. (2.2.1).

In n -dimensions, from Eq. (4.3) we have,

$$F \leq F_0(\beta) + \frac{1}{\beta} \langle S_0 \rangle_0 - \frac{2}{\hbar} \sum_{\mathbf{q}} |M_{\mathbf{q}}|^2 \int_0^{\hbar\beta} d\tau D_{\omega_0}(\tau) e^{-\hbar q^2 G(\tau)/2m_0}, \quad (4.11)$$

where we have used,

$$\int_0^{\hbar\beta} d\tau \int_0^{\hbar\beta} d\tau' f(|\tau - \tau'|) \sim 2\hbar\beta \int_0^{\hbar\beta} d\tau f(\tau), \quad (4.12)$$

which is valid when the Hamiltonian for the system is time-translation invariant and β is large.

To evaluate the remaining phonon-momentum integral, we can either evaluate it using Cartesian coordinates or we can transform the q -space summation into a spherical integral over the n -dimensional ball,

$$\begin{aligned} \langle \Phi_{\text{pol}} \rangle_{S_0} &= \sum_{\mathbf{q}} |M_{\mathbf{q}}|^2 e^{-\hbar q^2 G(\tau)/2m_0}, \\ &= \frac{VS_{n-1}}{(2\pi)^n} \int_0^R dq |M_q|^2 q^{n-1} e^{-\hbar q^2 G(\tau)/2m_0}, \end{aligned} \quad (4.13)$$

with $S_{n-1} = 2\pi^{n/2}/\Gamma(n/2)$ the hypervolume of the unit $(n-1)$ -sphere and R the radius of the ball.

For the Fröhlich self-interaction functional, we have,

$$\begin{aligned}\langle \Phi_F \rangle_{S_0} &= \frac{g_F^2 S_{n-1}}{(2\pi)^n} \int_0^\infty dq e^{-\hbar q^2 G(\tau)/2m_0}, \\ &= \alpha_F \hbar^2 \omega_0^{3/2} \frac{\Gamma(\frac{n-1}{2})}{2\Gamma(\frac{n}{2})} \frac{1}{\sqrt{G(\tau)}}.\end{aligned}\quad (4.14)$$

The variational inequality for the Fröhlich model is,

$$F_F \leq F_0(\beta) - \frac{1}{\beta} \langle S_0 \rangle_{S_0} - \alpha_F \hbar \omega_0^{3/2} \frac{\Gamma\left(\frac{n-1}{2}\right)}{\Gamma(\frac{n}{2})} \int_0^{\hbar\beta} d\tau \frac{D_{\omega_0}(\tau)}{\sqrt{G(\tau)}}. \quad (4.15)$$

For the parabolic Holstein model with a hypercubic lattice (i.e. cubic in 3D), the self-interaction functional is,

$$\begin{aligned}\langle \Phi_H \rangle_{S_0} &= g_H^2 \left[\frac{a}{2\pi} \int_{-\frac{\pi}{a}}^{\frac{\pi}{a}} dq e^{-\hbar q^2 G(\tau)/2m_0} \right]^n, \\ &= 2n\alpha_H J \hbar \omega_0 \left[\frac{\operatorname{erf}(\pi \sqrt{G(\tau)J/\hbar})}{\sqrt{4\pi G(\tau)J/\hbar}} \right]^n,\end{aligned}\quad (4.16)$$

where $\gamma = \hbar\omega_0/J$ is the adiabaticity.

Substituting the Holstein self-interaction functional into Eq. (4.3) gives the variational inequality for the Holstein model as

$$F_H \leq F_0(\beta) + \frac{1}{\beta} \langle S_0 \rangle_{S_0} - n\alpha_H J \omega_0 \int_0^{\hbar\beta} d\tau D_{\omega_0}(\tau) \left[\frac{\operatorname{erf}(\pi \sqrt{G(\tau)J/\hbar})}{\sqrt{4\pi G(\tau)J/\hbar}} \right]^n \quad (4.17)$$

4.4 Multiple Fictitious Particles

The first way to improve the trial action is to couple the electron to more than one fictitious particle, each with their respective mass and spring-constant that enter as multiple pairs of variational parameters in the model. This has been done before for one additional fictitious mass [81].

I have extended Feynman's trial action to represent a particle (the charge-carrier) coupled to n massive fictitious particles. This results in $2 \times n$ variational parameters (one for the coupling strength and one for the coupling frequency of each fictitious particle).

The generalised polaron trial action is,

$$S_0[\mathbf{r}(\tau)] = \frac{m_0}{2} \int_0^{\hbar\beta} d\tau \left(\frac{d\mathbf{r}(\tau)}{d\tau} \right)^2 + \frac{1}{8} \sum_{p=1}^n \kappa_p w_p \int_0^{\hbar\beta} d\tau \int_0^{\hbar\beta} d\sigma D_{w_p}(\tau - \sigma) (\mathbf{r}(\tau) - \mathbf{r}(\sigma))^2. \quad (4.18)$$

Here κ_p is the spring constant associated with the p th fictitious particle, and w_p is the corresponding oscillation frequency. The solution to the partition function for this action was evaluated in [82].

Following Feynman, I extend the trial free energy F_{S_0} and the expectation of the trial action $\langle S_0 \rangle_{S_0}$ to the case of multiple fictitious particles,

$$F_{S_0} = \frac{3}{\beta} \left[\sum_{p=1}^n \log \left(\frac{v_p \sinh(w_p \hbar\beta/2)}{w_p \sinh(v_p \hbar\beta/2)} \right) + \frac{1}{2} \log \left(2\pi\hbar^2\beta/m_0 \right) \right], \quad (4.19a)$$

$$\langle S_0 \rangle_{S_0} = \frac{3}{4} \sum_{p,q=1}^n \frac{C_{pq}}{v_q w_p} \left(\coth \left(\frac{v_q \hbar\beta}{2} \right) - \frac{2}{v_q \hbar\beta} \right), \quad (4.19b)$$

where,

$$C_{pq} = w_p \frac{\kappa_p h_q}{v_q^2 - w_p^2}, \quad (4.20a)$$

$$\kappa_p = \left(v_p^2 - w_p^2 \right) \prod_{\substack{q=1 \\ q \neq p}}^n \frac{v_q^2 - w_p^2}{w_q^2 - w_p^2}, \quad (4.20b)$$

$$h_p = \left(v_p^2 - w_p^2 \right) \prod_{\substack{q=1 \\ q \neq p}}^n \frac{w_q^2 - v_q^2}{v_q^2 - v_q^2}. \quad (4.20c)$$

C_{pq} are the components of a generalised $(n \times n)$ matrix version of Feynman's C variational parameter. The cross (off-diagonal) terms give the coupling (interaction) between the fictitious particles.

A generalisation of the polaron (quasiparticle) Green function is,

$$G(\tau) = \tau \left(1 - \frac{\tau}{\hbar\beta}\right) + \sum_{p=1}^n \frac{h_p}{v_p^3} \left(D_{v_p}(0) - D_{v_p}(\tau) - v_p \tau \left(1 - \frac{\tau}{\hbar\beta}\right)\right). \quad (4.21)$$

When $n = 1$ (a single fictitious particle) and $\tau \rightarrow it$, $G(\tau)$ is the same as $D(t)$ from Eq. (35c) in the FHIP [17] mobility theory.

From this trial Green function $G(\tau)$ I arrive at a generalisation to Osaka's $\langle S \rangle_{S_0}$ with multiple (n with index p) variational parameters v_p and w_p ,

$$\langle S \rangle_{S_0} = \frac{\hbar\alpha\omega_0^2}{\sqrt{\pi}} \int_0^{\hbar\beta} d\tau D_{\omega_0}(\tau) [G(\tau)]^{-\frac{1}{2}}. \quad (4.22)$$

I then obtain length vectors n for the variational parameters v_p and w_p that correspond to the minimum upper bound to the free energy, which will be used in evaluating the polaron mobility. Considering only two variational parameters ($n = 1$) simplifies to Ōsaka's free energy expression. Feynman's original athermal version can be obtained by taking the zero-temperature limit ($\beta \rightarrow \infty$).

4.4.1 Numerical Results

In this section, I present my numerical investigations into the result of the trial model generalised to multiple fictitious particles in the case of the Fröhlich polaron model. Adding fictitious particles adds two more variational parameters per particle to the trial model, representing each new particle's mass and frequency (or the spring constant) coupled to the electron. These can be transformed into corresponding v_p and w_p parameters where p labels each fictitious particle. The ordering of these parameters can be fixed such that $v_1 > w_1 > v_2 > w_2 > \dots$. Due to the additional computational difficulty in converging the variational solution, I only present the results up to $N = 4$ additional fictitious particles. Converging these results became increasingly difficult as my initial guess had to be reasonably close to the optimal result. Otherwise, the optimisation efficiently converged instead to other local minima or forced one or more fictitious particles to become infinite massive by collapsing the variational parameters $w \rightarrow 0$, $v \rightarrow \infty$. Likewise, the size of the optimisation box grew exponentially, making it harder to constrain the optimisation.

It is known that the Feynman variational result cannot obtain the true weak-coupling perturbative result. At small alpha α , Feynman's one fictitious mass model gives the weak coupling expansion for the polaron energy:

$$\frac{E}{\hbar\omega_0} = -\alpha - 0.0123\alpha^2. \quad (4.23)$$

It is known that using a general memory function in the trial model and finding its optimal form results in a α^2 coefficient 0.0125978 [83]. The accurate perturbative weak coupling result is 0.01592. So we can see that the gains in the free energy bound, at least for the Fröhlich model, will be small. As a side note, the Feynman variational method can be improved by including higher-order corrections in higher-order cumulants in the difference between the polaron and trial actions. This has been found to bring it much closer to the actual solution at the cost of significantly more computation. Despite small improvements in the energy bound of the variational method, we will see that the corresponding dynamical theory sees significant changes, likely due to the high sensitivity of analytic continuation on the optimal result.

4.4.2 The additional parameters

In Figs. (4.6) the coupling-dependence of the optimal v and w parameters for the Fröhlich model, an increasing number of fictitious particles in the trial model from $N = 1$ to $N = 5$. In the top-right figure ($N = 2$), I have also co-plotted the results obtained by Abe for the two-particle model in Ref. [81].

Notably, the first fictitious particle seems to follow a different trend for w , which asymptotes to $w = \omega_0$ at strong coupling, compared to any other additional particles where w follows a similar coupling dependence as the v parameter as we add more particles, the v and w corresponding to each additional particle become exponentially more prominent, whilst the previous v and w parameters decrease slightly. The gap between v and w for each additional particle becomes significantly smaller until it is unperceivable in the plots. This suggests that each successive particle becomes exponentially lighter with a larger spring constant. Looking at the energy, we will see that each additional particle contributes diminishingly to the system's free energy.

In Figs. (4.7) is the temperature-dependence of the optimal v and w parameters for the Fröhlich model, an increasing number of fictitious particles in the trial model from $N = 1$ to $N = 4$. Each v_p and $w_{p>2}$ appears to reach a low plateau for $\beta\omega_0 > 8$ whereas the first w_1 seems to have a minimum around $\beta\omega_0 \approx \alpha = 6$ before increasing to a plateau. This suggests that the trial model eventually becomes insensitive to changes in temperature below some critical temperature.

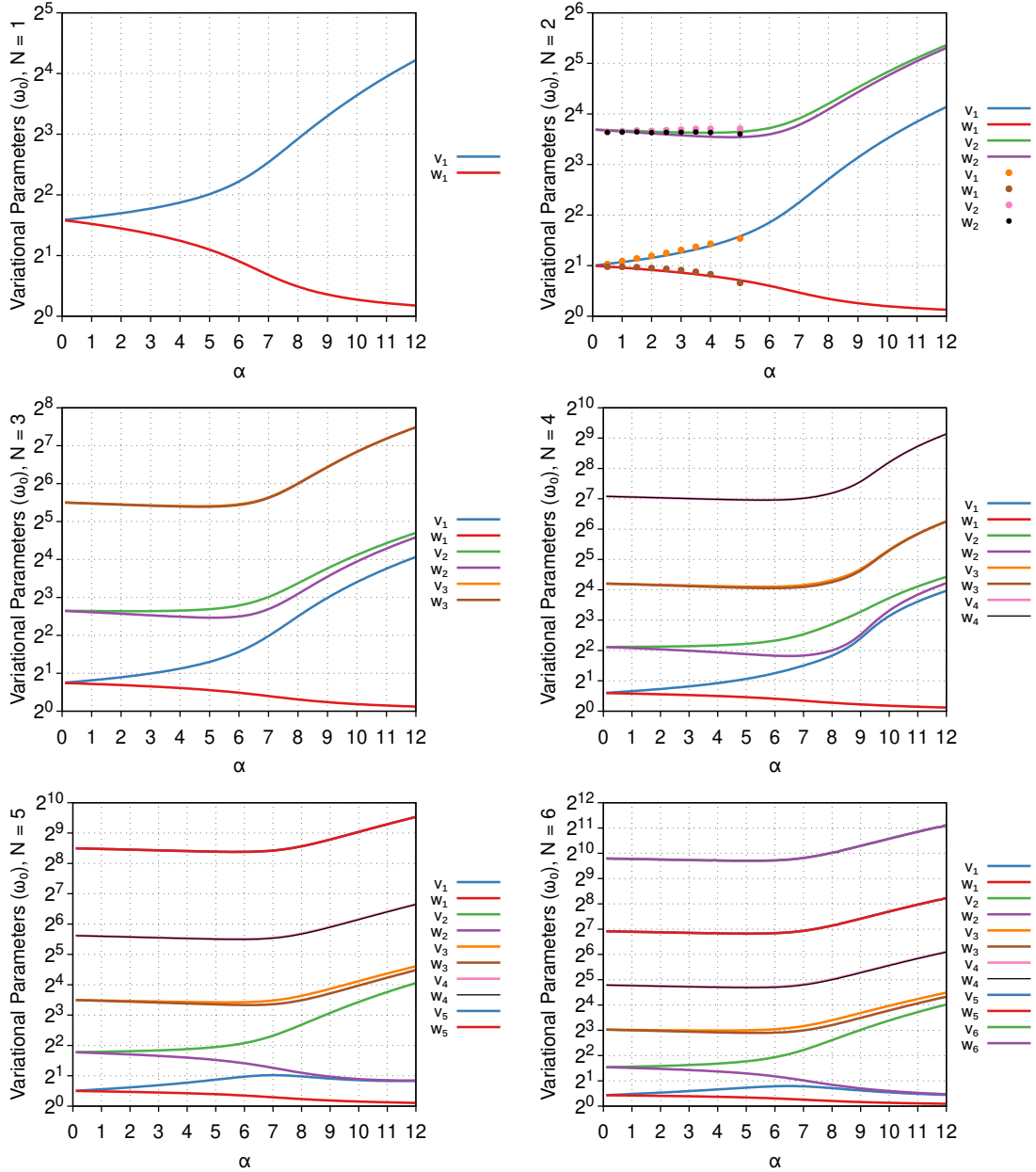


Figure 4.6: Successive optimal values of pairs of variational parameters v_i and w_i for the Fröhlich model, corresponding to additional fictitious particles in the trial model for a range of dimensionless electron-phonon $\alpha \in [0, 12]$. The first figure (**top-left**) is Feynman's original variational solution $N = 1$. The next generalisation to $N = 2$ fictitious particles (**top-right**) sees a shift down in the original v_1 and w_1 with the addition of two more v_2 and w_2 which follow a similar dependence on α as v_1 . I compare this result to those obtained for a specific $N = 2$ trial model used in Ref. [81]. The result for additional fictitious particles are shown in **middle-left** ($N = 3$), **middle-right** ($N = 4$) and **bottom** ($N = 5$). Each additional particle $N > 1$ is lighter than the last, whereas the corresponding spring constant increases conversely.

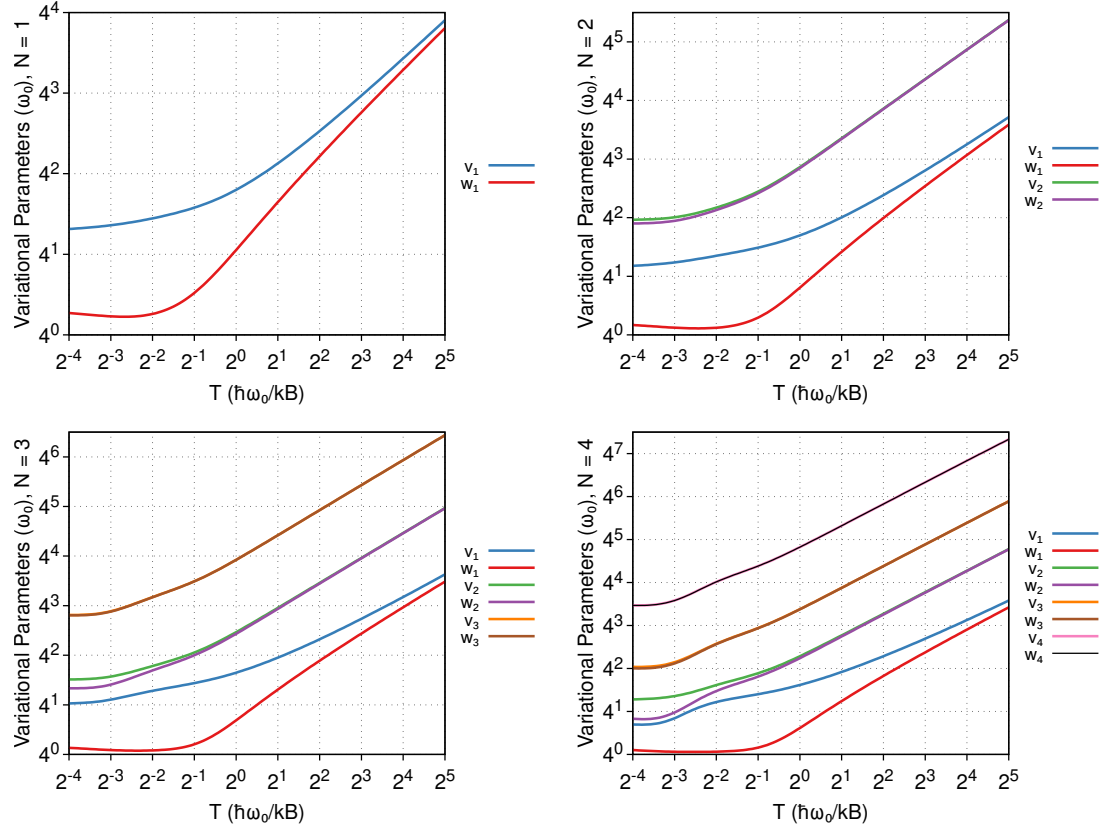


Figure 4.7: Successive optimal values of pairs of variational parameters v_i and w_i for the Fröhlich model, corresponding to additional fictitious particles in the trial model for coupling $\alpha = 6$ and a range of temperature $1/T \in [0.125\omega_0, 0.5\omega_0, 2.0\omega_0, 8.0\omega_0, 32.0\omega_0, 128.0\omega_0]$. The first figure (**top-left**) is Feynman's original variational solution $N = 1$. The result for additional fictitious particles are shown in **top-right** ($N = 2$), **bottom-left** ($N = 3$) and **bottom-right** ($N = 4$). Each v_i appears to reach a low plateau for $\beta\omega_0 > 8$ whereas each w_i appears to have a minimum around $\beta\omega_0 \approx \alpha = 6$.

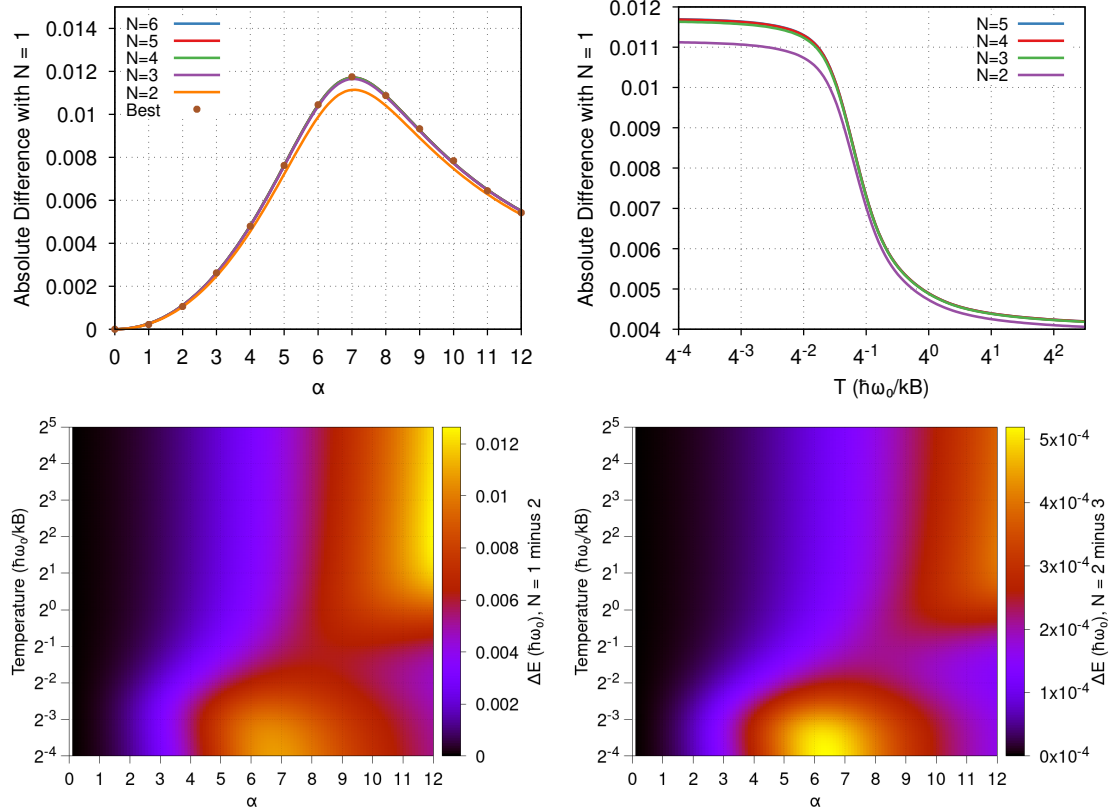


Figure 4.8: Polaron free energy for the Fröhlich model for increasing number N of fictitious particles in the trial model. **Top-left** Absolute change in the free energy for $N > 1$ compared to the free energy result for $N = 1$. The generalised trial models quickly converge to the optimal free-energy bound, with the greatest improvement on Feynman's original trial model seen around $\alpha = 7$. **Top-right** A complementary result to the first figure obtained in Ref using a general spectral function corresponding to the $N \rightarrow \infty$ limit. By comparison, I can see that only a few fictitious particles are needed to converge to the best possible variational solution. **Bottom-left:** The temperature-dependence of the percentage improvement of additional fictitious particles compared to just one. The most improvement appears around $\beta\hbar\omega_0 \approx 8$ of 0.16%, after which the improvement plateaus. **Bottom-right:** Similar to the previous figure, the percentage improvement is relative to the previous number of fictitious particles (e.g. $N = 3$ compared to $N = 2$). Any improvements peak at $\beta\hbar\omega_0 \geq 8$ and exponentially decrease with the addition of more particles, showing a rapid convergence to the optimal trial solution.

4.4.3 Improving the Energy Bound

In Figs. (4.8) the top-left figure shows the relative shift in the free energy for $N > 1$ compared to the free energy result for $N = 1$ as a function of the electron-phonon coupling from $\alpha = 1$ to $\alpha = 12$. Two key observations are: firstly, the largest improvement to the free energy bound can be seen at intermediate coupling around $\alpha \approx 7$. Secondly, there is rapid convergence to the optimal free energy bound with no discernible difference between the results for $N = 3$, $N = 4$ and $N = 5$ fictitious particles. The two asymptotes are given by $3 \times 10^{-4}\alpha^2$ at lower coupling and $0.81\alpha^{-2}$ at higher coupling. The top-right figure is borrowed from Fig. 3 in [72] in which Dries Sels obtained the optimal result for

the Feynman polaron model by using a general bath spectrum in the trial action, which corresponds to the $N \rightarrow \infty$ limit of our many fictitious particle trial action. Comparison with our results shows that we have obtained the correct optimal trial solution and that only $N = 3$ fictitious particles are required to do so, which is computationally tractable compared to more particles or a self-consistent approach with a general bath spectrum.

The lower figures in Figs. (4.8) show the temperature dependence of the percentage improvement of additional fictitious particles compared to just one. The bottom-left figure shows that the maximum improvement to the free energy bound is obtained around $\beta\omega_0 = 8$, the temperature when w_1 takes its minimum value. At lower temperatures, the improvement slightly decreases before plateauing. The bottom-right figure shows the percentage improvement relative to the previous number of fictitious particles (e.g., $N = 3$ compared to $N = 2$). Here, we can see that the relative improvement in the free energy bound is exponentially decreasing with each additional particle with a maximum improvement of $N = 3$ over $N = 2$ at just 0.01%.

4.5 The Optimal Functional Solution

4.5.1 Generalised Trial Action

The central quantity for the generalisation is the trial action functional,

$$S_0 = \frac{m_0}{2} \int_0^{\hbar\beta} \mathbf{r}(\tau)^2 - \frac{m_0}{2} \int_0^{\hbar\beta} \int_0^{\hbar\beta} d\tau d\tau' \Sigma(\tau - \tau') \mathbf{r}(\tau) \cdot \mathbf{r}(\tau'), \quad (4.24)$$

where $\Sigma(\tau - \tau')$ is a general memory kernel and is a real, continuous function defined for $|\tau| \leq \hbar\beta$ and can be assumed to be symmetric $\Sigma(-\tau) = \Sigma(\tau)$. This is the most general quadratic, isotropic, two-time action. We can restrict the memory kernel to be β -periodic and also assume a sum-rule,

$$\int_0^{\hbar\beta} \Sigma(\tau - \tau') d\tau' = 0 \quad \forall \tau \in [0, \hbar\beta], \quad (4.25a)$$

$$\Sigma(\tau - \hbar\beta) = \Sigma(\tau) \quad \forall \tau \in [0, \hbar\beta]. \quad (4.25b)$$

The first assumption is required for a translation invariant system, but the second assumption can be relaxed if required.

The goal is to find the optimal memory function $\tilde{\Sigma}(\tau)$ that minimises the upper bound to the free energy. Therefore, the free energy becomes a functional of the memory function,

$$F \leq F_{\text{trial}} [\Sigma] = F_{\text{ph}} + F_{S_0[\Sigma]} + \frac{1}{\beta} \langle S - S_0[\Sigma] \rangle_{S_0[\Sigma]}. \quad (4.26)$$

To evaluate this functional, we need to evaluate the density-density correlation function,

$$\langle \rho^\dagger(\tau) \rho(\tau') \rangle = \langle e^{i\mathbf{q} \cdot [\mathbf{r}(\tau) - \mathbf{r}(\tau')]} \rangle_{S_0}. \quad (4.27)$$

To evaluate the density-density correlation function, we introduce the generating functional,

$$Z[\mathbf{J}] = \left\langle \exp \left\{ \int_0^{\hbar\beta} d\tau \mathbf{J}(\tau) \cdot \mathbf{r}(\tau) \right\} \right\rangle_{S_0}, \quad (4.28)$$

where $\mathbf{J}(\tau)$ is an arbitrary source term. If we can evaluate this field integral, we can derive all correlation functions, and subsequently, we can calculate both $\langle S - S_0 \rangle_{S_0}$ and F_{S_0} . We recognise that the expectation $\langle \cdot \rangle_{S_0}$ indicates averaging with respect to an isotropic Gaussian stochastic process $\mathbf{r}(\tau)$ with zero mean and so is uniquely characterised by its

covariance $\langle \mathbf{r}(\tau) \cdot \mathbf{r}(\tau') \rangle_{S_0}$,

$$Z[\mathbf{J}] = \exp \left\{ \frac{m_0}{2n\hbar\beta} \int_0^{\hbar\beta} \int_0^{\hbar\beta} d\tau d\tau' \mathbf{J}(\tau) \cdot \langle \mathbf{r}(\tau) \cdot \mathbf{r}(\tau') \rangle_{S_0} \cdot \mathbf{J}(\tau') \right\}, \quad (4.29)$$

where n is the dimensionality. The covariance is also often referred to in this context as the single-particle Green's function $G(\tau, \tau') \equiv \langle \mathbf{r}(\tau) \cdot \mathbf{r}(\tau') \rangle$ and can be determined as an appropriate inverse of the integral kernel of the trial action,

$$S_0 = \frac{m_0}{2} \int_0^{\hbar\beta} \int_0^{\hbar\beta} d\tau d\tau' \mathbf{r}(\tau) \left[\frac{\partial}{\partial \tau} \delta(\tau - \tau') - \Sigma(\tau - \tau') \right] \mathbf{r}(\tau'), \quad (4.30)$$

where the integral kernel is $G^{-1}(\tau - \tau') = G_0(\tau - \tau') - \Sigma(\tau - \tau')$ with $G_0(\tau - \tau') = \partial_\tau \delta(\tau - \tau')$ the bare free particle Green's function. Under the assumption of translation invariance,

$$\int_0^{\hbar\beta} \Sigma(\tau) d\tau \neq 0, \quad (4.31)$$

the equation of motion of the polaron quasiparticle Green's function is,

$$\int_0^{\hbar\beta} d\tau'' G(\tau - \tau'') G^{-1}(\tau' - \tau'') = n\delta(\tau - \tau'), \quad (4.32)$$

where $\delta(\tau)$ is a periodic delta function and has the Fourier representation,

$$\delta(\tau) = \sum_{n=-\infty}^{\infty} e^{i\omega_n \tau}, \quad (4.33)$$

where $\omega_n = 2\pi n/\hbar\beta$ are the “even” Matsubara frequencies. The polaron Green's function is then given in Fourier representation as,

$$G(\tau - \tau') = \frac{1}{\hbar\beta} \sum_{n=-\infty}^{\infty} \frac{e^{i\omega_n(\tau-\tau')}}{\omega_n^2 - \Sigma_n}, \quad (4.34)$$

where we can identify the Fourier coefficients as $G_n = (\omega_n^2 - \Sigma_n)^{-1}$ where Σ_n is the n -th Fourier coefficient of the memory function,

$$\Sigma_n = \frac{1}{\hbar\beta} \int_0^{\hbar\beta} \Sigma(\tau) e^{-i\omega_n \tau} d\tau = \Sigma_{-n}. \quad (4.35)$$

If $\Sigma_0 = 0$ and we are in a translation-invariant system, the equation of motion for the Green function is still valid because we omit the term at $n = 0$.

Now equipped with the polaron quasiparticle Green's function and the generating functional, we can compute all the averages required in the free energy inequality. Setting the source

term to be,

$$\mathbf{J}(\tau) = i\mathbf{q} [\delta(\tau - \sigma) - \delta(\tau - \sigma')] \equiv \mathbf{J}_{\mathbf{q},\sigma,\sigma'}(\tau). \quad (4.36)$$

Within $\langle S \rangle_0$ we have to evaluate the density-density correlation,

$$\langle e^{i\mathbf{q} \cdot [\mathbf{r}(\tau) - \mathbf{r}(0)]} \rangle_{S_0} = \exp \left(-q^2 r_p^2 [G(0) - G(\tau)] \right). \quad (4.37)$$

For the Fröhlich polaron model, we have to evaluate the expectation of the two-time Coulomb interaction, which we do in the Fourier representation where we use the result from the density-density correlation,

$$\begin{aligned} \left\langle \frac{1}{|\mathbf{r}(\sigma) - \mathbf{r}(\sigma')|} \right\rangle_{S_0} &= \frac{S_{n-1}}{(2\pi)^n} \int d^n q \, q^{-2} Z [\mathbf{J}_{\mathbf{q},\sigma,\sigma'}], \\ &= \left(\frac{2n}{\pi \langle |\mathbf{r}(\sigma) - \mathbf{r}(\sigma')|^2 \rangle_{S_0}} \right)^{1/2}. \end{aligned} \quad (4.38)$$

We can evaluate the trial system free energy by using the “coupling constant” integration trick in which we extract a constant λ from the memory function $\Sigma \rightarrow \lambda\Sigma$. For a translation-invariant system, we can evaluate the free energy from,

$$F_{S_0}(\lambda) = F_{S_0}(0) + \int_0^\lambda d\lambda' \frac{\partial F_{S_0}(\lambda)}{\partial \lambda}. \quad (4.39)$$

The partial derivative is then,

$$\frac{\partial F_{S_0}(\lambda)}{\partial \lambda} = \frac{1}{\hbar\beta} \int_0^{\hbar\beta} \int_0^{\hbar\beta} d\tau d\tau' \Sigma(\tau - \tau') G(\tau - \tau'), \quad (4.40)$$

which implies,

$$F_{S_0}(0) = -\frac{1}{\beta} \ln \left\{ V_n \left(\frac{m_0}{2\pi\hbar^2\beta} \right)^{n/2} \right\} = F_{el}, \quad (4.41)$$

which is just the free energy for the free electron.

4.5.2 Self-consistent Equations

Overall, we have,

$$F \leq F_{ph} + F_{el} + \text{Tr} \ln \left(GG_0^{-1} \right) + \text{Tr} (\Sigma G) + \Phi[G], \quad (4.42)$$

where,

$$\begin{aligned}\Phi[G] &= \sum_{\mathbf{q}} |M_{\mathbf{q}}|^2 \int_0^{\hbar\beta} \int_0^{\hbar\beta} d\tau d\tau' D_{\omega_{\mathbf{q}}}(\tau - \tau') \exp\left(-q^2 r_p^2 G(\tau - \tau')\right), \\ &= 2 \sum_{\mathbf{q}} |M_{\mathbf{q}}|^2 \int_0^{\hbar\beta} d\tau (\hbar\beta - \tau) D_{\omega_{\mathbf{q}}}(\tau) \exp\left(-q^2 r_p^2 G(\tau)\right),\end{aligned}\quad (4.43)$$

where we have used that,

$$\int_0^{\hbar\beta} d\tau \int_0^{\hbar\beta} d\tau' f(|\tau - \tau'|) = 2 \int_0^{\hbar\beta} d\tau (\hbar\beta - \tau) f(\tau). \quad (4.44)$$

For the Fröhlich model, this becomes

$$\Phi^{(F)}[G] = |M_0|^2 \int_0^{\hbar\beta} d\tau \left(\frac{\tau}{\hbar\beta} - 1\right) \frac{D_{\omega_0}(\tau)}{\sqrt{G(\tau)}}. \quad (4.45)$$

Note that the free-electron energy is $F_{el} = \ln\{\det G_0^{-1}\} = \text{Tr} \ln G_0^{-1}$ and so the free-energy inequality is,

$$F \leq \frac{1}{2} \text{Tr} \ln (D_0) + \text{Tr} \ln (-G) + \text{Tr} (\Sigma G) + \Phi[G], \quad (4.46)$$

where we have used that for bosonic phonons $F_{ph} = \frac{1}{2} \text{Tr} \ln(D_0)$ where D_0 is the free phonon Green's function. We note that this takes on a similar form to the expression for the grand potential obtained by Luttinger and Ward [84] where $\Phi[G]$ is an approximation to the Luttinger-Ward functional; the sum of all closed, bold, two-particle irreducible diagrams. Other approximations to this function include GW theory, where it is truncated to include just ring-diagrams $\Phi[G] \approx GUG + GUGGUG + \dots$, and Density Mean-Field Theory (DMFT), where only local diagrams are accounted for.

4.6 Cumulant Expansion Corrections

As we have seen, the partition function for the polaron system described by the action S can be rewritten in terms of another action S_0 as

$$Z = e^{-\beta F} = e^{-\beta F_{S_0}} \langle e^{\Delta S[\mathbf{r}(\tau)]} \rangle_{S_0}, \quad (4.47)$$

with $\Delta S \equiv S - S_0$. The exponential can be expanded to give,

$$Z = e^{-\beta F_{S_0}} \sum_{n=0}^{\infty} \frac{1}{n!} \langle (\Delta S[\mathbf{r}(\tau)])^n \rangle_{S_0}. \quad (4.48)$$

if S_0 is chosen to be the action of the free particle,

$$S_0 = \frac{1}{2} \int_0^{\hbar\beta} d\tau \int_0^{\hbar\beta} d\tau' \mathbf{r}(\tau) G_0^{-1}(\tau, \tau') \mathbf{r}(\tau') = \frac{m_0}{2} \int_0^{\hbar\beta} d\tau \dot{\mathbf{r}}(\tau)^2, \quad (4.49)$$

where,

$$G_0^{-1}(\tau, \tau') = G_0^{-1}(\tau - \tau') = -m_0 \frac{\partial^2}{\partial \tau^2} \delta(\tau - \tau') \quad (4.50)$$

is the differential operator for the free particle with periodic boundary conditions (in imaginary time). Then $\Delta S = S_{\text{int}}$ will only depend on the particle self-interaction, and the expansion of the partition function is equivalent to a perturbative expansion since $S_{\text{int}} \propto \alpha$ is linearly proportional to the electron-phonon coupling. In this case,

$$\begin{aligned} \langle (\Delta S[\mathbf{r}(\tau)])^n \rangle_{S_0} &= \langle (S_{\text{int}}[\mathbf{r}(\tau)])^n \rangle_{S_0} \\ &= \prod_{j=1}^n \sum_{\mathbf{q}_j} \left| M_{\mathbf{q}_j} \right|^2 \int_0^{\hbar\beta} d\tau_j \int_0^{\hbar\beta} d\tau'_j D_{\omega_{\mathbf{q}_j}}(\tau_j - \tau'_j) \left\langle e^{i \sum_{j=1}^n \mathbf{q}_j \cdot [\mathbf{r}(\tau_j) - \mathbf{r}(\tau'_j)]} \right\rangle_{S_0}, \end{aligned} \quad (4.51)$$

where the expectation value can be evaluated with respect to S_0 to give,

$$\begin{aligned} \langle (S_{\text{int}}[\mathbf{r}(\tau)])^n \rangle_{S_0} &= \prod_{j=1}^n \sum_{\mathbf{q}_j} \left| M_{\mathbf{q}_j} \right|^2 \int_0^{\hbar\beta} d\tau_j \int_0^{\hbar\beta} d\tau'_j D_{\omega_{\mathbf{q}_j}}(\tau_j - \tau'_j) e^{-q_j^2 G_0(\tau_j - \tau'_j)} \\ &\times e^{-\frac{1}{2} \sum_{i=0}^n \sum_{j=1}^{i-1} \mathbf{q}_i \cdot \mathbf{q}_j [G_0(\tau_i - \tau'_j) + G_0(\tau_j - \tau'_i) - G_0(\tau_i - \tau_j) - G_0(\tau'_i - \tau'_j)]}, \end{aligned} \quad (4.52)$$

with the free electron Green function $G_0(\tau) = \frac{|\tau|}{2} \left(1 - \frac{|\tau|}{\hbar\beta} \right)$.

More generally, we may want to consider the trial polaron action,

$$S_0 = \frac{1}{2} \int_0^{\hbar\beta} d\tau \int_0^{\hbar\beta} d\tau' \mathbf{r}(\tau) G_{S_0}^{-1}(\tau, \tau') \mathbf{r}(\tau') \quad (4.53)$$

for some general trial (shifted) Green function $G_T(\tau)$ which satisfies,

$$\int_0^{\hbar\beta} d\sigma G_{S_0}^{-1}(\tau, \sigma) G_{S_0}(\sigma, \tau') = \delta(\tau - \tau'). \quad (4.54)$$

With this general polaron Green function, we consider,

$$\begin{aligned} \Delta S = & \frac{1}{2} \int_0^{\hbar\beta} d\tau \int_0^{\hbar\beta} d\tau' \left\{ \mathbf{r}(\tau) \left[G_0^{-1}(\tau, \tau') - G_{S_0}^{-1}(\tau, \tau') \right] \mathbf{r}(\tau') \right. \\ & \left. + 2 \sum_{\mathbf{q}} |M_{\mathbf{q}}|^2 \rho_{\mathbf{q}}(\tau) D_{\omega_{\mathbf{q}}}(\tau - \tau') \rho_{-\mathbf{q}}(\tau') \right\}, \end{aligned} \quad (4.55)$$

where $\rho_{\mathbf{q}}(\tau) = e^{i\mathbf{q}\cdot\mathbf{r}(\tau)}$ is the electron density. It's clear that choosing $G_{S_0}^{-1} = G_0^{-1}$ reproduces the perturbative expansion above. More generally, we have,

$$\begin{aligned} \langle (\Delta S[\mathbf{r}(\tau)])^n \rangle_{S_0} = & \sum_{k=0}^n \binom{n}{k} 2^{k-n} \prod_{i=1}^{n-k} \prod_{j=1}^k \sum_{\mathbf{q}_j} \left| M_{\mathbf{q}_j} \right|^2 \int_0^{\hbar\beta} d\tau_i d\tau'_i d\sigma_j d\sigma'_j \\ & \times \Sigma_{S_0}(\tau_i, \tau'_i) D_{\omega_{\mathbf{q}_j}}(\sigma_i, \sigma'_i) \left\langle \prod_{i=1}^{n-k} \prod_{j=1}^k \mathbf{r}(\tau_i) \cdot \mathbf{r}(\tau'_i) \rho_{\mathbf{q}_j}(\sigma_j) \rho_{-\mathbf{q}_j}(\sigma'_j) \right\rangle_{S_0} \end{aligned} \quad (4.56)$$

where we have defined $\Sigma_{S_0}(\tau, \tau') \equiv G_0^{-1}(\tau, \tau') - G_{S_0}^{-1}(\tau, \tau')$. The expectation can be evaluated from the generating functional,

$$\begin{aligned} Z_{S_0}[\mathbf{J}(t)] &= \left\langle \exp \left(\int_0^{\hbar\beta} dt \mathbf{J}(t) \cdot \mathbf{r}(t) \right) \right\rangle_{S_0} \\ &= \exp \left(\frac{1}{2} \int_0^{\hbar\beta} dt \int_0^{\hbar\beta} dt' \mathbf{J}(t) \cdot G_{S_0}(t, t') \cdot \mathbf{J}(t') \right), \end{aligned} \quad (4.57)$$

where we assume periodic boundary conditions $\mathbf{r}(0) = \mathbf{r}(\hbar\beta)$.

$$\begin{aligned} \langle \mathbf{r}(\tau) \cdot \mathbf{r}(\tau') \rho_{\mathbf{q}}(\sigma) \rho_{-\mathbf{q}}(\sigma') \rangle_{S_0} &= \left. \frac{\delta^2 Z_{S_0}[\mathbf{J}(t)]}{\delta \mathbf{J}(\tau) \delta \mathbf{J}(\tau')} \right|_{\mathbf{J}(t)=i\mathbf{q}[\delta(t-\sigma)-\delta(t-\sigma')]} \\ &= \left(G_{S_0}(\tau, \tau') - q^2 [G_{S_0}(\tau, 0) G_{S_0}(\tau', 0) - G_{S_0}(\tau, \sigma) G_{S_0}(\tau', \sigma')] \right) e^{-q^2 [G_{S_0}(0) - G_{S_0}(\sigma, \sigma')]}, \end{aligned} \quad (4.58)$$

where I have assumed the trial system is translation invariant such that $G_{S_0}(\tau, \tau') = G_{S_0}(|\tau - \tau'|)$ which implies $G_{S_0}(\tau, \tau') = G_{S_0}(\tau', \tau)$ and $G_{S_0}(\tau, \tau) = G_{S_0}(0)$.

We may choose S_0 as a trial action that better approximates the polaron action S over the free particle action. For example, we may choose Feynman's trial action, for which the

trial Green function is,

$$G_F(\tau) = \frac{|\tau|}{2} \left(1 - \frac{|\tau|}{\hbar\beta}\right) - \frac{1}{2} \frac{v^2 - w^2}{v^3} \left[D_v(\tau) - \frac{|\tau|}{\hbar\beta}\right]. \quad (4.59)$$

Or, we may choose the ‘variationally optimal’ trial action with the corresponding Green function derived in the previous subsection.

Truncating the series presents an approximation to the partition function of the polaron.

$$Z = \sum_{n=0}^{\infty} \frac{1}{n!} \langle (\Delta S[\mathbf{r}(\tau)])^n \rangle_{S_0} \approx Z_N = \sum_{n=0}^N \frac{1}{n!} \langle (\Delta S[\mathbf{r}(\tau)])^n \rangle_{S_0}. \quad (4.60)$$

Alternatively, we could take a mean-field approximation such that,

$$\langle (\Delta S[\mathbf{r}(\tau)])^n \rangle_{S_0} \approx \left(\langle \Delta S[\mathbf{r}(\tau)] \rangle_{S_0} \right)^n \quad (4.61)$$

which gives,

$$Z \approx e^{-\beta F_{S_0}} \sum_{n=0}^{\infty} \frac{1}{n!} \left(\langle \Delta S[\mathbf{r}(\tau)] \rangle_{S_0} \right)^n = e^{-\beta F_{S_0} + \langle \Delta S \rangle_{S_0}}, \quad (4.62)$$

which is just the Feynman-Jensen approximation.

We may attempt to combine this perturbative expansion with the variational approximation. Rather than expanding the partition function in terms of the *raw* moments $\mu'_n = \langle (\Delta S)^n \rangle_{S_0}$, we can rewrite the expansion for the partition function in terms of the *central* moments $\mu_n = \langle (\Delta S - \langle \Delta S \rangle_{S_0})^n \rangle_{S_0}$

$$\begin{aligned} Z &= Z_{S_0} \left\langle e^{\Delta S} \right\rangle_{S_0} \\ &= Z_{S_0} e^{\langle \Delta S \rangle_{S_0}} \left\langle e^{\Delta S - \langle \Delta S \rangle_{S_0}} \right\rangle_{S_0} \\ &= e^{-\beta F_{S_0} + \langle \Delta S \rangle_{S_0}} \sum_{n=0}^{\infty} \frac{1}{n!} \langle (\Delta S - \langle \Delta S \rangle_{S_0})^n \rangle_{S_0}, \end{aligned} \quad (4.63)$$

where we have extracted the average contribution corresponding to the Feynman-Jensen inequality. We note the first term $n = 0$ is just 1 and the second term $n = 1$ is zero, so we have

$$Z = e^{-\beta F_{S_0} + \langle \Delta S \rangle_{S_0}} \left[1 + \sum_{n=2}^{\infty} \frac{1}{n!} \langle (\Delta S - \langle \Delta S \rangle_{S_0})^n \rangle_{S_0} \right]. \quad (4.64)$$

From this we can recover the Feynman-Jensen inequality noting that since $\frac{d^2}{dx^2} e^x \geq 0$, then $e^X \geq e^{\langle X \rangle} [1 + (X - \langle X \rangle)]$. Naively, we may try including higher-order terms in this expansion. However, generally, this destroys the variational bound as the residual of the truncated Taylor expansion $R_N(X)$ for the exponential function is not strictly positive for

all orders of the expansion,

$$R_N(X) = e^X - e^{\langle X \rangle} \sum_{n=0}^N \frac{(X - \langle X \rangle)^n}{n!} \not\geq 0 \quad \forall \quad X \in \mathcal{R}, N \in \mathcal{N}_0, \quad (4.65)$$

since $R_N(X) \leq 0$ for $X \leq \langle X \rangle$ and N even. However, if we instead group the expansion in pairs of terms, e.g. $n = 0$ with $n = 1$, $n = 2$ with $n = 3$ etc., we can write,

$$R_N(X) = e^X - e^{\langle X \rangle} \sum_{n=0}^{2N-1} \frac{(X - \langle X \rangle)^n}{n!} \geq 0 \quad \forall \quad X \in \mathcal{R}, N \in \mathcal{N}_0, \quad (4.66)$$

which is strictly convex. We can then approximate the partition function as,

$$\begin{aligned} Z &= e^{-\beta F_{S_0} + \langle \Delta S \rangle_{S_0}} \left[1 + \sum_{n=1}^{\infty} \sum_{m=2n}^{2n+1} \frac{1}{m!} \langle (\Delta S - \langle \Delta S \rangle_{S_0})^m \rangle_{S_0} \right] \\ Z &\geq Z_N = e^{-\beta F_{S_0} + \langle \Delta S \rangle_{S_0}} \left[1 + \sum_{n=2}^{2N-1} \frac{1}{n!} \langle (\Delta S - \langle \Delta S \rangle_{S_0})^n \rangle_{S_0} \right]. \end{aligned} \quad (4.67)$$

We then get a generalised upper-bound to the free energy as,

$$F \leq F_{S_0} - \frac{1}{\beta} \langle \Delta S \rangle_{S_0} - \frac{1}{\beta} \ln \left[1 + \sum_{n=2}^{2N-1} \frac{1}{n!} \langle (\Delta S - \langle \Delta S \rangle_{S_0})^n \rangle_{S_0} \right] \quad (4.68)$$

which presents an alternative cumulant-type expansion that preserves the variational bound on the free energy.

CHAPTER 5



COMPUTING RESPONSE FUNCTIONS & POLARON MOBILITY

“This might suggest that the so-called imaginary time is really the real time, and that what we call real time is just a figment of our imaginations... a scientific theory is just a mathematical model we make to describe our observations: it exists only in our minds. So it is meaningless to ask: which is real, “real” or “imaginary” time? It is simply a matter of which is the more useful description.”

—Stephen Hawking, *A Brief History of Time*, 1988

In this chapter, I first confirm the accuracy of the FHIP method by comparing the predicted temperature- and frequency-mobility with Diagrammatic Monte Carlo (DMC) calculations by Mishchenko et al. [10]. Next, I generalise the FHIP method to compute the charge-carrier mobility and optical conductivity for more complicated models. This extends FHIP to the multimode Fröhlich polaron, the Holstein small polaron, the many spring-mass extended trial solution, general many-body polarons and for an optimal self-consistent solution that coincides with the optimal free energy solution.

5.1 Numerical Evaluation of the Memory Function

Previous work [17, 18], including my own (see Appendices), made use of the ‘doubly-oscillatory’ contour-rotated integral for the complex memory function in Eq. (2.202). The

imaginary component of the memory function is (Eqs. (47) in Ref. [17]),

$$\text{Im } \Sigma(\Omega) = \frac{2\alpha\omega_0^2}{3\Omega\sqrt{\pi}} \frac{(\hbar\omega_0\beta)^{\frac{3}{2}}}{\sinh(\hbar\omega_0\beta/2)} \left(\frac{v}{w}\right)^3 \sinh\left(\frac{\hbar\Omega\beta}{2}\right) \int_0^\infty d\tau \frac{\cos(\Omega\tau)\cos(\omega_0\tau)}{\left[\omega_0^2\tau^2 + a^2 - b \cos(v\omega_0\tau)\right]^{\frac{3}{2}}}, \quad (5.1)$$

where $a^2 \equiv (\hbar\omega_0\beta/2)^2 + R\hbar\beta\omega_0 \coth(\hbar\beta\omega_0 v/2)$, $b \equiv R\hbar\beta\omega_0/\sinh(\hbar\beta\omega_0 v/2)$ and $R \equiv (v^2 - w^2)/(w^2 v)$. The contour integral for the real component of the memory function (see Appendix C for a detailed derivation) is,

$$\begin{aligned} \text{Re } \Sigma(\Omega) = & \frac{2\alpha\omega_0^2}{3\Omega\sqrt{\pi}} \frac{(\hbar\omega_0\beta)^{\frac{3}{2}}}{\sinh(\hbar\omega_0\beta/2)} \left(\frac{v}{w}\right)^3 \\ & \times \left\{ \sinh\left(\frac{\hbar\Omega\beta}{2}\right) \int_0^\infty d\tau \frac{\sin(\Omega\tau)\cos(\omega_0\tau)}{\left[\omega_0^2\tau^2 + a^2 - b \cos(v\omega_0\tau)\right]^{\frac{3}{2}}} \right. \\ & \left. - \int_0^{\frac{\hbar\beta}{2}} d\tau \frac{(1 - \cosh(\Omega(\tau - \hbar\beta/2)) \cosh(\omega_0\tau)}{\left[a^2 - \omega_0^2\tau^2 - b \cosh(v\omega_0\tau)\right]^{\frac{3}{2}}} \right\}. \end{aligned} \quad (5.2)$$

The imaginary component of the memory function can be expanded in Bessel functions (originally, the derivation was outlined in Refs. [17, 18]. Still, in Appendix C), I provide another detailed derivation) and the real component in terms of Bessel and Struve functions (see Appendix C for a detailed derivation).

However, I found that the cost of evaluating these expansions became large at low temperatures, requiring arbitrary precision numerics to reach converged solutions slowly. Devreese et al. [18] found an alternative analytic expansion for the real component but similarly found it to have poor convergence for all temperatures, opting to transform the integrand to one with better convergence.

Instead of using any of the contour integrals or power-series expansions, I found that directly numerically integrating Eq. (2.202) using an adaptive Gauss-Kronrod quadrature algorithm leads to faster convergence and controlled errors. Asymptotic limits of these contour integral expansions, especially at low temperatures, may still prove helpful.

5.2 Violation of the Mott-Ioffe-Regel criterion versus Planckian bound

The usual MIR criterion puts bounds on transport coefficients of the Boltzmann equations for quasiparticle-mediated transport, where localised wavepackets are formed from superpositions of single-particle Bloch states. Beyond these bounds, the mean free path of a quasiparticle is of order or smaller than its Compton wavelength, where it is no longer possible to form a coherent quasiparticle from superpositions of Bloch states due to the uncertainty in the single-particle state positions.

Violation of the MIR limit is commonly observed in strongly correlated systems at high temperatures. It is often used to suggest that quasiparticle physics does not describe transport in these materials. The “thermal” MIR criterion also depends on the validity of the Boltzmann description. Still, it is subtly different to the usual MIR criterion as clearly explained by Hartnoll and Mackenzie [85, 86] who refer to it instead as a “Planckian bound”. Whereas the MIR criterion discerns the ability to form coherent particles from the superposition of Bloch states, the Planckian bound describes the ability of quasiparticles to survive inelastic many-body scattering.

Despite this, the Feynman variational method, a quasiparticle theory, predicts mobilities outside the Planckian bound, which agrees with DMC mobility predictions, as shown in the next section.

This cautions against using semi-classical mobility theories, such as Bloch waves, as their charge-carrier wavefunction ansatz to model polar materials.

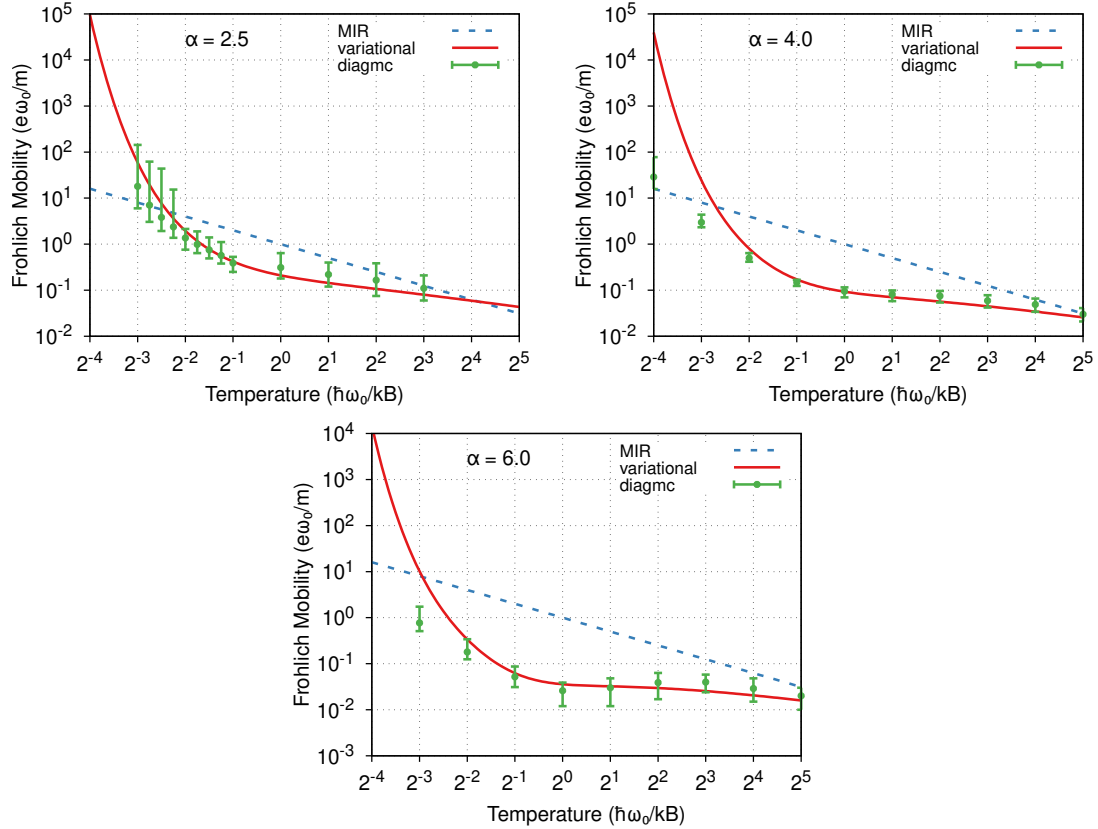


Figure 5.1: Comparison between the FHIP [17] (solid red line) and Mishchenko et al. [10] DMC (green dots with error bars) mobility (μ in units $e\omega_0/m_0$) temperature dependence (T in units of $\hbar\omega_0/k_B$) of the polaron mobility for $\alpha = 2.5$ (top-left), 4.0 (top-right) and 6.0 (bottom). The red dotted lines give the Mott-Ioffe-Regel (MIR) threshold.

5.3 Comparison to Diagrammatic Monte Carlo

Mishchenko et al. [10] recently used diagrammatic Monte Carlo (diagMC) calculations to investigate the violation of the so-called “thermal” analogue to the Mott-Ioffe-Regel (MIR) criterion in the Fröhlich polaron model. This “thermal” MIR criterion is perhaps better called the *Planckian bound* [86] under which a quasiparticle is stable to inelastic scattering.

For the quasiparticle to propagate coherently, the inelastic scattering time τ_{inel} must be greater than the “Planckian time” $\tau_{\text{Pl}} = \hbar/k_B T$. For the polaron mobility μ , this requires $\mu \gtrsim \frac{e\hbar}{Mk_B T}$. This Planckian bound can be reformulated into Mishchenko’s [10] “thermal” MIR criterion for the validity of the Boltzmann kinetic equation, $l \gg \lambda$ where l is the mean free path, and λ the de Broglie wavelength, of the charge carrier.

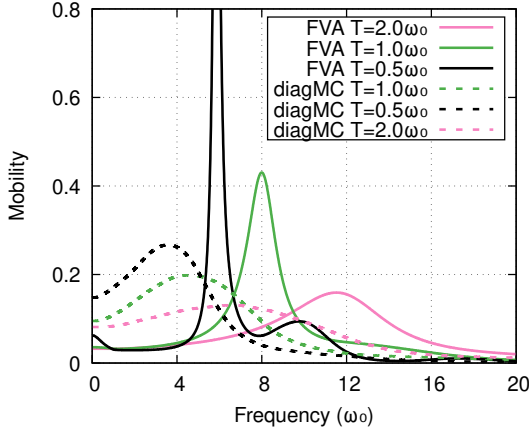


Figure 5.2: Comparison between the FHIP [17] (solid lines) and Mishchenko et al. [10] DMC (dashed lines) mobility (μ in units $e\omega_0/m_0$) frequency dependence (Ω in units ω_0) for temperatures $T = 0.5\hbar\omega_0/k_B$ (black), $1.0\hbar\omega_0/k_B$ (green) and $2.0\hbar\omega_0/k_B$ (pink).

The anti-adiabatic limit ($k_B T \ll \hbar\omega_0$) corresponds to the weak-coupling limit ($\alpha \ll 1$), where the perturbative theory results for the mobility is (Eq. (5) in [10])

$$\begin{aligned}\mu &= \frac{e}{2M\alpha\omega_0} e^{\hbar\omega_0/k_B T} \\ &= \frac{e}{2m_0\omega_0} \left(\frac{1}{\alpha} - \frac{1}{6} \right) e^{\hbar\omega_0/k_B T}, \quad (k_B T \ll \hbar\omega_0, \alpha \ll 1),\end{aligned}\tag{5.3}$$

where $M = m_0/(1 - \alpha/6)$ is the effective mass renormalisation of the polaron. In the adiabatic regime ($k_B T \gg \hbar\omega_0$), the mobility is obtained from the kinetic equation as (Eq. (6) in [10])

$$\mu = \frac{4e\sqrt{\hbar}}{3\sqrt{\pi\alpha M\sqrt{\omega_0 k_B T}}}, \quad (k_B T \gg \hbar\omega_0),\tag{5.4}$$

which is valid even when α is not small.

The top-left panel of Fig. 5.1 compares with Fig. 2 in [10] of the polaron mobility at $\alpha = 2.5$. At low temperatures ($k_B T \lesssim \hbar\omega_0/2$), the exponential behaviour matches the low-temperature mobility in Eq. (5.3). As in [10], there appears to be a delay in the onset of the exponential behaviour for $k_B T < \hbar\omega_0$. Likewise, the MIR criterion is violated over the temperature range $0.2 < k_B T/\hbar\omega_0 < 10$. At high temperatures, the FHIP mobility (Eq. (5.7)) has the same $1/\sqrt{T}$ dependence as Eq. (5.4).

In the bottom panel in Fig. 5.1, I compare the temperature dependence of the FHIP polaron mobility with the DMC polaron mobility (Fig. 3 [10]) at $\alpha = 6$. The DMC polaron mobility exhibits non-monotonic behaviour at $\alpha = 6$, with a clear local minimum around $k_B T = \hbar\omega_0$. Here, we see similar non-monotonic behaviour in the FHIP mobility with a small local minimum around $k_B T = \hbar\omega_0$ too. However, compared to the DMC mobility, the local minimum of the FHIP mobility is shallower. The onset of this minimum in the

FHIP mobility begins around $\alpha = 6$, with the minimum deepening at stronger couplings ($\alpha = 8$ & 10). Like the DMC mobility, the high-temperature limit is recovered after a maximum at $k_B T / \hbar \omega_0 \sim \alpha$, which shifts with larger α . The minimum too appears to be α -dependent, occurring at $k_B T / \hbar \omega_0 \sim 1$ for $\alpha = 6$ or $k_B T / \hbar \omega_0 \sim 1.5$ for $\alpha = 10$.

In Fig. 5.2, I compare the temperature and frequency dependence of the FHIP polaron mobility with the DMC polaron mobility (Fig. 4 in [10]) at $\alpha = 6$ for temperatures $T = 0.5\omega_0, 1.0\omega_0, 2.0\omega_0$. The FHIP mobility, obtained by integrating Eq. (5.7), has similar temperature dependence to the DMC mobility but differs in frequency response.

The FHIP mobility shows extra peaks where the first peak is blue-shifted compared to the DMCs single peak. In [18, 87], it is shown that these extra FHIP mobility peaks correspond to the polaron quasiparticle's internal relaxed excited states. These internal states correspond to multiple phonon scattering processes. For $k_B T / \hbar \omega_0 = 0.5$, the first peak around $\Omega / \omega_0 \sim 6$ corresponds to one-phonon processes, the peak at $\Omega / \omega_0 \sim 10$ corresponds to two-phonon processes, and so on. This is more clearly seen by analysing the memory function $\Sigma(\Omega)$ (Eq. (2.202)) at zero temperature, which similarly has peaks at $\Omega / \omega_0 = 1 + nv$, where $n = 0, 1, 2, \dots$ and v is one of the Feynman variational parameters. These peaks in the memory function correspond to the same Frank-Condon states. As the temperature increases, the first few peaks become more prominent and broaden due to an increased effective electron-phonon interaction. Eventually, the excitations can no longer be resolved at high temperatures.

The Feynman variational model of the electron harmonically coupled to a fictitious massive particle (c.f. Section 2.2.3) lacks a dissipative mechanism for the polaron such that the polaron state described by this model does not lose energy and has an infinite lifetime. However, in de Filippis et al. [87], dissipation is included in this model at zero temperature. This attenuates and spreads the harmonic peaks, obscuring the internal polaron transitions and giving closer agreement to the DMC mobility at zero temperature. We have not used these methods here, but they will be investigated in future work to complement the multiple phonon model action with a more generalised trial action.

5.4 Multiple Phonon Mode Dynamics

To generalise the frequency-dependent mobility in Eq. (5.7), I follow the same procedure as FHIP but use our generalised polaron action S in Eq. (3.8) and trial action S_0 in Eq. (4.18). The result is a memory function akin to Eq. (2.202) that is inclusive of multiple (m) phonon branches j and multiple ($2n$) variational parameters v_p and w_p ,

$$\Sigma(\Omega) = \sum_{j=1}^m \frac{2\alpha_j \omega_j^2}{3\Omega\sqrt{\pi}} \int_0^\infty dt \left[1 - e^{i\Omega t} \right] \text{Im } S_j(t) \quad (5.5)$$

where

$$S_j(\Omega) = D_{\omega_j}(t) G(t)^{-3/2} \quad (5.6)$$

where $G(t)$ is just $G(it)$ from Eq. (4.21) rotated back to real-time to give a generalised version of $D(u)$ in Eq. (2.199) from FHIP.,

The new multiple-phonon frequency-dependent mobility $\mu(\Omega)$ is then obtained from the real and imaginary parts of the generalised Σ using Eq. (5.7). The frequency-dependent mobility $\mu(\Omega)$ is obtained from the impedance using

$$\begin{aligned} \mu(\Omega)^{-1} &= \frac{m_0}{e} \sum_j^m \omega_j \text{Re} \{ z_j(\Omega) \} \\ &= \frac{m_0}{e} \sum_j^m \omega_j \frac{\Omega^2 - 2\Omega \text{Re } \Sigma_j(\Omega) + |\Sigma_j(\Omega)|^2}{v \Sigma_j(\Omega)} \end{aligned} \quad (5.7)$$

where $\Sigma_j(\Omega)$ is just the j th component of $\Sigma(\Omega)$. The limit that the frequency $\Omega \rightarrow 0$ gives the FHIP dc-mobility extended to multiple phonon modes,

$$\mu_{dc}^{-1} = \frac{m_0}{e} \lim_{\Omega \rightarrow 0} \sum_{j=1}^m \omega_j \text{Im } \Sigma_j(\Omega) \quad (5.8)$$

since $\text{Re } \Sigma(\Omega = 0) = 0$.

5.5 Multiple Fictitious Particle Dynamics

To generalise the frequency-dependent mobility in Eq. (5.12), we follow the same procedure as FHIP but use our generalised polaron trial action S_0 in Eq. (4.18). The result is a memory function akin to FHIP's Σ (Eq. (35) in FHIP [17]), but includes multiple ($2n$) variational parameters v_p and w_p ,

$$\Sigma(\Omega) = \frac{\alpha\omega_0^2}{3\sqrt{\pi}} \int_0^\infty dt \left[1 - e^{i\Omega t} \right] \text{Im } S(t). \quad (5.9)$$

Here,

$$S(t) = D_{\omega_0}(t)[G(t)]^{-3/2}, \quad (5.10)$$

where $G(t)$ is $G(\tau = it)$ from Eq. (4.21) rotated back to real-time to give a generalised version of $D(u)$ in Eq. (35c) in FHIP,

$$G(t) = it \left(1 - \frac{it}{\hbar\beta} \right) + \sum_{p=1}^n \frac{h_p}{v_p^3} \left(D_{v_p}(0) - D_{v_p}(\tau) - iv_p t \left(1 - \frac{it}{\hbar\beta} \right) \right). \quad (5.11)$$

The new frequency-dependent mobility $\mu(\Omega)$ is then obtained from the real and imaginary parts of the generalised $\Sigma(\Omega)$ using Eq. (5.12).

5.5.1 The Effect on Dynamics

Given that the multiple fictitious particle trial model rapidly converges to the optimal bound on the polaron-free energy, it is constructive to investigate how the dynamics of the trial system are altered. In Figs. (5.3) the left figure shows the frequency-dependent conductivity at $\alpha = 6$ and thermodynamic temperature $\beta = 12.375\omega_0$ for a number of fictitious particles coupled to the electron $N = 1, 2, 3$ and 4 . This is a regime where, from our previous observations, we expect to be close to the maximum potential improvement to the trial model by adding more fictitious particles. All four trial models agree at low frequencies below the phonon frequency. However, upon reaching the phonon frequency and beyond, we see that each trial model produces a conductivity with different oscillation periods and amplitudes. The frequency of this oscillation is smallest for the $N = 1$ trial model and increases with each additional particle. Meanwhile, the amplitude of the oscillation decreases with more particles. The right figure shows the coupling dependence of the conductivity at zero temperature for $N = 1, 2, 3$ and 4 . This figure shows that the maximum improvement in the zero-temperature conductivity is around $\alpha = 6$ with little discernible difference between $N = 3$ and 4 . Despite the apparent convergence of the conductivity for $N = 3$ and $N = 4$, the frequency dependence shows a significant difference, suggesting that

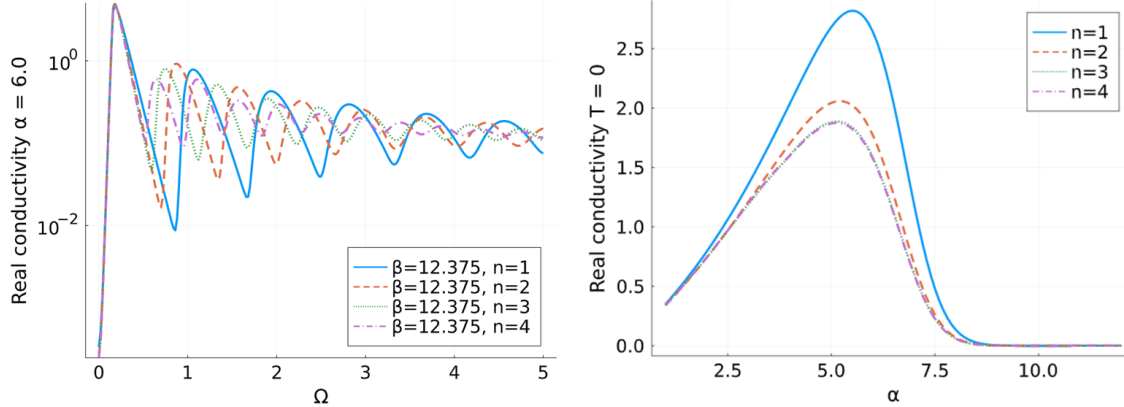


Figure 5.3: Real component of the complex conductivity $\text{Re } \sigma(\Omega)$ for the Fröhlich model for increasing number N of fictitious particles in the trial model. **Left:** The frequency-dependence of the real conductivity at $\alpha = 6$ and $\beta\omega_0 = 12.375$. Here I are in the regime for the maximum potential improvement on the trial model with the additional of fictitious particles. Despite minor improvements on the free energy approximation, the corresponding prediction for the real conductivity changes drastically due to the sensitivity of analytic continuation of the trial model. **Right:** Dependence of the ground-state ($T = 0$ K) real conductivity with the dimensionless electron-phonon coupling α . The real conductivity converges quickly to its optimal solution as soon as $N = 3$ with the maximal improvement occurring around $\alpha = 6$.

far more fictitious particles may be required to reach a truly converged optimal solution in the frequency response of the trial system.

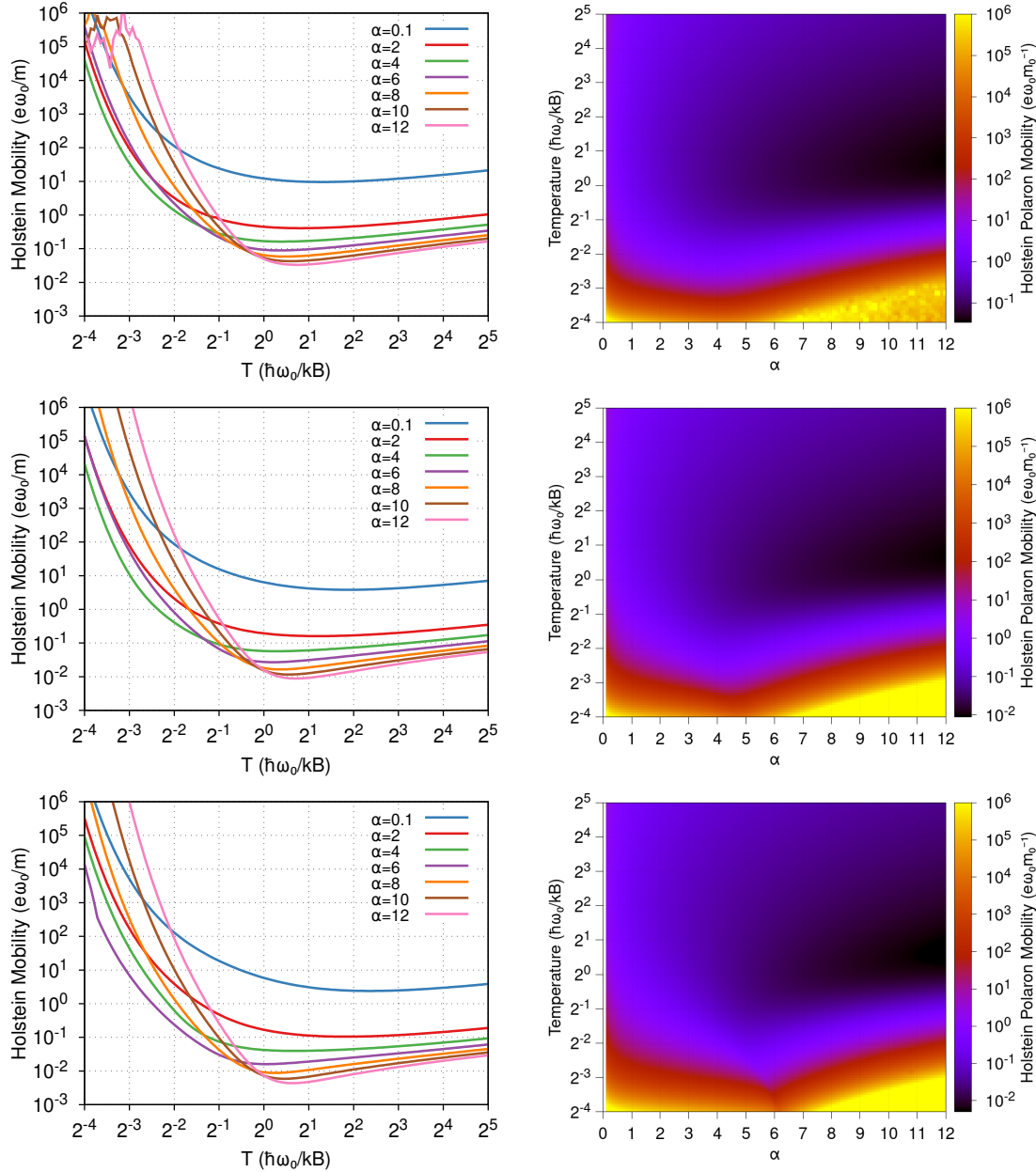


Figure 5.4: Temperature dependence (T , in units of phonon frequency $\hbar\omega_0/k_B$) of the Holstein polaron DC mobility μ in 1D (top), 2D (middle) and 3D (bottom).

5.6 The Holstein Model

5.6.1 Polaron Mobility

In Figs. (5.4) we have the temperature dependence of the polaron mobility for the Holstein polaron with varying electron-phonon coupling. At weaker coupling, mobility shows the typical exponentially decreasing band-like transport at temperatures below the phonon energy level. Above the phonon energy, the temperature dependence transitions to a power-law relationship T^{-x} where x is some number typically used to determine the dominant

scattering mechanism within a material. For example, this index is typically $x = 3/2$ for acoustic phonons.

Again, as we saw previously, 2D Holstein and 3D Fröhlich appear to be most alike. As the electron-phonon coupling increases, we begin to see the onset of the ski-slope feature where the mobility takes on a local minimum at the phonon energy $T = \omega_0$ before increasing to a local maximum at the polaron quasiparticle frequency ν and then transitioning back into a power-law relationship at higher temperatures. Each of the different dimensions of both polaron models seems to have a distinct dependence on the strength of the electron-phonon coupling when it comes to mobility. For the Fröhlich polaron, the ski-slope appears sooner for the 2D model than the 3D model. For the Holstein polaron, the opposite trend seems accurate, with the higher dimension model exhibiting the ski slope. The 2D Fröhlich polaron also appears to manifest a low-temperature maximum at larger electron-phonon couplings, which transitions in a linear decrease to some finite value in mobility as the temperature goes to zero.

At high temperatures, the Fröhlich polaron mobility follows the temperature power-law $\mu_H \sim T^{-1/2}$, consistent with mobility derived from the electron scattering with optical phonons. However, the Holstein polaron mobility becomes constant at high temperatures, independent of temperature. This may be attributed to the phonon-induced electron hopping between lattice sites along which the electron motion is coherent in the direction of that particular energy band. Likewise, at low temperatures, the mobility increases abruptly below the Debye temperature due to the increasing contribution of the electron transfer without phonon participation.

5.6.2 Holstein Memory Function at Zero Temperature

Fig. 5.5 presents the frequency dependence of the imaginary part of the polaron memory function at $T = 0$ K, $\Sigma(\Omega)$, for the Holstein small polaron model in 1D, 2D, and 3D, as a function of the electron-phonon coupling strength α and the frequency Ω (in units of the phonon frequency ω_0). The function captures the energy dissipation processes involving electron-phonon interactions, with peaks indicating resonances at which the electron effectively exchanges energy with the phonon modes. These resonances occur at specific frequencies given by $\Omega = \omega_0 + n \cdot \nu$, where ν is the Feynman variational parameter and n represents the number of phonon excitations.

One notable feature in all three dimensions is the **distinct transition** in the structure of the phonon peaks as the coupling strength α increases. For small α , the peaks are “washed out” and barely defined, indicating weak electron-phonon interactions and minimal energy dissipation. However, after a critical value of α , the phonon peaks become more sharply defined, reflecting stronger interactions and the onset of more efficient energy exchange

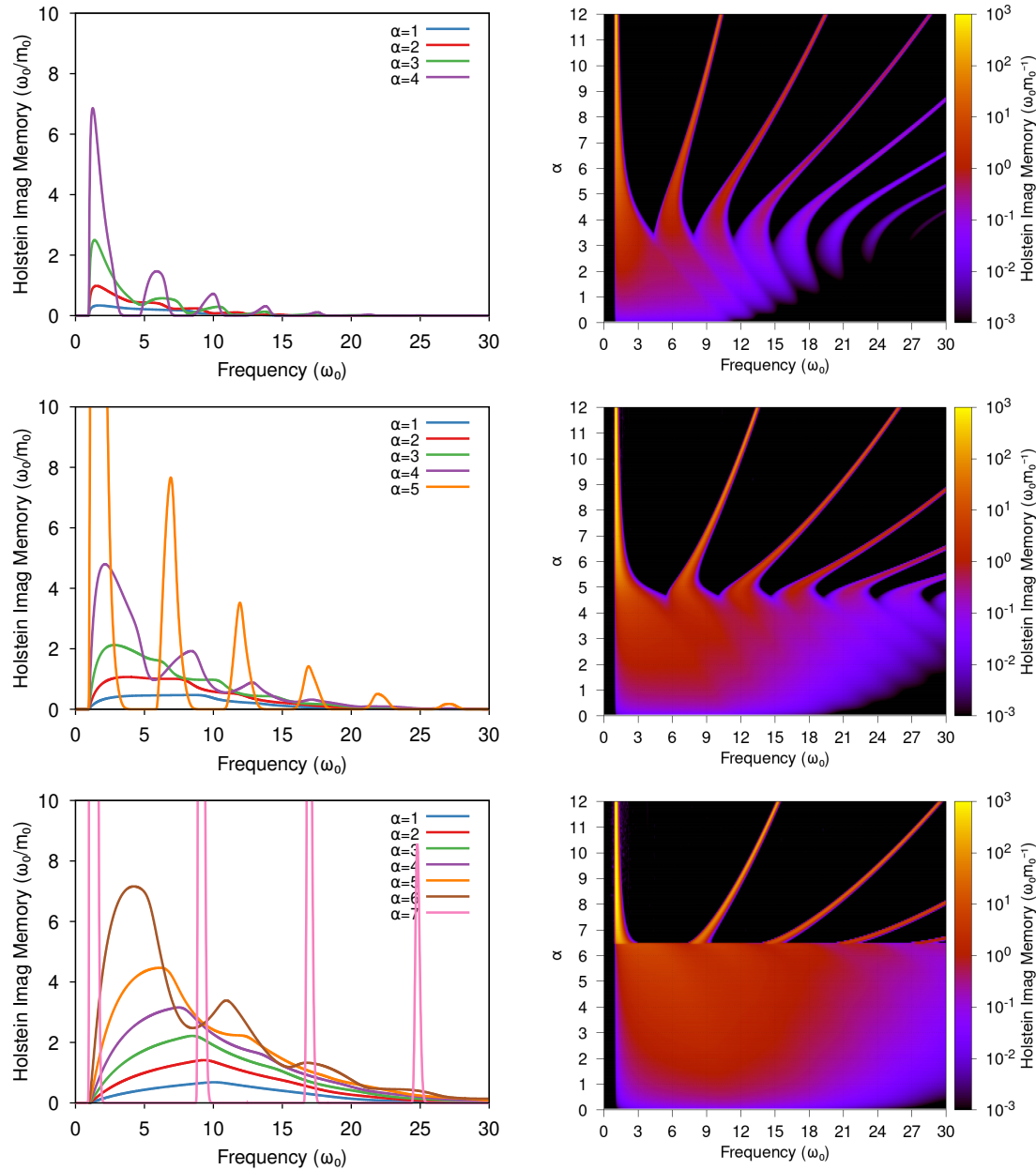


Figure 5.5: Frequency dependence (Ω , in units of the phonon frequency ω_0) of the polaron imaginary memory function $\text{Im } \Sigma(\Omega)$ for the Holstein model in 1D (top), 2D (middle) and 3D (bottom).

between the electron and phonons. This transition marks a regime where multi-phonon processes begin to dominate, with higher-order resonances appearing more clearly at frequencies $\Omega = \omega_0 + n \cdot v$. Notably, the coupling strength at which this transition occurs depends on the system's dimensionality: it occurs at smaller $\alpha \sim 2$ values in 1D and progressively larger $\alpha \sim 4$ in 2D and $\alpha \sim 6$ in 3D. This is due to the increasing number of available phonon modes and the more diffuse nature of electron-phonon interactions in higher-dimensional systems.

In 1D, the memory function exhibits sharp, well-defined peaks even at moderate values of α , reflecting electron-phonon interactions' discrete and constrained nature in low-dimensional systems. The electron predominantly interacts with specific phonon modes, leading to strong, frequency-dependent energy dissipation. As dimensionality increases, the peaks broaden, and the interactions become less sharply defined. In 2D, the peaks still emerge but are broader, suggesting that the electron dissipates energy over a wider frequency range, interacting with a larger number of phonon modes. In 3D, the dissipation profile becomes smoother and more continuous, with the electron losing energy across a broad spectrum of phonon frequencies, reflecting the delocalised nature of the interaction in higher dimensions.

In summary, the dimensionality and electron-phonon coupling strength α influence the behaviour of the Holstein polaron memory function. The transition from weak, washed-out phonon interactions at small α to sharply defined resonances at larger α marks a key feature of the system's dynamics, with dimensionality playing a crucial role in determining the coupling strength at which this transition occurs. The peaks in the memory function correspond to multi-phonon excitations, with their positions governed by Feynman's variational parameter v and the number of phonon interactions involved.

5.6.3 Holsten Optical Conductivity at Zero Temperature

Fig 5.6 shows the frequency dependence of the real part of the polaron optical conductivity, $\sigma(\Omega)$, for the Holstein model in 1D, 2D, and 3D systems at $T = 0$ K. The left panels plot the optical conductivity as a function of frequency Ω (in units of the phonon frequency ω_0) for different electron-phonon coupling strengths α . In contrast, the right panels display heat maps illustrating the conductivity's dependence on frequency and coupling strength. A key feature is that the peaks in the optical conductivity occur at frequencies $\Omega = \omega_0 + n \cdot v$, where v is Feynman's variational parameter, with n representing the number of phonon excitations involved. The results highlight how the polaron's optical properties evolve with dimensionality and coupling strength, mainly through features such as the Relaxed Excited State (RES) and Franck-Condon (FC) peaks, with additional complexity arising at strong couplings.

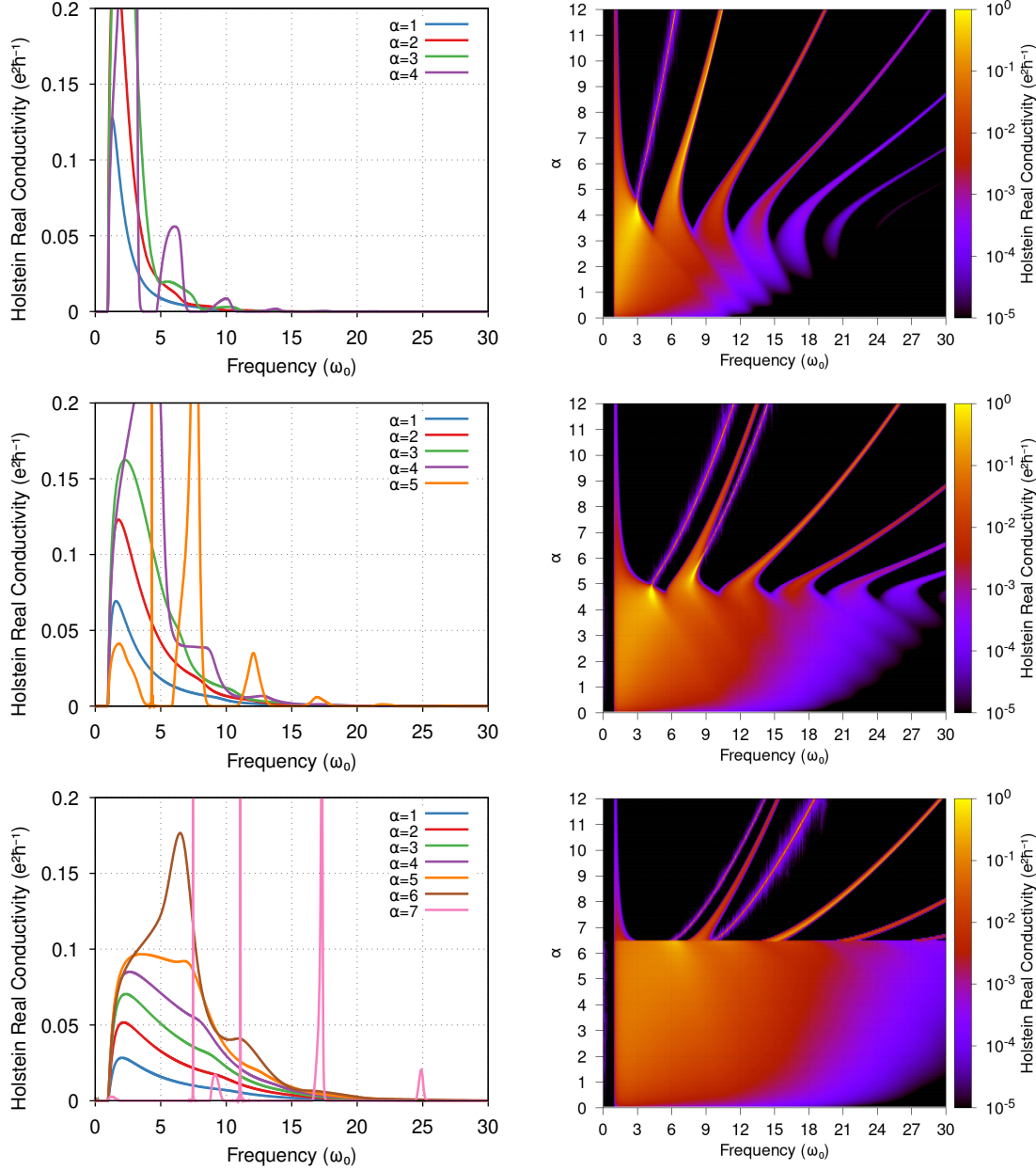


Figure 5.6: Frequency dependence (Ω , in units of the phonon frequency ω_0) of the polaron optical conductivity $\sigma(\Omega)$ for the Holstein model in 1D (top), 2D (middle) and 3D (bottom).

In 1D, the optical conductivity spectrum is characterised by sharp, distinct peaks. For weak coupling ($\alpha = 1$), a single peak appears around $\Omega/\omega_0 \approx 3$, reflecting a simple one-phonon interaction. As α increases, additional peaks emerge, consistent with multi-phonon processes described by $\Omega = \omega_0 + n \cdot v$. The RES peak becomes prominent at intermediate coupling strengths, corresponding to the transition to a relaxed excited state. In contrast, the FC peak emerges at higher frequencies, around $\Omega/\omega_0 \approx 4$, indicating transitions between vibrational states. The sharpness of these peaks in 1D reflects the constrained nature of the polaron's motion in this low-dimensional system, where fewer phonon modes are available, leading to well-separated resonances. The heat map further emphasises these

transitions, showing how the resonant peaks broaden and shift with increasing coupling strength, reflecting the growing complexity of the polaron-phonon interaction.

In 2D, the optical conductivity spectrum becomes broader and more complex. While the RES peak remains dominant, it shifts to lower frequencies and becomes less sharp as α increases due to stronger coupling and more distributed phonon interactions. The FC peak is still present but is less distinct than in 1D, reflecting the more diffuse nature of electron-phonon interactions in two dimensions. Notably, an additional RES peak emerges at strong couplings, indicating a second transition to a different relaxed excited state. This additional peak suggests that at high α , the polaron has become so strongly dressed by phonons that multiple stable excited states are possible, leading to distinct absorption features. The heat map illustrates a transition from discrete peaks at low α to a more continuous spectrum at higher α , where the interaction with multiple phonon modes becomes more significant.

In 3D, the broadening and smoothing of the optical conductivity spectrum are even more pronounced. The peaks visible in 1D and 2D, such as the RES peak, are now spread out and less distinct, indicating that the polaron's interaction with phonons in 3D is highly distributed across multiple excitations. The FC peak remains visible but is less prominent due to the more delocalised interaction between the polaron and the lattice. At strong coupling, an additional RES peak is observed, similar to the 2D case, indicating the formation of multiple stable excited states due to the increased complexity of the polaron-phonon interaction. The heat map reveals that at large α , the optical conductivity transitions into a smooth, continuous function of frequency, with the secondary RES peak signalling the increasing complexity of the polaron's internal structure. This peak broadening and shifting trend, consistent with $\Omega = \omega_0 + n \cdot v$, reflects the growing significance of multi-phonon interactions as the dimensionality increases.

The optical conductivity $\sigma(\Omega)$ measures how efficiently the polaron can conduct optical energy, and the appearance of peaks in the conductivity spectrum indicates resonant interactions between the polaron and specific phonon modes. For small α , the conductivity is dominated by sharp peaks corresponding to one-phonon interactions. In contrast, at larger α , multi-phonon processes dominate, leading to additional peaks and broadening of the spectrum. The RES peak represents the transition to a relaxed excited state, and the emergence of an additional RES peak at strong coupling signals the formation of multiple stable excited states as the polaron becomes increasingly dressed by the phonon cloud. The FC peak appears at higher frequencies and represents transitions where the electron moves between vibrational states without significant nuclear relaxation. As the dimensionality increases from 1D to 3D, the peaks become broader and less distinct, indicating that the polaron interacts with increasing phonon modes. In 1D, the constrained motion of the

polaron leads to sharp, well-separated peaks, while in 2D and 3D, the interaction becomes more continuous, resulting in a broader, smoother conductivity spectrum.

The key transitions in the heat maps highlight how the coupling strength and dimensionality shape the polaron's optical response. For weak coupling, the polaron primarily interacts with a single phonon mode, resulting in a sharp, well-defined peak in the optical conductivity. As the coupling strength increases, the polaron interacts with multiple phonons simultaneously, broadening the conductivity spectrum and introducing additional peaks, such as RES and FC. At strong coupling, the emergence of additional RES peaks indicates the increasing complexity of the polaron's excitation spectrum as new stable excited states form. In 1D, these transitions are more discrete, with clearly defined shifts in the peak positions as α increases, consistent with $\Omega = \omega_0 + n \cdot v$. In higher dimensions, the transitions become smoother, with the conductivity gradually broadening and spreading over a larger range of frequencies as α increases.

Overall, the optical conductivity of polarons evolves with both the electron-phonon coupling strength α and the system's dimensionality. In 1D, the polaron's optical response is characterised by sharp, resonant peaks corresponding to interactions with specific phonon modes, including the RES and FC peaks. In contrast, in 2D and 3D, the optical conductivity becomes broader and more continuous, reflecting the increasingly complex interactions between the polaron and the lattice. As the coupling strength increases, the polaron's ability to conduct optical energy is enhanced, with multi-phonon processes, particularly involving RES and FC transitions, playing a significant role in shaping the conductivity spectrum. The transitions observed in the heat maps highlight how the polaron's interaction with the phonon field becomes more distributed as both coupling strength and dimensionality increase, leading to a broader, more diffuse optical response, with peak positions determined by $\Omega = \omega_0 + n \cdot v$. The additional RES peaks at strong coupling point to form multiple stable excited states in the polaron's internal structure, further enriching the spectrum.

5.6.4 Holsten Optical Conductivity at Finite Temperature

Figs. 5.7, 5.8 and 5.9 illustrate the temperature dependence of the real part of the polaron optical conductivity $\sigma(\Omega)$ in the 1D, 2D, and 3D Holstein models for varying electron-phonon coupling strengths, α . The temperature T is expressed in units of the phonon frequency $\hbar\omega_0/k_B$, and the conductivity is displayed as a function of both temperature and frequency Ω (in units of ω_0). These plots highlight how the polaron optical conductivity changes with temperature, coupling strength, and dimensionality, providing insights into the thermal excitation of phonons and the corresponding impact on polaron dynamics.

In the 1D case, shown in Fig. 5.7, we observe that for low coupling ($\alpha = 1$), the optical conductivity is relatively weak and concentrated at low frequencies and low temperatures.

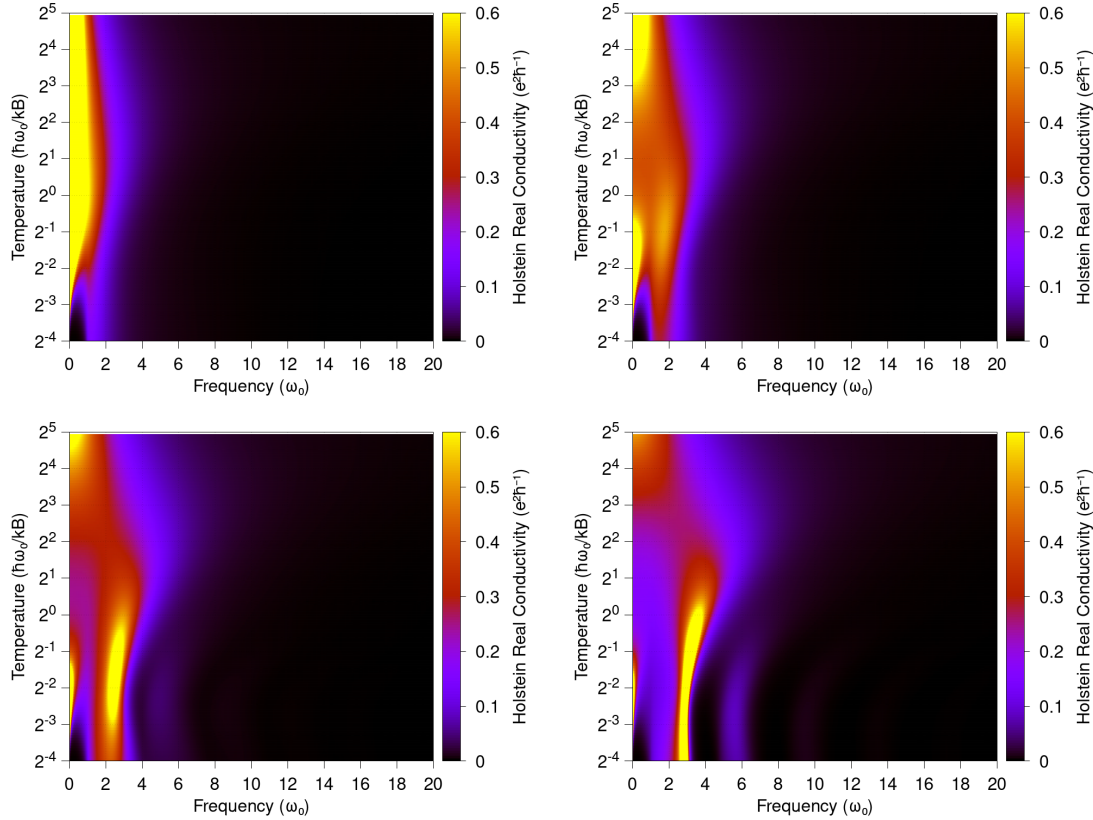


Figure 5.7: Temperature dependence (T , in units of the phonon frequency $\hbar\omega_0/k_B$) of the polaron optical conductivity $\sigma(\Omega)$ for the 1D Holstein model for electron-phonon couplings $\alpha = 1$ (top-left), 2 (top-right), 3 (bottom-left) and 4 (bottom-right).

As temperature increases, there is a slight increase in conductivity at low frequencies, reflecting thermal excitation of the phonons, which enhances the polaron's ability to interact with the lattice. At higher coupling strengths ($\alpha = 2, 3, 4$), the conductivity broadens to cover a wider frequency range. As temperature increases, we see a more pronounced enhancement of the optical conductivity at higher frequencies. This broadening reflects stronger multi-phonon processes becoming active at higher temperatures as more phonons are thermally excited, allowing the polaron to interact with a larger number of vibrational modes. The primary feature across all coupling strengths is the dominance of low-frequency conductivity at low temperatures, which gradually shifts and broadens toward higher frequencies with increasing temperature, reflecting the increased complexity of the polaron-phonon interaction in one dimension.

In the 2D case, shown in Fig. 5.8, the temperature dependence of the optical conductivity exhibits a similar but more pronounced pattern. At weak coupling ($\alpha = 1, 2$), the conductivity is concentrated mainly at low temperatures and frequencies. However, as the coupling strength increases to $\alpha = 3, 4, 5$, we see a significant enhancement of the conductivity at intermediate and higher temperatures, with the spectrum broadening and extending to higher frequencies. In 2D, the peaks in conductivity are more noticeable

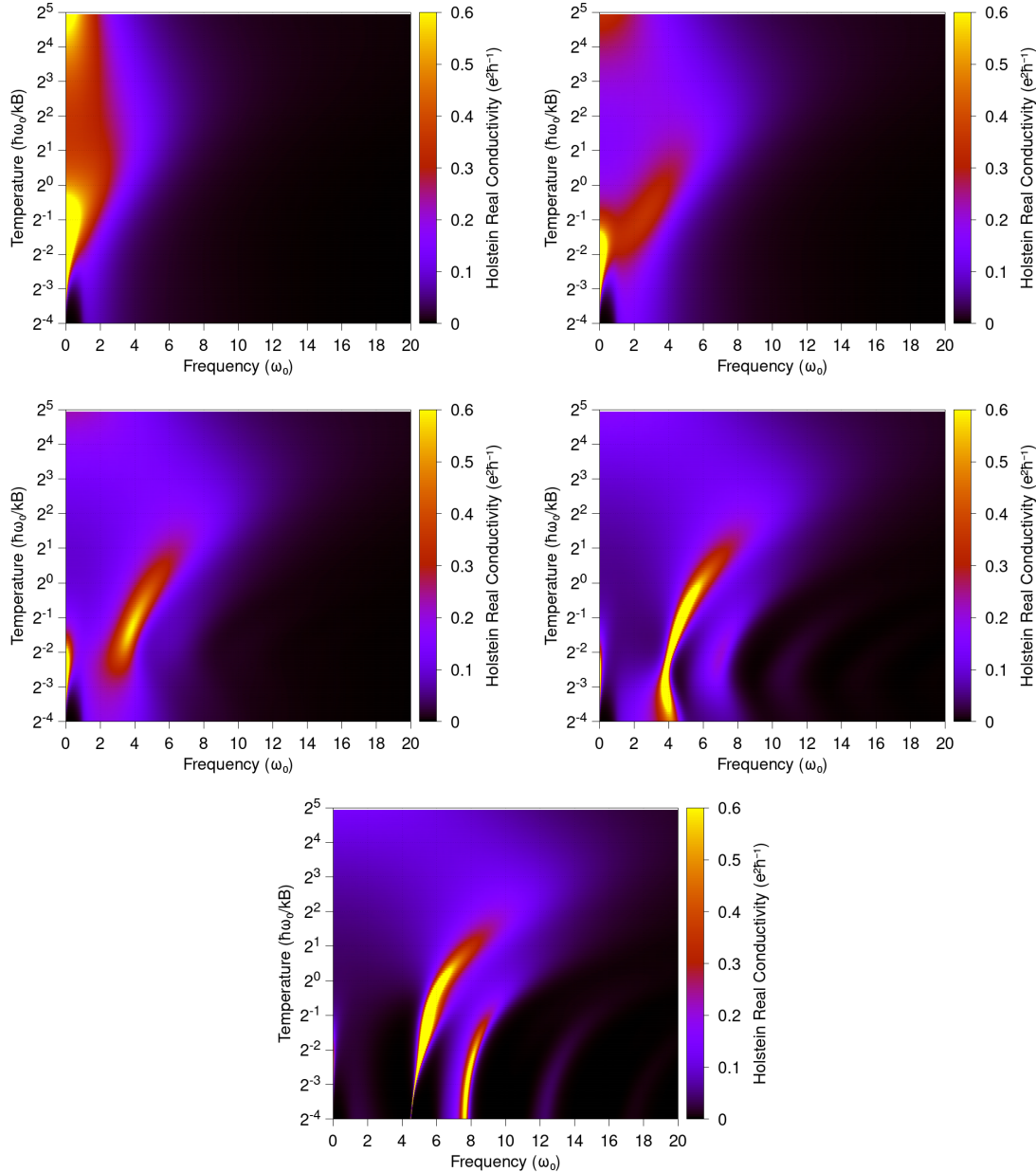


Figure 5.8: Temperature dependence (T , in units of the phonon frequency $\hbar\omega_0/k_B$) of the polaron optical conductivity $\sigma(\Omega)$ for the 2D Holstein model for electron-phonon couplings $\alpha = 1$ (top-left), 2 (top-right), 3 (middle-left), 4 (middle-right) and 5 (bottom).

compared to the 1D case, with distinct features appearing at higher temperatures. These peaks reflect resonant interactions between the polaron and the phonon modes, which are more pronounced in two dimensions due to the increased number of available phonon excitations. The heat maps show clear transitions as the temperature increases, with the conductivity spreading out from the low-frequency regime to cover a wider frequency range, driven by enhanced thermal excitation. At stronger coupling, the interactions are sufficient to sustain this broader response, highlighting the impact of multi-phonon processes and the more complex interaction between the polaron and the lattice in 2D.

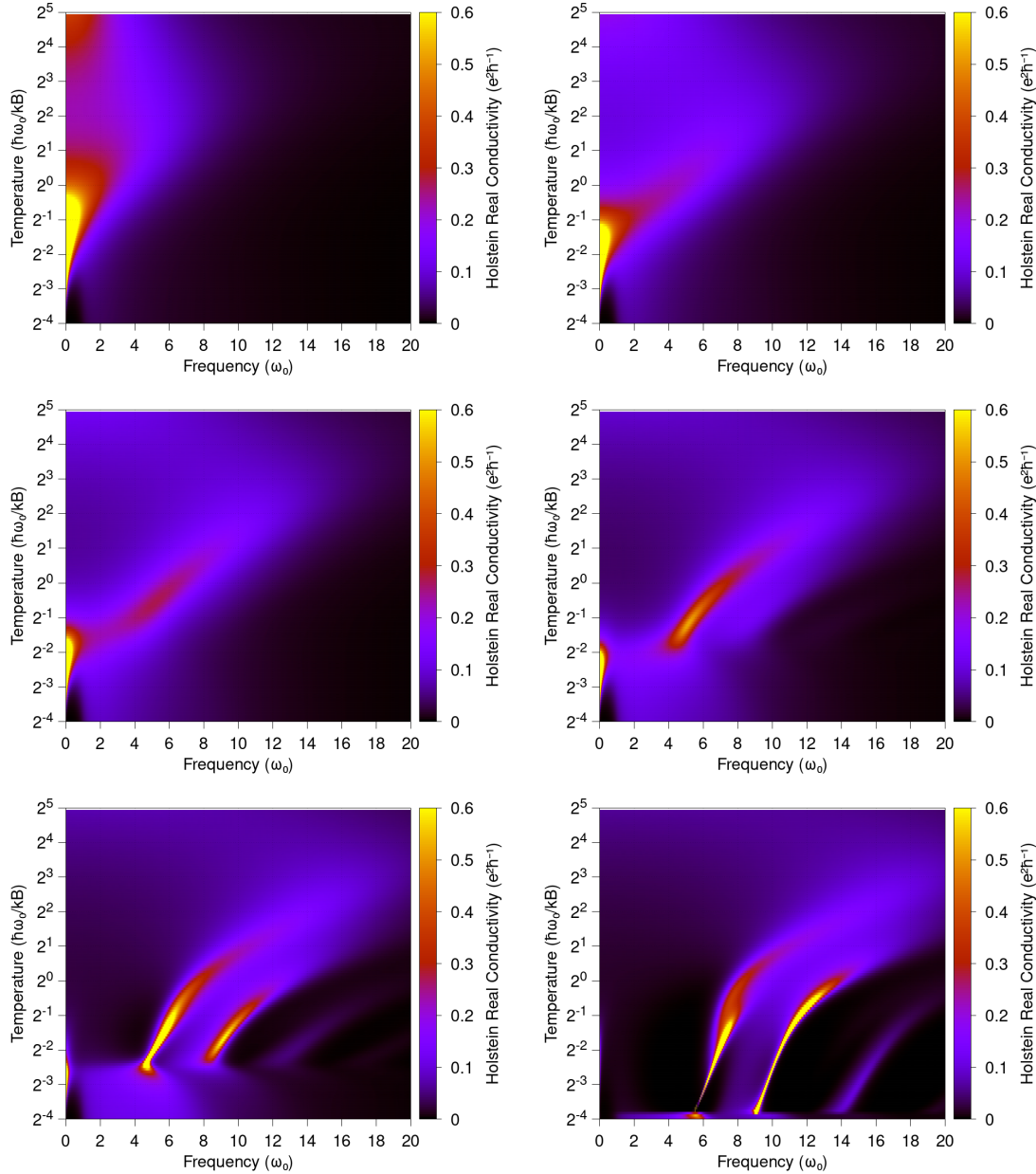


Figure 5.9: Temperature dependence (T , in units of the phonon frequency $\hbar\omega_0/k_B$) of the polaron optical conductivity $\sigma(\Omega)$ for the 3D Holstein model for electron-phonon couplings $\alpha = 1$ (top-left), 2 (top-right), 3 (middle-left), 4 (middle-right), 5 (bottom-right) and 6 (bottom-right).

In the 3D case, depicted in Fig. 5.9, the optical conductivity shows a more pronounced broadening across both temperature and frequency compared to the 1D and 2D cases. At low coupling ($\alpha = 1, 2$), the conductivity is still focused at low frequencies and temperatures, but as the coupling strength increases ($\alpha = 3, 4, 5, 6$), the conductivity extends significantly to higher frequencies and temperatures. The appearance of distinct peaks and their movement toward higher frequencies with increasing temperature is more evident in 3D than in lower dimensions. This broadening suggests that in 3D, the polaron interacts with a larger number of phonon modes, and the multi-phonon processes become more dominant as

temperature rises. In particular, for stronger coupling values, the conductivity heat maps show distinct features corresponding to the interaction between the polaron and multiple phonons, especially at higher temperatures. This behaviour reflects the increased phonon density of states in 3D systems, where the electron-phonon interaction is distributed over a larger number of phonon modes, leading to more complex temperature-dependent behaviour.

Physically, the temperature dependence of the optical conductivity can be interpreted as a result of the thermal excitation of phonons, which facilitates the polaron's interaction with the lattice. Phonon activity is minimal at low temperatures, and the polaron interacts primarily with the lowest-energy modes. As the temperature increases, more phonons are thermally excited, allowing the polaron to interact with a wider range of vibrational modes, reflected in the broadening of the conductivity spectrum. In higher-dimensional systems (2D and 3D), this effect is more pronounced due to the larger number of phonon modes available for interaction, resulting in more complex behaviour and the emergence of distinct peaks at higher temperatures. In all cases, the coupling strength α plays a key role in determining the magnitude and frequency range of the conductivity, with stronger coupling leading to more significant broadening and the activation of multi-phonon processes, especially at higher temperatures.

In summary, the temperature-dependent broadening of the polaron's optical conductivity across different dimensions and coupling strengths. In 1D, the conductivity remains relatively constrained, with more gradual shifts as temperature increases. In 2D, the conductivity broadens more significantly, with distinct peaks emerging at higher temperatures, reflecting stronger phonon interactions. In 3D, the conductivity exhibits the most pronounced broadening, with clear peaks at higher frequencies and temperatures, indicative of complex multi-phonon interactions. This behaviour underscores the role of dimensionality and coupling strength in shaping the temperature dependence of polaron dynamics and optical response.

5.7 General Polaron Mobility

The polaron DC mobility may be obtained in the same way as was done for the Fröhlich model from real components of the frequency- and temperature-dependent impedance function,

$$\mu_{dc} = \lim_{\Omega \rightarrow 0} \operatorname{Re} \left\{ \frac{1}{z(\Omega)} \right\}, \quad (5.12)$$

where the impedance function is expressed in terms of the memory function $\Sigma(\Omega)$,

$$z(\Omega) = i(\Omega - \Sigma(\Omega)). \quad (5.13)$$

More specifically, we can express the inverse DC mobility just in terms of the memory function,

$$\mu_{dc}^{-1} = \lim_{\Omega \rightarrow 0} \operatorname{Im} \{ \Sigma(\Omega) \}. \quad (5.14)$$

Starting from expressing the dynamic memory function for a general polaron and specialising in the Holstein case, the general memory function can be written as,

$$\Sigma(\Omega) = \frac{4}{nm_0\hbar\Omega} \int_0^\infty dt \left(1 - e^{i\Omega t}\right) \operatorname{Im} \left\{ \sum_{\mathbf{q}} |M_{\mathbf{q}}|^2 q^2 D_{\omega_{\mathbf{q}}}(t) \left\langle e^{i\mathbf{q} \cdot [\mathbf{r}(t) - \mathbf{r}(0)]} \right\rangle \right\}, \quad (5.15)$$

where we assume the system to be rotationally invariant.

As done earlier, the expectation value can be expressed as a path integral. However, even the full Fröhlich model cannot be evaluated exactly. We approximate this by evaluating this expectation value with respect to the Feynman Polaron model,

$$\langle \rho_{\mathbf{q}}(t) \rho_{\mathbf{q}}^*(0) \rangle_0 = e^{-q^2 r_p^2 G(t)}, \quad (5.16)$$

where $G(t)$ is the polaron Green function evaluated in real-time (i.e. substitute $\tau \rightarrow it$ into Eq. (4.10)),

$$G(t) = it \left(1 - \frac{it}{\hbar\beta}\right) + \frac{v^2 - w^2}{v^3} \left[D_v(0) - D_v(t) - ivt \left(1 - \frac{it}{\hbar\beta}\right) \right]. \quad (5.17)$$

In n -dimensions, we need to evaluate the reciprocal-space integral,

$$\begin{aligned} I(n) &= V_0 \int \frac{d^n q}{(2\pi)^n} |M_{\mathbf{q}}|^2 q^2 D_{\omega_{\mathbf{q}}}(t) e^{-q^2 r_p^2 G(t)}, \\ &= \frac{V_0 S_{n-1}}{(2\pi)^n} \int_0^R dq q^{n+1} |M_q|^2 D_{\omega_q}(t) e^{-q^2 r_p^2 G(t)}, \end{aligned} \quad (5.18)$$

where we have used that the system is rotation-invariant. For a general polaron model, we then have the memory function,

$$\Sigma(\Omega) = \frac{4}{nm_0\hbar\Omega} \frac{V_0 S_{n-1}}{(2\pi)^n} \int_0^\infty dt \left(1 - e^{i\Omega t}\right) \int_0^\Lambda dq |M_q|^2 q^{n+1} \operatorname{Im}\left\{D_{\omega_q}(t)e^{-q^2 r_p^2 G(t)}\right\}. \quad (5.19)$$

In the zero frequency limit, we have,

$$\lim_{\Omega \rightarrow 0} \frac{\left(1 - e^{i\Omega t}\right)}{\Omega} \rightarrow -it, \quad (5.20)$$

so for the general polaron DC mobility, we get,

$$\mu_{dc}^{-1} = -\frac{4e^2}{nm_0\hbar} \frac{V_0 S_{n-1}}{(2\pi)^n} \int_0^\infty dt t \int_0^\Lambda dq q^{n+1} |M_q|^2 \operatorname{Im}\left\{D_{\omega_q}(t)e^{-q^2 r_p^2 G(t)}\right\}. \quad (5.21)$$

5.7.1 Specialising to the Fröhlich Model

Now equipped with the general polaron variational equations for the free energy and the corresponding memory function, we can specialise in the Fröhlich model by substituting

$$|M_q|^2 = g_F^2(n)/V_0 q^{n-1}, \quad (5.22a)$$

$$\omega_q = \omega_0, \quad (5.22b)$$

$$\Lambda \rightarrow \infty. \quad (5.22c)$$

The q -space integral is evaluated,

$$\begin{aligned} I_F(n) &= \frac{g_F^2(n) S_{n-1}}{(2\pi)^n} D_{\omega_0}(t) \int_0^\infty dq q^2 e^{-q^2 r_p^2 G(t)}, \\ &= \frac{g_F^2(n) S_{n-1} \sqrt{\pi}}{(2\pi)^n 4r_p^3} \frac{D_{\omega_0}(t)}{G(t)^{\frac{3}{2}}}, \\ &= \alpha_F \frac{\sqrt{\pi}}{2r_p^3} \frac{(2\sqrt{\pi})^{-n}}{\Gamma\left(\frac{n}{2}\right)} \frac{D_{\omega_0}(t)}{G(t)^{\frac{3}{2}}}. \end{aligned} \quad (5.23)$$

The memory function for the Fröhlich model is then,

$$\Sigma_F(\Omega) = \frac{1}{m_0 \hbar \Omega r_p^3} \frac{\pi \sqrt{2\pi} \alpha_F}{\Gamma\left(\frac{n}{2} + 1\right) (2\sqrt{\pi})^n} \int_0^\infty dt \left(1 - e^{i\Omega t}\right) \frac{D_{\omega_0}(t)}{\left[G(t)\right]^{3/2}}. \quad (5.24)$$

and the inverse Fröhlich DC mobility is,

$$\mu_{dc}^{-1} = -\frac{e^2}{m_0 \hbar r_p^3} \frac{\pi \sqrt{2\pi} \alpha_F}{\Gamma\left(\frac{n}{2} + 1\right) \left(2\sqrt{\pi}\right)^n} \int_0^\infty dt \frac{t D_{\omega_0}(t)}{[G(t)]^{3/2}}. \quad (5.25)$$

5.7.2 Specialising to the Holstein Model

We can specialise in the Holstein model by substituting,

$$|M_{\mathbf{q}}|^2 = g_H^2(n)/N, \quad (5.26a)$$

$$\omega_{\mathbf{q}} = \omega_0, \quad (5.26b)$$

$$\Lambda = 2\sqrt{\pi} \left(V_0 \Gamma\left(\frac{n}{2} + 1\right) \right)^{1/n} \equiv \Lambda_n. \quad (5.26c)$$

The q -space integral is evaluated,

$$\begin{aligned} I_H(n) &= \frac{g_H^2(n) S_{n-1}}{(2\pi)^n} D_{\omega_0}(t) \int_0^{\Lambda_n} dq q^{n+1} e^{-q^2 r_p^2 G(t)}, \\ &= \frac{g_H^2(n) S_{n-1}}{2(2\pi)^n r_p^{n+2}} \frac{D_{\omega_0}(t)}{G(t)^{\frac{n}{2}+1}} \left[\Gamma\left(\frac{n}{2} + 1\right) - \Gamma\left(\frac{n}{2} + 1, r_p^2 \Lambda_n^2 G(t)\right) \right], \\ &= \frac{1}{2r_p^2} \frac{ng_H^2(n)}{(2r_p \sqrt{\pi})^n} \frac{D_{\omega_0}(t)}{G(t)^{\frac{n}{2}+1}} \left[1 - \frac{\Gamma\left(\frac{n}{2} + 1, r_p^2 \Lambda_n^2 G(t)\right)}{\Gamma\left(\frac{n}{2} + 1\right)} \right]. \end{aligned} \quad (5.27)$$

The memory function for the Holstein model is then:

$$\Sigma_H(\Omega) = \frac{1}{m_0 \hbar \Omega \gamma r_p^{n+2}} \frac{4n\alpha_H}{(2\sqrt{\pi})^n} \int_0^\infty dt \left(1 - e^{i\Omega t}\right) \frac{D_{\omega_0}(t)}{G(t)^{\frac{n}{2}+1}} \left[1 - \frac{\Gamma\left(\frac{n}{2} + 1, r_p^2 \Lambda_n^2 G(t)\right)}{\Gamma\left(\frac{n}{2} + 1\right)} \right], \quad (5.28)$$

where $\gamma = \hbar\omega_0/J$ is the adiabaticity. The inverse Holstein DC mobility is then,

$$\mu_{dc}^{-1} = \frac{e^2}{m_0 \hbar \gamma r_p^{n+2}} \frac{4n\alpha_H}{(2\sqrt{\pi})^n} \int_0^\infty dt \frac{D_{\omega_0}(t)}{G(t)^{\frac{n}{2}+1}} \left[1 - \frac{\Gamma\left(\frac{n}{2} + 1, r_p^2 \Lambda_n^2 G(t)\right)}{\Gamma\left(\frac{n}{2} + 1\right)} \right]. \quad (5.29)$$

5.8 The Optimal Self-Consistent Response Function

5.8.1 Statics = Dynamics

The function $\Sigma(\Omega)$, which gives the lowest energy in the variational principal at zero temperature, satisfies the integral equation,

$$\Sigma(\Omega) = \frac{2}{n} \sum_{\mathbf{q}} |M_{\mathbf{q}}|^2 q^2 \int_0^\infty d\tau (1 - \cos(\Omega\tau)) e^{-\omega_{\mathbf{q}}\tau} e^{-q^2 r_p^2 [G(0) - G(\tau)]}, \quad (5.30)$$

where,

$$G(\tau) = \int_{-\infty}^{\infty} \frac{d\omega}{2\pi} \frac{e^{i\omega\tau}}{m\omega^2 - \Sigma(\omega)}. \quad (5.31)$$

The polaron Green's function $G(\tau)$ that minimises the polaron free energy at arbitrary temperature without applied electric and magnetic fields also produces the optimal impedance function $z(\Omega)$.

Generalising the variational equations to a general polaron system, we obtain,

$$F \leq \frac{n}{\beta} \sum_{l=1}^{\infty} \ln \left(\frac{Z(\omega_l)}{m\omega_l^2} \right) - \frac{n}{\beta} \sum_{l=1}^{\infty} \frac{1 - m\omega_l^2}{Z(\omega_l)} - \int_0^{\frac{\hbar\beta}{2}} d\tau \sum_{\mathbf{q}, j} |M_{\mathbf{q}, j}|^2 D_{\mathbf{q}, j}(\tau) e^{-q^2 r_p^2 [G(0) - G(\tau)]}, \quad (5.32)$$

where,

$$\Sigma(\tau) = \frac{2}{\beta} \sum_{l=1}^{\infty} \frac{1 - \cos(\omega_l \tau)}{Z(\omega_l)}, \quad (5.33)$$

and,

$$Z(\omega_l) = m\omega_l^2 + 4 \int_{-\infty}^{\infty} d\Omega \frac{P}{\Omega} \frac{G(\Omega)\omega_l^2}{\Omega^2 + \omega_l^2}, \quad (5.34)$$

and $\omega_l \equiv 2\pi l/\beta$, $l \in \mathbb{N}$.

CHAPTER 6

APPLICATION FOR MATERIALS

“One shouldn’t work on semiconductors, that is a filthy mess; who knows whether any semiconductors exist.”

—Wolfgang Pauli, *Letter to Peierls, 1931*

In this chapter, I apply these methods to calculate the polaronic properties of materials. Using the multimode extension to the Fröhlich polaron, I evaluate the polaron energy, mass, mobility and optical conductivity of bulk Methylammonium Lead Iodide Perovskites using material data from Brivio et al. [20] and compare the results to the single effective mode method of Hellwarth and Biaggio [21]. I use the small Holstein polaron extension to calculate the polaron energy, mass, mobility and optical conductivity of bulk Rubrene crystals using material data obtained from Ordejon et al. [22]. I use the anisotropic band extension to calculate the Zero-Point Renormalisation (ZPR) and polaron size with weak coupling perturbation results for dozens of II-VI, III-V and oxide semiconductor materials to characterise the validity of the continuum approximation in the Fröhlich model and the use of the perturbation approximation. The data for these materials was taken from Guster et al. [8]. Finally, do a high-throughput analysis of 1258 materials from the Materials Project [13] used in the Liege Dataset [14]. Here, I compare my ZPR results with those obtained from perturbation theory [23] and further calculate these materials’ polaron mass and mobility.

6.1 Methylammonium Lead Halide Perovskites

Having extended the Feynman theory with explicit phonon modes in the *model* action, I now try and answer what improvement this makes.

Material	$\epsilon_{\text{optical}}$	ϵ_{static}	ω_0	m_b
MAPbI ₃ -e	4.5	24.1	2.25	0.12
MAPbI ₃ -h	4.5	24.1	2.25	0.15

Table 6.1: Parameters of the Feynman polaron model (single effective phonon mode) are used in this work. Relative high frequency (ϵ_∞) and static (ϵ_0) dielectric constants are given in units of the permittivity of free space (ϵ_{vac}). Frequency (f) is in THz. Effective mass (m_b) is in units of the bare electron mass. These data are as in Ref. [59].

Base Frequency	Polaron Frequency	Infrared Activity	Coupling α_j
4.02	10.8	0.0817	0.0340
3.89	10.4	0.00631	0.00300
3.53	9.46	0.0535	0.0310
2.76	7.38	0.0213	0.0230
2.44	6.53	0.232	0.336
2.25	6.03	0.262	0.465
2.08	5.57	0.234	0.505
2.03	5.45	0.0623	0.142
1.57	4.20	0.0367	0.161
1.02	2.73	0.0126	0.162
1.00	2.69	0.00682	0.0910
0.997	2.67	0.0104	0.141
0.920	2.47	0.011	0.182
0.801	2.14	0.00168	0.0400
0.574	1.54	0.00646	0.349

Table 6.2: Infrared activity of phonon modes in MAPbI₃ taken from [20], scaled to their ground-state polaron value by the multimodal $w = 2.6792$ factor for MAPbI₃-e of this work (Table 6.3).

Halide perovskites are relatively new semiconductors of considerable technical interest. Due to their unusual mix of light, effective mass, and strong dielectric electron-phonon coupling, they host strongly interacting large polarons. Recently, the coherent charge-carrier dynamics upon photo-excitation are being measured, the Terahertz spectroscopy showing rich transient vibrational features [88].

Therefore, I use this system to represent the more complex systems that could be modelled with our extended theory. Applied to the 15 optical solid-state phonon modes in MAPbI_3 , I show that my explicit mode method predicts slightly higher mobility for temperatures 0 K to 400 K, to a maximum of 20 % increase at 100 K. At 300 K I predict electron and hole mobilities of 160 and 112 $\text{cm}^2\text{V}^{-1}\text{s}^{-1}$ respectively. This is to be compared to previous predictions of 133 and 94 $\text{cm}^2\text{V}^{-1}\text{s}^{-1}$ for one effective phonon mode evaluated using Hellwarth and Biaggio's [21] 'B scheme' (see Eqs. (2.261) and of 2.25 THz, as evaluated in [59]. More importantly, this theory recovers considerable structure in the complex conductivity and impedance functions as individual phonon modes are activated. The effective and explicit methods show the same temperature and frequency dependence towards higher temperatures - the quantum details are washed out.

In what follows, I take the materials data from [59], which I reproduce here in Table 6.1.

6.1.1 MAPI Polaron Free energy

I compare the polaron free energy and variational parameters evaluated by our explicit phonon frequency method presented in Eq. (4.2) to Hellwarth and Biaggio's effective phonon frequency scheme (scheme 'B' in Eqs. (58) and (59) in [21]),

$$\frac{\kappa_{\text{eff}}^2}{\omega_{\text{eff}}^2} = \sum_{j=1}^m \frac{\kappa_j^2}{\omega_k^2} \quad (6.1\text{a})$$

$$\kappa_{\text{eff}}^2 = \sum_{j=1}^m \kappa_j^2, \quad (6.1\text{b})$$

that use an effective LO phonon mode frequency ω_{eff} and associated infrared oscillator strength κ_{eff} derived from sums over the phonon modes j .

I apply these methods to the 15 solid-state optical phonon branches of MAPbI_3 , of which the frequencies and infrared activities are shown in Table 6.2.

Using the Hellwarth and Biaggio [21] effective phonon frequency 'B' scheme, the effective phonon frequency for MAPbI_3 is $\omega_0 = 2.25 \cdot 2\pi$ THz and the Fröhlich alpha for MAPbI_3 -e is $\alpha = 2.39$ and MAPbI_3 -h is $\alpha = 2.68$, as in [59] (values from bulk dielectric constants).

Using Eq. (3.5), we calculated the partial Fröhlich alpha α_j parameters for each of the 15 phonon branches in MAPbI_3 , which are given in Table 6.2. For $\text{MAPbI}_3\text{-e}$ the partial Fröhlich alphas sum to $\alpha = 2.66$ and for $\text{MAPbI}_3\text{-h}$ they sum to $\alpha = 2.98$. These 15 partial alphas α_j and corresponding phonon frequencies ω_j were then used in the variational principle for the multiple phonon-dependent free energy in Eq. (4.2). From Eq. (4.2), we variationally evaluate a v and w parameter.

Fig. 6.1 shows the polaron free energy comparison. The explicit multiple phonon mode approach predicts a higher free energy at temperatures $T < 65\text{K}$ and a lower free energy at temperatures $T > 65\text{K}$. See Table 6.3 for our athermal results, where we find new multiple-mode estimates for the polaron binding energy E_b (at 0 K) for $\text{MAPbI}_3\text{-e}$ as $E_b = -19.52$ meV and $\text{MAPbI}_3\text{-h}$ as $E_b = -21.92$ meV. Also see Table 6.4 for our thermal results at $T = 300$ K, where we find new multiple-mode estimates for the polaron free energy F for $\text{MAPbI}_3\text{-e}$ at 300 K as $F = -42.84$ meV and $\text{MAPbI}_3\text{-h}$ as $F = -50.40$ meV. These are to be compared to our previous results in [59], which are also provided in Tables (6.3, 6.4).

Fig. 6.1 shows the comparison in polaron variational parameters v and w . We have different trends for the polaron free energy and variational v and w parameters, which shows that we find quite a different quasi-particle solution from our multiple phonon scheme compared to the single effective frequency scheme.

The results in Fig. 6.1 provide a comparative analysis of polaron properties in methylammonium lead iodide (MAPbI_3) using two theoretical approaches: the single effective phonon mode approach (represented by blue lines) and the explicit multiple phonon mode approach (represented by red lines). This analysis focuses on three key aspects: polaron free energy, variational parameters, and temperature-dependent mobility.

The left panel shows the polaron binding energy as a function of temperature. The single-mode and multimode approaches indicate a reduction in polaron free energy as temperature increases. However, the multimode approach (red) predicts a more pronounced decrease in the polaron free energy across the entire temperature range, suggesting that accounting for multiple phonon modes leads to stronger electron-lattice interactions. The difference between the approaches at higher temperatures becomes increasingly noticeable, with the multimode model yielding a considerably lower polaron binding energy than the single-mode result (blue).

The temperature dependence of the two polaron variational parameters, v and w , is depicted in the top-right panel. Both models reveal an increase in these parameters with rising temperature, where v reflects the harmonic coupling strength and w represents the temporal decay rate of the coupling. The multimode approach (red) results in slightly lower values for both parameters than the single-mode approach (blue), particularly at higher temperatures.

Material	α	v	w	E_b
MAPbI ₃ -e	2.39	3.31	2.66	-23.0 meV
MAPbI ₃ -h	2.68	3.36	2.62	-25.9 meV
MAPbI ₃ -e	2.66	3.29	2.68	-19.5 meV
MAPbI ₃ -h	2.98	3.34	2.63	-21.9 meV

Table 6.3: Athermal 0 K results. Dielectric electron-phonon coupling (α), Feynman athermal variational parameters (v and w) and polaron binding energy (E_b) for an effective phonon mode (top rows) and for multiple explicit phonon modes (bottom rows).

Material	α	v	w	F	μ	M	r_f
MAPbI ₃ -e	2.39	19.9	17.0	-35.5	136	0.37	43.6
MAPbI ₃ -h	2.68	20.1	16.8	-43.6	94	0.43	36.9
MAPbI ₃ -e	2.66	35.2	32.5	-42.8	160	0.18	44.1
MAPbI ₃ -h	2.98	35.3	32.2	-50.4	112	0.20	37.2

Table 6.4: 300 K Results. Dielectric electron-phonon coupling (α), Feynman thermal variational parameters (v and w), polaron free energy (F , meV), dc mobility (μ , $\text{cm}^2\text{V}^{-1}\text{s}^{-1}$), polaron effective mass (M , m^*) and Schultz polaron radius (r_f , Å) for an effective phonon mode (top rows) and for multiple explicit phonon modes from Table 6.2 (bottom rows).

This difference suggests that the multimode model more accurately captures the complex interactions between the electron and various phonon modes, leading to more subtle but significant changes in the polaron properties.

6.1.2 MAPI DC Polaron Mobility

I calculate the zero-frequency (direct current, dc) electron-polaron mobility μ in MAPbI₃ using the effective phonon mode and explicit multiple phonon mode approaches. Both approaches have the same relationship between the mobility and the memory function (Eqs. (2.202, 2.211)), but the effective mode approach uses the memory function $\Sigma(\Omega)$ from Eq. (2.202) (the FHIP [17] memory function, Eq. (35) *ibid.*), whereas the multiple phonon mode approach uses our $\Sigma_{\text{multi}}(\Omega)$ from Eqn. (5.9) (with a sum over the phonon modes).

The bottom panel of Fig. 6.1 presents the temperature dependence of polaron mobility. Contrary to expectations, the multimode approach (red) consistently predicts higher mobility than the single-mode approach (blue) across all temperatures. This suggests that the more accurate treatment of phonon modes in the multimode model may reduce scattering effects or result in more efficient charge transport. One possible reason is that the multimode approach allows the electron to couple more effectively to the different phonon modes, distributing the interaction across multiple modes and reducing the overall scattering rates.

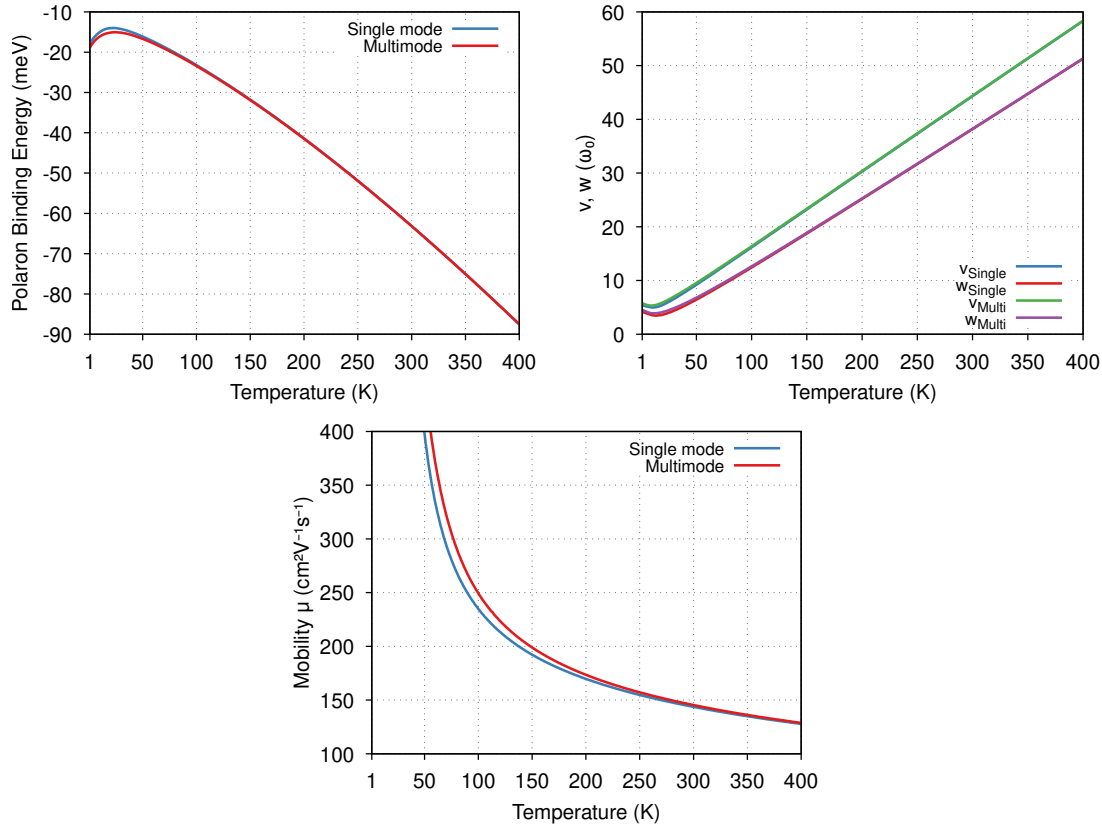


Figure 6.1: Left: Comparison of the polaron free energy as a function of temperature for MAPbI_3 , using the single effective phonon mode approach (blue) and the explicit multiple phonon mode approach (red). Top-right: Comparison of the two polaron variational parameters, v and w , for MAPbI_3 , with the single effective phonon mode approach (blue) and the explicit multiple phonon mode approach (red). Bottom: Comparison of the temperature-dependent mobility predicted for MAPbI_3 , using the single effective phonon mode approach (blue) and the explicit multiple phonon mode approach (red).

In contrast, the single-mode approach confines the interaction to a single phonon mode, which may overestimate the scattering effects and consequently predict lower mobility. This highlights the importance of considering multiple phonon interactions when modelling polaron transport, especially in materials with complex phonon spectra like MAPbI_3 .

6.1.3 MAPI Polaron Optical Conductivity

I calculate the complex impedance $z_{\text{multi}}(\Omega)$ for the polaron in MAPbI_3 using Eq. (2.210), where the only difference between the effective mode and multiple mode approaches is in the form of the memory function $\Sigma_{\text{multi}}(\Omega)$ as described for the polaron mobility above. The complex conductivity $\sigma_{\text{multi}}(\Omega)$ is the reciprocal of the complex impedance, $\sigma_{\text{multi}}(\Omega) = 1/z_{\text{multi}}(\Omega)$.

Fig. 6.2 illustrates the temperature and frequency dependence of the real and imaginary components of the complex conductivity for MAPbI_3 , focusing on the impact of phonon

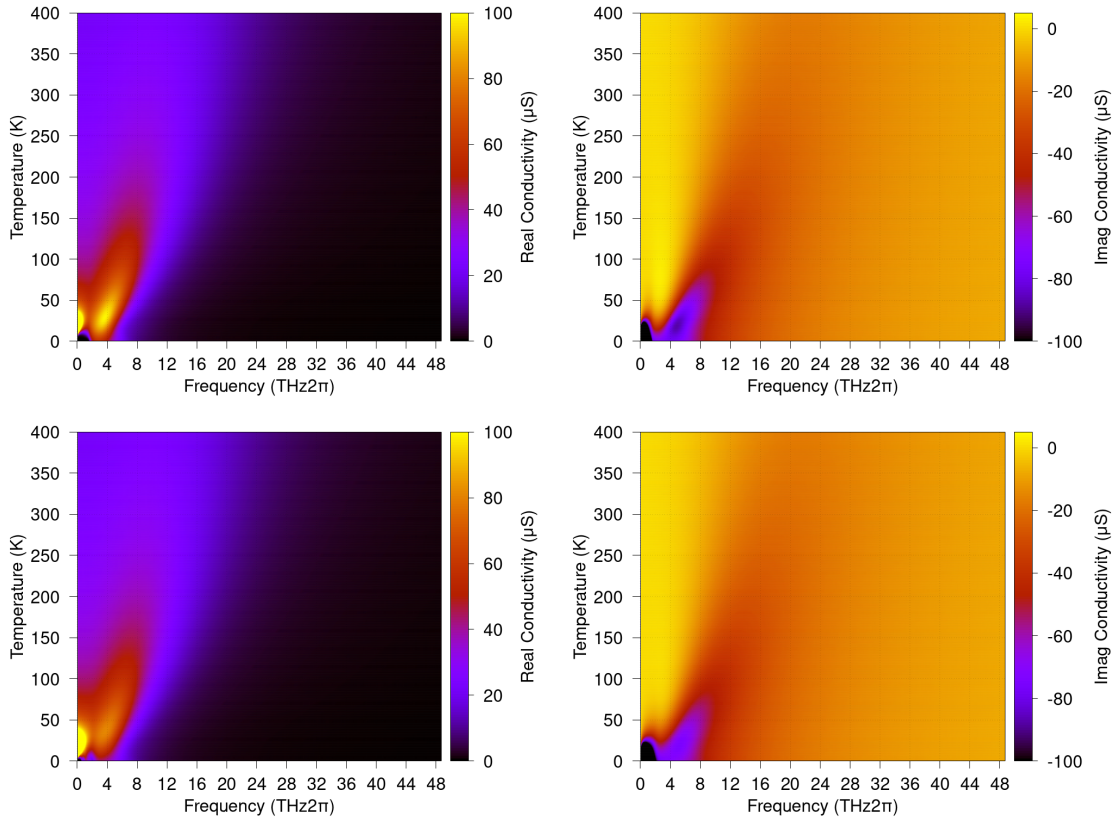


Figure 6.2: Temperature and frequency dependence of the real (left) and imaginary (right) components of the complex conductivity for MAPbI_3 , comparing two theoretical models for phonon interactions. The top row represents the single effective phonon mode approach, while the bottom row includes all explicit phonon branches.

interactions. The top row corresponds to a model that uses a single effective phonon frequency of Hellwarth's B scheme. In contrast, the bottom row incorporates all the explicit phonon branches of the material. These two approaches allow for a comparative analysis of how phonon modes influence the dynamic conductivity of polarons within the material.

In the real conductivity plots (left panels), both models demonstrate a strong temperature and frequency dependence, with a pronounced increase in conductivity at lower temperatures (below approximately 150 K) and lower frequencies (below 10 THz). In the top row, where a single effective phonon mode is used, the real conductivity increases sharply and then plateaus as the temperature rises, particularly at low frequencies. This behaviour reflects the simplified interaction between electrons and phonons when only one representative phonon mode is considered. However, in the bottom row, where all phonon branches are included, the conductivity in the same low-temperature and low-frequency regions shows a more pronounced detail. This suggests that accounting for multiple phonon branches enables the electron to interact with a broader spectrum of lattice vibrations, facilitating greater charge carrier mobility at lower temperatures and frequencies.

As temperature increases, the influence of phonon scattering becomes more significant in both models, leading to a more uniform conductivity response across the frequency spectrum. However, the conductivity in the model with multiple phonon branches remains slightly higher at intermediate temperatures, indicating that the additional phonon interactions may reduce scattering effects or allow more efficient charge transport across a range of temperatures.

The imaginary conductivity (right panels) offers further insight into the material's dynamic behaviour. In both models, the imaginary conductivity remains negative across the temperature and frequency range, indicating capacitive-like behaviour where charge carriers are delayed relative to the applied electric field. At low temperatures, the imaginary conductivity increases in magnitude with frequency, particularly in the single-mode model (top row). In the bottom row, where all phonon branches are considered, the imaginary conductivity exhibits more pronounced transitions at low temperatures and frequencies. This suggests that including multiple phonon branches allows for a more detailed description of how electron-phonon interactions evolve with increasing temperature and frequency. Specifically, the sharper transitions in the imaginary conductivity reflect a more complex phase shift behaviour that arises when a broader spectrum of phonon interactions is included.

The comparison between the single-mode and multi-mode models highlights the importance of accurately accounting for the phonon spectrum in predicting polaron transport properties. The single-mode model provides a simpler, more averaged view of electron-phonon interactions, resulting in smoother transitions in both the real and imaginary conductivity. However, by including explicit phonon branches, the multi-mode model captures the complexity of the interactions more effectively, particularly at lower temperatures and frequencies where polaron mobility is highest. The enhanced real conductivity in the multi-mode model at low temperatures suggests that the broader phonon interactions lead to less resistance to charge transport. In contrast, the sharper imaginary conductivity transitions indicate more nuanced phase dynamics.

6.1.4 MAPI Polaron Memory Function

Fig. 6.3 presents a detailed analysis of the temperature and frequency dependence of the real and imaginary components of the memory function for polarons in MAPbI_3 , calculated using two different approaches for phonon interactions. The top row employs a model based on a single effective phonon frequency, while the bottom row incorporates explicit phonon branches. The real component of the memory function is shown in the left panels, while the imaginary component is depicted in the right panels.

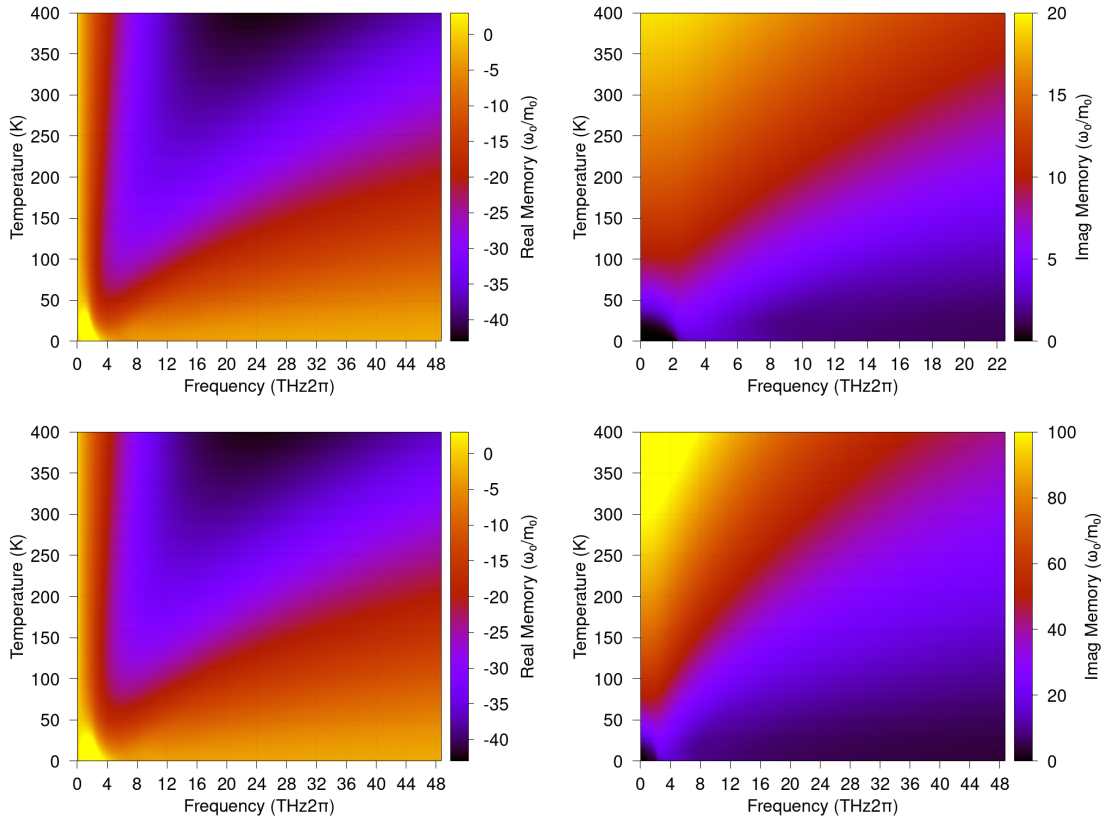


Figure 6.3: Temperature and frequency dependence of the real (left) and imaginary (right) components of the polaron memory function for MAPbI_3 , comparing two theoretical models for phonon interactions. The top row uses a single effective phonon frequency, while the bottom row includes all explicit phonon branches.

The imaginary memory function (right panels) describes the energy dissipation in the polaron system due to interactions with the phonon modes. The imaginary memory function strongly depends on temperature and frequency in both the single-mode (top row) and multi-mode (bottom row) approaches. The imaginary memory function is relatively small at low temperatures and frequencies, reflecting minimal energy loss due to scattering. However, as temperature and frequency increase, the imaginary memory function becomes larger, signifying greater energy dissipation. The transition occurs more gradually in the single-mode approach, while the multi-mode model shows sharper transitions, particularly at higher temperatures and frequencies. This suggests that including multiple phonon branches leads to more complex and efficient scattering processes, contributing to energy dissipation.

A notable difference between the approaches is higher frequencies (above approximately 20 THz) and temperatures. In the single-mode model, the imaginary memory function continues to decrease. Still, it remains relatively uniform, whereas the multi-mode approach shows a steeper decline, indicating stronger energy loss due to more pronounced phonon scattering. This effect can be attributed to the fact that in the multi-mode model, the

interaction between the electron and various phonon modes becomes increasingly important at higher energies, resulting in more intricate dissipation dynamics.

The real component of the memory function (left panels) provides insight into the phase dynamics of the polaron system, representing the lag in the system's response to external perturbations. In both models, the real memory function increases with temperature and frequency, indicating a larger phase shift as the system is subjected to stronger phonon interactions. In the single-mode approach, the real memory function gradually increases with temperature and frequency, reaching moderate values at high frequencies. On the other hand, the multi-mode model predicts a significantly stronger increase in the real component, especially at higher frequencies, reflecting the increased complexity of the phase dynamics when multiple phonon branches are explicitly included.

The difference between the two models becomes particularly pronounced at low temperatures and high frequencies, where the multi-mode model shows a much sharper rise in the real memory function. This suggests that including explicit phonon branches leads to stronger phase shifts due to more varied interactions between the electron and the phonon spectrum. The broader range of phonon interactions captured by the multi-mode model provides a more comprehensive picture of the system's dynamic response.

6.1.5 Modelling Terahertz Spectroscopy Photoconductivity Dynamics in Metal-Halide Perovskites

Recently, we used ultrafast visible pump-infrared push-terahertz probe spectroscopy to measure the real-time photo-conductivity of methyl-ammonium lead iodide in [89]. In this paper, I provided my multiple phonon mode mobility, applied to the 15 modes of MAPI in Table 6.2, to model the complex conductivity and compare the results to the photo-conductivity measurements.

Fig. 6.4 presents key results from a frequency-resolved pump-push-probe (PPP) experiment in the terahertz (THz) range. The two-dimensional map in panel (a) illustrates the evolution of the THz probe intensity as a function of both frequency and push-probe delay, with the pump-push delay set to 10 ps. Two clear resonances at approximately 1.25 and 2.25 THz are visible in the map, corresponding to strong carrier-phonon coupling, specifically with phonon modes associated with the Pb-I bond vibrations in the material. These phonons are essential to the system's polaron dynamics, as indicated by the significant reduction in absorption around these frequencies when the "push" arrives, indicating an energetic shift in the carriers.

In panel (b), the THz photoconductivity spectra decompose the real ($\Delta\sigma_{Re}$) and imaginary ($\Delta\sigma_{Im}$) components of the complex conductivity at various times relative to the arrival of

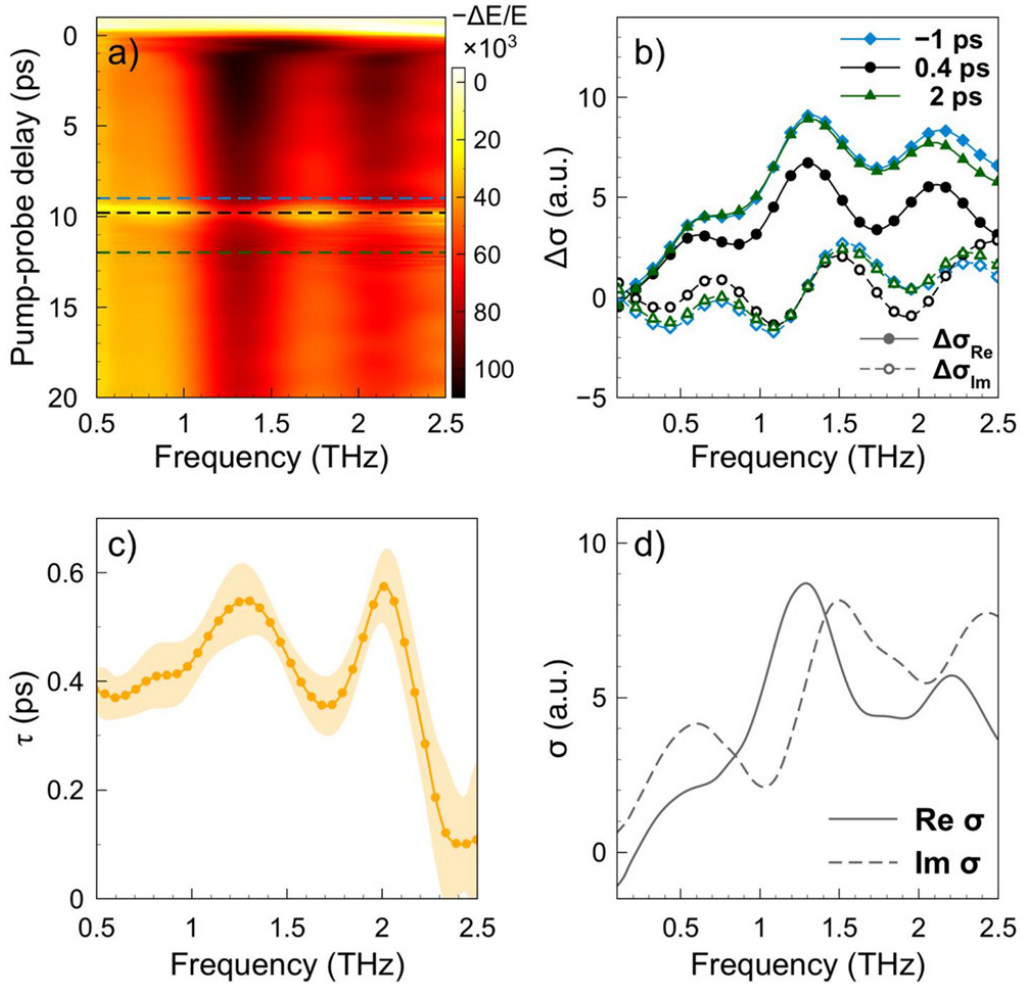


Figure 6.4: Reprinted from ref. [89]. (a) Two-dimensional probe frequency vs. push–probe delay intensity map from a pump–push–THz probe experiment, with the pump–push delay set to 10 ps. (b) THz photoconductivity spectra showing the real and imaginary components of the complex conductivity ($\Delta\sigma = \Delta\sigma_{Re} + \Delta\sigma_{Im}$) before, during, and after the push. (c) Probe recovery time at different frequencies. (d) Simulated frequency-resolved conductivity using the FHIP polaron mobility theory, showing agreement with experimental peaks at 1.25 and 2.25 THz, corresponding to carrier-phonon coupling.

the push. The data show that before the push (blue line), the photoconductivity peaks at the resonant frequencies of 1.25 and 2.25 THz are dominant. As the push arrives (black line), there is a substantial reduction in both real and imaginary components, particularly at these frequencies. This supports the idea that these phonon modes are strongly coupled to the carriers. After the push (green line), the conductivity begins to recover. Still, the phonon-coupled peaks remain diminished, reflecting the non-Drude-like behaviour associated with polaronic effects rather than free carriers. This suggests that the carriers behave not simply as free charges but are coupled to the phonon modes, leading to a complex photoconductivity response.

Panel (c) shows the THz probe signal's recovery time (τ) across different frequencies. The recovery time is frequency-dependent, with the slowest recovery occurring at the two resonant frequencies (1.25 and 2.25 THz). This further reinforces the notion that these phonon modes are strongly coupled to the carriers. This behaviour suggests that when the push excites the carriers, the phonon modes are directly heated, and their energy dissipation back into the lattice takes longer, particularly at the coupled phonon frequencies. The strong coupling between carriers and phonons likely prolongs the recovery time at these frequencies, as the energy stored in these modes must dissipate before the carriers can fully relax back to equilibrium.

Panel (d) shows a simulated frequency-resolved conductivity using the FHIP polaron mobility theory and an extended material-specific model. The real part of the simulated conductivity shows peaks at frequencies that correspond well to the observed resonances in the experimental data, specifically around 1.25 and 2.25 THz, confirming the relevance of polaron dynamics in the material. This simulation supports that polaron-renormalised carrier interactions with phonon modes drive the observed response. The best fit to the data is achieved using a zero-temperature mobility theory, suggesting that the subpicosecond timescale of the THz measurements corresponds to a prethermal regime, where the polaron mobility is not yet fully equilibrated with the lattice.

In summary, incorporating multiple phonon branches provides a more comprehensive and accurate depiction of polaron dynamics in MAPbI_3 . The multi-mode model consistently predicts higher real conductivity and more pronounced imaginary conductivity transitions, particularly at low temperatures and frequencies, with more substantial energy dissipation and stronger phase shifts in the memory function, especially at higher temperatures and frequencies. These findings underscore the critical role that phonon interactions play in determining the material's dynamic and transport properties. The enhanced scattering and phase dynamics captured by the multi-mode model highlight the importance of accounting for the full phonon spectrum to model the electron-phonon interactions that govern polaron behaviour accurately. These insights are crucial for optimising the charge transport properties of MAPbI_3 in electronic and optoelectronic devices, where charge carrier mobility and dynamic response are key factors for performance.

g (meV)	ω_0 (THz)	J (meV)	a (Å)	γ	m_b (m_e)	λ^2	α
106.8	5.768	134.0	14.06	0.178	0.144	19.75	0.586

Table 6.5: 3D Rubrene Bulk crystal data derived from [22]. Here g is the Holstein hole-phonon coupling element, ω_0 is the single-mode effective phonon frequency, J is the electron transfer/hopping integral, a is the geometric-meaned crystal lattice constant, γ is the Holstein adiabaticity unitless parameter, m_b is the effective hole band-mass, $\lambda^2 = (g/\hbar\omega_0)^2$ is the unitless squared hole-phonon coupling element and $\alpha = \lambda^2\gamma/6$ is the 3D unitless Holstein electron-phonon parameter.

	v_0 (THz)	w_0 (THz)	M_0 (m_e)	R_0 (Å)	F_0 (meV)
Holstein	21.01	7.258	0.146	121.3	-6.867
Fröhlich	17.66	16.88	0.149	304.2	-5.842

Table 6.6: Ground-state polaron properties for a Rubrene Bulk crystal calculated using the variational Holstein and Fröhlich models.

6.2 Rubrene & Organic Crystals

The charge-carrier state is often considered a small polaron in organic electronic materials. This is frequently modelled with semi-classical transfer rate theories as a classical object hopping from site to site. The matrix elements that parameterise these rate equations can be calculated within certain approximations using electronic structure calculations. Still, defining the sites where the charge carriers are localised is challenging (and often input to the simulation and calculations).

One of the prototypical materials studied frequently to investigate electron-phonon coupling is Rubrene (5,6,11,12-tetraphenyltetracene), which has one of the highest carrier mobilities and can reach a few tens of cm^2/Vs for holes. This is a good test for applying our newly derived variational Holstein model to predict its charge-carrier mobility in bulk. We take parameters for Rubrene from Ordejon et al. [22] where they derived Peierls (off-site) and Holstein (on-site) contributions by fitting the generalise Holstein-Peirels model with Density Functional Theory (DFT) calculations performed using SEISTA code. I use their Holstein parameters coupling, which we list in Table 6.5, and use them within our newly derived variational Holstein method. For simplicity, we consider a single effective phonon

	v (THz)	w (THz)	M (m_e)	R (Å)	F (meV)	μ ($\text{cm}^2\text{V}^{-1}\text{s}^{-1}$)
Holstein	77.22	74.37	0.155	34.28	-18.10	47.72
Fröhlich	43.56	41.15	0.151	99.10	-10.95	92.59

Table 6.7: Room temperature (300 K) polaron properties for a Rubrene Bulk crystal calculated using the variational Holstein and Fröhlich models.

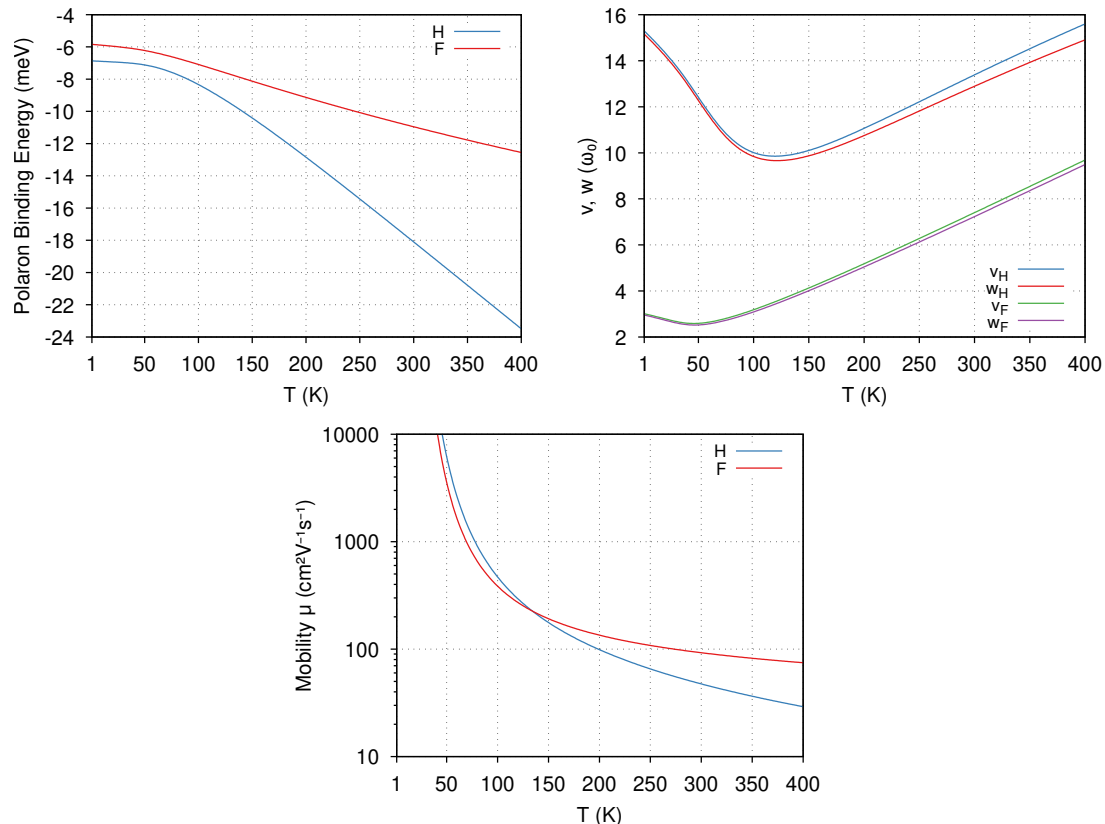


Figure 6.5: Polaron properties predicted from the variational parabolic Holstein and Fröhlich models for a bulk 3D Rubrene organic crystal. **Top-left:** The polaron binding energy (the polaron self-energy relative to the band extrema) F (meV) in Rubrene as a function of temperature (K). **Top-right:** Optimal variational parameters v and w (THz) as a function of temperature (K). **Bottom** The DC polaron mobility $\mu(T)$ ($\text{cm}^2\text{V}^{-1}\text{s}^{-1}$) as a function of temperature T (K).

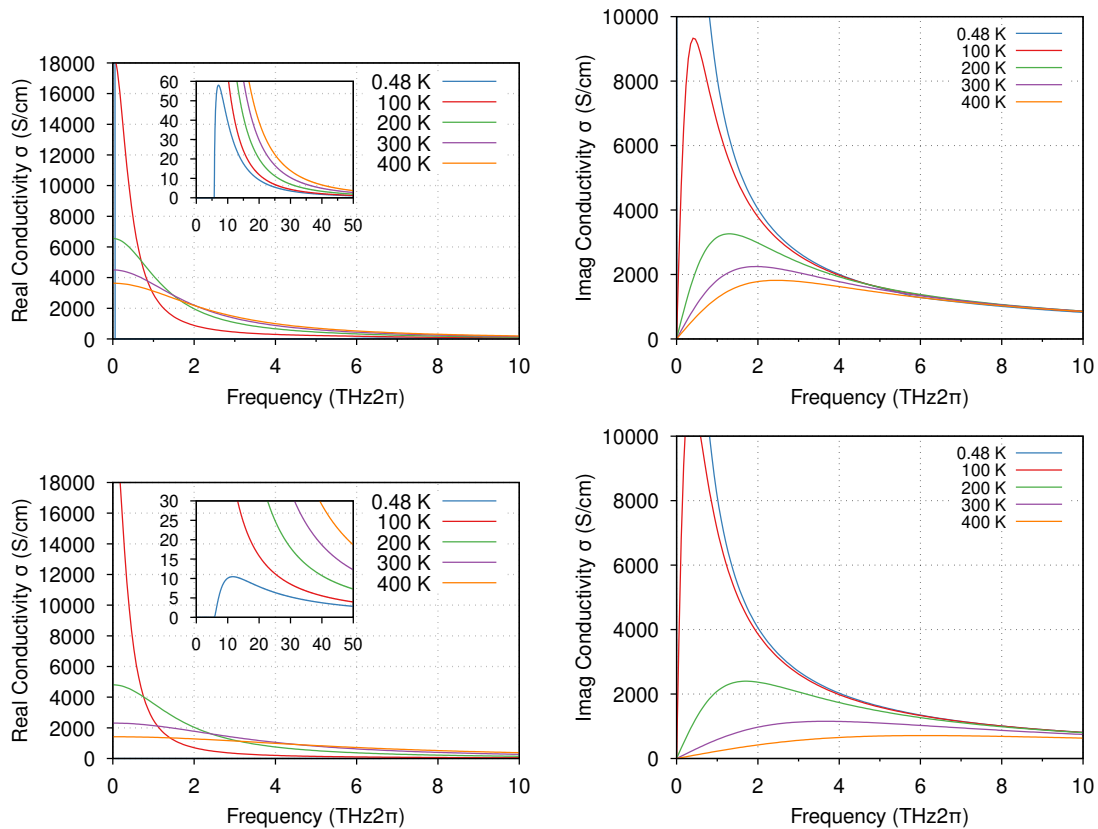


Figure 6.6: Frequency dependence of the polaron complex conductivity (in units of S cm^{-1}) predicted by the variational parabolic Holstein and Fröhlich models for a bulk 3D Rubrene organic crystal, for temperatures $T = 0.48 \text{ K}$, 100 K , 200 K , 300 K and 400 K . The top row shows the real (left) and imaginary (right) components of the Fröhlich complex conductivity. The bottom row shows the components of the parabolic Holstein complex conductivity's real (left) and imaginary (right).

frequency, though the technique presented here could be extended to multiple phonon modes, as we have demonstrated for the Fröhlich Hamiltonian [4].

6.2.1 Rubrene Athermal Properties

The results for ground-state Holstein and Fröhlich polarons for Rubrene are shown in Table 6.6. Likewise, Table 6.7 gives the result for $T = 300$ K, including the finite temperature DC mobility, which we calculate to be $\mu_{\text{Rubrene}}^{(H)} = 47.72 \text{ cm}^2\text{V}^{-1}\text{s}^{-1}$ for the Holstein polaron and $\mu_{\text{Rubrene}}^{(F)} = 92.59 \text{ cm}^2\text{V}^{-1}\text{s}^{-1}$ for the Fröhlich polaron. Immediately, the Holstein prediction is more inline with what's observed in experiments whereas the Fröhlich overestimates.

6.2.2 Rubrene Thermal Properties

In Fig. 6.5, I analyse the polaron properties predicted by the variational parabolic Holstein and Fröhlich models in a bulk 3D Rubrene organic crystal. This figure includes three subplots: the polaron binding energy, the optimal variational parameters, and the DC polaron mobility, each as a function of temperature.

The top-left subplot of Fig. 6.5 depicts the polaron binding energy, F , as a function of temperature (T). The binding energy is presented in millielectronvolts (meV). Both the Holstein (H) and Fröhlich (F) models show a decrease in binding energy with increasing temperature. Notably, the Holstein model (blue curve) predicts a more pronounced decline in binding energy compared to the Fröhlich model (red curve). At lower temperatures, the binding energy in the Holstein model is significantly higher, indicating stronger polaron formation. As temperature increases, the binding energies of both models converge, reflecting a reduction in polaron stabilisation due to thermal agitation.

The top-right subplot illustrates the optimal variational parameters v (dimensionless) and w (in units of ω_0) as functions of temperature. The parameters v_H and v_F (blue and red curves) represent the Holstein and Fröhlich models. Similarly, w_H and w_F (green and magenta curves) correspond to the w parameters. Both variational parameters exhibit non-monotonic behaviour with temperature, with distinct minima observed around 120 K for the Holstein model and 50 K for the Fröhlich model. This suggests that the polaron wavefunction undergoes significant changes at certain temperatures, potentially due to the competing effects of electron-phonon coupling and thermal excitation.

The bottom subplot shows the DC polaron mobility, $\mu(T)$, in units of $\text{cm}^2\text{V}^{-1}\text{s}^{-1}$, as a function of temperature. Both models' mobility decreases sharply with increasing temperature, indicating enhanced phonon scattering at higher temperatures. The two models predict similar mobilities below 120 K, with the Holstein mobility (blue curve) a

little higher than the Fröhlich model (red curve). However, the Fröhlich model predicts consistently higher mobility compared to the Holstein model above this temperature. This can be attributed to the long-range nature of the electron-phonon interactions in the Fröhlich model, which tends to preserve higher mobility despite thermal disruptions.

These results provide insights into the temperature dependence of polaron properties in 3D Rubrene crystals. The distinct behaviours of the Holstein and Fröhlich models highlight the importance of considering different electron-phonon interaction mechanisms when analysing organic semiconductors. The findings underscore the complex interplay between thermal effects and electron-phonon coupling, which governs polarons' formation, stability, and mobility in these materials.

6.2.3 Rubrene Complex Conductivity

Fig. 6.6 illustrates the frequency dependence of the polaron complex conductivity, presented in units of Siemens per centimetre (S/cm), as predicted by the variational parabolic Holstein and Fröhlich models for a bulk 3D Rubrene organic crystal at various temperatures. This figure contains four subplots: the real and imaginary components of the Fröhlich and Holstein complex conductivities, each plotted against frequency.

The top-left subplot of Fig. 6.6 displays the real component of the Fröhlich model's conductivity across a range of temperatures: 0.48 K, 100 K, 200 K, 300 K, and 400 K. At the lowest temperature (0.48 K), the real conductivity shows a significant one-phonon peak at low frequencies starting at the phonon frequency $\Omega = \omega_0 = 5.768$ THz, which rapidly decreases with increasing frequency. As temperature rises, the peak becomes less pronounced and is no longer visible, indicating a reduction in the polaronic response due to thermally excited phonons that generate an extra background response. The inset in the top-left subplot provides a closer view of the high-frequency behaviour, emphasising the one-phonon peak and the gradual decline in real conductivity across all temperatures.

The top-right subplot represents the imaginary component of the Fröhlich model's conductivity for the same temperature range. Like the real component, the imaginary conductivity peaks at low frequencies, with the magnitude decreasing as the temperature rises. This peak indicates the reactive part of the polaron response, which is dominant at lower frequencies and diminishes with increasing thermal agitation.

The bottom-left subplot shows the real component of the Holstein model's conductivity at the specified temperatures. The conductivity profile is similar to that of the Fröhlich model, with a prominent one-phonon peak at low frequencies starting at the phonon frequency that diminishes with increasing temperature to be replaced by a Drude-like background

response. The inset highlights the high-frequency region, revealing the temperature-dependent decrease in real conductivity.

The bottom-right subplot illustrates the imaginary component of the Holstein model's conductivity. This component also shows a peak at low frequencies, which decreases in magnitude as temperature increases. The behaviour is consistent with the Fröhlich model, although the absolute values and specific trends differ due to the distinct nature of electron-phonon interactions in the Holstein model.

These plots collectively demonstrate the frequency-dependent behaviour of polaron complex conductivity in 3D Rubrene crystals, as the Holstein and Fröhlich models predicted. The observed trends underscore the significant impact of temperature on the real and imaginary conductivity components. The strong polaronic interactions at low temperatures result in a high conductivity one-phonon peak at low frequencies. In contrast, increased thermal energy at higher temperatures disrupts these interactions due to thermally excited phonons, leading to a diminished polaronic response. These insights are crucial for understanding the dynamic electrical properties of organic semiconductors under varying thermal conditions.

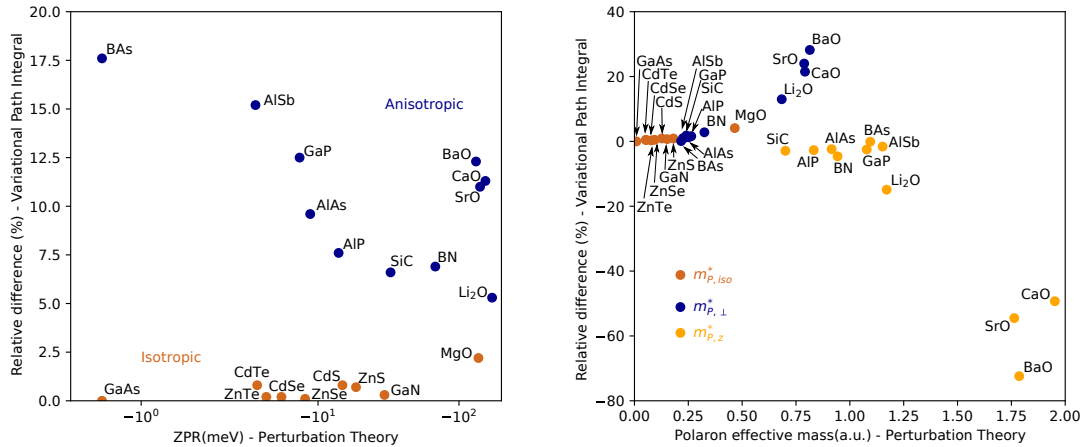


Figure 6.7: Both figures are taken from [8]. (left): The relative differences between the ground-state energy of the polaron determined using perturbation theory (which fully accounts for any anisotropy) and the Feynman variational approach (using my approximate treatment of anisotropy). (right): The relative difference between the effective masses was determined using perturbation theory and the Feynman variational approach (again, only approximately accounting for anisotropy). $m_{P,iso}^*$ is the isotropic effective mass, $m_{P,\perp}^*$ and $m_{P,z}^*$ are the in-plane and out-of-plane polaron effective masses.

6.3 Cubic & Anisotropic Materials

In [8], we investigate the polaron effective mass, radius and ground-state energy that arise from a generalised Fröhlich Hamiltonian that incorporates degenerate bands with anisotropy and multiple phonon branches. These polaron properties are calculated for 20 cubic materials (including II-VI compounds: CdS, CdSe, CdTe, ZnS, ZnSe, ZnTe; III-V compounds: AlAs, AlSb, AIP, BAs, BN, GaAs, GaN, GaP; oxides: BaO, CaO, Li₂O, MgO, SrO; and SiC) using the lowest order of perturbation theory and the strong coupling limit.

In the non-degenerate case, I provide a naïve extension of Feynman's path integral approach to include anisotropic effective band masses, which is used as a point of comparison with the full perturbative treatment for characterising the polaron in the weak-coupling limit (see section IIb in [8]). From Figure 6.7 (left), we see that the variational approach gives a lower estimate for the ground-state compared to the perturbative result for both isotropic (up to 2.5% lower) and anisotropic (up to 17.5% lower) materials. In Figure 6.7 (right), we have the relative difference in polaron effective mass between the two approaches. The most significant difference is found in materials that, within the Fröhlich approach, are found in [8] to be at the continuum limit breakdown where the discrete nature of the lattice cannot be ignored. These materials include BaO, CaO, SrO and, to a lesser extent, Li₂O. In both the anisotropic and isotropic cases, the relative difference increases with polaron

effective mass, and the in-plane and out-of-plane effective mass differences seem to diverge. This sudden increase in the relative difference is associated with a breakdown limit around $\alpha = 6$ in the perturbative approach for determining the polaron effective mass.

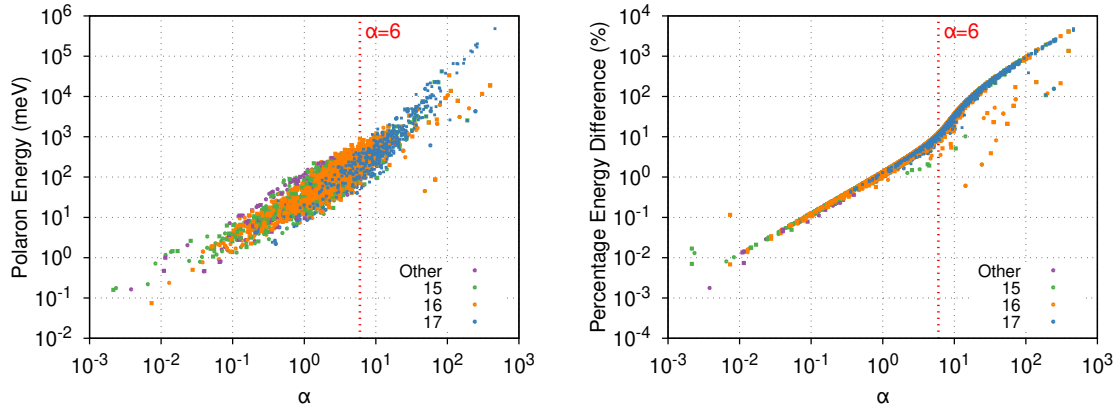


Figure 6.8: The left panel shows the polaron energy E meV as a function of the electron-phonon coupling constant α , calculated using Feynman's variational path integral theory for various materials, with groups 15, 16, and 17 highlighted. The right panel compares the percentage energy difference between the weak-coupling perturbation theory and the Feynman result, showing increasing deviations at higher α , particularly beyond $\alpha = 6$, indicating the breakdown of perturbation theory in the strong-coupling regime.

6.4 High-Throughput Material Classification

In this section, I analyse a comprehensive dataset of 1,258 materials from de Melo [23] using the FVA. I extend this approach to address scenarios involving multiple phonon modes in electron-phonon coupling, analogous to Miglio's Fröhlich model generalisation [63]. I examine these materials to illustrate the distribution of ground-state energy and the errors introduced by perturbation theories. Additionally, I calculate the room-temperature FHIP mobilities for all these materials and discuss trends that may offer design clues for future potential high-mobility materials.

6.4.1 Polaron Zero-Point-Renormalisation Energy

Fig. 6.8 analyses polaron energy for various materials, highlighting the electron-phonon coupling constant α , based on Feynman's variational path integral theory (left panel). In contrast, the right panel compares the weak coupling perturbation results for the Fröhlich polaron free energy and the Feynman result. The materials are categorised into groups 15, 16, and 17, with their data points distinguished by colour for easy comparison.

In the left panel, the polaron energy is plotted as a function of α on a logarithmic scale. The data spans a wide range of α , from 10^{-3} to over 10^3 , covering a broad spectrum of coupling strengths. The trend shows a general increase in polaron energy as α increases, with a near-linear relationship on the log-log scale for most of the data. The energy remains low for small values of α , indicating weak coupling and more delocalised polarons. As α exceeds one and moves towards stronger coupling, the polaron energy rapidly increases,

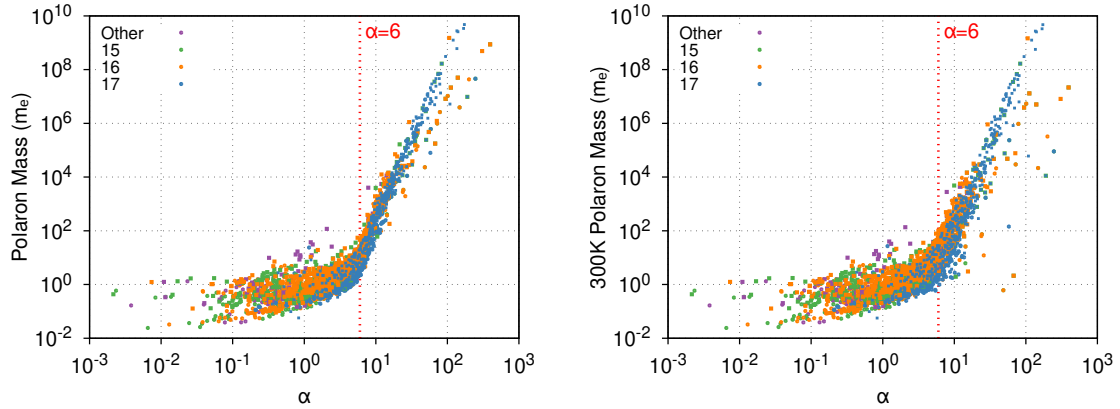


Figure 6.9: Polaron effective mass as a function of the electron-phonon coupling constant α for 1258 materials, with group 15, 16, and 17 elements highlighted. The left panel shows the effective polaron mass at zero temperature, while the right panel displays the results at room temperature (300 K). The critical value of $\alpha = 6$ (red dashed line) marks the transition from weak to strong coupling.

reflecting stronger localisation effects. A vertical dashed line at $\alpha = 6$ marks a significant coupling threshold, where the polaron becomes more localised. Materials from groups 15, 16, and 17 follow this general trend, but individual points show some scattering, indicating material-specific deviations from the general behaviour.

The right panel compares the percentage difference between the weak-coupling perturbation results for the Fröhlich polaron and the Feynman variational results. This comparison highlights the accuracy of the weak-coupling approximation for small α values, where the percentage difference is minimal (below 1%). As α increases, particularly beyond $\alpha = 6$, the deviation grows significantly, reaching several orders of magnitude at large α , indicating the breakdown of the weak-coupling approximation in the strong coupling regime. Materials in groups 15, 16, and 17 show similar trends, but again, some variation exists depending on the material, with some points deviating from the general behaviour at intermediate values of α . The significant deviation at large α highlights the necessity of using Feynman's path integral method for accurate calculations in the strong coupling regime, where perturbative approaches fail.

The figure emphasises the importance of non-perturbative methods like Feynman's theory as the electron-phonon coupling strengthens. The threshold at $\alpha = 6$ marks the transition to a regime where the weak-coupling perturbation theory is no longer valid, necessitating more advanced methods to capture the polaron's energy accurately.

6.4.2 Polaron Effective Mass

Fig. 6.9 illustrates the polaron effective mass renormalisation for 1258 materials, with group elements 15, 16, and 17 highlighted. The left plot represents the effective polaron

mass at zero temperature, while the right plot displays the same at room temperature (300 K). Both plots show the polaron mass as a function of the electron-phonon coupling constant α , with a clear trend of increasing mass as α grows. At small α , corresponding to weak electron-phonon coupling, the polaron mass remains close to the bare electron mass, indicating that the electron is only weakly dressed by phonons. However, as α increases, especially beyond the critical threshold of $\alpha = 6$, the polaron mass rises sharply, reflecting the strong coupling regime where the electron becomes heavily localised due to interactions with the surrounding phonon cloud.

Comparing the two plots, the overall trends at zero and room temperature are similar, though there is slightly more scatter in the room-temperature data, particularly at larger values of α . This increased scatter at higher temperatures suggests that thermal effects contribute to more significant variability in polaron behaviour across different materials. At room temperature, phonons are thermally activated, leading to more pronounced interactions between the polaron and the phonon field, further enhancing mass renormalisation. As a result, the effective polaron mass increases faster for some materials at room temperature, indicating the role of thermal phonons in exacerbating polaron localisation and the associated mass increase.

A critical transition at $\alpha = 6$ marks a shift from weak to strong coupling. The electron interacts weakly with the phonon field below $\alpha = 6$, maintaining a relatively low mass. Above this threshold, the mass increases exponentially as the polaron becomes more localised, with the electron trapped in the potential well created by the lattice distortion. This behaviour is consistent with theoretical models such as the Fröhlich polaron model and Feynman's variational approach, which predict that the polaron mass should increase sharply with α in the strong coupling regime. The materials in groups 15, 16, and 17 follow this trend. However, some deviations at high α suggest that these materials exhibit slightly stronger electron-phonon interactions or unique phonon modes that enhance mass renormalisation.

At large values of α , particularly in the room-temperature plot, there is noticeable scatter in the data, with some materials displaying much higher or lower polaron masses than the general trend. This suggests that material-specific factors such as lattice structure, phonon dispersion, and dielectric properties significantly influence mass renormalisation in the strong coupling regime. While the overall trend is consistent with theoretical expectations, the deviations observed for certain materials highlight the complexity of real systems, where factors beyond the simple α parameter, such as thermal effects and material-specific phonon interactions, play a crucial role in determining the extent of polaron mass renormalisation.

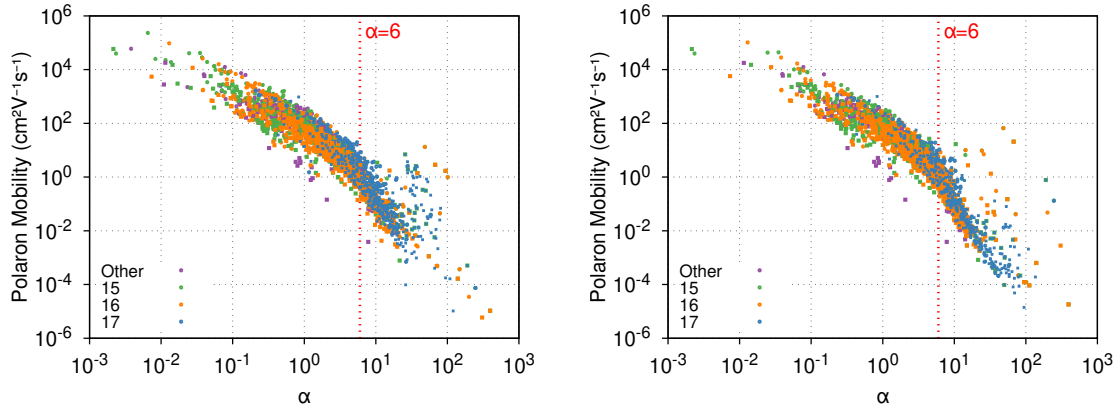


Figure 6.10: Polaron mobility as a function of the electron-phonon coupling constant α at room temperature for 1258 materials, with group 15, 16, and 17 elements highlighted. The left plot shows mobility results using a single effective phonon mode based on Hellwarth and Biaggio's B scheme [21], while the right plot accounts for all phonon branches in the material. The red vertical line marks $\alpha = 6$, indicating a critical transition between weak and strong coupling regimes.

6.4.3 Room Temperature Polaron Mobility

Fig. 6.10 presents the polaron mobility at room temperature for 1258 materials, explicitly focusing on group elements 15, 16, and 17. The left plot shows results obtained using a single effective phonon mode derived from Hellwarth and Biaggio's B scheme [21], while the right plot accounts for all the different phonon branches in the materials. The x-axis represents the coupling constant α , related to electron-phonon interaction strength, while the y-axis depicts the polaron mobility μ in units of $\text{cm}^2\text{V}^{-1}\text{s}^{-1}$ on a logarithmic scale.

Across both plots, there is a general trend of decreasing polaron mobility with increasing α , which reflects the expected behaviour from polaron theory. As the electron-phonon coupling strength grows, phonon interactions impede polaron movement, reducing mobility. The materials highlighted from groups 15, 16, and 17 mostly follow this trend, although some deviations suggest that subtle differences in the materials' electronic structures and phonon dynamics may influence their respective mobilities. While not enough to disrupt the overall trend, these differences indicate that factors beyond the coupling constant α play a role in determining mobility.

A key observation is the marked decrease in mobility as α crosses the critical threshold of 6, highlighted by the red vertical line in both plots. This crucial point aligns with theoretical predictions for the transition between weak and strong coupling regimes, where the polaron becomes more localised, and its mobility is significantly reduced. This behaviour is consistent with the Fröhlich polaron model, which predicts a sharp decrease in mobility for large α due to increased localisation and phonon scattering. In Feynman's path integral approach, this regime represents a transition from a quasi-free polaron to a

strongly localised one, characterised by a steep reduction in its ability to move through the material.

Interestingly, a few materials at high α values exhibit higher polaron mobility again, defying the overall trend of decreasing mobility with stronger coupling. This phenomenon is noted by Ōsaka [31], who explains that when the coupling becomes very strong, the phonons' wavelength contributing to polaron scattering decreases more steeply than the polaron's localisation length. As a result, the polaron becomes less sensitive to phonon scattering, leading to an increase in mobility. This occurs because the effective wavelength of the phonons, proportional to $1/\alpha^2$, decreases faster than the localisation length of the polaron, proportional to $1/\alpha$. While this explanation assumes that the polaron mobility is influenced by scattering due to the phonon cloud surrounding the polaron, Ōsaka also points out that the scattering of the electronic part of the polaron primarily determines the mobility tied to the electronic current. Therefore, some uncertainty remains regarding the exact behaviour of the mobility at high α , suggesting the need for further investigation.

In comparing the two plots, using a single effective phonon mode versus accounting for all phonon branches does not drastically alter the overall trend of decreasing mobility with increasing α . Still, the explicit treatment of multiple phonon branches (right plot) introduces more scatter into the data. This suggests that considering all phonon modes may provide a more nuanced understanding of polaron dynamics, particularly at intermediate to high values of α , where different phonon branches may interact with the polaron in distinct ways. Nonetheless, both models show a consistent decrease in mobility with increasing coupling strength, which aligns with theoretical expectations from the Fröhlich model and Feynman's variational method. The subtle differences in scatter between the two approaches highlight the complexity of accurately modelling polaron behaviour in real materials, especially when multiple phonon interactions are considered at room temperature.

Fig. 6.11 extends these results by colour-coding the polaron mobility data according to the effective band mass of the materials, measured in terms of the electron mass ($m - e$). The top two plots show polaron mobility as a function of α , similar to the previous figure, but with band mass colour-coded along the mobility data. The bottom two plots present polaron mobility as a function of the band mass directly, with the x-axis representing band mass instead of α . The left column uses the single effective phonon mode approximation, while the right column accounts for all phonon branches.

The inclusion of band mass adds another dimension to understanding the relationship between α and mobility. As expected, materials with lower effective band masses (indicated by the darker purple regions) generally have higher polaron mobility across all α values. In comparison, materials with larger band masses (yellow areas) exhibit lower mobility. This is consistent with theoretical expectations, where a larger effective mass increases

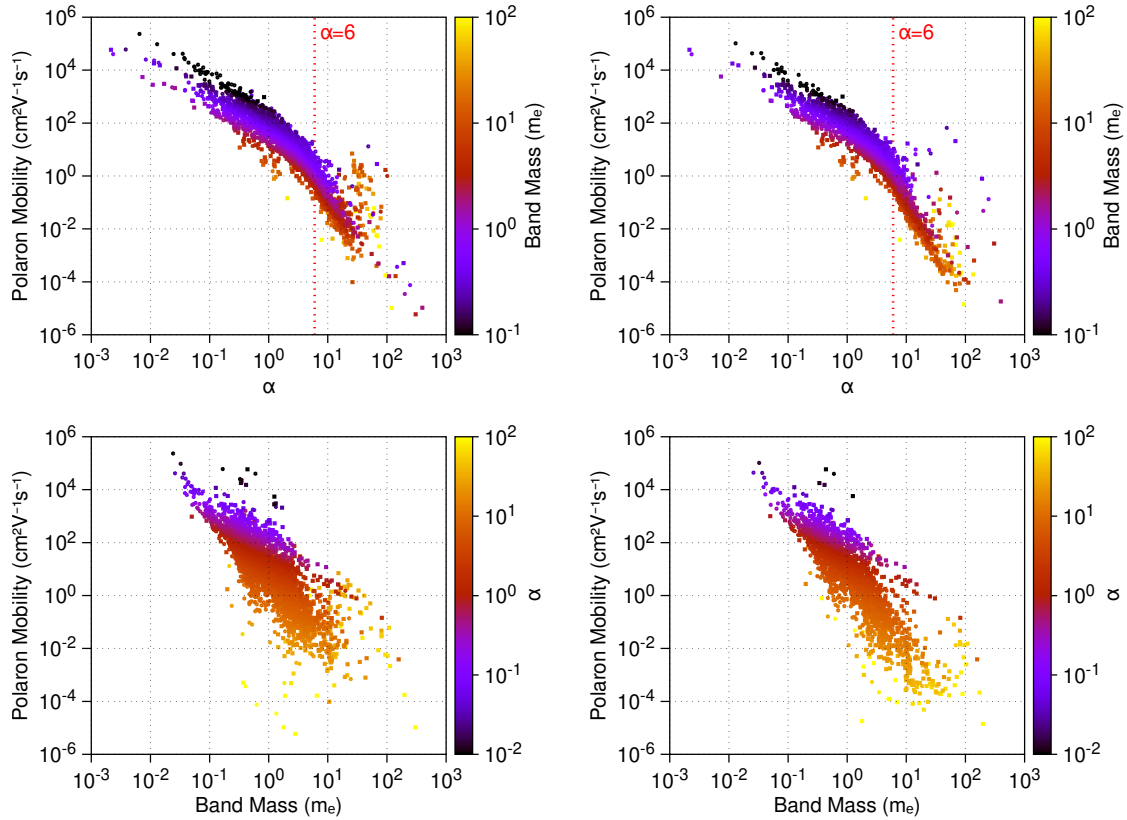


Figure 6.11: Polaron mobility at room temperature as a function of the electron-phonon coupling constant α (top row) and effective band mass m_e (bottom row) for 1258 materials, colour-coded by the band mass. The left column uses a single effective phonon mode from Hellwarth and Biaggio's B scheme [21], while the right column accounts for all phonon branches. A critical point at $\alpha = 6$ (red dashed line) marks the transition to the strong coupling regime, where mobility decreases sharply, especially for materials with larger band masses.

the difficulty of polaron movement, as the mass term contributes to both the localisation and scattering effects of the electron-phonon interaction. The plots also reveal that as α increases, the mobility tends to fall off more rapidly for materials with higher band masses, reflecting a compounded effect of strong electron-phonon coupling and increased inertia from the heavier effective mass.

The bottom two plots directly visualise the relationship between polaron mobility and band mass. These plots show a similarly sharp decrease in mobility for increasing band mass, particularly for materials with masses greater than $10m_e$, where polaron mobility drops precipitously. At lower band masses, the decrease is more gradual, with a notable spread of mobility values reflecting variations in the phonon interaction strength and the nature of the phonon modes. Like in the top plots, materials with high band mass in the strong coupling regime show significantly reduced mobility, further emphasising the role of the effective band mass in governing polaron dynamics.

While the trend of decreasing mobility with increasing α and band mass holds consistently, the observed scatter suggests that subtle material-specific factors, such as phonon dispersion and electron localisation, also play essential roles in determining the precise mobility of polarons at room temperature.

CHAPTER 7



CONCLUSION & OUTLOOK

In this dissertation, I have extended the theoretical framework of polaron physics by developing and generalising path integral methods, offering more accurate polaronic behaviour models in real materials. Building upon Feynman's pioneering work on the variational path integral approximation (FVA) [2], the research presented here has systematically addressed several key limitations of traditional models by enhancing the theoretical structure to include multiple phonon modes, complex phonon dispersions, and anisotropic electronic band structures. These advances improve the understanding of polaron formation and transport, contributing practical computational tools capable of predicting polaronic properties in a wide range of technologically significant materials, including semiconductors and organic crystals.

One of the thesis' principal contributions is generalising the material action to incorporate multiple phonon modes. This development is significant, as many real materials possess multiple longitudinal optical (LO) phonon branches, rendering the standard single-mode Fröhlich model inadequate for capturing the full complexity of electron-phonon interactions. The extended formalism introduced in this thesis integrates coherent-state path integrals (CSPI) and techniques from quantum field theory, enabling the treatment of both small Holstein polarons and more complex polaron dynamics involving several phonon branches. This approach enhances the accuracy of polaron transport models across weak, intermediate, and strong electron-phonon coupling regimes, offering a significant improvement in predicting material-specific polaron properties.

A second core advancement presented in this thesis is improving the trial action within the variational framework. While innovative, Feynman's original spring-mass harmonic trial model was limited in its capacity to model real materials with multiple interacting phonon modes. By introducing a more flexible trial action in which the electron is coupled to multiple fictitious particles, this trial action systematically improves the variational

approximation of critical polaronic properties such as self-energy, effective mass, and charge-carrier mobility. Combined with higher-order cumulant corrections, this generalised model allows for a more nuanced description of electron-phonon coupling, thereby providing better approximations for polarons' static and dynamic properties. Rigorous comparisons with state-of-the-art Diagrammatic Monte Carlo (DMC) simulations validate the accuracy of this approach, particularly in predicting temperature-dependent mobility at varying coupling strengths.

A critical practical outcome of this research is the co-development of the `PolaronMobility.jl` computational package, implemented in the Julia programming language. This package encapsulates the advanced path integral techniques developed throughout this thesis and facilitates high-throughput computational screening of materials for their polaronic properties. The utility of the computational framework was demonstrated through detailed case studies on materials such as methylammonium lead halide perovskites and rubrene organic crystals. These case studies revealed the importance of accounting for material-specific characteristics, such as phonon mode dispersion and effective mass anisotropy, in predicting polaronic behaviour. Furthermore, these studies illustrate how the path integral approach can provide insights into material performance, particularly for optoelectronic applications like photovoltaic cells.

This thesis highlights the high-throughput analysis of 1,258 materials of the Materials Project [13] and Liege [14] databases. Fundamental polaronic properties—including zero-point renormalisation energy (ZPR), effective mass, and room-temperature mobility—were systematically calculated using the extended path integral formalism. This large-scale study comprehensively classifies materials based on their polaronic characteristics. It offers a valuable resource for the computational discovery and design of materials optimised for high mobility and low charge trapping. Such insights are essential for developing next-generation semiconductors, organic electronics, and energy-harvesting devices.

To accomplish this, I derived the path integral corresponding to the Holstein model and identified the challenges associated with applying Feynman's variational method in this context. These challenges arise from the non-quadratic nature of the electron kinetic action and the constrained electronic paths characteristic of lattice models. I presented a series of approximations that maintain the lattice description of the phonons while transforming the problem into one that is tractable using a parabolic-band Hamiltonian. This allowed me to apply the variational method successfully, and I subsequently derived the polaronic properties of the organic semiconductor Rubrene, a material of particular interest. My analysis yielded key properties such as the polaron binding energy, size, effective mass, and dynamical properties, including charge-carrier mobility and complex conductivity. A comparison of these results with those obtained from the original Fröhlich

large-polaron model demonstrated that the new variational Holstein model produces more realistic predictions for Rubrene, especially in the case of room-temperature mobility, as evidenced in Tables 6.6 and 6.7.

One fascinating insight from this research is the connection I identified between the optimal spectral function derived from the Feynman variational method and the memory function used in FHIP theory to describe dynamical properties such as complex conductivity and charge-carrier mobility. This connection can be understood via a Wick rotation since the memory function is analytic across a semi-infinite strip in the complex plane. Furthermore, comparisons between the free energy inequality derived in this work and the expression for the Luttinger-Ward function suggest that the memory and spectral functions are analogous to the non-local one-particle self-energy functions in real or imaginary time, respectively. This interpretation positions the Feynman variational method as a potential approximation to the Luttinger-Ward-like functional, in which one variationally or self-consistently optimises the trial self-energy or Green's function.

This analogy is particularly compelling when considering the possibility of generalising the Feynman variational method to many-body Hamiltonians or grand canonical systems with a variable number of particles. By leveraging many-body Green function techniques, extending this method to study systems with more complex interactions may be possible. In this context, the Feynman variational method may be seen as a variational approximation analogous to how exchange-correlation functionals are handled in Density Functional Theory (DFT), where one self-consistently solves for the optimal electron density to minimise the ground-state energy.

A logical next step would be to derive the variational method for arbitrary path integral representations, such as the phase-space representation for canonical ensembles or coherent-state path integrals for grand-canonical ensembles. Such extensions could move beyond the parabolic-band approximation, thereby allowing the treatment of more complex band structures and addressing discrepancies, such as those observed between the predicted polaron binding energy at higher coupling in the Holstein model and results from Diagrammatic Monte Carlo methods.

This project's ultimate vision is to develop a highly accurate, potentially ab initio, variational method capable of predicting real, complex materials' thermodynamic and dynamical properties. This approach could then be applied across broad classes of materials, identifying trends and guiding materials design and discovery. Compared to other methods, such as Monte Carlo approaches (e.g., Path Integral or Diagrammatic Monte Carlo) or self-consistent methods (e.g., GW theory or Dynamical Mean-Field Theory), the variational path integral method offers significant advantages. Its efficiency and well-defined variational bound make it an attractive option for studying various quantum systems. Unlike

Monte Carlo methods, it provides controlled errors and is computationally tractable due to the convex nature of the path integrand, allowing for optimised solutions.

However, it is important to acknowledge certain limitations of the variational method. My multiple fictitious particle trial action analysis demonstrated that the system's higher frequency dynamics can be susceptible to the derived ground-state properties. This issue, also investigated by Dries Sels, stems from the limited physics captured by the trial system, which remains quadratic in its variables. A quadratic action typically corresponds to a non-interacting system, limiting its ability to represent interacting particles accurately. A clearer understanding of which diagrams are retained in the Feynman variational method—likely akin to those kept in cumulant Green function methods—could improve the method's accuracy. Ultimately, adding higher-order cumulant corrections to the Feynman-Jensen inequality would further refine this approximation, incorporating additional infinite sets of diagrams and improving the method's predictive power, albeit at the cost of increased computational complexity.

An exciting avenue for overcoming these challenges lies in integrating machine learning with the variational method. The Feynman-Jensen inequality can be interpreted as mapping an intractable probability distribution onto a simpler Gaussian distribution in an infinite-dimensional function space—a process that resembles variational inference in machine learning. By employing normalising flows or diffusion methods, it may be possible to minimise the Kullback-Leibler divergence between the trial model's likelihood and the true distribution, offering a new pathway for improving the method. Using deep neural networks to solve for the optimal trial self-energy function would circumvent the need for self-consistently solving complex functional equations. While the practical application of this idea remains speculative at this stage, the potential for combining machine learning and path integrals presents a compelling direction for future research.

In conclusion, this work has extended the scope of the Feynman variational path integral method, enabling its application to more realistic materials and providing a more nuanced understanding of polaronic systems. This dissertation lays the groundwork for future studies of organic semiconductors and other technologically significant materials by deriving a variational Holstein model and its successful application to materials like Rubrene. The theoretical and computational tools developed herein provide an efficient and flexible framework for predicting polaronic properties and open the door to further innovations in theory and application, including nonequilibrium dynamics, machine learning-enhanced methods, and studying many-body systems.

— B I B L I O G R A P H Y —

- ¹R. P. Feynman Mathematical Formulation of the Quantum Theory of Electromagnetic Interaction, *Physical Review*. **80** (3), 440–457 (1950).
- ²R. P. Feynman Slow Electrons in a Polar Crystal, *Physical Review*. **97** (3), Publisher: American Physical Society, 660–665 (1955).
- ³H. Fröhlich Electrons in lattice fields, en, *Advances in Physics*. **3** (11), 325–361 (1954).
- ⁴B. A. A. Martin & J. M. Frost Multiple phonon modes in Feynman path-integral variational polaron mobility, *Physical Review B*. **107** (11), Publisher: American Physical Society, 115203 (2023).
- ⁵T. Holstein Studies of polaron motion: Part II. The “small” polaron, *Annals of Physics*. **8** (3), 343–389 (1959).
- ⁶T. Holstein Studies of polaron motion: Part I. The molecular-crystal model, *Annals of Physics*. **8** (3), 325–342 (1959).
- ⁷B. A. A. Martin & J. M. Frost *Predicting polaron mobility in organic semiconductors with the Feynman variational approach*, arXiv:2207.06846 [cond-mat], June 2024.
- ⁸B. Guster, P. Melo, B. A. A. Martin, V. Brousseau-Couture, J. C. de Abreu, A. Miglio, M. Giantomassi, M. Côté, J. M. Frost, M. J. Verstraete & X. Gonze Fröhlich polaron effective mass and localization length in cubic materials: Degenerate and anisotropic electronic bands, *Physical Review B*. **104** (23), Publisher: American Physical Society, 235123 (2021).
- ⁹R. P. Feynman & F. L. Vernon The theory of a general quantum system interacting with a linear dissipative system, *Annals of Physics*. **24**, 118–173 (1963).
- ¹⁰A. S. Mishchenko, L. Pollet, N. V. Prokof'ev, A. Kumar, D. L. Maslov & N. Nagaosa Polaron Mobility in the “Beyond Quasiparticles” Regime, *Physical Review Letters*. **123** (7), Publisher: American Physical Society, 076601 (2019).

¹¹J. M. Frost *Jarvist/PolaronMobility.jl*, original-date: 2017-04-03T12:47:43Z, November 2023.

¹²J. Bezanson, A. Edelman, S. Karpinski & V.B. Shah Julia: A Fresh Approach to Numerical Computing, *SIAM Review*. **59** (1), Publisher: Society for Industrial and Applied Mathematics, 65–98 (2017).

¹³A. Jain, S. P. Ong, G. Hautier, W. Chen, W. D. Richards, S. Dacek, S. Cholia, D. Gunter, D. Skinner, G. Ceder & K. A. Persson Commentary: The Materials Project: A materials genome approach to accelerating materials innovation, *APL Materials*. **1** (1), 011002 (2013).

¹⁴P. Melo, J. Abreu, M. Verstraete, B. Guster, M. Giantomassi, X. Gonze & Z. Zanolli *High-throughput analysis of Fröhlich-type polaron models*, en, March 2023.

¹⁵C. Franchini, M. Reticcioli, M. Setvin & U. Diebold Polarons in materials, en, *Nature Reviews Materials*. **6** (7), Number: 7 Publisher: Nature Publishing Group, 560–586 (2021).

¹⁶F.L. Vernon *The Theory of a General Quantum System Interacting with a Linear Dissipative System*, en, phd (California Institute of Technology, 1959).

¹⁷R. P. Feynman, R. W. Hellwarth, C. K. Iddings & P. M. Platzman Mobility of Slow Electrons in a Polar Crystal, *Physical Review*. **127** (4), Publisher: American Physical Society, 1004–1017 (1962).

¹⁸J. Devreese, J. De Sitter & M. Goovaerts Optical Absorption of Polarons in the Feynman-Hellwarth-Iddings-Platzman Approximation, *Physical Review B*. **5** (6), Publisher: American Physical Society, 2367–2381 (1972).

¹⁹L. P. Kadanoff Boltzmann Equation for Polarons, *Physical Review*. **130** (4), Publisher: American Physical Society, 1364–1369 (1963).

²⁰F. Brivio, J. M. Frost, J. M. Skelton, A. J. Jackson, O. J. Weber, M. T. Weller, A. R. Goñi, A. M. A. Leguy, P. R. F. Barnes & A. Walsh Lattice dynamics and vibrational spectra of the orthorhombic, tetragonal, and cubic phases of methylammonium lead iodide, *Physical Review B*. **92** (14), Publisher: American Physical Society, 144308 (2015).

²¹R. W. Hellwarth & I. Biaggio Mobility of an electron in a multimode polar lattice, *Physical Review B*. **60** (1), Publisher: American Physical Society, 299–307 (1999).

²²P. Ordejón, D. Boskovic, M. Panhans & F. Ortmann Ab initio study of electron-phonon coupling in rubrene, *Physical Review B*. **96** (3), Publisher: American Physical Society, 035202 (2017).

- ²³P. M. M. C. de Melo, J. C. de Abreu, B. Guster, M. Giantomassi, Z. Zanolli, X. Gonze & M. J. Verstraete High-throughput analysis of Fröhlich-type polaron models, en, *npj Computational Materials.* **9** (1), Publisher: Nature Publishing Group, 1–13 (2023).
- ²⁴H. Fröhlich, H. Pelzer & S. Zienau XX. Properties of slow electrons in polar materials, *The London, Edinburgh, and Dublin Philosophical Magazine and Journal of Science.* **41** (314), Publisher: Taylor & Francis _eprint: <https://doi.org/10.1080/14786445008521794>, 221–242 (1950).
- ²⁵L. D. Landau The motion of electrons in a crystal lattice, *Physikalische Zeitschrift der Sowjetunion.* **3**, 664–665 (1933).
- ²⁶S. I. Pekar Local quantum states of electrons in an ideal ion crystal, *Zhurnal Eksperimentalnoi I Teoreticheskoi Fiziki.* **16** (4), 341–348 (1946).
- ²⁷S. I. Pekar, *J. Phys. USSR.* **10**, 341 (1946).
- ²⁸S. I. Pekar, *Zhurnal Eksperimentalnoi I Teoreticheskoi Fiziki.* **17**, 868 (1947).
- ²⁹T. D. Schultz Slow Electrons in Polar Crystals: Self-Energy, Mass, and Mobility, *Physical Review.* **116** (3), Publisher: American Physical Society, 526–543 (1959).
- ³⁰Y. Ōsaka Polaron State at a Finite Temperature, *Progress of Theoretical Physics.* **22** (3), 437–446 (1959).
- ³¹Y. Ōsaka Theory of Polaron Mobility: *Progress of Theoretical Physics.* **25** (4), 517–536 (1961).
- ³²K. K. Thornber *L. Electronic Processes in -Sulfur. II. Polaron Motion in a D.C. Electric Field*, en, phd (California Institute of Technology, 1966).
- ³³K. K. Thornber & R. P. Feynman Velocity Acquired by an Electron in a Finite Electric Field in a Polar Crystal, *Physical Review B.* **1** (10), Publisher: American Physical Society, 4099–4114 (1970).
- ³⁴K. K. Thornber Linear and Nonlinear Electronic Transport in Electron-Phonon Systems: Self-Consistent Approach within the Path-Integral Formalism, *Physical Review B.* **3** (6), Publisher: American Physical Society, 1929–1941 (1971).
- ³⁵J. Adamowski, B. Gerlach & H. Leschke Feynman's Approach to the Polaron Problem Generalized to Arbitrary Quadratic Actions, en, in J.-P. Antoine & E. Tirapegui (eds.), *Functional Integration: Theory and Applications*, Boston, MA, Springer US, 1980, pp. 291–301.

- ³⁶J. Adamowski, B. Gerlach & H. Leschke General Aspects of the Functional-Integral Approach to the Polaron and Related Systems, en, in J. T. Devreese & F. Peeters (eds.), *Polarons and Excitons in Polar Semiconductors and Ionic Crystals*, NATO ASI Series, Boston, MA, Springer US, 1984, pp. 245–269.
- ³⁷H. De Raedt & A. Lagendijk Numerical calculation of path integrals: The small-polaron model, *Physical Review B*. **27** (10), Publisher: American Physical Society, 6097–6109 (1983).
- ³⁸H. De Raedt & A. Lagendijk Monte Carlo simulation of quantum statistical lattice models, *Physics Reports*. **127** (4), 233–307 (1985).
- ³⁹F. M. Peeters, W. Xiaoguang & J. T. Devreese Ground-state energy of a polaron in n dimensions, *Physical Review B*. **33** (6), Publisher: American Physical Society, 3926–3934 (1986).
- ⁴⁰F. M. Peeters & J. T. Devreese Scaling relations between the two- and three-dimensional polarons for static and dynamical properties, *Physical Review B*. **36** (8), Publisher: American Physical Society, 4442–4445 (1987).
- ⁴¹N. V. Prokof'ev & B. V. Svistunov Polaron Problem by Diagrammatic Quantum Monte Carlo, *Physical Review Letters*. **81** (12), Publisher: American Physical Society, 2514–2517 (1998).
- ⁴²A. S. Mishchenko, N. V. Prokof'ev, A. Sakamoto & B. V. Svistunov Diagrammatic quantum Monte Carlo study of the Fröhlich polaron, *Physical Review B*. **62** (10), Publisher: American Physical Society, 6317–6336 (2000).
- ⁴³J. T. Titantah, C. Pierleoni & S. Ciuchi Free Energy of the Fröhlich Polaron in Two and Three Dimensions, *Physical Review Letters*. **87** (20), Publisher: American Physical Society, 206406 (2001).
- ⁴⁴P. E. Kornilovitch & E. R. Pike Polaron effective mass from Monte Carlo simulations, *Physical Review B*. **55** (14), Publisher: American Physical Society, R8634–R8637 (1997).
- ⁴⁵P. E. Kornilovitch Giant enhancement of anisotropy by electron-phonon interaction, *Physical Review B*. **59** (21), Publisher: American Physical Society, 13531–13534 (1999).
- ⁴⁶P. E. Kornilovitch Band Structure of the Jahn-Teller Polaron from Quantum Monte Carlo, *Physical Review Letters*. **84** (7), Publisher: American Physical Society, 1551–1554 (2000).

- ⁴⁷P. E. Kornilovitch Continuous-Time Quantum Monte Carlo Algorithm for the Lattice Polaron, *Physical Review Letters*. **81** (24), Publisher: American Physical Society, 5382–5385 (1998).
- ⁴⁸P. E. Kornilovitch *On Feynman's calculation of the Froehlich polaron mass*, arXiv:cond-mat/0404121, April 2004.
- ⁴⁹P. E. Kornilovitch Ground-state dispersion and density of states from path-integral Monte Carlo: Application to the lattice polaron, *Physical Review B*. **60** (5), Publisher: American Physical Society, 3237–3243 (1999).
- ⁵⁰P. Kornilovitch Path Integrals in the Physics of Lattice Polarons, en, in A. S. Alexandrov (ed.), *Polarons in Advanced Materials*, Springer Series in Materials Science, Dordrecht, Springer Netherlands, 2007, pp. 192–230.
- ⁵¹J. Tempere & J. T. Devreese Optical absorption of an interacting many-polaron gas, *Physical Review B*. **64** (10), Publisher: American Physical Society, 104504 (2001).
- ⁵²J. Tempere, W. Casteels, M. K. Oberthaler, S. Knoop, E. Timmermans & J. T. Devreese Feynman path-integral treatment of the BEC-impurity polaron, *Physical Review B*. **80** (18), Publisher: American Physical Society, 184504 (2009).
- ⁵³J. T. Devreese, S. N. Klimin, J. L. M. van Mechelen & D. van der Marel Many-body large polaron optical conductivity in $\text{SrTi}_{1-x}\text{Nb}_x\text{O}_3$, *Physical Review B*. **81** (12), Publisher: American Physical Society, 125119 (2010).
- ⁵⁴A. S. Mishchenko, N. Nagaosa & N. Prokof'ev Diagrammatic Monte Carlo Method for Many-Polaron Problems, *Physical Review Letters*. **113** (16), Publisher: American Physical Society, 166402 (2014).
- ⁵⁵A. S. Mishchenko, N. Nagaosa, G. De Filippis, A. de Candia & V. Cataudella Mobility of Holstein Polaron at Finite Temperature: An Unbiased Approach, *Physical Review Letters*. **114** (14), Publisher: American Physical Society, 146401 (2015).
- ⁵⁶S. N. Klimin & J. T. Devreese Optical conductivity of a strong-coupling Fröhlich polaron, *Physical Review B*. **89** (3), Publisher: American Physical Society, 035201 (2014).
- ⁵⁷S. N. Klimin, J. Tempere & J. T. Devreese All-coupling polaron optical response: Analytic approaches beyond the adiabatic approximation, *Physical Review B*. **94** (12), Publisher: American Physical Society, 125206 (2016).
- ⁵⁸S. Klimin, J. Tempere, J. T. Devreese, C. Franchini & G. Kresse Optical Response of an Interacting Polaron Gas in Strongly Polar Crystals, en, *Applied Sciences*. **10** (6), Number: 6 Publisher: Multidisciplinary Digital Publishing Institute, 2059 (2020).

- ⁵⁹J. M. Frost Calculating polaron mobility in halide perovskites, *Physical Review B*. **96** (19), Publisher: American Physical Society, 195202 (2017).
- ⁶⁰T. Ichmoukhamedov & J. Tempere Feynman path-integral treatment of the Bose polaron beyond the Fröhlich model, *Physical Review A*. **100** (4), Publisher: American Physical Society, 043605 (2019).
- ⁶¹T. Ichmoukhamedov & J. Tempere Path-integral approach to the thermodynamics of bosons with memory: Partition function and specific heat, *Physical Review A*. **104** (2), Publisher: American Physical Society, 023322 (2021).
- ⁶²T. Ichmoukhamedov & J. Tempere General memory kernels and further corrections to the variational path integral approach for the Bogoliubov-Fröhlich Hamiltonian, *Physical Review B*. **105** (10), Publisher: American Physical Society, 104304 (2022).
- ⁶³A. Miglio, V. Brousseau-Couture, E. Godbout, G. Antonius, Y.-H. Chan, S. G. Louie, M. Côté, M. Giantomassi & X. Gonze Predominance of non-adiabatic effects in zero-point renormalization of the electronic band gap, en, *npj Computational Materials*. **6** (1), Publisher: Nature Publishing Group, 1–8 (2020).
- ⁶⁴M. Houtput & J. Tempere Beyond the Fröhlich Hamiltonian: Path-integral treatment of large polarons in anharmonic solids, *Physical Review B*. **103** (18), Publisher: American Physical Society, 184306 (2021).
- ⁶⁵S. N. Klimin, J. Tempere, M. Houtput, S. Ragni, T. Hahn, C. Franchini & A. S. Mishchenko Analytic method for quadratic polarons in nonparabolic bands, *Physical Review B*. **110** (7), Publisher: American Physical Society, 075107 (2024).
- ⁶⁶S. I. Pekar & L. D. Landau Effective Mass of a Polaron, *Zh. Eksp. Teor. Fiz.* **18** (5), 419–423 (1948).
- ⁶⁷F. M. Peeters & J. T. Devreese Theory of Polaron Mobility, in H. Ehrenreich, D. Turnbull & F. Seitz (eds.), *Solid State Physics*, Vol. 38, Academic Press, January 1984, pp. 81–133.
- ⁶⁸F. M. Peeters & J. T. Devreese Impedance function of large polarons: An alternative derivation of the Feynman-Hellwarth-Iddings-Platzman theory, *Physical Review B*. **28** (10), Publisher: American Physical Society, 6051–6060 (1983).
- ⁶⁹V. F. Los' On the theory of the conductivity of crystals, en, *Theoretical and Mathematical Physics*. **60** (1), 703–711 (1984).
- ⁷⁰V. F. Los Influence of Initial Correlations on Evolution of a Subsystem in a Heat Bath and Polaron Mobility, en, *Journal of Statistical Physics*. **168** (4), 857–872 (2017).
- ⁷¹V. F. Los Evolution of a subsystem in a heat bath with no initial factorized state assumption, *Physica A: Statistical Mechanics and its Applications*. **503**, 476–490 (2018).

- ⁷²D. Sels *Dynamic polaron response from variational imaginary time evolution*, arXiv:1605.04998 [cond-mat], May 2016.
- ⁷³J. Nitta, K. Miwa, N. Komiya, E. Annese, J. Fujii, S. Ono & K. Sakamoto The actual electronic band structure of a rubrene single crystal, en, *Scientific Reports.* **9** (1), Publisher: Nature Publishing Group, 9645 (2019).
- ⁷⁴X. Gonze & C. Lee Dynamical matrices, Born effective charges, dielectric permittivity tensors, and interatomic force constants from density-functional perturbation theory, *Physical Review B.* **55** (16), Publisher: American Physical Society, 10355–10368 (1997).
- ⁷⁵G. Verbist, F. M. Peeters & J. T. Devreese Extended stability region for large bipolarons through interaction with multiple phonon branches, *Ferroelectrics.* **130** (1), 27–34 (1992).
- ⁷⁶H. F. Trotter On the Product of Semi-Groups of Operators, *Proceedings of the American Mathematical Society.* **10** (4), Publisher: American Mathematical Society, 545–551 (1959).
- ⁷⁷N. Hatano & M. Suzuki Finding Exponential Product Formulas of Higher Orders, en, in A. Das & B. K. Chakrabarti (eds.), *Quantum Annealing and Other Optimization Methods*, Lecture Notes in Physics, Berlin, Heidelberg, Springer, 2005, pp. 37–68.
- ⁷⁸DLMF: §10.32 *Integral Representations Modified Bessel Functions Chapter 10 Bessel Functions.*
- ⁷⁹A. S. Alexandrov & J. T. Devreese *Advances in Polaron Physics*, en, Vol. 159, Springer Series in Solid-State Sciences, Berlin, Heidelberg, Springer, 2010.
- ⁸⁰A. Altland & B. D. Simons *Condensed Matter Field Theory*, 2nd ed., Cambridge, Cambridge University Press, 2010.
- ⁸¹R. Abe & K. Okamoto An Improvement of the Feynman Action in the Theory of Polaron. I, *Journal of the Physical Society of Japan.* **31** (5), Publisher: The Physical Society of Japan, 1337–1343 (1971).
- ⁸²J. Poulter & V. Sa-yakanit A complete expression for the propagator corresponding to a model quadratic action, en, *Journal of Physics A: Mathematical and General.* **25** (6), 1539 (1992).
- ⁸³R. Rosenfelder & A. W. Schreiber On the best quadratic approximation in Feynman's path integral treatment of the polaron, *Physics Letters A.* **284** (2), 63–71 (2001).
- ⁸⁴J. M. Luttinger & J. C. Ward Ground-State Energy of a Many-Fermion System. II, *Physical Review.* **118** (5), Publisher: American Physical Society, 1417–1427 (1960).

- ⁸⁵C. H. Mousatov & S. A. Hartnoll On the Planckian bound for heat diffusion in insulators, en, *Nature Physics*. **16** (5), Publisher: Nature Publishing Group, 579–584 (2020).
- ⁸⁶S. A. Hartnoll & A. P. Mackenzie Colloquium: Planckian dissipation in metals, *Reviews of Modern Physics*. **94** (4), Publisher: American Physical Society, 041002 (2022).
- ⁸⁷G. De Filippis, V. Cataudella, A. S. Mishchenko, C. A. Perroni & J. T. Devreese Validity of the Franck-Condon Principle in the Optical Spectroscopy: Optical Conductivity of the Fröhlich Polaron, *Physical Review Letters*. **96** (13), Publisher: American Physical Society, 136405 (2006).
- ⁸⁸B. Guzelturk, R. A. Belisle, M. D. Smith, K. Bruening, R. Prasanna, Y. Yuan, V. Gopalan, C. J. Tassone, H. I. Karunadasa, M. D. McGehee & A. M. Lindenberg Terahertz Emission from Hybrid Perovskites Driven by Ultrafast Charge Separation and Strong Electron–Phonon Coupling, en, *Advanced Materials*. **30** (11), _eprint: <https://onlinelibrary.wiley.com/doi/pdf/10.1002/adma.201704737>, 1704737 (2018).
- ⁸⁹X. Zheng, T. R. Hopper, A. Gorodetsky, M. Maimaris, W. Xu, B. A. A. Martin, J. M. Frost & A. A. Bakulin Multipulse Terahertz Spectroscopy Unveils Hot Polaron Photoconductivity Dynamics in Metal-Halide Perovskites, *The Journal of Physical Chemistry Letters*. **12** (36), Publisher: American Chemical Society, 8732–8739 (2021).

APPENDIX A

PATH INTEGRAL DERIVATION

$$\rho(r_i, r_f; \hbar\beta) = \int_{r(0)=r_i}^{r(\hbar\beta)=r_f} \mathcal{D}r(\tau) \exp\left\{-\frac{1}{\hbar} \int_0^{\hbar\beta} d\tau \left[\frac{m}{2} \dot{r}(\tau)^2 + V(r(\tau))\right]\right\} \quad (\text{A.1})$$

The free energy can be obtained using,

$$e^{-\beta F} = \int_{-\infty}^{\infty} dr \rho(r, r; \hbar\beta) \quad (\text{A.2})$$

The classical limit corresponds to high temperature $\beta \ll 1$. Expanding around the classical path r_{cl} and neglecting the quantum fluctuations gives the classical free energy,

$$e^{-\beta F_{\text{cl}}} = \int_{-\infty}^{\infty} dr \rho_{\text{cl}}(r, r; \hbar\beta) = \left(\frac{m}{2\pi\hbar^2\beta}\right)^{\frac{1}{2}} \int_{-\infty}^{\infty} dr e^{-\beta V(r)}. \quad (\text{A.3})$$

The classical path tends to let $V(r(\tau))$ to be lower than $V(r_{\text{cl}})$. This means,

$$\rho_{\text{cl}}(r_i, r_f; \hbar\beta) < \rho(r_i, r_f; \hbar\beta), \quad (\text{A.4})$$

and

$$F_{\text{cl}} \gtrsim F. \quad (\text{A.5})$$

The density matrix for a free particle is,

$$\rho(r_i, r_f; \hbar\beta) = \int_{r(0)=r_i}^{r(\hbar\beta)=r_f} \mathcal{D}r(\tau) \exp\left\{-\frac{1}{\hbar} \frac{m}{2} \int_0^{\hbar\beta} d\tau \dot{r}(\tau)^2\right\} \quad (\text{A.6})$$

Expand about the classical path $r(\tau) = r_{\text{cl}}(\tau) + \delta r(\tau)$ in the action,

$$\begin{aligned} S[r_{\text{cl}}(\tau) + \delta r(\tau)] &= \frac{m}{2} \int_0^{\hbar\beta} [r'_{\text{cl}}(\tau) + \dot{\delta r}(\tau)]^2 \\ &= \frac{m}{2} \int_0^{\hbar\beta} [r'_{\text{cl}}(\tau)^2 + r'_{\text{cl}}(\tau)\dot{\delta r}(\tau) + \dot{\delta r}(\tau)^2] \\ &\quad \frac{m}{2} [2r'_{\text{cl}}]_{r_i}^{r_f} \end{aligned} \quad (\text{A.7})$$

A.1 Particle interacting with a harmonic oscillator

$$H = \frac{p^2}{2m} + \left(\frac{P^2}{2M} + \frac{M\omega^2}{2} R^2 \right) - \gamma r R + V(r) \quad (\text{A.8})$$

$$\begin{aligned} Z &= \int \mathcal{D}r(\tau) \mathcal{D}R(\tau) \exp \left\{ -\frac{1}{\hbar} \int_0^{\hbar\beta} d\tau \left(\frac{m}{2} \dot{r}(\tau)^2 + V(r(\tau)) \right) \right\} \\ &\quad \times \exp \left\{ -\frac{1}{\hbar} \int_0^{\hbar\beta} d\tau \left(\frac{M}{2} \dot{R}(\tau)^2 + \frac{M\omega^2}{2} R(\tau)^2 - \gamma r(\tau) R(\tau) \right) \right\} \end{aligned} \quad (\text{A.9})$$

The path integral over the harmonic oscillator is

$$\begin{aligned} Z_{\text{osc}}[f] &= \int_{x(0)=x_i}^{x(\hbar\beta)=x_f} \mathcal{D}R(\tau) \exp \left[-\frac{1}{\hbar} \int_0^{\hbar\beta} d\tau \left(\frac{M}{2} \dot{R}(\tau)^2 + \frac{M\omega^2}{2} R^2 + i f(\tau) R(\tau) \right) \right] \\ &= \left(\frac{M\omega}{2\pi\hbar \sinh(\hbar\omega\beta)} \right)^{1/2} e^{-\Phi[f]/\hbar} \end{aligned} \quad (\text{A.10})$$

$$\begin{aligned} \Phi[f] &= \frac{1}{4M\omega} \int_0^{\hbar\beta} \int_0^{\hbar\beta} d\tau d\tau' e^{-\omega|\tau-\tau'|} f(\tau) f(\tau') \\ &\quad + \frac{M\omega}{2 \sinh(\omega\hbar\beta)} \left[(R^2 - R'^2) \cosh(\hbar\omega\beta) - 2RR' \right] \\ &\quad + \frac{M\omega}{2 \sinh(\omega\hbar\beta)} [] \end{aligned} \quad (\text{A.11})$$

APPENDIX B



FEYNMAN-VERNON INFLUENCE FUNCTIONALS

APPENDIX C

MEMORY FUNCTION EXPANSIONS

C.1 Contour integration of the memory function

Following Devreese et al. [18] I derived infinite-power-series expansions of the real and imaginary components of Eq. (2.202) (or Eq. (35) in FHIP [17]) in terms of Bessel and Struve special functions, and hypergeometric functions.

The practical computational implementation of these expansions was made difficult by the high precision required for the special functions to converge. A partially working implementation was developed using arbitrary precision numerics. Still, it was discovered that direct numeric integration of Eq. (2.202) could achieve the same result with less computation time and less complex code.

We start by changing the contour of the memory function as done in FHIP [17]. The memory function for the polaron is defined to linear order [67] as $\Sigma(\Omega) = \chi(\Omega)/\Omega$, where,

$$\chi(\Omega) = \int_0^\infty \left[1 - e^{i\Omega u} \right] \text{Im}S(u) du, \quad (\text{C.1})$$

is the

$$S(u) = \frac{2\alpha}{3\sqrt{\pi}} \left[D(u) \right]^{-\frac{3}{2}} \left(e^{iu} + \frac{2}{e^\beta - 1} \cos(u) \right), \quad (\text{C.2})$$

and

$$D(u) = \frac{w^2}{\beta v^2} \left\{ a^2 - \beta^2/4 - b \cos(vu) \cosh(v\beta/2) + u^2 - i [b \sin(vu) \sinh(v\beta/2) + u\beta] \right\}, \quad (\text{C.3})$$

with $R \equiv (v^2 - w^2)/(w^2 v)$, $a^2 = \beta^2/4 + R\beta \coth(\beta v/2)$ and $b = R\beta / \sinh(\beta v/2)$, which are the same as Eqs. (47b) in FHIP [17].

Solving for the real and imaginary parts of $\Sigma(\Omega)$ gives the real and imaginary parts of $\chi(\Omega)$,

$$\operatorname{Re} \chi(\Omega) = \int_0^\infty [1 - \cos(\Omega u)] \operatorname{Im} S(u) du, \quad (\text{C.4a})$$

$$\operatorname{Im} \chi(\Omega) = \int_0^\infty \sin(\Omega u) \operatorname{Im} S(u) du. \quad (\text{C.4b})$$

As both $[1 - \cos(\Omega u)]$ and $\sin(\Omega u)$ are real we can take ‘Im’ outside the integral,

$$\operatorname{Re} \chi(\Omega) = \operatorname{Im} \int_0^\infty [1 - \cos(\Omega u)] S(u) du, \quad (\text{C.5a})$$

$$\operatorname{Im} \chi(\Omega) = \operatorname{Im} \int_0^\infty \sin(\Omega u) S(u) du. \quad (\text{C.5b})$$

Now we promote $u \in \mathbb{R}$ to a complex variable $u = x + iy \in \mathbb{C}$. The integrals then become integrals on the complex plane,

$$\operatorname{Re} \chi(\Omega) = \operatorname{Im} \int_{\Gamma} [1 - \cos(\Omega x) \cosh(\Omega y) + i \sin(\Omega x) \sinh(\Omega y)] S(x + iy) du, \quad (\text{C.6a})$$

$$\operatorname{Im} \chi(\Omega) = \operatorname{Im} \int_{\Gamma} [\sin(\Omega x) \cosh(\Omega y) + i \cos(\Omega x) \sinh(\Omega y)] S(x + iy) du, \quad (\text{C.6b})$$

where Γ is our contour of integration. To motivate a choice of contour, let’s consider the form of $D(x + iy)$ and $S(x + iy)$,

$$D(x + iy) = \frac{w^2}{\beta v^2} \left\{ \left[a^2 - \beta^2/4 - b \cos(vx) \cosh(v(y - \beta/2)) + x^2 + y(\beta - y) \right] + i \left[b \sin(vx) \sinh(v(y - \beta/2)) + 2x(y - \beta/2) \right] \right\} \quad (\text{C.7})$$

$$S(x + iy) = \frac{2\alpha}{3\sqrt{\pi}} \frac{\cos(x + i(y - \beta/2))}{\sinh(\beta/2) [D(x + iy)]^{\frac{3}{2}}}. \quad (\text{C.8})$$

Now we notice that $D(x + iy)$ and $S(x + iy)$ are trivially real when $y = \beta/2$. This gives the results,

$$D(x + i\beta/2) = \frac{w^2}{\beta v^2} \left[x^2 + a^2 - b \cos(vx) \right] \in \mathbb{R} \quad (\text{C.9})$$

$$S(x + i\beta/2) = \frac{2\alpha}{3\sqrt{\pi}} \frac{\beta^{\frac{3}{2}}}{\sinh(\beta/2)} \left(\frac{v}{w} \right)^3 \frac{\cos(x)}{[x^2 + a^2 - b \cos(vx)]^{\frac{3}{2}}} \in \mathbb{R}. \quad (\text{C.10})$$

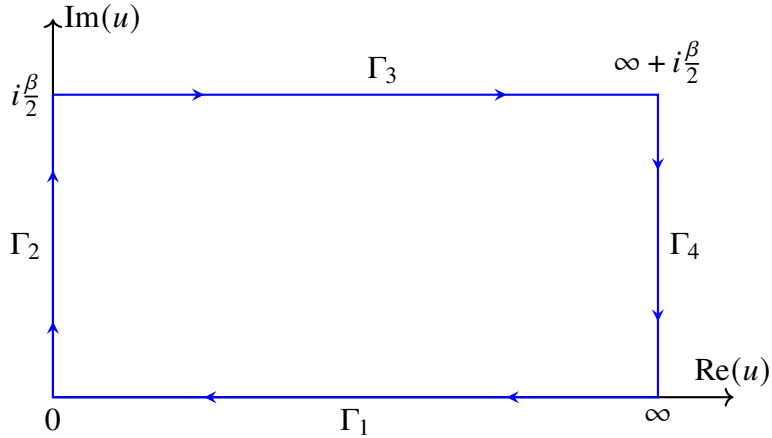


Figure C.1: The complex contour chosen to transform the integral in Eq. (C.1). No singularities lie within the closed contour so the contour integral is zero.

From this, we choose to integrate over the contours $\Gamma_1 \in (\infty + 0i, 0 + 0i] \rightarrow \Gamma_2 \in [0 + i0, 0 + i\beta/2] \rightarrow \Gamma_3 \in [0 + i\beta/2, \infty + i\beta/2] \rightarrow \Gamma_4 \in (\infty + i\beta/2, \infty + 0i)$ as shown in Fig. C.1. Since the integrands in Eqs. (C.6a) and (C.6b) are analytic in this region, this closed contour integral will be zero. (There is a pole in $\text{Im}S(x + iy)$ at $0 + i0$, but this is cancelled by the zero of the elementary/trigonometric functions in front of it at this point.) The closing piece of the contour lies at $x \rightarrow \infty$ and can be neglected as $S(x + iy) \rightarrow 0$ in this limit. Thus, for the real part of $\chi(\Omega)$ we have,

$$\begin{aligned} \int_0^\infty [1 - \cos(\Omega x)] S(x) dx &= \int_0^{\beta/2} [1 - \cosh(\Omega y)] S(iy) d(iy) \\ &+ \int_0^\infty \left[1 - \cos(\Omega x) \cosh\left(\frac{\Omega\beta}{2}\right) + i \sin(\Omega x) \sinh\left(\frac{\Omega\beta}{2}\right) \right] S\left(x + \frac{i\beta}{2}\right) dx, \end{aligned} \quad (\text{C.11})$$

and for the imaginary part of $\chi(\Omega)$ we have,

$$\begin{aligned} \int_0^\infty \sin(\Omega x) S(x) dx &= i \int_0^{\beta/2} \sinh(\Omega y) S(iy) d(iy) \\ &+ \int_0^\infty \left[\sin(\Omega x) \cosh\left(\frac{\Omega\beta}{2}\right) + i \cos(\Omega x) \sinh\left(\frac{\Omega\beta}{2}\right) \right] S\left(x + \frac{i\beta}{2}\right) dx. \end{aligned} \quad (\text{C.12})$$

We can now see more clearly why we integrate at $y = \beta/2$. Since $S(x + i\beta/2)$ is real, acting ‘Im’ on these integrals will cancel the second integral in the contour integral for $\text{Im}\chi(\Omega)$ (which is entirely real), and the third integral for both $\text{Re}\chi(\Omega)$ and $\text{Im}\chi(\Omega)$ is simplified due to the absence of any cross-terms that would have resulted for other values of y as $S(x + iy)$ would have been complex. To see that the second integral for $\text{Im}\chi(\Omega)$ is real, we

need to see if $S(iy)$ is real. First, we look at $D(iy)$, which is given by,

$$D(iy) = \frac{w^2}{\beta v^2} \left[a^2 - \frac{\beta^2}{4} + y(\beta - y) - b \cosh\left(vy - \frac{\beta v}{2}\right) \right] \in \mathbb{R}, \quad (\text{C.13})$$

and then $S(iy)$ is given by,

$$S(iy) = \frac{2\alpha}{3\sqrt{\pi}} \frac{\beta^{3/2}}{\sinh(\beta/2)} \left(\frac{v}{w}\right)^3 \frac{\cosh(y - \beta/2)}{\left[a^2 - \beta^2/4 + y(\beta - y) - b \cosh(v(y - \beta/2))\right]^{3/2}} \in \mathbb{R}, \quad (\text{C.14})$$

so $S(iy)$ is indeed real. Since the second integral for $\text{Im}\chi(\Omega)$ has two complex i 's and $S(iy)$ is real, the whole integral is entirely real and so it doesn't contribute to $\text{Im}\chi(\Omega)$. Unfortunately, $\text{Re}\chi(\Omega)$ does not simplify as nicely as $\text{Im}\chi(\Omega)$ because the second integral is imaginary, and so is still present after taking only the imaginary parts. Nonetheless, for $\text{Re}\chi(\Omega)$ we get,

$$\begin{aligned} \text{Re}\chi(\Omega) &= \text{Im} \int_0^\infty [1 - \cos(\Omega x)] S(x) dx \\ &= \frac{2\alpha}{3\sqrt{\pi}} \frac{\beta^{3/2}}{\sinh(\beta/2)} \left(\frac{v}{w}\right)^3 \left\{ \sinh\left(\frac{\Omega\beta}{2}\right) \int_0^\infty \frac{\sin(\Omega x)\cos(x) dx}{[x^2 + a^2 - b \cos(vx)]^{3/2}} \right. \\ &\quad \left. + \int_0^{\beta/2} \frac{[1 - \cosh(\Omega x)] \cosh(x - \beta/2) dx}{[a^2 - \beta^2/4 + x(\beta - x) - b \cosh(v(x - \beta/2))]^{3/2}} \right\}, \end{aligned} \quad (\text{C.15})$$

and for $\text{Im}\chi(\Omega)$ we get,

$$\begin{aligned} \text{Im}\chi(\Omega) &= \text{Im} \int_0^\infty \sin(\Omega x) S(x) dx \\ &= \frac{2\alpha}{3\sqrt{\pi}} \frac{\beta^{3/2} \sinh(\Omega\beta/2)}{\sinh(\beta/2)} \left(\frac{v}{w}\right)^3 \int_0^\infty \frac{\cos(\Omega x)\cos(x) dx}{[x^2 + a^2 - b \cos(vx)]^{3/2}}. \end{aligned} \quad (\text{C.16})$$

C.2 $\text{Im}\chi$ expansion in Bessel-K functions

In Devreese et al. [18], the integral in Eq. (C.16) is expanded in an infinite sum of modified Bessel functions of the second kind. Here, we follow the same procedure and arrive at the same result, but provide detailed workings. Specifically, we are interested in solving the integral,

$$\int_0^\infty \frac{\cos(\Omega x)\cos(x) dx}{[x^2 + a^2 - b \cos(vx)]^{3/2}}. \quad (\text{C.17})$$

We start by noticing that,

$$\left| \frac{b \cos(vx)}{x^2 + a^2} \right| < 1 \quad \text{if } v > 0 \text{ and } \beta > 0 , \quad (\text{C.18})$$

so we can do a binomial expansion of the denominator,

$$\begin{aligned} & \int_0^\infty \frac{\cos(\Omega x)\cos(x)}{(x^2 + a^2)^{3/2}} \left[1 - \frac{b \cos(vx)}{x^2 + a^2} \right]^{-3/2} dx \\ &= \int_0^\infty dx \frac{\cos(\Omega x)\cos(x)}{(x^2 + a^2)^{3/2}} \sum_{n=0}^{\infty} \binom{-3/2}{n} \frac{(-b)^n \cos^n(vx)}{(x^2 + a^2)^n} dx \\ &= \sum_{n=0}^{\infty} \binom{-3/2}{n} (-b)^n \int_0^\infty \frac{\cos(\Omega x)\cos(x)\cos^n(vx)}{(x^2 + a^2)^{n+3/2}} dx, \end{aligned} \quad (\text{C.19})$$

where $\binom{-3/2}{n}$ is a binomial coefficient. Next we expand $\cos^n(vx)$ using the power-reduction formula,

$$\cos^n(vx) = \frac{2}{2^n} \sum_{k=0}^{\lfloor \frac{n-1}{2} \rfloor} \binom{n}{k} \cos((n-2k)vx) + \frac{(1-n \bmod 2)}{2^n} \binom{n}{\frac{n}{2}}, \quad (\text{C.20})$$

where the second term comes from even n contributions only. Substituting this into our integral gives,

$$\begin{aligned} & \sum_{n=0}^{\infty} \binom{-3/2}{n} \left(-\frac{b}{2} \right)^n \left[2 \sum_{k=0}^{\lfloor \frac{n-1}{2} \rfloor} \binom{n}{k} \int_0^\infty \frac{\cos(\Omega x)\cos(x)\cos((n-2k)vx)}{(x^2 + a^2)^{n+3/2}} dx \right. \\ & \quad \left. + (1-n \bmod 2) \binom{n}{\frac{n}{2}} \int_0^\infty \frac{\cos(\Omega x)\cos(x)}{(x^2 + a^2)^{n+3/2}} dx \right]. \end{aligned} \quad (\text{C.21})$$

We can now combine the cosines inside of the integrals into sums of single cosines using,

$$\begin{aligned} & \cos(\Omega x)\cos(x)\cos(vx(n-2k)) = \\ & \quad \frac{1}{4} \{ \cos(x(\Omega + 1 + v(n-2k))) + \cos(x(\Omega - 1 + v(n-2k))) \\ & \quad + \cos(x(\Omega + 1 - v(n-2k))) + \cos(x(\Omega - 1 - v(n-2k))) \} \end{aligned} \quad (\text{C.22})$$

$$\equiv \frac{1}{4} \sum_{z_4} \cos(x z_{k,4}^n)$$

where for brevity we have defined $z_{k,4}^n \in \{\Omega + 1 + v(n - 2k), \Omega - 1 + v(n - 2k), \Omega + 1 - v(n - 2k), \Omega - 1 - v(n - 2k)\}$. Likewise,

$$\begin{aligned}\cos(\Omega x)\cos(x) &= \frac{1}{2}\{\cos(x(\Omega + 1)) + \cos(x(\Omega - 1))\} \\ &\equiv \frac{1}{2} \sum_{z_2} \cos(xz_2)\end{aligned}\tag{C.23}$$

where for brevity we have defined $z_2 \in \{\Omega + 1, \Omega - 1\}$. Substituting these into our expansion gives,

$$\begin{aligned}\sum_{n=0}^{\infty} \binom{-3/2}{n} \left(-\frac{b}{2}\right)^n &\left[2 \sum_{k=0}^{\lfloor \frac{n-1}{2} \rfloor} \binom{n}{k} \sum_{z_4} \int_0^{\infty} \frac{\cos(xz_{k,4}^n(\Omega))}{(x^2 + a^2)^{n+3/2}} dx \right. \\ &\left. + (1 - n \text{mod} 2) \binom{n}{\frac{n}{2}} \sum_{z_2} \int_0^{\infty} \frac{\cos(xz_2(\Omega))}{(x^2 + a^2)^{n+3/2}} dx \right].\end{aligned}\tag{C.24}$$

We now have a lot of integrals of the form,

$$\int_0^{\infty} \frac{\cos(xz)}{(x^2 + a^2)^{n+3/2}} dx,\tag{C.25}$$

which is an integral representation of modified Bessel functions of the second kind,

$$\begin{aligned}\int_0^{\infty} \frac{\cos(xz)}{(x^2 + a^2)^{n+3/2}} dx &= \frac{\sqrt{\pi}}{\Gamma(n + 3/2)} K_{n+1}(|z|a) \left| \frac{z}{2a} \right|^{n+1} \\ &\equiv B_n(z)\end{aligned}\tag{C.26}$$

Thus, overall we can expand $\text{Im}\chi(\Omega)$ in a series of these Bessel functions,

$$\begin{aligned}\text{Im}\chi(\Omega) &= \frac{2\alpha\beta^{\frac{3}{2}}}{3\sqrt{\pi}} \frac{\sinh(\frac{\Omega\beta}{2})}{\sinh(\frac{\beta}{2})} \left(\frac{v}{w} \right)^3 \sum_{n=0}^{\infty} \binom{-\frac{3}{2}}{n} \left(-\frac{b}{2} \right)^n \left[\sum_{k=0}^{\lfloor \frac{n-1}{2} \rfloor} \binom{n}{k} \sum_{z_4} B_n(z_{k,4}^n(\Omega)) \right. \\ &\quad \left. + (1 - n \text{mod} 2) \binom{n}{\frac{n}{2}} \sum_{z_2} B_n(z_2(\Omega)) \right]\end{aligned}\tag{C.27}$$

where $a^2 = \beta^2/4 + R\beta \coth(\beta v/2)$, $b = R\beta / \sinh(\beta v/2)$ and $R = (v^2 - w^2)/(w^2 v)$. Also, $z_{k,4}^n(\Omega) \in \{\Omega + 1 + v(n - 2k), \Omega - 1 + v(n - 2k), \Omega + 1 - v(n - 2k), \Omega - 1 - v(n - 2k)\}$ and $z_2(\Omega) \in \{\Omega + 1, \Omega - 1\}$.

C.3 $\text{Re}\chi$ expansion in Bessel-I, Struve-L and ${}_1F_2$ hypergeometric functions

Motivated by the expansion of $\text{Im}\chi(\Omega)$ in Devreese et al. [18], we provide a similar expansion for $\text{Re}\chi(\Omega)$. I follow a similar procedure as for $\text{Im}\chi(\Omega)$ and notice that our efforts focus on solving the integrals,

$$\int_0^\infty \frac{\sin(\Omega x)\cos(x) dx}{[x^2 + a^2 - b \cos(vx)]^{3/2}}, \quad (\text{C.28})$$

$$\int_0^{\beta/2} \frac{[1 - \cosh(\Omega x)] \cosh(x - \beta/2) dx}{[a^2 - \beta^2/4 + x(\beta - x) - b \cosh(v(x - \beta/2))]^{3/2}}. \quad (\text{C.29})$$

The first integral is similar to Eq. (C.17), just with a cosine swapped out for a sine. Following a similar procedure as for Eq. (C.17) gives,

$$\begin{aligned} & \int_0^\infty \frac{\sin(\Omega x)\cos(x) dx}{[x^2 + a^2 - b \cos(vx)]^{3/2}} \\ &= \sum_{n=0}^{\infty} \binom{-3/2}{n} \left(-\frac{b}{2}\right)^n \left[2 \sum_{k=0}^{\lfloor \frac{n-1}{2} \rfloor} \binom{n}{k} \sum_{z_4} \int_0^\infty \frac{\sin(xz_{k,4}^n(\Omega))}{(x^2 + a^2)^{n+3/2}} dx \right. \\ &+ (1 - n \bmod 2) \binom{n}{\frac{n}{2}} \sum_{z_2} \int_0^\infty \frac{\sin(xz_2(\Omega))}{(x^2 + a^2)^{n+3/2}} dx \Big], \end{aligned} \quad (\text{C.30})$$

where we now look for any special functions for which,

$$\int_0^\infty \frac{\sin(xz)}{(x^2 + a^2)^{n+3/2}} dx \quad (\text{C.31})$$

is the integral representation. We found that,

$$\begin{aligned} \int_0^\infty \frac{\sin(xz)}{(x^2 + a^2)^{n+3/2}} dx &= \frac{\sqrt{\pi}}{2} \frac{\Gamma(-\frac{1}{2} - n) \operatorname{sgn}(z)|z|^{n+1}}{(2a)^{n+1}} [I_{n+1}(|z|a) - \mathbf{L}_{-(n+1)}(|z|a)] \\ &\equiv J_n(z) \end{aligned} \quad (\text{C.32})$$

for $n \geq 0$ and $a \geq 0$. Here $\operatorname{sgn}(x)$ is the signum function, $I_n(x)$ is the modified Bessel function of the first kind, $\mathbf{L}_n(x)$ is the modified Struve function. Therefore, for $\text{Re}\chi(\Omega)$

we have,

$$\begin{aligned}
\operatorname{Re}\chi(\Omega) = & \frac{2\alpha\beta^{3/2}}{3\sqrt{\pi}} \frac{\sinh\left(\frac{\Omega\beta}{2}\right)}{\sinh(\beta/2)} \left(\frac{v}{w}\right)^3 \left\{ \sum_{n=0}^{\infty} \binom{-\frac{3}{2}}{n} \left(\frac{b}{2}\right)^n \left[\sum_{k=0}^{\lfloor \frac{n-1}{2} \rfloor} \binom{n}{k} \sum_{z_4} J_n(z_{k,4}^n(\Omega)) \right. \right. \\
& + (1 - n \bmod 2) \binom{n}{\frac{n}{2}} \sum_{z_2} J_n(z_2(\Omega)) \Big] \Big\} \\
& + \frac{2\alpha}{3\sqrt{\pi}} \frac{\beta^{3/2}}{\sinh(\beta/2)} \left(\frac{v}{w}\right)^3 \int_0^{\beta/2} \frac{[1 - \cosh(\Omega x)] \cosh(x - \beta/2) dx}{[a^2 - \beta^2/4 + x(\beta - x) - b \cosh(v(x - \beta/2))]^{3/2}}
\end{aligned} \tag{C.33}$$

where a , b , z_4 and z_2 are the same as before. Expanding the second integral with the hyperbolic integrand is more complicated. We start by doing a change of variables $x \rightarrow (1 - x)\beta/2$ to transform the denominator into a similar form as before and to change the limits to $[0, 1]$,

$$\begin{aligned}
& \int_0^{\beta/2} \frac{[1 - \cosh(\Omega x)] \cosh(x - \beta/2) dx}{[a^2 - \beta^2/4 + x(\beta - x) - b \cosh(v(x - \beta/2))]^{3/2}} \\
& \longrightarrow \frac{\beta}{2} \int_0^1 \frac{[1 - \cosh(\Omega\beta[1 - x]/2)] \cosh(\beta x/2) dx}{[a^2 - (\beta x/2)^2 - b \cosh(\beta vx/2)]^{3/2}}.
\end{aligned} \tag{C.34}$$

Now we see that for $x \in [0, 1]$

$$\left| \frac{b \cosh(v\beta x/2)}{a^2 - (\beta x/2)^2} \right| < 1 \quad \text{if } v > 0 \text{ and } \beta > 0 \tag{C.35}$$

so we can do a binomial expansion of the denominator as before,

$$\sum_{n=0}^{\infty} \binom{-\frac{3}{2}}{n} \left(\frac{2}{\beta}\right)^{2n+2} (-b)^n \int_0^1 \frac{[1 - \cosh(\Omega\beta[1 - x]/2)] \cosh(\beta x/2) \cosh^n(v\beta x/2)}{((2a/\beta)^2 - x^2)^{n+3/2}} dx. \tag{C.36}$$

Then, I do another binomial expansion of the remaining denominator

$$\begin{aligned}
& \sum_{n=0}^{\infty} \binom{-\frac{3}{2}}{n} \left(\frac{2}{\beta}\right)^{2n+2} (-b)^n \sum_{m=0}^{\infty} \binom{-n - \frac{3}{2}}{m} (-1)^m \left(\frac{\beta}{2a}\right)^{2n+2m+3} \\
& \times \int_0^1 \left[1 - \cosh\left(\frac{\Omega\beta[1 - x]}{2}\right) \right] \cosh\left(\frac{\beta x}{2}\right) \cosh^n\left(\frac{v\beta x}{2}\right) x^{2m} dx.
\end{aligned} \tag{C.37}$$

We can then expand the product of hyperbolic cosines in the integrand,

$$\begin{aligned}
& \sum_{n=0}^{\infty} \binom{-\frac{3}{2}}{n} \left(\frac{2}{\beta}\right)^{2n+2} (-b)^n \sum_{m=0}^{\infty} \binom{-n - \frac{3}{2}}{m} (-1)^m \left(\frac{\beta}{2a}\right)^{2n+2m+3} \frac{1}{2^n} \\
& \times \left\{ \binom{n}{\frac{n}{2}} (1 - n \bmod 2) \left[\int_0^1 \frac{\cosh\left(\frac{\beta z_1 x}{2}\right)}{x^{-2m}} dx \right. \right. \\
& - \frac{1}{2} \sum_{z_2} \left(\cosh\left(\frac{\Omega\beta}{2}\right) \int_0^1 \frac{\cosh\left(\frac{\beta z_2 x}{2}\right)}{x^{-2m}} dx - \sinh\left(\frac{\Omega\beta}{2}\right) \int_0^1 \frac{\sinh\left(\frac{\beta z_2 x}{2}\right)}{x^{-2m}} dx \right) \\
& \left. \left. + \sum_{k=0}^{\left[\frac{n-1}{2}\right]} \binom{n}{k} \left[\sum_{z_3} \int_0^1 \frac{\cosh\left(\frac{\Omega\beta z_3 x}{2}\right)}{x^{-2m}} dx \right. \right. \right. \\
& \left. \left. \left. - \frac{1}{2} \sum_{z_4} \left(\cosh\left(\frac{\Omega\beta}{2}\right) \int_0^1 \frac{\cosh\left(\frac{\Omega\beta z_4 x}{2}\right)}{x^{-2m}} dx - \sinh\left(\frac{\Omega\beta}{2}\right) \int_0^1 \frac{\sinh\left(\frac{\Omega\beta z_4 x}{2}\right)}{x^{-2m}} dx \right) \right] \right\} \quad (C.38)
\end{aligned}$$

where $z_1 = 1$, $z_2(\Omega) \in \{\Omega + 1, \Omega - 1\}$, $z_{k,3}^n \in \{1 + v(n - 2k), 1 - v(n - 2k)\}$ and $z_{k,4}^n(\Omega) \in \{\Omega + 1 + v(n - 2k), \Omega - 1 + v(n - 2k), \Omega + 1 - v(n - 2k), \Omega - 1 - v(n - 2k)\}$.

Now we have two integrals of the forms

$$\int_0^1 \cosh(zx)x^{2m} dx, \quad \int_0^1 \sinh(zx)x^{2m} dx, \quad (C.39)$$

which are the integral forms of the generalised hypergeometric functions

$$\int_0^1 \cosh(zx)x^{2m} dx = {}_1F_2 \left[\begin{matrix} m + \frac{1}{2} \\ \frac{1}{2} \end{matrix} ; \frac{z^2}{4} \right] = \sum_{t=0}^{\infty} \frac{z^{2t}}{(2t + 2m + 1)(2t)!}, \quad m > -\frac{1}{2} \quad (C.40a)$$

$$\int_0^1 \sinh(zx)x^{2m} dx = \frac{z}{2m + 2} {}_1F_2 \left[\begin{matrix} m + 1 \\ \frac{3}{2} \end{matrix} ; \frac{z^2}{4} \right] = \sum_{t=0}^{\infty} \frac{z^{2t+1}}{(2t + 2m + 2)(2t + 1)!}, \quad m > -1. \quad (C.40b)$$

For brevity, we will define

$${}_1F_2^c(z) \equiv {}_1F_2 \left[\begin{matrix} m + \frac{1}{2} \\ \frac{1}{2} \end{matrix} ; \frac{\beta^2 z^2}{16} \right] = \sum_{t=0}^{\infty} \frac{(\beta z/2)^{2t}}{(2t + 2m + 1)(2t)!} \quad (C.41a)$$

$${}_1F_2^s(z) \equiv \frac{\beta z}{4m + 4} {}_1F_2 \left[\begin{matrix} m + 1 \\ \frac{3}{2} \end{matrix} ; \frac{\beta^2 z^2}{16} \right] = \sum_{t=0}^{\infty} \frac{(\beta z/2)^{2t+1}}{(2t + 2m + 2)(2t + 1)!} \quad (C.41b)$$

so that Eq. (C.38) becomes

$$\begin{aligned} & \sum_{n=0}^{\infty} \binom{-\frac{3}{2}}{n} \left(\frac{2}{\beta}\right)^{2n+2} (-b)^n \sum_{m=0}^{\infty} \binom{-n - \frac{3}{2}}{m} (-1)^m \left(\frac{\beta}{2a}\right)^{2n+2m+3} \frac{1}{2^n} \\ & \times \left\{ \binom{n}{\frac{n}{2}} (1 - n \text{mod} 2) \left[{}_1F_2^c(z_1) - \frac{1}{2} \sum_{z_2} \left(\cosh\left(\frac{\Omega\beta}{2}\right) {}_1F_2^c(z_2) - \sinh\left(\frac{\Omega\beta}{2}\right) {}_1F_2^s(z_2) \right) \right] \right. \\ & \left. + \sum_{k=0}^{\lfloor \frac{n-1}{2} \rfloor} \binom{n}{k} \left[\sum_{z_3} {}_1F_2^c(z_3) - \frac{1}{2} \sum_{z_4} \left(\cosh\left(\frac{\Omega\beta}{2}\right) {}_1F_2^c(z_4) - \sinh\left(\frac{\Omega\beta}{2}\right) {}_1F_2^s(z_4) \right) \right] \right\} \end{aligned} \quad (\text{C.42})$$

which we can reduce further by defining,

$$M_n^{c/s}(z) \equiv \sum_{m=0}^{\infty} \binom{-n - \frac{3}{2}}{m} (-1)^m a^{-2(n+m+1)} \left(\frac{\beta}{2}\right)^{2m+1} {}_1F_2^{c/s}(z), \quad (\text{C.43})$$

to give,

$$\begin{aligned} & \sum_{n=0}^{\infty} \binom{-\frac{3}{2}}{n} \left(\frac{-b}{2}\right)^n \left\{ \binom{n}{\frac{n}{2}} (1 - n \text{mod} 2) \left[M_n^c(z_1) - \frac{1}{2} \sum_{z_2} \left(\cosh\left(\frac{\Omega\beta}{2}\right) M_n^c(z_2) \right. \right. \right. \\ & \left. \left. \left. - \sinh\left(\frac{\Omega\beta}{2}\right) M_n^s(z_2) \right) \right] \right. \\ & \left. + \sum_{k=0}^{\lfloor \frac{n-1}{2} \rfloor} \binom{n}{k} \left[\sum_{z_3} M_n^c(z_3) - \frac{1}{2} \sum_{z_4} \left(\cosh\left(\frac{\Omega\beta}{2}\right) M_n^c(z_4) \right. \right. \right. \\ & \left. \left. \left. - \sinh\left(\frac{\Omega\beta}{2}\right) M_n^s(z_4) \right) \right] \right\}. \end{aligned} \quad (\text{C.44})$$

Combining this with the rest of $\text{Re}\chi(\Omega)$ gives,

$$\begin{aligned} \text{Re}\chi(\Omega) = & \frac{2\alpha\beta^{3/2}v^3}{3\sqrt{\pi}w^3 \sinh(\beta/2)} \sum_{n=0}^{\infty} \binom{-\frac{3}{2}}{n} \left(-\frac{b}{2}\right)^n \\ & \times \left\{ \binom{n}{\frac{n}{2}} (1 - n \text{mod} 2) \left[M_n^c(1) + \frac{1}{2} \sum_{z_2} \left(\sinh\left(\frac{\Omega\beta}{2}\right) [M_n^s(z_2(\Omega)) + J_n(z_2(\Omega))] \right. \right. \right. \\ & \left. \left. \left. - \cosh\left(\frac{\Omega\beta}{2}\right) M_n^c(z_2(\Omega)) \right) + \sum_{k=0}^{\lfloor \frac{n-1}{2} \rfloor} \binom{n}{k} \left[\sum_{z_3} M_n^c(z_{k,3}^n) + \frac{1}{2} \sum_{z_4} \left(\sinh\left(\frac{\Omega\beta}{2}\right) [M_n^s(z_{k,4}^n(\Omega)) + J_n(z_{k,4}^n(\Omega))] \right. \right. \right. \\ & \left. \left. \left. - \cosh\left(\frac{\Omega\beta}{2}\right) M_n^s(z_{k,4}^n(\Omega)) \right) \right] \right\}. \end{aligned} \quad (\text{C.45})$$

So, altogether, I have the expansion for the memory function,

$$\begin{aligned}
\chi(\Omega) = & \frac{2\alpha\beta^{3/2}v^3}{3\sqrt{\pi}w^3\sinh(\beta/2)} \sum_{n=0}^{\infty} \binom{-\frac{3}{2}}{n} \left(-\frac{b}{2}\right)^n \\
& \times \left\{ \binom{n}{\frac{n}{2}} (1 - n \bmod 2) \left[M_n^c(1) + \frac{1}{2} \sum_{z_2} \left(\sinh\left(\frac{\Omega\beta}{2}\right) [M_n^s(z_2) + J_n(z_2) + iB_n(z_2)] \right. \right. \right. \\
& - \cosh\left(\frac{\Omega\beta}{2}\right) M_n^c(z_2(\Omega)) \\
& + \sum_{k=0}^{\lfloor \frac{n-1}{2} \rfloor} \binom{n}{k} \left[\sum_{z_3} M_n^c(z_{k,3}^n) + \frac{1}{2} \sum_{z_4} \left(\sinh\left(\frac{\Omega\beta}{2}\right) [M_n^s(z_{k,4}^n) + J_n(z_{k,4}^n) + iB_n(z_{k,4}^n)] \right. \right. \\
& \left. \left. \left. - \cosh\left(\frac{\Omega\beta}{2}\right) M_n^s(z_{k,4}^n) \right) \right] \right\}.
\end{aligned} \tag{C.46}$$

APPENDIX D



COHERENT STATES